CORONARY VESSEL QUANTIFICATION FOR INTERVENTIONAL DEVICE SIZING USING INVERSE GEOMETRY X-RAY FLUOROSCOPY

By

Michael T. Tomkowiak

A dissertation submitted in partial fulfillment of the
requirements for the degree of

Doctor of Philosophy
(Biomedical Engineering)

At the
UNIVERSITY OF WISCONSIN – MADISON
2013

Date of final oral examination: October 2, 2013

The dissertation is approved by the following members of the Final Oral Committee:
Walter Block, Professor, Biomedical Engineering
Michael Speidel, Assistant Professor, Medical Physics
Amish Raval, Assistant Professor, Medicine
Charles Mistretta, Professor, Medical Physics
Oliver Wieben, Assistant Professor, Medical Physics

Coronary Vessel Quantification for Interventional Device Sizing using Inverse Geometry X-ray Fluoroscopy

Abstract

Michael T. Tomkowiak
Under the supervision of Professor Michael A. Speidel
At the University of Wisconsin – Madison

Proper interventional device selection is critical for effective treatment of lesions in coronary arteries. Ideally, the interventional device (angioplasty balloon, stent, etc.) should be as long as the coronary stenosis, and when deployed, the diameter of the device should match that of nearby healthy artery segments. Quantitative coronary angiography (QCA) can be used to support device size selection for cardiovascular interventions, but the accuracy of QCA measurements using conventional x-ray fluoroscopy depends on proper calibration of vessel magnification with a reference object and the avoidance of vessel foreshortening. Scanning Beam Digital X-ray (SBDX) is a low-dose inverse geometry x-ray fluoroscopy system that produces multiple tomosynthetic images at 15-30 frame/sec instead of conventional 2D projections. It is hypothesized that by using the out-of-plane blurring property of tomosynthesis imaging, the coronary vessels can be localized in 3D in a single frame period, which can be used to directly calculate the magnification of the vessel, as well as to determine the true vessel length when the vessel appears foreshortened. This would overcome the limitations of conventional

QCA methods, enabling calibration-free vessel sizing that is automated, rapid, and accurate over a range of imaging conditions.

This dissertation describes the design and validation of a vessel sizing algorithm based on tomosynthesis imaging with SBDX. An initial implementation of the method demonstrated the feasibility of calibration-free vessel sizing in phantoms over a range of vessel magnifications and degrees of foreshortening. The algorithm was then redesigned to improve robustness under sub-optimal imaging conditions. Further validation was performed in phantoms using a range of vessel magnifications, degrees of foreshortening, and levels of image quality. Provided that a minimal image quality was met (peak signal difference to noise ratio > 2) and vessel foreshortening was not extreme (angle relative to image plane ≤ 45°), sub-millimeter accuracy was achieved for both vessel length and diameter measurements. The algorithm was then validated in vivo by comparing vessel measurements between the algorithm and "gold standard" techniques (intravascular ultrasound for diameter, coronary CT angiography for segment length). Using a healthy porcine model, vessel measurement errors (mean ± 1 SD) were -0.49 ± 1.76 mm for length and 0.07 ± 0.27 mm for diameter. Results in phantoms and in vivo demonstrate this technique is capable of accurately determining vessel lengths and diameters in a range of clinically relevant conditions, without the limitations of conventional methods which require a magnification calibration step and the avoidance of foreshortening. Potential future areas of research include algorithm parameter optimization, validation in human subjects, and user interface design.

Acknowledgement

I would like express my sincere gratitude to my two advisors during the course of the work presented in this dissertation, Professor Michael Van Lysel and Professor Michael Speidel. Thank you both for your patience and encouragement over the years. The balance of guiding my research while allowing me to tackle problems in my own way gave me a sense of ownership over my work and fostered confidence in my abilities. You taught me how to be a good scientist, how to solve new problems, and how to effectively present my work to others. Your passion and enthusiasm for the SBDX project was inspiring, and I hope that my contributions lived up to your expectations.

I would also like to thank Professor Walter Block for helping me navigate the BME graduate program. I valued your support and guidance past the various PhD milestones, especially the dreaded BME qualifying exam.

The technical and scientific support for the SBDX system provided by our colleagues at Triple Ring Technologies has been outstanding. Many thanks go out to Joe Heanue, Tobias Funk, Brian Wilfley, Jamie Ku, Willem Ouborg, Quinn La, Steve Burion, Pallavi Chakravarty, Paul Kahn, Walt Cecka, Nick Lopez, and Jerry Pretti for keeping us up and running. I would also thank the NovaRay, Inc, for their ongoing development of the SBDX project.

I also thank everyone who worked with me on the MR/X-ray fusion project when I first started at UW. Special thanks go to Dr. Amish Raval, who brought me on as a research assistant and through whom I was introduced to the SBDX project. I appreciate all of those who spent many evenings participating in the validation experiments, including Drs. Karl Vigen, Drew Klein, Tim Hacker, Jill Koch, Gouging Song, and Larry Whitesel.

In addition to the professors and staff at UW, I also owe a lot to my fellow graduate students. To Matt McCormick, my long-time friend and go-to person for all things Linux and open source; to Brad McCabe, my fellow disciple of SBDX who provided me with a home base when I was commuting from Milwaukee to Madison; and to Chuck Hatt, for the helpful discussions on imaging processing and home-brewing: I thank you all.

I am grateful to my parents and my sister, who for as long as I can remember have always been there for me when I needed them and encouraged me to pursue my goals. They are also the only family members who knew me well enough to stop asking when I was going to be finished with my PhD.

I thank my daughter Zelda, who came into this world towards the end of my graduate school life when cynicism and apathy were at their peak. You arrived, and again I knew what it was to feel happiness.

Most of all, I thank my wife Emily, who, like me, had no idea what I was getting into when I started this journey. You stayed by my side through the ups and downs and supported me when I needed it most. You helped me to enjoy life, even when it required dragging me kicking and screaming. You are my best friend and the love of my life, always.

Table of Contents

List of Tables

List of Figures

List of Acronyms and Abbreviations

Cath-lab – Catheterization Laboratory

CCTA – Coronary Computed Tomography Angiography

CNR – Contrast to Noise Ratio

IVUS – Intravascular Ultrasound

PFU – Portable Fluoroscopy Unit

PMMA – Poly(methyl methacrylate)

QCA – Quantitative Coronary Angiography

SBDX – Scanning Beam Digital X-ray

SD – Standard Deviation

SDNR – Signal Difference to Noise Ratio

XA – X-ray Angiography

XRF – X-Ray Fluoroscopy

Chapter 1 – Introduction

1.1 Overview

Percutaneous coronary interventions (PCI) are among the most common procedures performed to treat heart disease. In 2006, an estimated 1.3 million PCIs were performed in the United States [1]. The devices used to perform PCI, namely angioplasty balloons and stents, come in a variety of sizes to match coronary vessels. The primary imaging tool that interventionalists use to guide PCI is x-ray fluoroscopy (XRF), which can easily visualize devices such as catheters and guide wires as well as vessel lumen edges with the use of contrast agents. For general procedure image guidance, XRF provides the necessary temporal resolution, spatial resolution, and anatomic field-of-view. However, measuring a vessel's length and diameter in physical dimensions in order to size a balloon or stent can be problematic using XRF alone. The XRF projection images compress 3D anatomy onto a 2D image, and vessel size and orientation can become distorted. Quantitative coronary angiography (QCA) methods exist to estimate true vessel dimensions from conventional XRF images, however these methods have some shortcomings directly related to conventional XRF imaging. Specifically, they require optimal, non-foreshortening views and means to scale the magnified x-ray image to physical units, which limits the accuracy and usability of the methods.

Scanning Beam Digital X-ray (SBDX) was developed as an alternative to conventional XRF to reduce the x-ray dose during long interventional procedures [2, 3]. As a result of its inverse geometry beam-scanning approach to image acquisition, SBDX produces tomosynthetic images instead of standard x-ray projections. The out-of-plane blurring quality of tomosynthesis images can be used to recover 3D depth information that is lost when using conventional XRF. This depth localization principle has been demonstrated for small, high contrast (metal) objects [4, 5], but the same methodology can be applied to contrast filled, coronary vessels. In this work, a novel method for measuring coronary vessels is presented, which adapts QCA methods from conventional XRF with the 3D localization properties of SBDX images in order to overcome the shortcomings of conational QCA techniques. The primary goal of this work is to create a method to match interventional devices to coronary vessels that is more accurate and easier to use than conventional QCA, which would, in turn, reduce complications, repeat procedures and improve patient outcomes.

1.2 Background

1.2.1 Coronary Artery Disease

The coronary arteries supply the heart with oxygenated blood and nutrients. Healthy arteries are strong, elastic, and have a smooth inner lumen, which allows blood to flow with little resistance. Atherosclerosis is a type of cardiovascular disease marked by thickening of the arterial walls and the development of fat and cholesterol deposits (plaques). As the plaques grow, the lumen cross section shrinks, restricting the flow of blood. As flow becomes restricted through the coronary arteries, the myocardium becomes starved for oxygen, leading to myocardial ischemia, which can cause chest pain and shortness of breath. The restriction of blood flow by the plaque also increases the probability of clot formation near the plaque. When a piece of the clot breaks free and travels down the coronary artery, it can completely block blood flow and cause a heart attack (myocardial infarction) [6].

1.2.2 Percutaneous Coronary Interventions (PCI)

Percutaneous coronary interventions (PCI) are minimally invasive procedures that aim to restore blood flow through the coronary vessels. After accessing the arterial system through an artery in the arm or leg, catheters and guide wires are steered to the aorta and coronary arteries, providing an avenue for therapeutic devices. Typically, a thin guide wire is pushed through the lesion, and an angioplasty balloon is guided over the wire and positioned within the lesion. As the balloon inflates, the plaque is compressed against the walls of the vessel increasing the inner diameter of the artery and restoring blood flow (Figure 1.1). A stent may also be deployed within the affected vessel to keep it open after the procedure. PCI is often preferred over coronary artery bypass grafts (CABG) for treating coronary artery disease because PCI carries fewer risks and has shorter recovery times.

The American Heart Association estimates that 1.3 million PCI procedures were performed in the 2006 in the United States, approximately half of which involved deploying a stent. Given the high volume of these procedures, any improvement in PCI methodology that reduces the costs and improves outcomes can have an overall large impact. Proper interventional device sizing (i.e. choosing the size of the angioplasty balloon or stent to use during PCI) directly impacts patient outcomes. Ideally, the device should cover the length of the lesion, and the diameter should match the healthy vessel on either side of the stenosis (reference diameter). Underdeployed devices increase the risk of acute closure due to stent thrombosis [7, 8] and gradual restenosis with recurrence of anginal symptoms [9, 10]. Over-sized devices may cause dissection leading to acute closure or coronary perforation [10-12]. Devices that are too short with respect to the lesion can result in edge dissection [13], restenosis [14], and unanticipated use of more devices. Overlapping multiple stents can also lead to restenosis [15, 16]. Excessively long devices risk thrombosis [17] and restenosis [18-20]. Choosing the correct device improves patient outcomes, avoids additional interventions, and reduces excess device utilization.

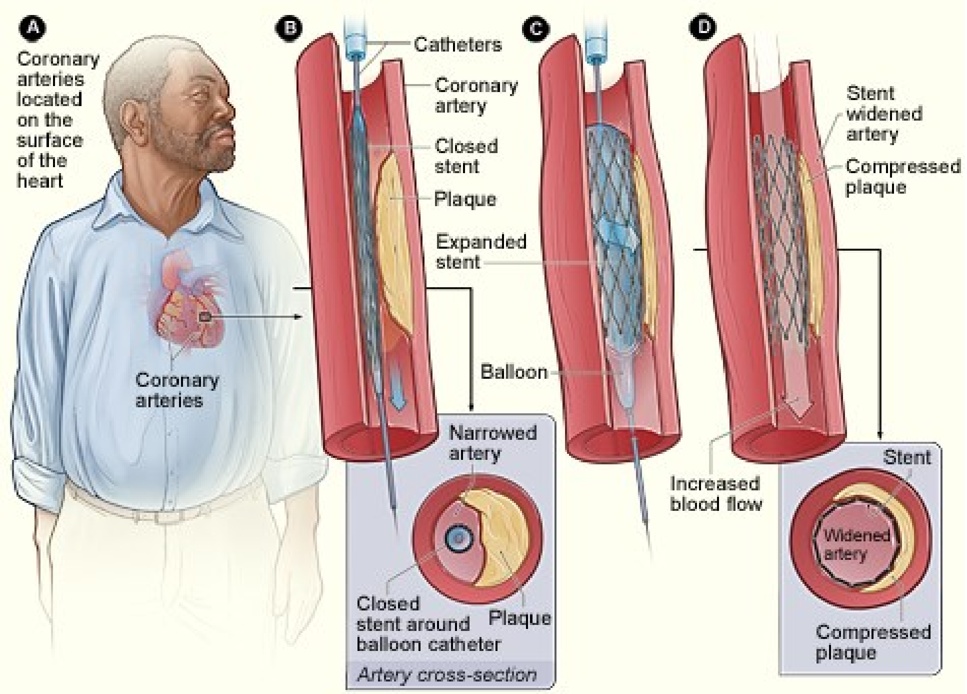

Figure 1.1 – Angioplasty with Stent Placement

(A) shows the location of the heart and coronary arteries. (B) shows the deflated balloon catheter and closed stent inserted into the narrow coronary artery. The inset image shows a cross-section of the artery with the inserted balloon catheter and closed stent. In figure (C), the balloon is inflated, expanding the stent and compressing the plaque against the artery wall. (D) shows the stent-widened artery. The inset image shows a cross-section of the compressed plaque and stent-widened artery. Figure and caption reproduced with permission from [21].

Given the impact of proper device sizing, interventional imaging techniques have been developed to quantitatively measure vessel dimensions. However, experience with our own catheterization lab (cath-lab) at the University of Wisconsin has shown that interventionalists are reluctant to routinely measure vessels before deploying devices, favoring experience and visual estimates from XRF imaging to determine the device size. Quantitative measurements are too cumbersome for impatient interventionalists. The following section summarizes the quantitative measurement techniques available in the cath-lab, as well as their strengths and weaknesses.

1.3 Quantitative Vessel Measurements

1.3.1 Intravascular Ultrasound (IVUS)

Intravascular ultrasound (IVUS) is the current gold standard for measuring lesions during an intervention [22-24]. An ultrasonic transducer in the tip of a special imaging catheter creates a high-resolution 2D tomographic image of the vessel cross section, which can be used to accurately measure lumen cross sectional area, minimal lumen diameter, and lesion eccentricity (Figure 1.2). After advancing the IVUS catheter tip past the lesion, a controlled mechanical pullback of the catheter can be used to image the cross section over the length of the lesion, providing the necessary information to select an interventional device.

Despite these imaging capabilities, IVUS is not routinely used for device sizing because of the cost of the imaging catheters, additional procedure time, and risk. Individual, single-use IVUS catheters cost on the order of $1000. The IVUS catheter must be guided into each vessel to be measured, which is time consuming. Although their occurrence is low, complications related to IVUS include vessel spasm, dissection, and damage to deployed stents [25, 26]. Accordingly, interventionalists must weigh the benefits of IVUS against the drawbacks to determine when it is warranted.

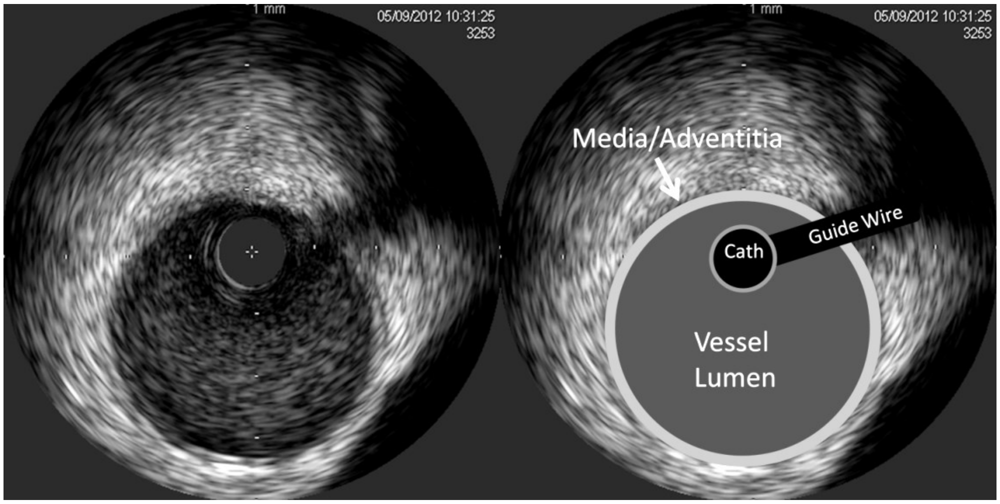

Figure 1.2 – Intravascular Ultrasound Image of a Health Vessel
IVUS shows a 2D cross section of a healthy coronary artery. The key in the right panel identifies the IVUS catheter, guide wire, and layers of the artery. Atherosclerosis causes a thickening of the media layer, which encroaches on the vessel lumen, restricting blood flow.

1.3.2 Quantitative coronary angiography

The main alternative to IVUS for interventional sizing of vessels is conventional quantitative coronary angiography (QCA), which measures vessel dimensions from XRF images. During an XRF cine angiogram, iodinated contrast is injected into the vessel of interest. The diameter and length of the vessel can be measured from the XRF projection (Figure 1.3). Conventional QCA was the gold standard for vessel measurements before IVUS technology was available. QCA software packages are still offered by the imaging vendors and third party companies.

QCA methods can be described by three main approaches: edge detection, videodensitometry, and model-fitting. Typically, the first step in each technique is to extract intensity profiles that are perpendicular to the vessel centerline. Edge detection algorithms look for the sharp transition between the background intensity and the contrast filled lumen to locate the vessel edge[27, 28]. This is usually accomplished by approximating the first and second derivatives of the vessel profile with difference operators, calculating a weighted sum of the two derivatives using empirically determined weights, and identifying the lumen edges as local extrema in the weighted sum. Since these methods rely on derivatives of the vessel profile, they are sensitive to image noise. Videodensitometry ignores the shape of the profile and calculates vessel diameter based on the relationship between the integral across the observed vessel profile and vessel cross sectional area[29]. While videodensitometric methods are less sensitive to image noise, they rely on accurate estimation of the background intensity[30]. Model based QCA methods, assume a parameterized vessel profile model and find a maximum likelihood solution that best matches the observed profile [31]. The model-based approach can be considered as a hybrid of edge detection and videodensitometry because both the shape and area of the vessel profile influence the parameter optimization. While this method is robust against image noise, it is more computationally intensive. The algorithm described in this dissertation uses a model based edge detection approach, which will be described in the following chapter.

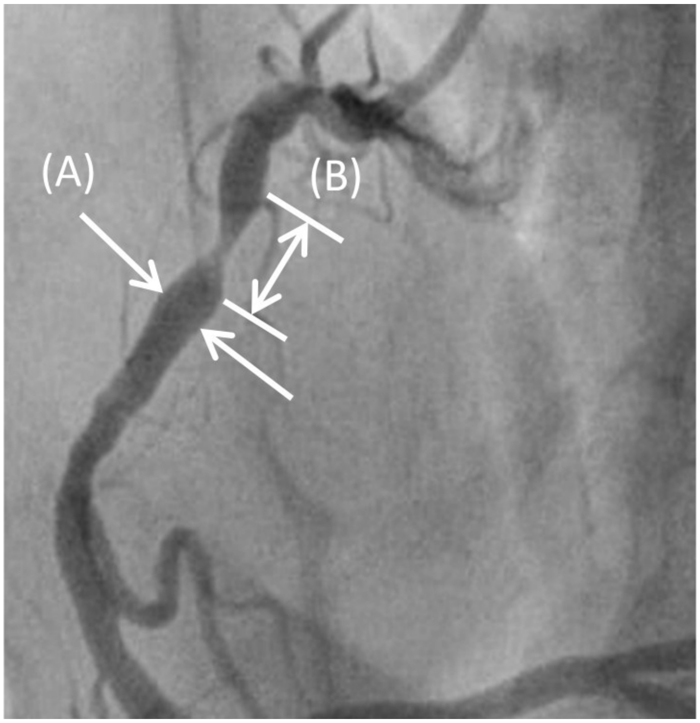

Figure 1.3 – Measuring Vessel Dimensions from a Coronary Angiogram.
Vessel dimensions can be measured from the vessel's projection in a coronary angiogram. The angioplasty balloon or stent should match the (A) diameter of the healthy vessel and (B) length of the lesion. Figure from [32].

Though widely available, QCA is not frequently used, presumably because of the time required to obtain accurate results. A key component to accurate QCA is the calibration step required to convert image measurements, in units of pixels, to physical dimensions, in units of millimeters [33]. In x-ray imaging with a point source and large area detector, all anatomy is projected onto a plane, and the magnification of each point on a vessel must be determined to accurately convert image pixel measurements to physical vessel dimensions. In practice, imaging an object of known size, such as a contrast filled catheter, in the same field of view provides a reference to determine the magnification of the angiogram. However, an extra step to analyze the reference object is required. Furthermore, this approach assumes that all points along the vessel have the same magnification as the reference object. Inaccuracy in this assumption and/or error in the measurement of the reference object carries over to vessel measurements [34, 35]. Another weakness of conventional QCA is the potential of foreshortening of vessels in the image. Vessels that are not parallel to the image plane will appear shortened by the projection imaging process, which in turn will lead to underestimation of vessel lesion length. Consequently, special attention must be paid to the angulation of the gantry when recording the images. Figure 1.4 illustrates the concepts of magnification and foreshortening in projection imaging. In practice, most interventionalists make an educated guess of vessel diameter and lesion length instead of using quantitative measurements.

1.3.3 3D Reconstruction Methods

A 3D volumetric reconstruction of the coronary arteries could be used for measuring vessel dimensions, if available. A conventional pre-procedure coronary CT angiogram (CCTA) could be used for length, although the accuracy of diameter measurements is limited by CT spatial resolution. Compared to IVUS, CT-based measurements overestimate the vessel lumen area [36]. An intraprocedural cone beam CT reconstruction using the XRF system is currently not practical due to cardiac motion, but several groups have proposed methods that reconstruct only the coronary tree [37-42]. The feasibility of measuring vessel segment length and diameter directly from these 3D reconstructions has been demonstrated in phantoms and *in vivo*, however they may still require a reference object to calibrate diameter measurements [42]. Although 3D reconstructions may provide accurate vessel dimensions, they require multiple views or a rotational angiogram. For the purposes of device sizing, this additional complexity may be prohibitive for routine use. Furthermore, both pre-procedural CT and intra-procedural 3D reconstruction techniques require additional ionizing radiation to the patient, whereas IVUS imaging is non-ionizing and QCA methods utilize images acquired during the normal course of a diagnostic catheterization exam.

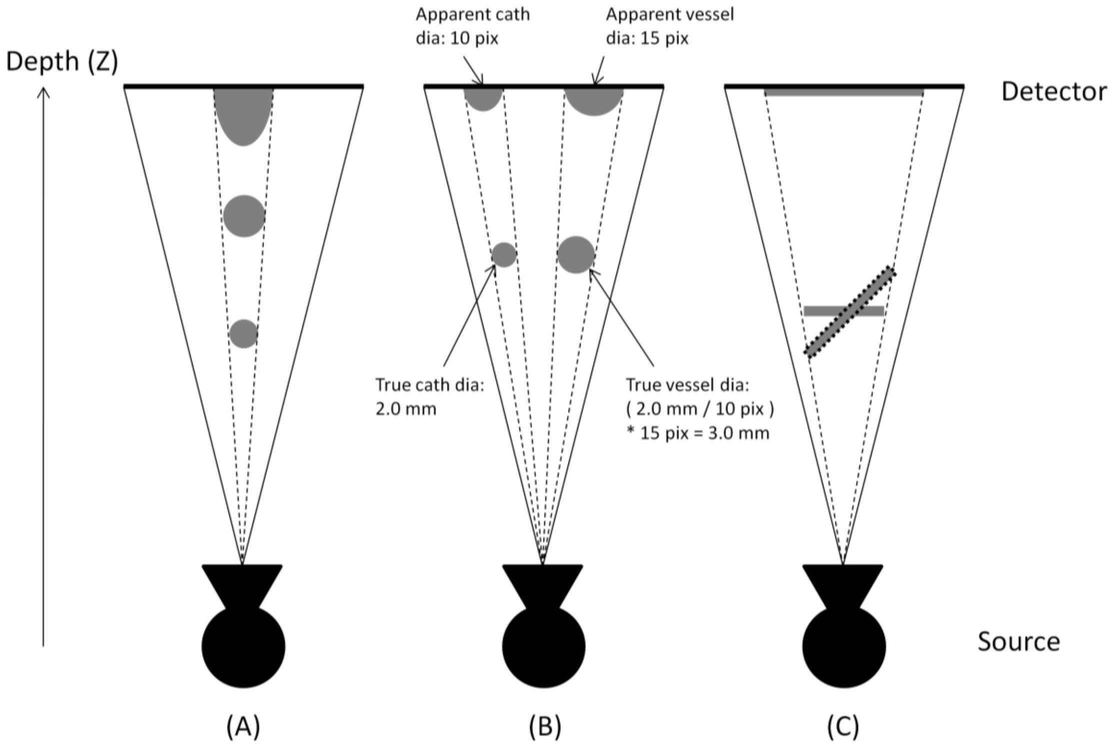

Figure 1.4 – Magnification and Foreshortening

(A) Two vessels with circular cross sections and different diameters are shown at different depths. The difference in depth leads to different magnifications of the two vessels, causing them to have the same apparent diameter at the detector. (B) A reference diameter, such as that from a catheter (left) can be used to determine the true diameter of a vessel (right) based on the ratio of the known diameter to its apparent diameter in the image and the apparent diameter of the vessel. (C) Two vessels with different lengths have the same apparent length at the detector due to a difference in the orientation of the vessel relative to the detector plane.

1.4 Scanning-Beam Digital X-ray (SBDX)

1.4.1 Overview

Scanning Beam Digital X-ray is a low dose x-ray fluoroscopy system for guiding cardiac interventions [2, 3]. SBDX uses an “inverse geometry”, in which a large area target is located near the patient and a small area detector is located far from the patient (Figure 1.5). A pre-patient multi-hole collimator with 100 x 100 holes defines a series of narrow overlapping x-ray beams directed at the detector. As an electron beam in the source is scanned over the large area transmission target, from collimator hole to collimator hole, the x-ray beams are sequentially activated. For each 1.04 μs beam dwell, a narrow field-of-view image of the patient is captured by a high speed photon-counting CdTe detector array. The stream of detector images generated during scanning is sent to a real-time reconstructor which generates full-field-of-view images. The reconstructor performs shift-and-add tomosynthesis at multiple planes simultaneously for each scan period, at a rate of up to 30 scans/second (e.g. 32 planes x 30 scans/second). As detailed later, these plane stacks are combined into a single image for live display. The combination of an efficient detector, scatter rejection (from the narrow x-ray beam and large air gap), and distributed entrance exposure results in high skin dose efficiency, which in turn enables a reduction of patient exposure while maintaining image quality comparable to conventional XRF systems.

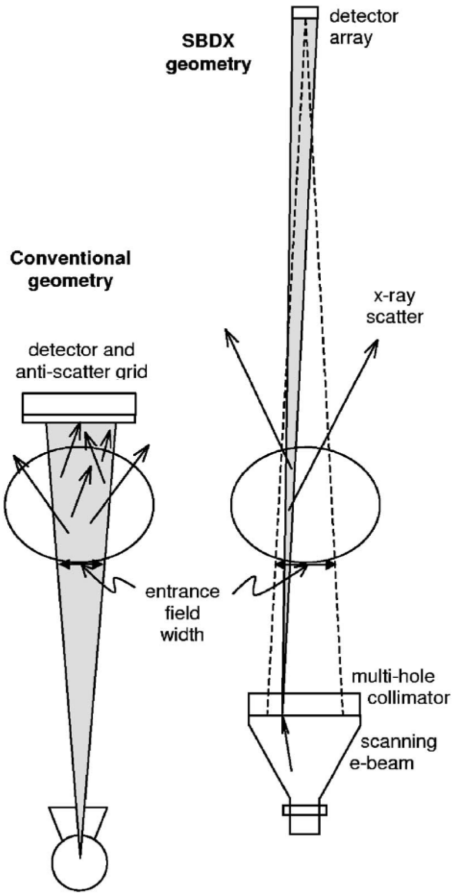

Figure 1.5 – Conventional XRF Geometry vs. SBDX.
The conventional geometry (left) uses a single point x-ray source, wide beam, and large area detector. The inverse geometry of SBDX uses a scanned x-ray source, narrow overlapping beams and a small area detector, which reduces scatter detection relative to the conventional XRF system. Figure from [3].

The single plane tomosynthetic images created by SBDX correspond to a plane through the patient volume, parallel to the source and detector. Structures located in the plane have sharp focus in the image, and structures above and below the plane are blurred depending on their distance from the plane [43]. The previous hardware prototype could reconstruct up to 16 independent image planes in real time; the most recent redesign of the imaging chassis accommodates up to 32 image planes. To create an image where all features are in focus, a multiplane composite image is formed from a set of single plane images. The multiplane composite is generated by a plane selection algorithm, in which the local contrast and sharpness is evaluated at each pixel in each plane, and then, on a pixel-by-pixel basis, the pixel from the plane of highest focus is selected for display (Figure 1.6). The multiplane composite image is the primary image display for interventional procedures. However the out-of-plane blurring properties of the single plane tomosynthesis image are the basis for a 3D localization technique, which overcomes the depth ambiguity of conventional XRF imaging.

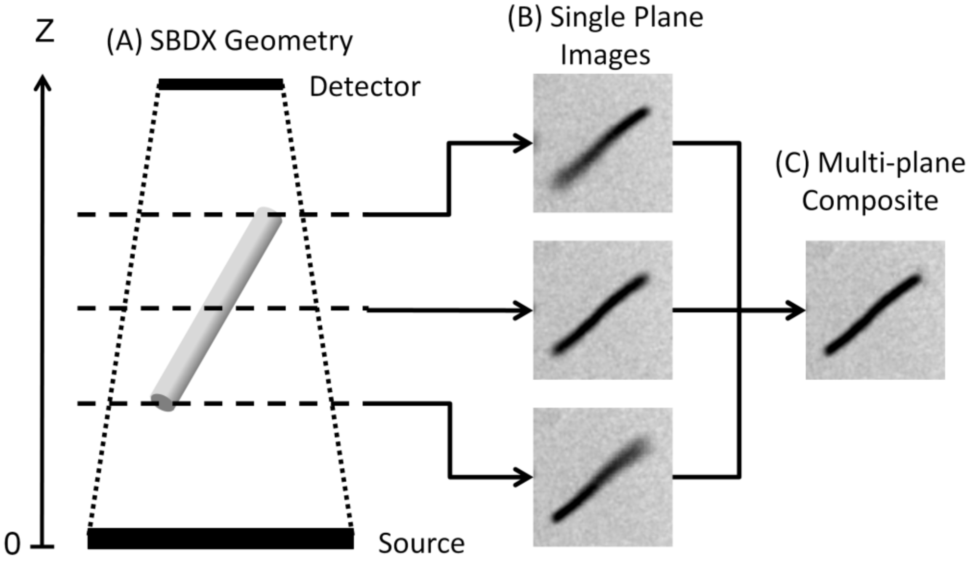

Figure 1.6 – Tomographic Blur of Single Plane Images and Multiplane Composite.
(A) Schematic showing a vessel segment (gray) spanning several image planes (dotted lines). (B) In each of the single plane images the part of the vessel near the image plane is in focus, while portions above and below are blurred. (C) A set of single plane images is combined into a multiplane composite, where all portions of the vessel appear in focus, similar to conventional XRF. Note that the curve in the vessel phantom wire is physical and is not an imaging artifact. For clarity, the system dimensions have been exaggerated. Figure and caption from [32].

1.4.2 3D Localization with SBDX

In the single plane tomosynthesis images produced by SBDX, the degree of blurring an object's edges increases with the distance between the plane and the object. By reconstructing multiple tomosynthetic image planes throughout the volume, the degree of object blurring as a function of image plane position can be used to calculate the depth of the object. The feasibility of this approach has been demonstrated in simulations [4] and phantom experiments [5] using discrete, high contrast objects, diagnostic catheters, and ablation catheters. The target application is 3D device and catheter tip tracking during cardiac ablation procedures.

The general localization algorithm as described in Ref. [5] can be summarized by four main steps. These steps are:

1. Reconstruct tomosynthetic images at regularly spaced planes along the depth direction across the volume of interest.
2. For each tomosynthetic image, compute a "score image" in which pixel values represent the local sharpness in the tomosynthesis image.
3. Given the stack of score images, determine which image regions contain the objects to be localized.
4. For each object region, calculate the depth of the object's center based on the distribution of score values across plane positions located within the object region.

Figure 1.7 shows a detailed graphical representation of the localization algorithm. For a full description, see Ref. [5]. Note steps 1 & 2 are existing capabilities of the SBDX reconstructor, since they are needed for generation of the multiplane composite display.

The original design and implementation of 3D localization with SBDX was aimed at tracking small, discrete, high-contrast objects, and the algorithm used all of the object's edges to localize its centroid. In this dissertation, the original tracking algorithm is modified to localize individual edges of contrast filled vessels. If the vessel edges are localized in an incremental fashion, the vessel's 3D position along its length can be determined. This has two important implications for QCA measurements. First, the 3D location of the vessel can be used to estimate its magnification, which eliminates the need for a separate magnification calibration step. Second, vessel length measurements can be based on the 3D localization of the vessel instead of its 2D projection, which mitigates vessel foreshortening effects. In the context of device sizing, these improvements may greatly simplify the task of obtaining accurate vessel dimensions by eliminating the calibration step and not requiring optimal non-foreshortening view angles.

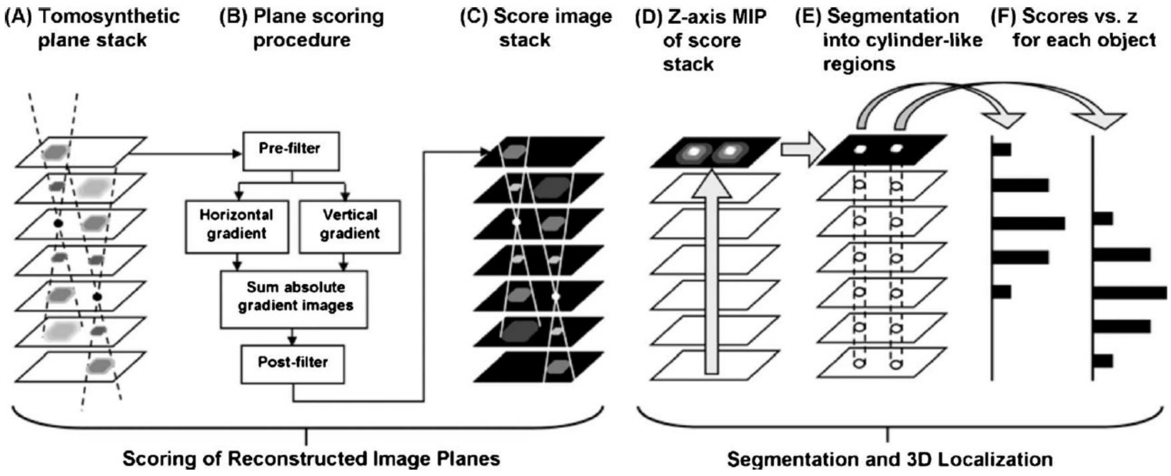

Figure 1.7 – Overview of the SBDX 3D Tracking Algorithm.
[(A) – (C)] Score images are generated from the tomosynthetic images reconstructed at planes spaced throughout the volume of interest. (D) A MIP of the score data is formed and connected component labeling is applied to the MIP. (E) Each detected object (connected component) defines a cylinder-like region in the imaging volume. The row and column coordinates of an object are calculated from the MIP. (F) The z-coordinate is calculated from the scores versus z-plane inside the object cylindrical region. Figure and caption from [5].

1.5 Thesis Organization

The purpose of this thesis is to demonstrate that the 3D localization capability of the tomosynthesis images produced by SBDX enables accurate and precise vessel measurements.

Chapter 2 presents a phantom study demonstrating the feasibility of SBDX vessel sizing. In this proof-of-concept study, highly integrated, low-noise images of vessel phantoms were analyzed over a range of magnifications and degrees of foreshortening. Using an initial "bare bones" implementation of the vessel sizing algorithm, this chapter demonstrates that the depth localization properties of SBDX images can be used to calculate vessel diameter and length without using a magnification calibration object or having an optimal, non-foreshortening view.

Chapter 3 presents a comprehensive revision of the vessel sizing algorithm to improve robustness, accuracy, and usability in the presence of image noise and complex image scenes. This chapter describes improvements to each step in algorithm that leverage existing QCA techniques and a priori knowledge to create an algorithm that is tuned to localize and measure vessel dimensions on a variety of images with minimal user interaction.

Chapter 4 presents phantom studies that explore the limits of the revised algorithm's accuracy and precision as a function of signal difference to noise ratio (SDNR), vessel diameter, magnification, and vessel foreshortening. Vessel phantoms of various diameters were imaged over a range of magnifications and degrees of foreshortening. The noise level in each image was adjusted by integrating frames. Then, for a range of noise levels, the behavior of the length and diameter measurement error was characterized in terms of mean error (accuracy) and the standard deviation of the error (precision). Additional factors affecting the algorithm performance are also examined.

Finally, in Chapter 5, an *in vivo* study of the vessel sizing algorithm is presented to show that coronary vessel dimensions can be accurately measured in a beating heart. Using a healthy porcine model, the coronary arteries were imaged with SBDX. The SBDX-derived measurements of coronary vessel length and diameter were compared to "gold standard" measurements from coronary CT angiography (CCTA) and intravascular ultrasound (IVUS), respectively. These compelling results show that a single frame from SBDX can be used to derive vessel dimensions accurate enough for interventional device sizing.

Chapter 6 presents conclusions to the work presented in this document, as well as future directions for this research.

This page was intentionally left blank.

Chapter 2 – Feasibility of a Calibration-Free Vessel Sizing for Interventional Device Selection Using an Inverse Geometry X-ray System[1]

2.1 Introduction

To test the feasibility of using the 3D localization capabilities of SBDX to address the shortcomings of conventional quantitative coronary angiography (QCA) methods, a simple vessel sizing algorithm was developed for the measurement of the length and diameter of vessel segments (phantoms) in low-noise images. This initial implementation of the algorithm used a previously described model-based QCA method to identify the vessel centerline and edges, as well as measure the diameter in units of pixels. The principles from the SBDX catheter tracking algorithm were used to incrementally localize the depth of the vessel, which was used to build a 3D centerline of the vessel [5]. Finally, the 3D centerline was used to directly compute the length of the vessel and the magnification of the vessel; the latter was used instead of a calibration object to convert the diameter measurements into physical units.

2.2 Background – Model-based QCA

Essential to this implementation of the vessel sizing algorithm is the ability to extract information from vessel intensity profiles by fitting a parameterized model to the data. The original intent of the model fitting procedure was to accurately calculate the vessel diameter by

---

[1] The work presented in this chapter has been published as M. T. Tomkowiak, M. A. Speidel, A. N. Raval, and M. S. Van Lysel, "Calibration-free device sizing using an inverse geometry x-ray system," *Med Phys,* vol. 38, pp. 283-293, 2011.

incorporating information about the entire shape of the profile while accounting for imaging system's line spread function (LSF) [31]. This model-based approach also provides valuable information about the location of the vessel center and edges within the profile. When performed on profiles extracted serially along the length of the vessel, the model parameters can be used to define the centerline and edge contours of the vessel. For the sake of simplicity, the parameterized model fitting method is used for edge and centerline segmentation in addition to diameter measurements. A brief primer of the method is presented below. For a more thorough explanation, the reader is directed to Ref. [31] and to Ref. [44].

Model-based methods assume that the cross sectional profile corresponds to that of a generalized cylinder, and the parameters of a multi-parameter model are jointly optimized to find the set that yields the best fit between the observed and modeled profile in a least-squares sense. Note that these methods were originally developed to work on digitized cine-film images, which featured bright vessels with dark background. Here, the method has been adapted to modern fluoroscopic images, which feature dark vessels on a bright background. The overall model for an observed profile $\hat{p}(t)$ is summarized by

$$\hat{p}(t) = b(t) - \big(v(t) * lsf(t)\big) + n(t) \tag{2.1}$$

where t is the position along the length of the profile. The observed profile $\hat{p}(t)$ is the result of the background $b(t)$ minus the ideal vessel profile $v(t)$ convolved with the system line spread function $lsf(t)$. The function $n(t)$ represents the noise component.

The ideal vessel profile is modeled by assuming the signal difference profile generated by a contrast-enhanced vessel is the projection of through cylinder:

$$v(t) = \begin{cases} 2\alpha\sqrt{r^2 - (t-c)^2} & |t-c| \leq r \\ 0 & otherwise \end{cases} \tag{2.2}$$

where c is the center of the profile with respect to t, r is the radius of the vessel, and α is a scaling factor that depends on the vessel contrast, detected x-ray fluence, and the imaging gain of the system. The background term $b(t)$ is generalized as

$$b(t) = \sum_{i=0}^{N} k_i b_i(t) \tag{2.3}$$

where k_i are coefficients of orthonormal basis functions of polynomials, $b_i(t)$. In related literature [31, 44] and our own experience, a 5th order polynomial has been sufficient to model intensity variations from background anatomy and uneven x-ray exposure.

Including the model parameters explicitly, the noise-free profile model $p(t)$ is given by

$$p(t, \mathbf{a}) = b(t, \mathbf{a}) - \big(v(t, \mathbf{a}) * lsf(t)\big) \tag{2.4}$$

with **a** as the vector of model parameters $\{c, r, \alpha, k_0, k_1, k_2, k_3, k_4, k_5\}$. The maximum likelihood fit of the model to the observed profile $\hat{p}(t)$ (which may include noise) is found by optimizing **a** such that

$$[\mathbf{a}]_{ML} = \text{argmin}_{[\mathbf{a}]} \int [\hat{p}(t) - p(t, \mathbf{a})]^2 dt \tag{2.5}$$

When the processing is performed in the discrete domain, the discrete sum rather than a continuous integral is minimized. Figure 2.1 graphically illustrates the components of a model-based diameter measurement.

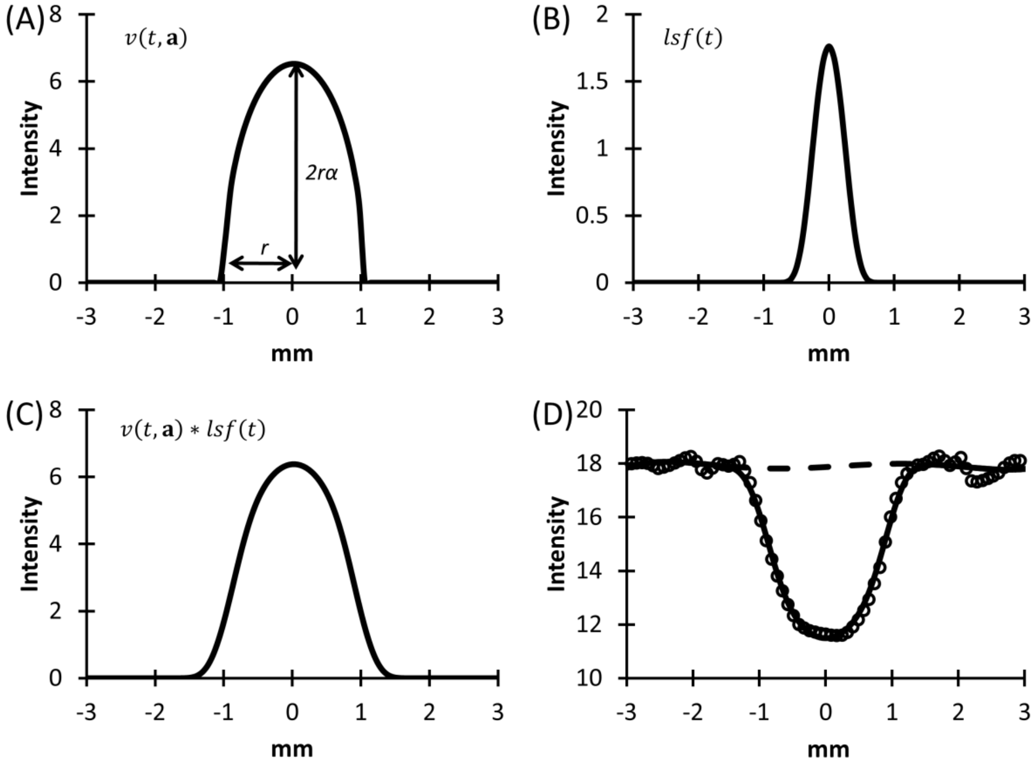

Figure 2.1 – Vessel Profile Model.

(A) The unblurred vessel model assumes a circular cross section with the profile shown in the figure. (B) The LSF is estimated based on actual measurements or an imaging model. (C) The unblurred profile is convolved with the LSF to create a blurred vessel profile. (D) The blurred profile (solid line) is subtracted from the background (dashed line) to approximate the observed profile (circles).

The line spread function $lsf(t)$ is not explicitly defined with this method; it must be determined by other means and inserted into the model described in Eq. 2.4. While the LSF can be measured directly, it is dependent on the z position of the object (vessel) relative to the image planes as well as the orientation of the vessel parallel to the image plane. It would not be feasible to make direct LSF measurements to cover all possible imaging scenarios. Instead of relying on direct LSF measurements, the relevant system and reconstruction parameters and estimated position of the vessel are used to model the LSF. This gives us the flexibility to calculate the LSF to match the imaging scene. Details on the LSF model can be found in Appendix A.

2.3 Methods

2.3.1 Vessel sizing Algorithm with SBDX

2.3.1.1 2D Vessel Centerline

The vessel sizing algorithm begins with the definition of a vessel centerline in a displayed SBDX angiographic image (multiplane composite). An iterative method was implemented to define the centerline. A 2D piecewise cubic spline was fit through 2-4 user-selected points along the vessel centerline in the image. The remaining steps, described below, were automated in software. Intensity profiles perpendicular to the spline were sampled at 2 pixel intervals along the length of the spline. The model-based sizing algorithm, using an ideal (point) LSF, was applied to calculate the center of each vessel profile. Another smoothing spline was fit through the profile center points to create a more refined 2D centerline.

2.3.1.2 3D Localization of vessel borders

At 1 pixel intervals along the refined 2D vessel centerline, intensity profiles were extracted perpendicular to the centerline, and the model-based sizing algorithm was applied, again assuming an ideal LSF. The optimal model parameters were used to identify the locations of the vessel edges in the profile. Small ROIs were defined over the vessel edges along the profile for each sampled point as shown in Figure 2.2. Given a point, **x**, along the 2D centerline and the normalized vector **d** perpendicular to the tangent of the centerline at **x**, two ROIs were centered at $(\boldsymbol{x} - \hat{r}\boldsymbol{d})$ and $(\boldsymbol{x} + \hat{r}\boldsymbol{d})$. ROI height and width were $2\hat{r}$, where $\hat{r}$ was the vessel radius estimate assuming an ideal LSF.

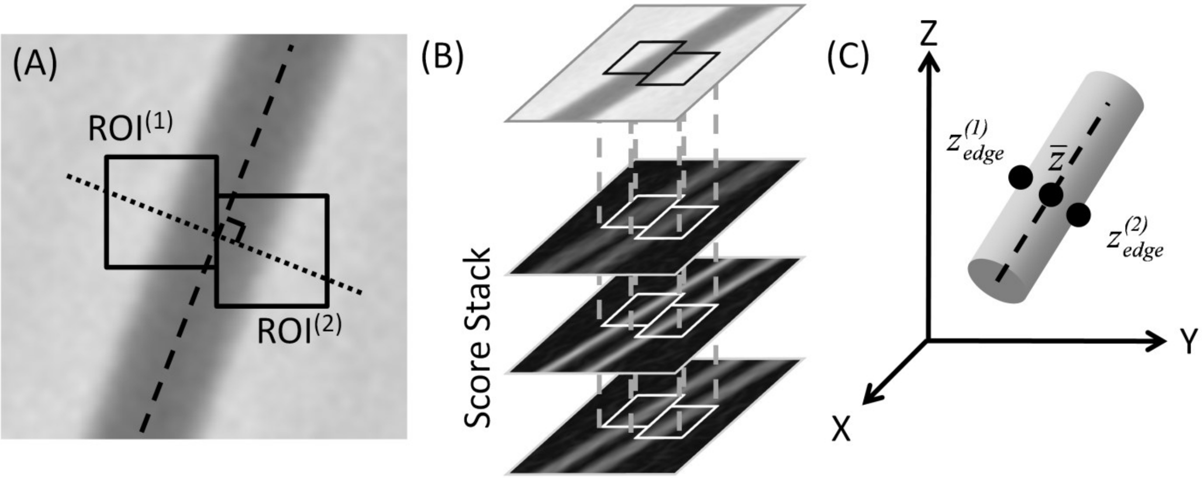

Figure 2.2 – ROIs for 3D Vessel Localization.
(A) An intensity profile is extracted perpendicular to the centerline, and two ROIs, ROI$^{(1)}$ and ROI$^{(2)}$, are defined at either edge of the vessel along the profile. (B) The ROIs defined on the composite image are applied to the score image stack. The 3D localization algorithm is executed on each ROI score stack to produce a Z coordinate for each ROI, $z^{(1)}_{edge}$ and $z^{(2)}_{edge}$. (C) The two Z coordinates from the ROI score stack correspond to opposite edges of the vessel. The two values are averaged to estimate $\bar{z}$, the Z coordinate of the 3D vessel centerline.

A “score image" stack was created from the single-plane image stack as described by Speidel et al [5]. Each image was low pass filtered to reduce noise, and vertical and horizontal gradient images of each smoothed image were created using vertical and horizontal 3x3 Prewitt kernels [45]. The absolute values of the gradient filtered images were summed together to make a score image. The collection of score images from all plane positions formed the score image stack $S(u, v, z)$, where u and v are the column and row pixel coordinates and z corresponds to the Z coordinate of the image plane. The Z axis runs from the source to the detector, with $z = 0$

at the target plane in the x-ray source. In this case, z is only defined for discrete values corresponding to the Z coordinates of a finite set of single image planes. Using the pixel coordinates from a vessel edge ROI, the same ROI was extracted from each of the score images to create an ROI score stack, $S_{ROI}(u,v,z)$. A maximum intensity projection, $M_{ROI}(u,v)$, along the Z direction of $S_{ROI}(u,v,z)$ was calculated. $M_{ROI}(u,v)$ was then used to create a binary mask of the vessel edge, $B_{edge}(u,v)$, by setting pixels in $M_{ROI}(u,v)$ with values greater than 80% of the maximum score in $M_{ROI}(u,v)$ to 1 and all other pixels to 0. The vessel edge score stack, $S_{edge}(u,v,z)$, was defined as

$$S_{edge}(u,v,z) = B_{edge}(u,v) \cdot S_{ROI}(u,v,z) \tag{2.6}$$

Baseline subtraction of $S_{edge}(u,v,z)$ was performed by subtracting 40% of the maximum score in $M_{ROI}(u,v)$ from all values in $S_{edge}(u,v,z)$, followed by setting negative values to 0, which removed gradient influence from image noise and created $\hat{S}_{edge}(u,v,z)$. An overall Z coordinate for the vessel edge was calculated by summing the values of $\hat{S}_{edge}(u,v,z)$, such that

$$f_{edge}(z) = \sum_{v}\sum_{u}\hat{S}_{edge}(u,v,z) \tag{2.7}$$

The Z coordinate for the vessel edge, z_{edge}, was calculated as

$$z_{edge} = \frac{\sum_z f_{edge}(z) \cdot z}{\sum_z f_{edge}(z)} \tag{2.8}$$

which was the "center of mass" of the score sums. Note that this assumes that image plane set is nearly symmetrically distributed about the target vessel along the Z axis. Figure 2.3 shows each of the edge localization stages graphically. This same process was applied to the other score stack ROIs for the opposite vessel edge, and the two Z coordinates were averaged (Figure 2.2C). The 2D coordinate (u, v) along the vessel centerline and the mean Z coordinate were converted to a 3D coordinate (x, y, z) and stored as a point along the 3D centerline of the vessel. This process was repeated for each of the profiles extracted along the 2D centerline to create a set of points along the 3D centerline of the vessel.

2.3.1.3 Vessel Length Measurements

A 3D piecewise cubic smoothing spline was fit through the series of 3D centerline points to reduce noise and create a continuous function. The physical length of the vessel segment corresponding to this 3D centerline was calculated by sampling the cubic spline at regular intervals and summing the arc length of a piecewise linear function through each of these points.

2.3.1.4 Vessel Diameter Measurements

Measurements of the physical diameter of a vessel, in mm, were performed using the model-based approach previously described with pixel-to-mm conversion factors and LSF approximations determined from the 3D vessel centerline. The 2D centerline in the composite image was sampled at 1.5 pixel intervals along its length, and intensity profiles were extracted perpendicular to the centerline at each point. The 1.5 pixel spacing between adjacent profiles minimized the chance that the profiles would contain values extracted from the same pixels in the image, keeping the diameter measurements independent. Along the perpendicular profile, pixel values were sampled every 0.5 pixels using bilinear interpolation. For each sampled point along the 2D centerline and corresponding intensity profile, the pixel spacing and LSF were computed as described in the following paragraphs.

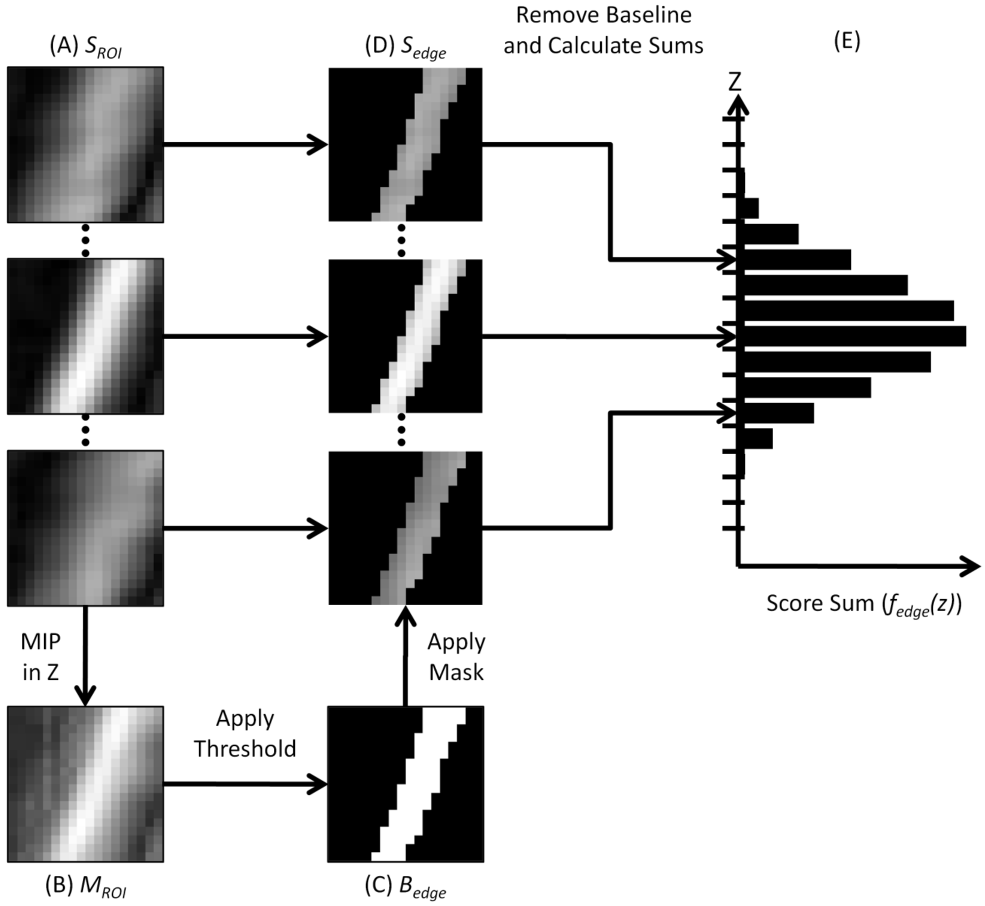

Figure 2.3 – 3D Vessel Edge Localization.

(A) The vessel edge ROI was applied to the score image stack to produce the ROI score stack, S_{ROI}. (B) M_{ROI}, maximum intensity projection (MIP) of S_{ROI},was created. (C) A threshold equal to 80% of the maximum value in M_{ROI} is applied to M_{ROI} to create the binary mask of the vessel edge, B_{edge}. (D) The binary mask, B_{edge}, was applied to each image in the score image stack to create S_{edge}. A value equal to 40% of the maximum value in M_{ROI} was subtracted from each image in S_{edge}. Negative values were set to zero, and the values in each score image were summed. (E) The Z position of the vessel edge in the ROI was calculated as the weighted average of the score sums, which was equivalent to the center of mass of the shown distribution.

The sampled point along the 2D centerline was projected onto the 3D centerline, and the closest image plane in the set of single plane images to the projected point was identified. The pixel size, Δ_p, for this image plane was used to convert the width of the measured profile from pixels to physical dimensions (mm). Pixel size in a plane is given by the relationship

$$\Delta_p = \frac{Z_d - z}{Z_d} \cdot \frac{\Delta_s}{m} \tag{2.9}$$

where Z_d is the source-to-detector distance (1500 mm in the current prototype), z is the Z coordinate of the image plane, Δ_s is the spacing between adjacent focal spot positions in the scanning x-ray source (2.3 mm), and m, is a reconstruction parameter set to 10 in this study. Figure 2.4 shows the pixel width, Δ_p, as a function of plane position. The range of planes shown represents ± 20 cm about gantry isocenter (z = 45.0 cm).

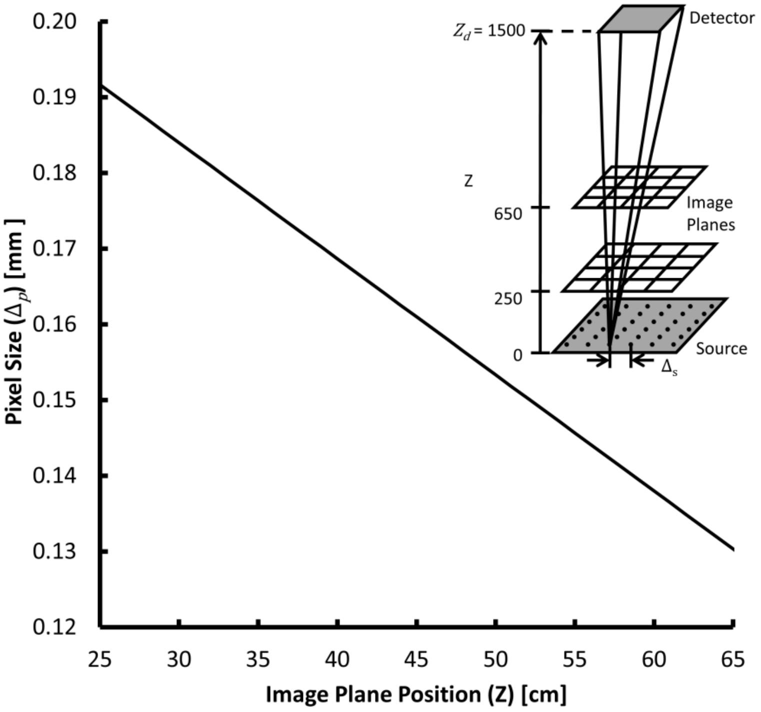

Figure 2.4 – Pixel Size Versus Plane Position.
The pixel size of single plane images decreases monotonically as the Z position of the plane increases. (Inset) Pixel size is a function of the position of the image plane (z), the source to detector distance (Z_d), the spacing between focal spot positions (Δ_s), and a constant, m. Image field-of-view decreases as the plane moves toward the detector and the number of pixels in each image is fixed (e.g. 710 x 710 pixels).

The LSF component of the model fitting, $lsf(t)$, was approximated based on the optical transfer function (OTF) model of the SBDX system [2]. The OTF model for a single image plane reconstruction was dependent on x-ray source and detector geometry, reconstruction parameters, and the Z coordinate of the image plane position. In addition, the Z coordinate of the 3D centerline point relative to the image plane was incorporated into the OTF model to account for out-of-plane blurring effects. The OTF was assumed to be spatially invariant within the image plane. A detailed description of the OTF model for SBDX can be found in Appendix A.

The LSF is dependent on the orientation of the extracted intensity profile within each image plane. The angle of the extracted profile relative to the image coordinate axes, θ, was calculated. According to the projection slice theorem, the LSF for the profile was the inverse Fourier transform of a line passing through the center of frequency space at angle θ relative to the spatial frequency axes, which is equivalent to

$$lsf_\theta(t) = \int_{-\infty}^{\infty} OTF(\rho\cos\theta, \rho\sin\theta)e^{2\pi i\rho t}d\rho \tag{2.10}$$

The model-based diameter measurement algorithm was applied to each of the extracted intensity profiles using their corresponding pixel spacing and LSF. Model parameters (e.g. approximate diameter) were initialized using an intensity threshold method. The background intensity was initialized as the least-squares fit line going through the first and last 5 samples of the extracted profile, which were always outside of the vessel projection. Optimization of model parameters was performed using a Nelder-Mead simplex method. The results of the model fitting provided the physical diameter of the vessel (i.e. diameter = $2r$, where r is the model radius parameter after optimization).

2.3.2 Phantom Validation Study

Vessel phantoms were used to validate the proposed algorithm. Vessel segments of different diameters were simulated using linear segments of solid MgCd alloy wire. This alloy is designed to have attenuation properties similar to iodinated contrast agent (350 mg/mL iodine) for diagnostic x-ray beam energies (60 - 120 kVp) [46]. Wires with nominal diameters of 0.5, 0.7, 1.0, 1.4, 2.1, and 2.8 mm were used. The nominal length of each segment was 42 mm. Sheets of poly(methyl methacrylate) (PMMA) were used as the background attenuator and had a total thickness of 23 cm.

Different phantom configurations were used to test two hypotheses: 1) vessel diameter and length can be accurately measured over a range of plane positions without the use of a magnification calibration step and 2) vessel diameter and length can be accurately measured when the vessel appears foreshortened in the 2D image display. The first phantom configuration had vessels (one 4 cm length per diameter) oriented parallel to the image planes (i.e. all points along a vessel centerline at the same z-distance from the x-ray source). Images were acquired with the vessels positioned from 16 cm below to 16 cm above the mechanical isocenter of the gantry, in 2 cm increments. In the second phantom, the vessel plane was placed on a stage that rotated around an axis through mechanical isocenter and orthogonal to the Z axis; rotating the vessel plane around this axis produced different degrees of vessel foreshortening in the 2D image display. Two 4 cm lengths per nominal diameter were imaged. Images were acquired with the vessel plane oriented 0°, 15°, 30°, 45°, 60°, and 75° with respect to the source plane. Figure 2.5 demonstrates the various appearances of vessel orientations in the SBDX multiplane composite images.

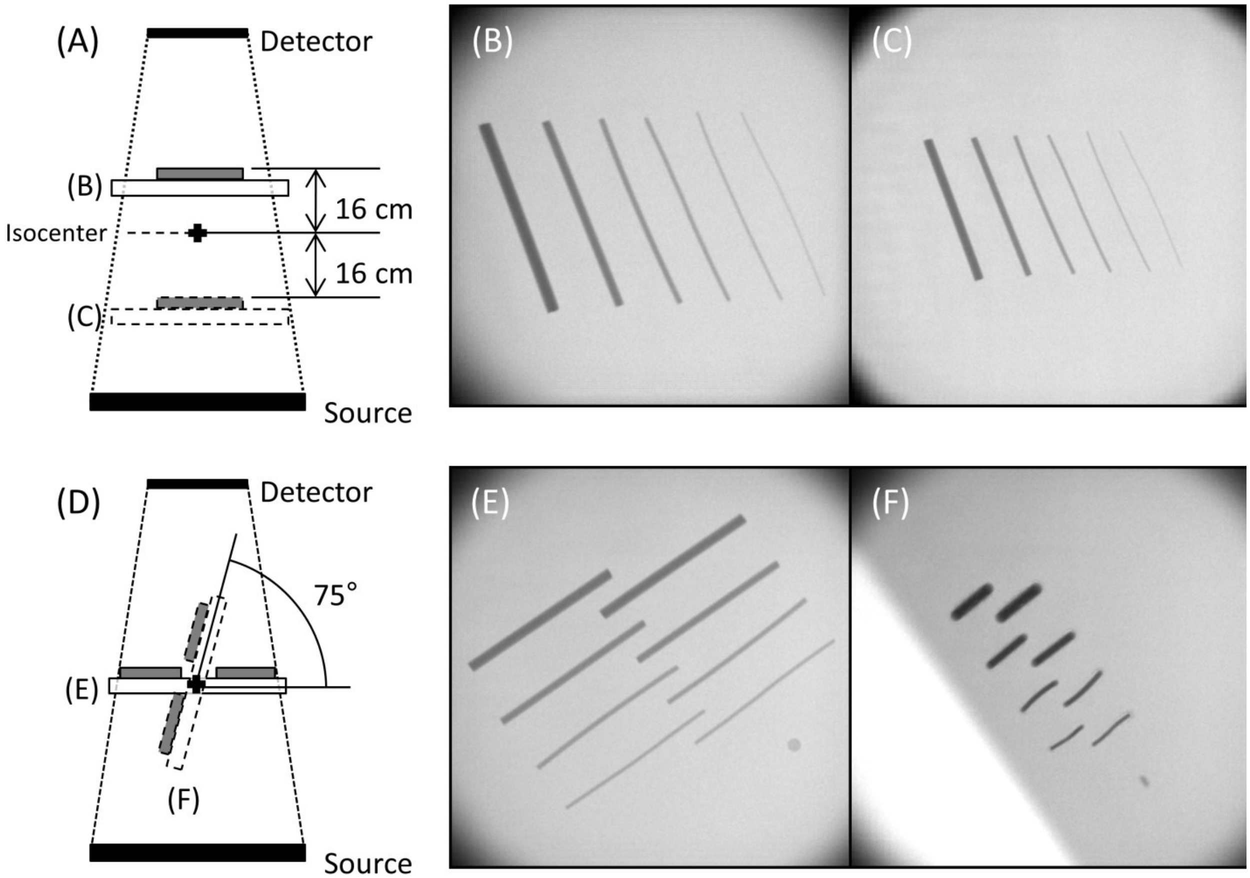

Figure 2.5 – Vessel Phantom Orientations.

(A) To test the algorithm with different levels of vessel magnification, the phantoms were imaged parallel to the image plane from 16 cm above isocenter to 16 cm below ((B) and (C), respectively) in 2 cm increments. Note that the inverse geometry causes the magnification to increase as the object moves toward the detector. (D) To test the algorithm with foreshortened vessels, the vessel phantom plane was rotated about isocenter from 0° to 75° ((E) and (F), respectively) in 15° increments. The cross indicates isocenter. For clarity, the system dimensions have been exaggerated.

2.3.3 Imaging Parameters

The vessel phantoms were imaged using the SBDX prototype hardware system [2]. The vessel phantom was imaged at 100 kVp and 120 mAp, using 71 x 71 source positions scanned at a rate to produce images at 15 frames per second. At the time of this study, the detector was 5.5 cm by 5.5 cm, composed of 48 x 48 detector elements with a detector element pitch of 1.14 mm. Each image plane had 710 x 710 pixels, with pixel width given by Eq. 2.9. For an isocenter plane image, the field of view was 11.4 cm x 11.4 cm and the pixel size was 0.161 mm x 0.161 mm. The effective pulse width was 9.4 ms. The effective pulse width is the time between the first and last illumination of a given point in the field-of-view during one frame period, and thus represents the temporal blurring window for that point. For each acquisition, 16 single image planes spaced 12 mm apart were defined symmetrically above and below the Z position of the vessel phantom. The number of reconstructed planes matched the hardware capabilities of the SBDX prototype at the time of the experiment, and 12 mm plane spacing was sufficient to minimize the impact of out-of-plane blurring in the 2D composite image while ensuring adequate coverage over the phantom volume (or, in the case of clinical imaging, the heart). Vessel measurements were performed on images integrated across 30 frame periods to test the algorithm under low noise conditions.

Single plane images and composite images were reconstructed using a software simulation of the hardware-based shift-and-add reconstruction algorithm. In brief, the algorithm first defines the boundaries for each pixel in the tomosynthesis image plane. The detector images are back-projected and summed at the image plane. The contribution of each back-projected detector element to a reconstructed image pixel is based on the area of overlap.

Finally, a post-processing “pattern correction” step accounts for differing amounts of detector image overlap in the tomosynthesis image, as well as spatial variations in detector element sensitivity. For 2D display purposes, the stack of single plane images generated in a frame period is combined into a multiplane composite image analogous to a conventional angiogram. The multiplane composite displays, for each pixel position, the pixel value from the image plane with the highest local sharpness and contrast. Details of SBDX image reconstruction may be found in Ref. [2].

2.3.4 Accuracy and Precision Measurements

The error in diameter or length measurements of the vessel phantoms was calculated by subtracting the true dimensions from the measured dimensions produced by the vessel sizing algorithm for each phantom configuration. The true length and diameter were determined by measuring each vessel wire phantoms with high precision calipers. Length measurement errors were averaged for segments with similar nominal diameters, and the mean and standard deviation of length error across all nominal diameters was calculated. The mean and standard deviation of diameter measurement errors were calculated over all diameter measurements for segments with the same nominal diameter in each configuration. Mean measurement errors represent systematic error (i.e. accuracy), and the standard deviation of the error represents the variability (i.e. precision).

To quantify changes in the apparent length of the vessel due to magnification and foreshortening, the length of the 2D centerline of each vessel (in pixel units) was calculated as a percentage of the reference 2D centerline length, which was measured with the vessel phantom positioned at isocenter and parallel to the image plane (i.e. no foreshortening). The apparent full length of the vessel was calculated as the arc length of the 2D centerline after extrapolation to the ends of the vessel segment. Each "end" of the vessel phantom was defined as the point along the 2D centerline where the intensity was 50% of the maximum vessel contrast.

Length and diameter measurements were performed along the inner 75% of the 2D centerline of each segment. This avoided introducing measurement errors near the endpoints of the cylindrical segments, which have a changing cross sectional profile when angulated relative to an image plane.

2.4 Results

The length and diameter of each vessel phantom segment were successfully measured for each configuration. Diameter measurements on average were accurate to within 0.1 mm of the true diameter for all but the largest diameter vessels. Error variability increased for small diameter vessels (≤ 1.0 mm diameter). Typical length errors were less than 1.0 mm, with variability increasing as the apparent foreshortening of the vessel increased.

Imaging the vessel phantoms parallel to the image and source planes while varying the position in the Z direction produced images of non-foreshortened vessel wires at various magnifications. The apparent size (diameter and length) of the vessel phantoms was 13% smaller when positioned 16 cm below isocenter and 18% larger when positioned 16 cm above isocenter. Despite the changes in the apparent size of the vessel, mean error of the vessel diameter measurements remained consistently less than 0.1 mm for all vessel diameters at all Z positions, except for the 2.8 mm diameter vessel measurements, which were within 0.15 mm (Figure 2.6). No trends in vessel diameter error were observed; as the apparent size of the vessel increased or decreased, the mean error of the diameter measurement remained consistent (Figure 2.7). The precision of the diameter measurements was greater for larger diameter vessels. The variability of the measurements increased as the true diameter decreased, especially for diameters ≤ 1.0 mm. Changes in the variability were irrespective of the apparent magnification of the vessel. The average number of diameter measurements per segment was 134 (Range: 114-161).

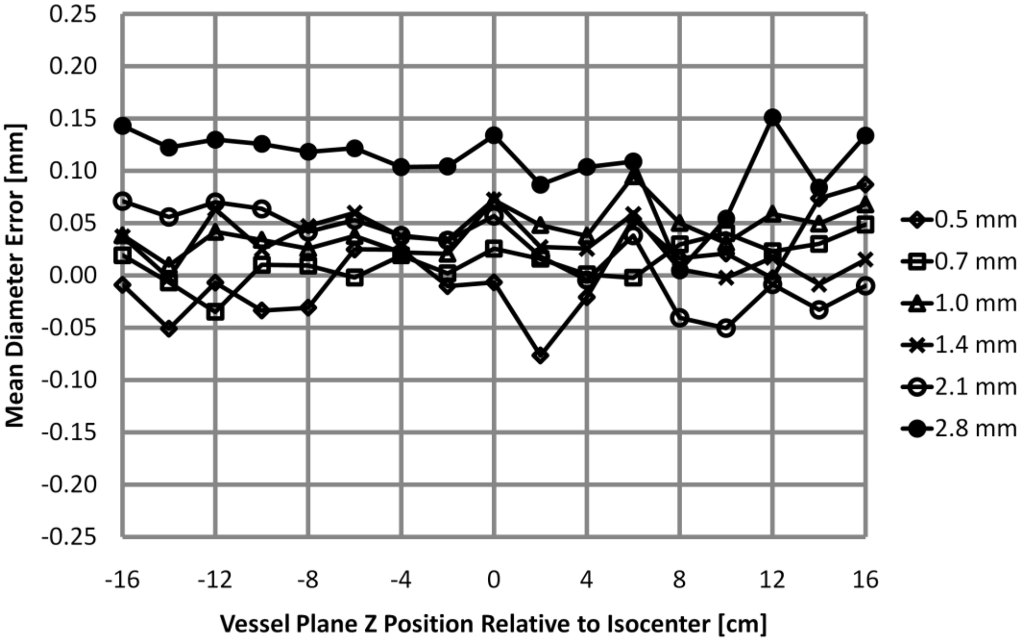

Figure 2.6 – Diameter Error for Different Vessel Magnifications.
The mean diameter error for each vessel phantom diameter was calculated for vessels parallel to the image plane but at different distances from the source, producing different magnifications in the composite images. Average diameter errors remained relatively constant, remaining ≤ 0.15 mm for all diameters.

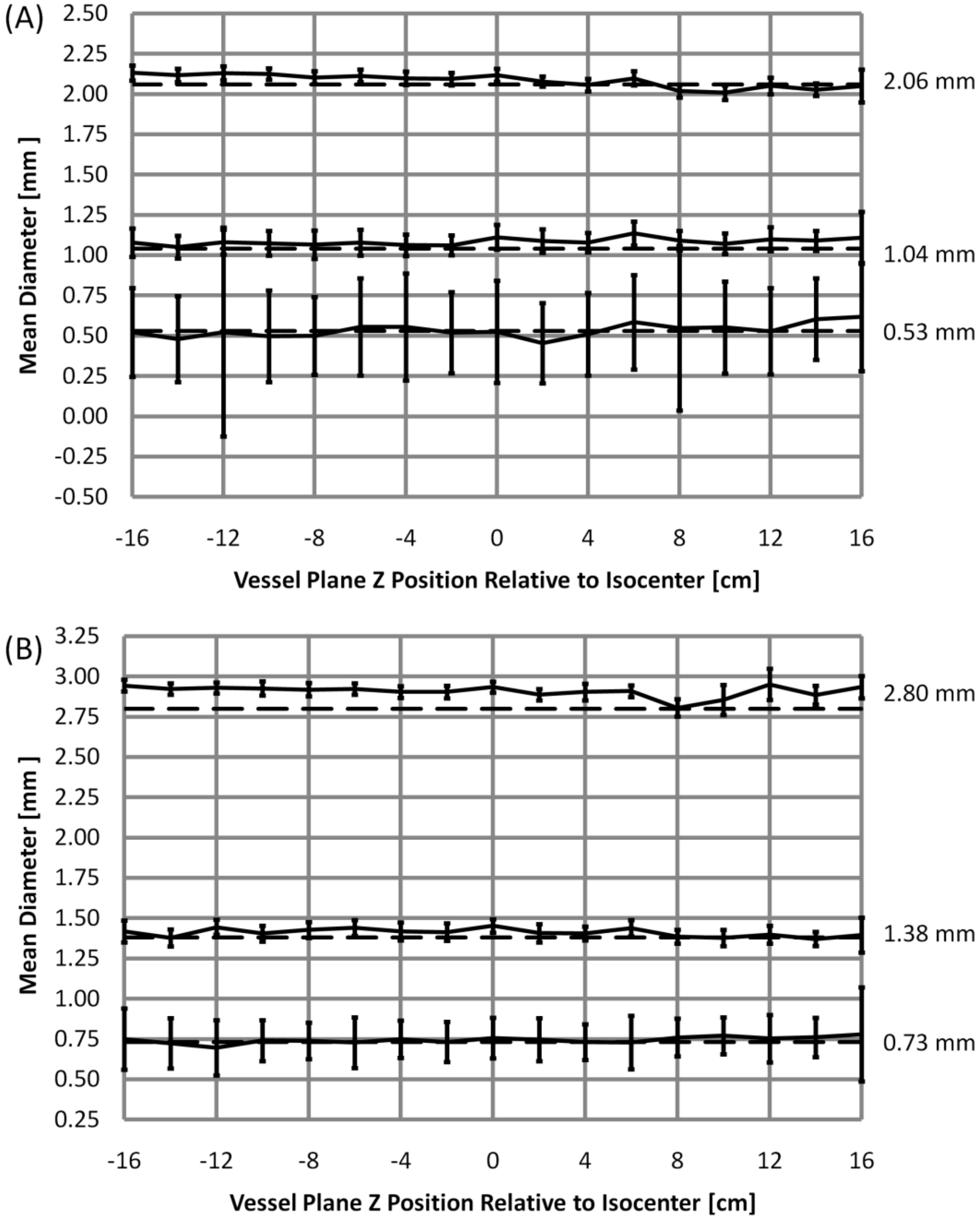

Figure 2.7 – Measured Diameter for Different Vessel Magnifications.

Plot (A) shows the measured diameter versus Z position for the 0.5, 1.0, and 2.1 mm diameter vessels. Plot (B) shows the measured diameter for 0.7, 1.4, and 2.8 mm diameter vessels. Dashed lines represent true diameter. Labels in right margin indicate the true diameter of each segment. Error bars represent ± 1 SD.

As the angle of the vessels relative to the source plane increased (i.e. the vessel became foreshortened), mean diameter errors remained within 0.1 mm for smaller vessel diameters (0.5-1.4 mm) across all angles as well as for larger diameters (2.1 and 2.8 mm) at low to moderate angulation (0°-45°). Errors exceeded 0.1 mm for larger diameters when foreshortening was severe (60°-75°). There was a general trend for the mean error to increase as the angle of the vessels increased as shown in Figure 2.8. Variability of the diameter measurements decreased as the angulation increased, as shown in Table 2.1. The average number of diameter measurements per vessel segment was 97 (Range: 34-139).

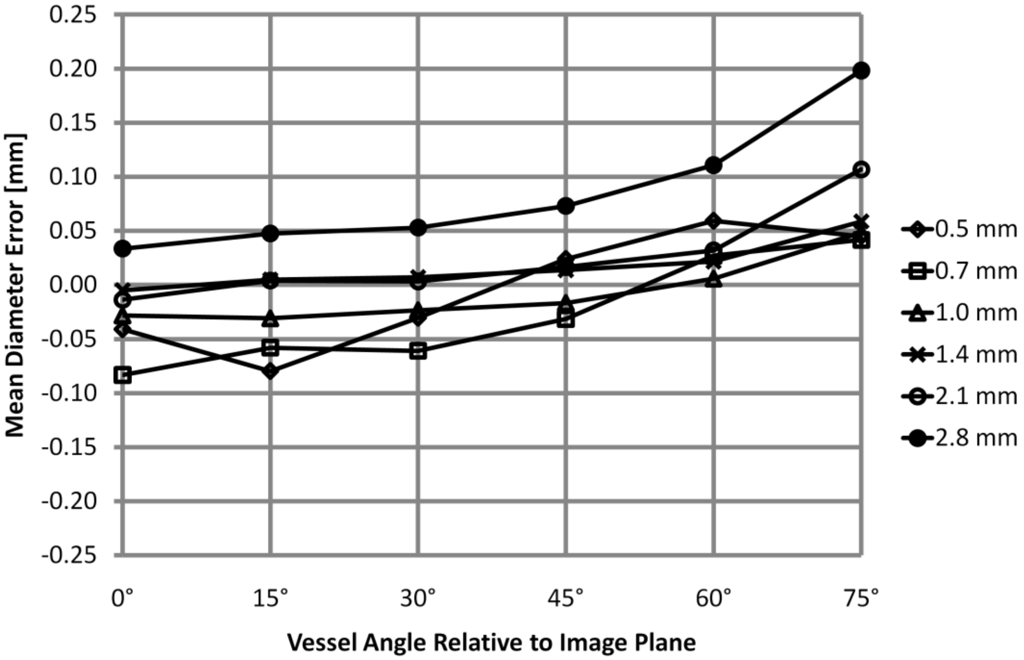

Figure 2.8 – Measured Diameter Error for Different Angulations.
The average diameter error showed little to no dependence on the vessel orientation for low to moderate foreshortening (vessel angle ≤ 45°). Diameter errors generally increased for all vessel diameters when the vessels were severely foreshortened (vessel angle > 45°).

	Mean error ± 1 SD [mm]					
Nominal Diameter [mm]	**0°**	**15°**	**30°**	**45°**	**60°**	**75°**
0.5	-0.04 ± 0.30	-0.08 ± 0.26	-0.03 ± 0.25	0.02 ± 0.23	0.06 ± 0.20	0.05 ± 0.15
0.7	-0.08 ± 0.22	-0.06 ± 0.19	-0.06 ± 0.21	-0.03 ± 0.17	0.03 ± 0.13	0.04 ± 0.07
1.0	-0.03 ± 0.07	-0.03 ± 0.07	-0.02 ± 0.07	-0.02 ± 0.06	0.01 ± 0.05	0.05 ± 0.04
1.4	0.00 ± 0.06	0.00 ± 0.05	0.01 ± 0.05	0.01 ± 0.04	0.02 ± 0.04	0.06 ± 0.03
2.1	-0.01 ± 0.04	0.00 ± 0.04	0.00 ± 0.04	0.02 ± 0.03	0.03 ± 0.03	0.11 ± 0.03
2.8	0.03 ± 0.04	0.05 ± 0.05	0.05 ± 0.04	0.07 ± 0.04	0.11 ± 0.04	0.20 ± 0.05
Overall	**-0.02 ± 0.16**	**-0.02 ± 0.14**	**-0.01 ± 0.14**	**0.01 ± 0.13**	**0.04 ± 0.11**	**0.09 ± 0.09**

Table 2.1 – Diameter Error with Apparent Foreshortening
Angle corresponds to angle between the vessel center axis and the image planes.

Length measurements of vessels parallel to the image plane imaged at different Z positions (i.e. different magnifications) were unaffected by the change in apparent size of the vessel. Figure 2.9 shows the measured length relative to the true length, averaged across all nominal diameters, compared to the apparent size of the vessels at each position along the Z axis. Across all vessel phantom positions and individual nominal diameters, each measured length was within 1% (~0.3mm) of its true value. No trends were observed in the length measurements across different nominal diameters.

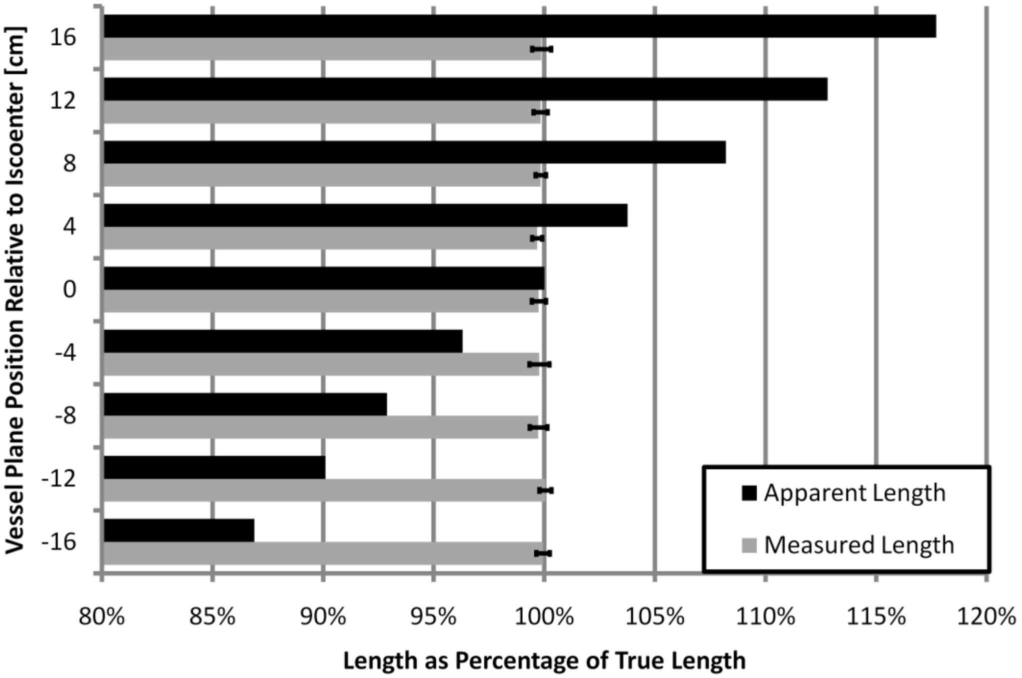

Figure 2.9 – Measured Relative Length for Different Vessel Magnifications.
The measured relative vessel length (measured vessel length / true vessel length) (gray) was calculated and averaged for all vessel segments at each Z position. Apparent length (black) is the relative length measurement expected using conventional methods, assuming the magnification calibration was performed only at isocenter. Error bars represent ± 1 SD.

Length measurements of foreshortened vessels remained accurate despite large changes in apparent length. As the angle of the vessel relative to the image plane increased, the apparent length of the vessel decreased down to 28% of the non-foreshortened length. Averaged across all nominal diameters for a given orientation, the error was less than 1% (~0.3 mm). Length errors were greater for individual segments but remained less than 5% (~1.5 mm) overall. Variability in the length measurements tended to increase as the vessels appeared more foreshortened. Figure 2.10 shows the measured lengths relative to the true lengths compared to the changes in the apparent length of the vessels due to foreshortening.

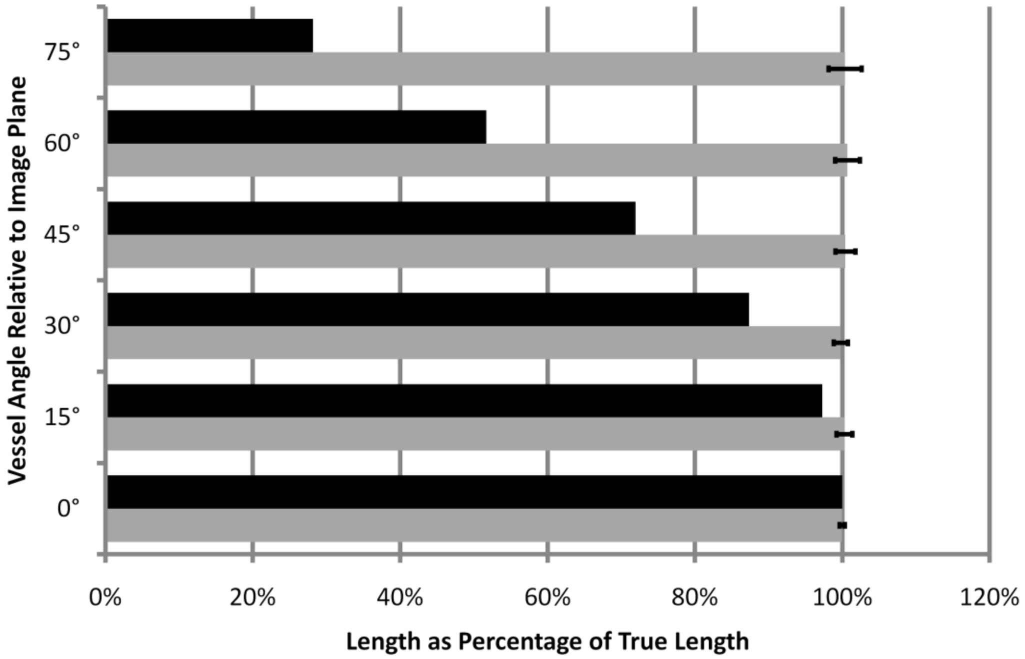

Figure 2.10 – Measured Relative Length for Different Angulations.

Relative vessel length (measured vessel length / true vessel length) (gray) was averaged for all vessel segments imaged at each orientation. The apparent vessel length (black) assumes a conventional magnification calibration and no compensation for the degree of vessel foreshortening. Error bars represent ± 1 SD.

2.5 Discussion

Using a calibration-free vessel sizing algorithm with tomosynthesis-based 3D localization, accurate diameter and length measurements were performed in a vessel phantom. The 3D localization method enabled accurate measurements over a 32 cm volume along the source-detector axis. The vessel contrast and diameters used in this study were representative of those encountered in coronary angiography with arterial injection of iodinated contrast. In orientations where the vessels appeared foreshortened in the images, the algorithm was able to calculate accurate diameters and lengths.

Interventional devices (e.g. balloons and stents) are available in a variety of diameters and lengths in order to closely match lesion length and the adjacent reference (healthy) vessel diameter. Typical device lengths are available in 4-5 mm increments, and diameters are available in increments of 0.25 mm with the narrowest devices having diameters of ~2.0 mm. Based on our experiments, the errors in the estimated diameters and lengths are within these incremental values for vessel diameters that can be treated with interventional devices (≥ 2.0 mm). This suggests the potential for the algorithm to provide guidance during clinical device size selection. While accurately measuring narrow vessels (< 2.0 mm) has diagnostic value (e.g. for measuring % stenosis), it is less critical for vessel sizing because devices that can match these small diameters are not available.

One noticeable trend when measuring the vessel phantoms in cases of severe foreshortening was increased overestimation of the vessel diameter. The assumption that the LSF was constant over the Z extent of the vessel cross section appeared to be adequate for shallow foreshortening angles but not for steep angles. The clinical impact of the observed overestimation of severely foreshortened vessels is likely minimal because trained interventionalists recognize extreme foreshortening effects and are accustomed to adjusting the projection angle to avoid this problem. Under conditions where the vessel angle is less than 60° relative to the image plane, the diameter and length are accurately measured using the proposed algorithm.

Interestingly, the same severe phantom orientation that increased mean diameter error resulted in a lower variation of the diameter measurements, specifically for smaller diameter vessels. As the vessels changed orientation from parallel to the source plane to being angled in the direction of the x-ray beam, the path length through the vessel phantom increased. This led to greater attenuation and improved the signal difference to noise ratio (SDNR), thereby lowering the random variation of the diameter measurements. However, for a given orientation smaller diameter vessels will have a lower SDNR than larger vessels and diameter measurements of smaller diameter vessels will correspondingly have lower precision. A more thorough exploration of SBDX vessel sizing performance as a function of SDNR is presented in Chapter 4.

All absolute dimensions were quantified without requiring a separate calibration step. Various calibration methods have been proposed for conventional QCA algorithms [33], the most common of which is to image a contrast filled catheter near the vessel of interest. Alternatively, an external calibration object, such as an x-ray visible ruler with more conspicuous features can be used, however this increases calibration uncertainty because a vessel within the body and a calibration object outside of the body experience different magnifications. Eliminating the calibration step altogether removes a potential source of error and improves procedure workflow, which increases the likelihood that such a QCA method would be used clinically.

Recent 3D coronary vessel reconstruction methods may also provide alternatives to conventional vessel measurement methods. Multiple angiographic views or rotational angiography acquisitions are typically used as the source images. These methods may use a priori assumptions to model coronaries [37-40] while others use volumetric reconstruction techniques [41, 42]. In terms of vessel sizing, 3D reconstructions may be used to determine optimal angiographic views that minimize foreshortening and overlap [47], which may improve conventional QCA results. Vessel bifurcation angles and tortuosity can also be quantified from

3D reconstructions, which may help support interventional decision making. The feasibility of measuring vessel segment length and diameter directly from these 3D reconstructions has been demonstrated in phantoms and *in vivo* [42]. Although 3D reconstructions may provide other useful information in addition to vessel dimensions, they require image acquisition from multiple gantry angles, whereas the proposed SBDX QCA method requires only a single gantry angle.

Both derivative-based and model-based edge detection methods could have served as the foundation for the calibration-free QCA routine. The greatest benefit of 3D vessel localization is the determination of vessel magnification to convert pixel measurements to physical dimensions, which is necessary for any QCA technique. The model-based approach was chosen because it allowed us to also exploit knowledge of the z-dependent LSF in any image plane using the OTF model. This may produce more accurate results at small vessel diameters (< 1.0 mm) where the apparent diameter is mainly due to the system LSF. Further work is required to determine which diameter measurement method produces the best results within the calibration-free QCA framework.

2.5.1 Limitations and Future Work

Although the algorithm produced satisfactory results, the validation was performed on straight vessel phantoms imaged under low noise imaging conditions with a flat background. The results thus represent the limit against which future results obtained under clinical conditions (background anatomy, branching vessels, eccentric lesions, higher noise levels) can be compared.

The diameter measurements were based on a model that assumes a circular cross section of the vessel. Although this assumption may be accurate for healthy vessels, lesions can be eccentric, and a single diameter measurement from one view may not accurately characterize the severity of an occlusion. This weakness is common to all single projection QCA methods, including ours but can be addressed if angiograms are acquired at multiple projection angles.

In this initial study, vessel analysis was performed offline in software. A fast intraprocedural implementation would be desirable. Minimizing the time required to perform the measurements will increase the likelihood that interventionalists will use the algorithm to guide clinical decisions.

Some of the future work identified in this study is presented later in this dissertation. In Chapter 4, vessel sizing performance was analyzed as a function of vessel SDNR. In Chapter 5, the vessel sizing algorithm was tested *in vivo*, which challenged the algorithm with a heterogeneous background, overlapping structures, and cardiac motion. The remaining items, including eccentric lesions, vessel branching, and algorithm execution time, are still potential topics for future investigation.

2.6 Conclusions

This initial phantom study demonstrated that, using inverse geometry x-ray fluoroscopy and tomosynthesis, it is feasible to perform calibration-free measurements of vessel dimensions with sub-millimeter accuracy and precision on the order of the pixel size. Accurate measurements of diameter and length were obtained using a wide range of foreshortening angles and vessel positions along the source-detector axis. Reducing the overhead of the calibration step simplifies the QCA measurement, making it easier to use in an interventional setting. This could lead to better device selection, thereby improving outcomes and reducing costs.

This page was intentionally left blank.

Chapter 3 – Vessel Sizing Algorithm Revisited

3.1 Introduction

The vessel sizing algorithm and feasibility study presented in Chapter 2 demonstrated the principle of using out-of-plane blur from tomosynthetic images to track the depth of vessel-like structures. The depth information was used calculate geometric magnification and true 3D lengths without requiring multiple views or a calibration object for a size reference in the field of view. From this information, the diameter and length of a vessel segment could be accurately computed and used for interventional device size selection.

The algorithm was divided into four basic steps:

1. 2D Vessel Centerline Initialization
2. 2D Vessel Edge Segmentation and 2D Centerline Refinement
3. 3D Edge Depth Localization and 3D Centerline Creation
4. Model-based Diameter Measurement

While the initial implementation produced satisfactory results and basic proof of principle, the successful completion of each step was due in large part to the simple image scene and noise-free nature of the images. These near-ideal imaging conditions allowed for simple methods to be used for localizing vessel centerlines and edges. However, these methods routinely failed to produce usable results (or they required considerable user interaction and parameter tuning to run to completion) when used with more clinically realistic image scenes and noisy images. This chapter describes the development of a more robust algorithm, designed to produce results on a wide variety of images without constant user intervention.

The following sections describe the revised vessel sizing method in terms of the four steps listed above. This revised method was designed to require the user to only specify the endpoints of the segment of interest and to use the same set of parameters regardless of the nature of the image being analyzed.

3.2 Imaging Conditions and Reconstruction Parameters

The vessel sizing algorithm assumes conventional SBDX imaging and reconstruction methods, which are reiterated here for convenience. In general, these are the same as those used in the feasibility study of Chapter 2, with changes made to reflect new detector hardware and changes to the reconstruction engine. It is assumed that the vessel of interest is positioned in the x-ray field-of-view near mechanical isocenter of the gantry, approximately 45 cm above the x-ray target plane. The x-ray source was operated using 71 x 71 focal spot positions ("7 inch" mode), at a frame rate of 15 scan frames per second, although 10 frames per second was also used for the *in vivo* studies of Chapter 5. Raw image data was acquired using the most recent photon counting detector, which has 160 x 80 detector elements with 0.66 mm detector element pitch. Tomosynthesis image reconstruction was used to generate a stack of 32 tomosynthetic image planes, with 5 mm spacing between planes and the central plane located near the vessel of interest (typically at mechanical isocenter). The algorithm does not require that a plane coincide with the vessel; however it is desirable for the plane stack to be roughly centered on the vessel.

The image reconstruction parameters used include shift parameter *m* equal to 10 pixels, and spread parameter *s* equal to 1 with fractional binning enabled. Pattern correction was performed to remove the stationary repeating variation due to the back projection process. Pixel values were calculated with floating point precision in units of counts per pixel, followed by scaling to fill the dynamic range of unsigned 16 bit file format prior to writing the image to disk. For each frame, a multiplane composite image was formed using the Triple Ring Technology Inc. plane selection implementation. The composite image was derived from no less than 16 of the 32 planes in the tomosynthetic image plane stack.

3.3 Revised Algorithm Implementation

3.3.1 2D Vessel Centerline Initialization

The purpose of the initial 2D centerline is to provide a point of reference inside the vessel boundaries at any point along its length. This initial centerline rarely falls on the true center of the vessel and is often referred to as a "pathline" instead of a centerline in the literature [48]. Ideally, a pathline algorithm only requires the user to identify points within the vessel that mark the start and end of the segment of interest, and the algorithm returns a series of 2D points that connect the endpoints [49]. For the purposes of the vessel sizing algorithm, only a pathline was required for initialization because a precise centerline is derived from the vessel edges localized in the following step.

Numerous approaches have been proposed for identifying 2D vessel centerlines or pathlines from angiographic images [50]. The initial vessel sizing algorithm (See Chapter 2) created an initial centerline (pathline) from a series of user specified points connected as a piecewise linear path. Thus, the starting point of the entire algorithm was dependent on the user's ability to roughly identify the segment centerline, and errors at this stage propagated through the remaining steps. For the revised vessel sizing algorithm, a wavefront propagation method was implemented to define an initial centerline path between user selected segment endpoints [48, 51]. This method acts on a "propagation speed" image derived from the angiographic image whose values are positive and proportional to the likelihood that the pixel falls on a vessel. A "wavefront" emanating from the start point travels through the pixels in the image, moving faster through the high value pixels (i.e. those belonging to the vessel). When the wavefront reaches the endpoint, the fastest path to the endpoint is traced back to the start point to create the pathline.

Figure 3.1 shows the stages of this method as well as a typical result on an angiographic image. After the user identifies the start and end points of the path line, the propagation speed image is calculated. First, the composite image is log transformed to compress the bright background regions and stretch the dark regions created by the iodinated contrast in the vessels. Next, a morphological bottom-hat filter is applied with a disk-shaped structuring element whose diameter is slightly larger than the largest vessel diameter expected, typically 40 pixels (~6.4 mm). The bottom hat filter has the effect of making vessel pixels bright and background pixels dark, while suppressing large background features and intensity gradients. The propagation speed image is shown in Figure 3.1(B), where high intensities indicate fast propagations speed. The pathline is created by calculating the propagation time from the starting point outward until the endpoint is reached. Figure 3.1(C) shows the propagation time image, where the pixel intensity is proportional to the propagation time from the starting point to every pixel in the image; dark pixels indicate fast propagation of the wavefront. Finally, the pathline is converted from a series of 2D image coordinates to a smooth piecewise cubic spline parameterized by the arclength.

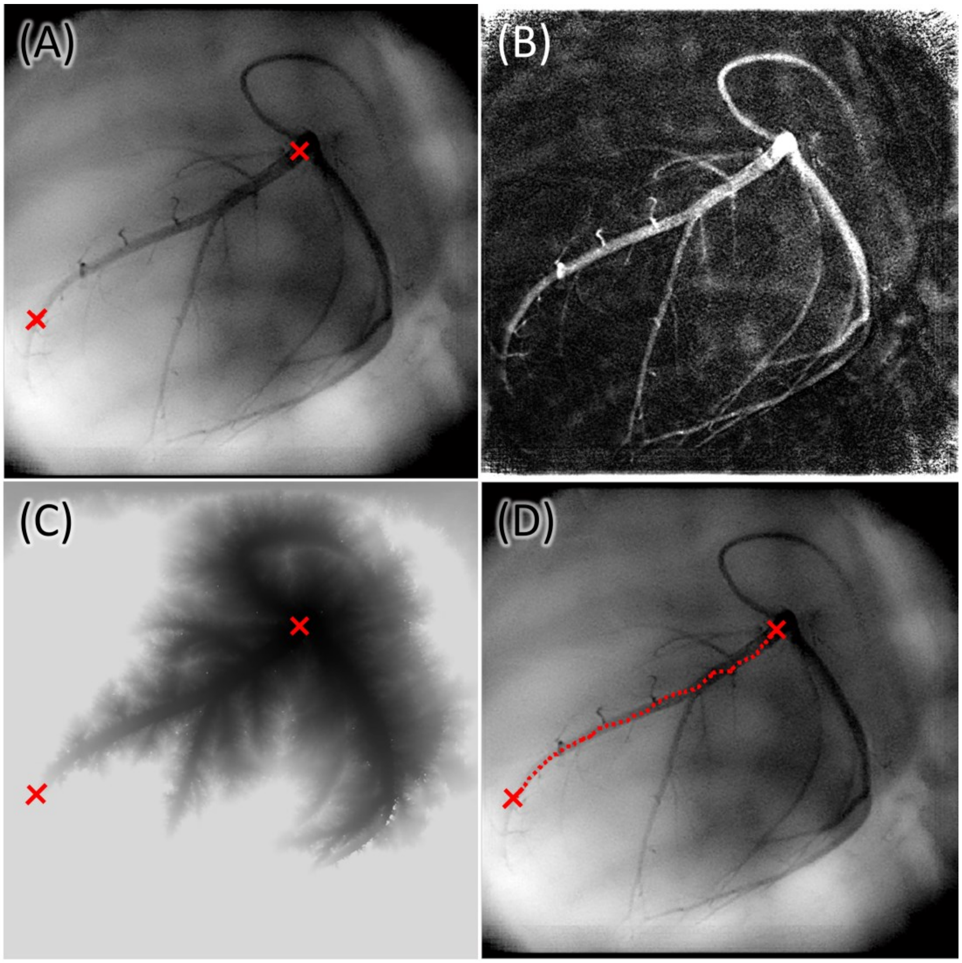

Figure 3.1 – Initial Centerline using Wavefront Propagation
(A) Initial SBDX multiplane composite angiographic image with segment endpoints, starting with the upper point and ending at the lower. (B) Wavefront propagation speed image (C) Final result of propagating the wavefront from the segment start point. Pixel intensity is proportional to the “time” for the wavefront to propagate from the starting point. (D) Resulting initial centerline (pathline) from the algorithm before it is converted into a smooth cubic spline.

3.3.2 2D Vessel Edge Segmentation and 2D Centerline Refinement

The next stage of the algorithm uses the previously defined pathline to localize both edges of the vessel lumen from the multiplane composite image. From the initial centerline, the 2D luminal borders of the vessel segment can be identified which serves two key purposes in the remainder of the vessel sizing algorithm. A more precise 2D vessel centerline can be derived by taking the midpoint between the luminal edges along the vessel length. Also, identifying the lumen edges allows us to limit the scope of the depth localization to pixels on or near the vessel edges.

Originally, the 2D vessel edge localization was performed by connecting the results of the parameterized model fit to single perpendicular intensity profiles extracted regularly along the initial centerline. Since each profile was analyzed independently, image noise or vessel side branches could easily mislead the edge segmentation from the true trajectory. For the low-noise phantom data used in Chapter 2, this method sufficed, but the results quickly fell apart in the presence of image noise and overlapping anatomy present in the studies described in Chapter 4 and Chapter 5.

A more reliable method to segment the 2D vessel edges from the multiplane composite image is to use a technique that exploits the continuity of the lumen edge. From the smoothed initial centerline, perpendicular intensity profiles are extracted from the multiplane composite image at regular intervals along the centerline length. When these profile intensities are plotted as distance along the profile versus distance along the centerline, it appears as a “straightened” vessel whose centerline corresponds to the central column of the image as shown in Figure

3.2(C). From this straightened vessel image, a minimum cost path method was used to find the position of the lumen edge for each profile in a way that is globally optimal.

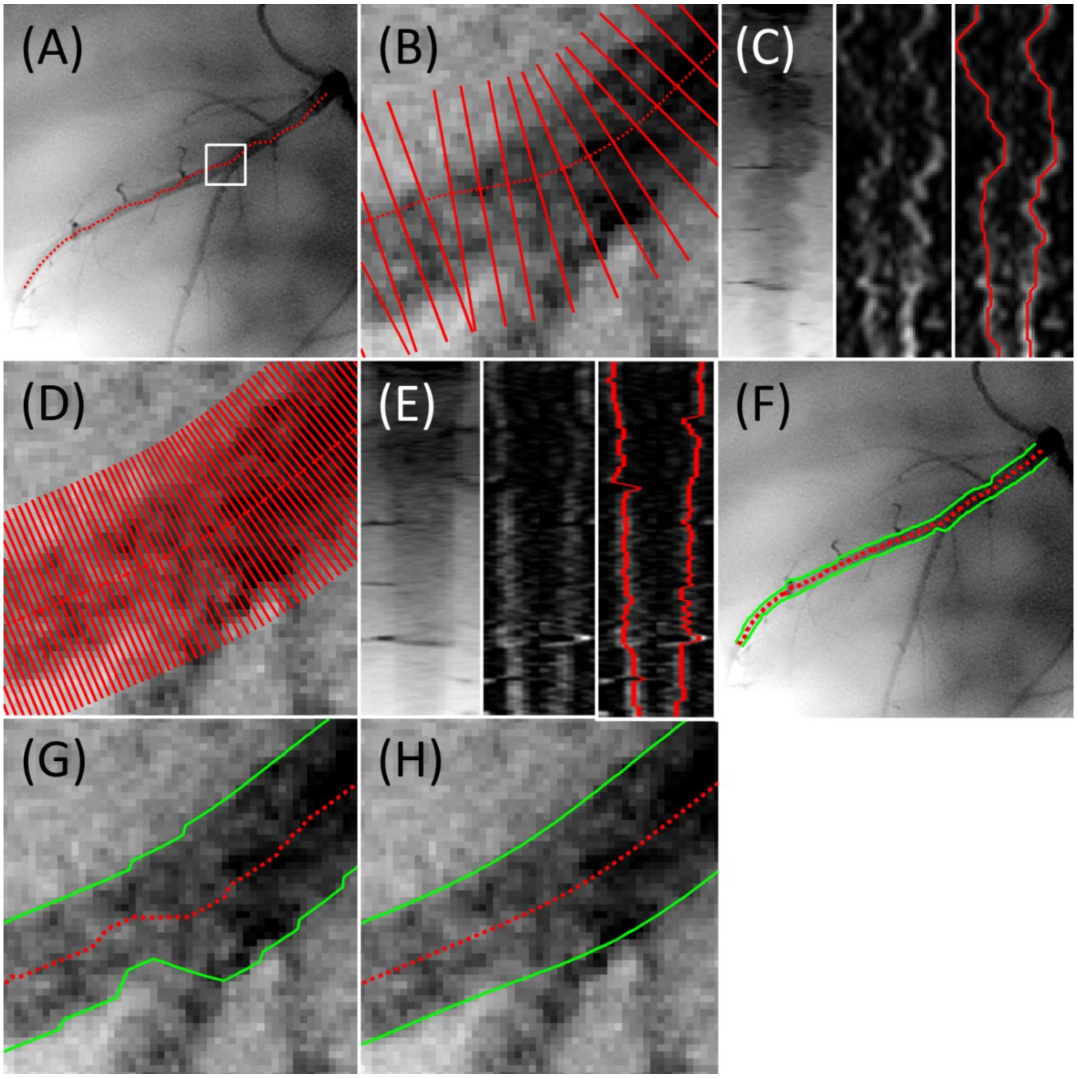

Figure 3.2 – Edge detection and 2D Centerline Refinement

(A) The initial centerline is the basis for 2D vessel edge detection. (B) The ROI shown in the white square of (A) shows the initial centerline with sparsely spaced perpendicular profiles. (C) A straightened vessel image from the perpendicular profiles with the corresponding edge strength and results from a minimum cost path search for the left and right edges of the vessel. (D) The detected edges are used to define a new centerline, along which perpendicular profiles are more densely sampled. (E) The minimum cost path edge detection is applied to the straightened vessel image created from the intermediate centerline. (F) Final results showing the detected edges and the refined centerline. (G) Zoomed view of detected edges and centerline. (H) Detected edges and centerline after smoothing.

The minimum cost path method has been applied previously for calculating vessel lumen diameters from angiographic images [27, 28]. The typical steps for the minimum cost path method are as follows: Using the straightened vessel image, the first and second derivatives along the profile direction are approximated by convolving with first and second difference operators. An edge strength image is created from the weighted sum of the first and second derivative images. When this edge segmentation method is used for actual diameter measurements, the weighting factor is empirically determined to produce the most accurate diameter results. For the purposes of this algorithm, a path corresponding to the first derivative maximum is desired because the depth localization tracks how the first derivative of the edge changes with plane position. Thus all weight was given to the first derivative image and the second derivative image was ignored. The minimum cost path algorithm then transforms the derivative image into a directed graph network and uses Djikstra's algorithm to find the globally optimum path for each side of the vessel lumen[52, 53].

The resulting edges are transformed to the coordinate system of the original 2D multiplane composite image of the angiogram, smoothed, and converted into a piecewise polynomial spline parameterized by the arclength of the original centerline. A new centerline is then formed by sampling the smoothed lumen edges at regular intervals and finding the midpoint between the two edges. This new centerline is used to create a smooth piecewise polynomial which replaces the crude, initial centerline. At this point another iteration of the 2D lumen edge detection and centerline refinement can be performed by using the new centerline as the input. In the refined vessel sizing algorithm, three iterations of lumen edge and centerline detection are performed. The first iteration samples perpendicular profiles 20 pixels long with 1 pixel sample pitch at 5 pixel intervals along the centerline. The following two iterations use 15 pixel long profiles at 1 pixel intervals along the centerline.

By enforcing continuity of the vessel edges and centerline using the minimum cost path method, 2D edge detection is more robust against image noise and overlapping structures. More accurate localization of the edges in 2D ensures that the following edge-depth localization step is tracking the true edge of the vessel across plane positions and ignoring noise artifacts and non-vessel structures. Having a high quality 2D centerline also allows for the summation of multiple perpendicular profiles to reduce noise for the final model-based vessel diameter measurement.

3.3.3 3D Edge Depth Localization and 3D Centerline Creation

From the 2D edge localization results, the 2D image coordinates of the vessel lumen edges as a function of distance along the 2D centerline can be determined. For each point along the 2D vessel edges, the change in edge sharpness within a small ROI is measured across all images in the tomosynthetic image stack. Each ROI of the edge is localized to a particular depth (Z coordinate), and the 2D centerline coordinates (in x,y) and local depth of the vessel are used to compute a centerline of the vessel in 3D physical coordinates. This 3D centerline is used to compute the physical length of the vessel as well as to estimate the magnification and line spread function (LSF) of the vessel edge at each plane to compute an accurate diameter from perpendicular intensity profiles.

The original implementation performed depth localization of the vessel edges by sequentially analyzing small overlapping ROIs over the length of the edge. Within the ROI, the depth localization method previously designed for catheter tracking was applied [4, 5]. This method calculated the threshold-subtracted edge magnitude within the ROI across plane position and determined the edge depth from the center of mass of the edge magnitude versus z-plane distribution [54]. Each edge was localized separately, and the results from each side of the vessel were averaged together. The dependence of the depth localization results on the selection of the two thresholds (T_1 and T_2 in Ref. [5]) was mitigated by the uniform vessel intensity and flat background. When this same method was applied to noisy phantom or *in vivo* images, it was apparent that the thresholds required dynamic adjustment depending on the local image conditions to produce consistent and accurate results. In addition, the fact that each ROI was analyzed independently did not incorporate the known continuity of the vessel edge.

This section describes an alternative depth localization method that eliminates the dependence on thresholds and utilizes *a priori* knowledge of the vessel continuity. Using the two vessel edge contours defined in the previous step, the 2D image coordinates are defined for a series of perpendicular profiles for each edge which occur at regular intervals along the length of the 2D vessel centerline. These image coordinates are used to extract pixel values at the same location in each image in the tomosynthetic image stack, creating a straightened vessel edge image for each edge at each image plane. Each row represents a perpendicular profile along the vessel, with the vessel edge running down the central column of each straightened vessel edge image sets as shown in Figure 3.3. The same row of the two straightened edge images represents intensity profiles of the vessel edge on either side of the same point of the 2D centerline. Thus each edge has a straightened edge image stack, which is used to measure edge strength across image plane position.

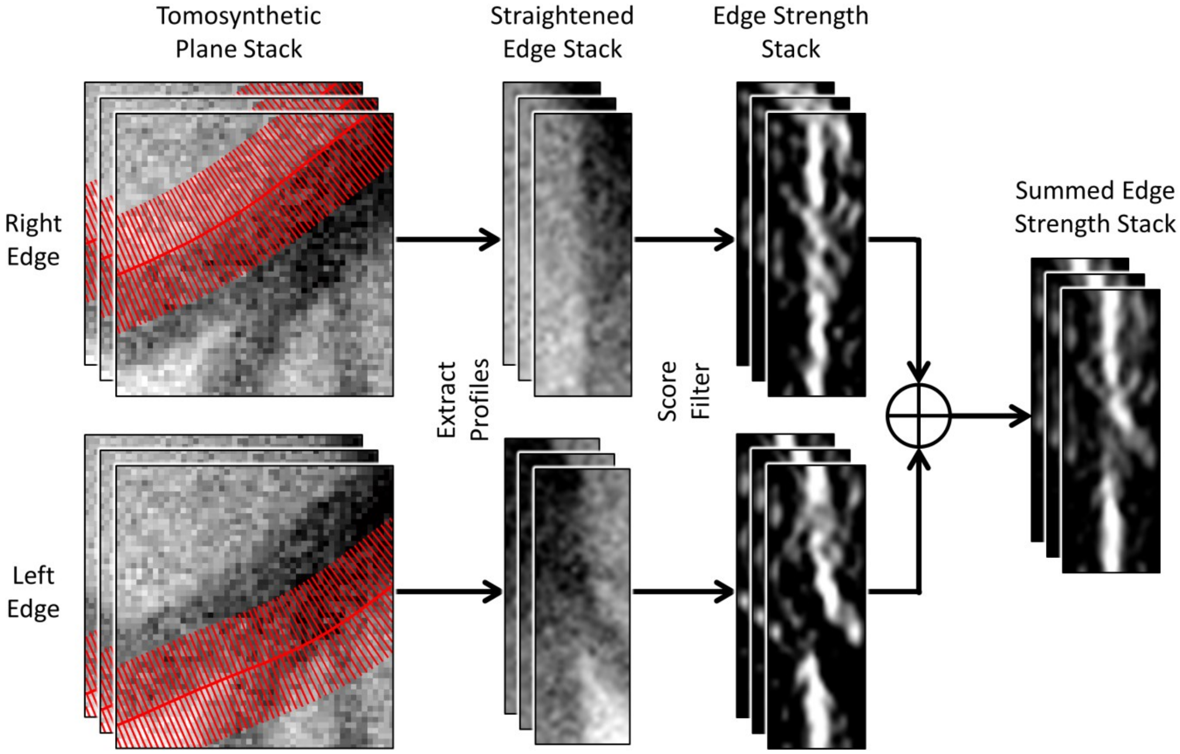

Figure 3.3 – Straightened Edge Strength Stack.
From left to right, perpendicular profiles centered over the left and right edges of the vessel are extracted at each image plane to create a stack of straightened edges images for each side. The score filter is applied to create a stack of images whose values are proportional to the strength of the edge to be localized. The two edge strength stacks are summed together on a plane-by-plane basis.

The following edge filtering procedure is applied to both of the edge image stacks to enhance the vessel edge and suppress noise and non-vessel edges prior to depth localization. First, each image in the edge image stack is log transformed, followed by a 3x3 boxcar smoothing filter. Then, each image is convolved with a vertical 3x3 Prewitt filter to produce a positive response at the vessel edge. The resulting image is inverse-log transformed, and negative values are set to zero, as they can only be due to image noise or non-vessel edge features. The final image has units of local image contrast, similar to the “score image” described in [5], however the pixel values are due to edges oriented similarly to the vessel edge, reducing the influence of other non-vessel edge features as demonstrated in Figure 3.4. Applying this procedure to each image in both of the straightened edge image stacks produces two stacks of straightened edge strength images. The images in the two stacks are summed on a plane by plane basis to create a single straightened edge strength image stack. The advantage of summing the two edge score stacks together is to reduce the impact of areas where there is no edge strength signal due to image noise fluctuations, an overlapping structure, or side branch (see the “left edge” in Figure 3.3). The edge strength at each point along the vessel length can be measured from the combined edge strength image stack to localize the depth of the vessel edge across the entire vessel segment.

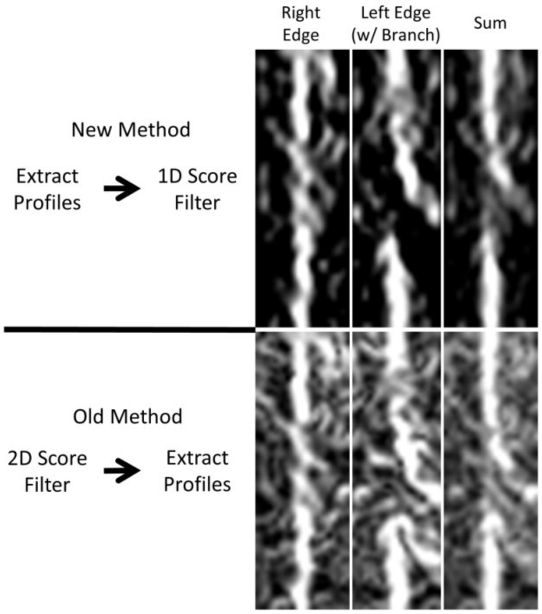

Figure 3.4 – Vessel Specific Edge Detection.
By extracting the profiles first, then applying the score filter along the profile direction only, the signal from noise and non-vessel edges is suppressed. The previous implementation performed the score filter along both dimensions, which creates extraneous values from non-vessel pixels.

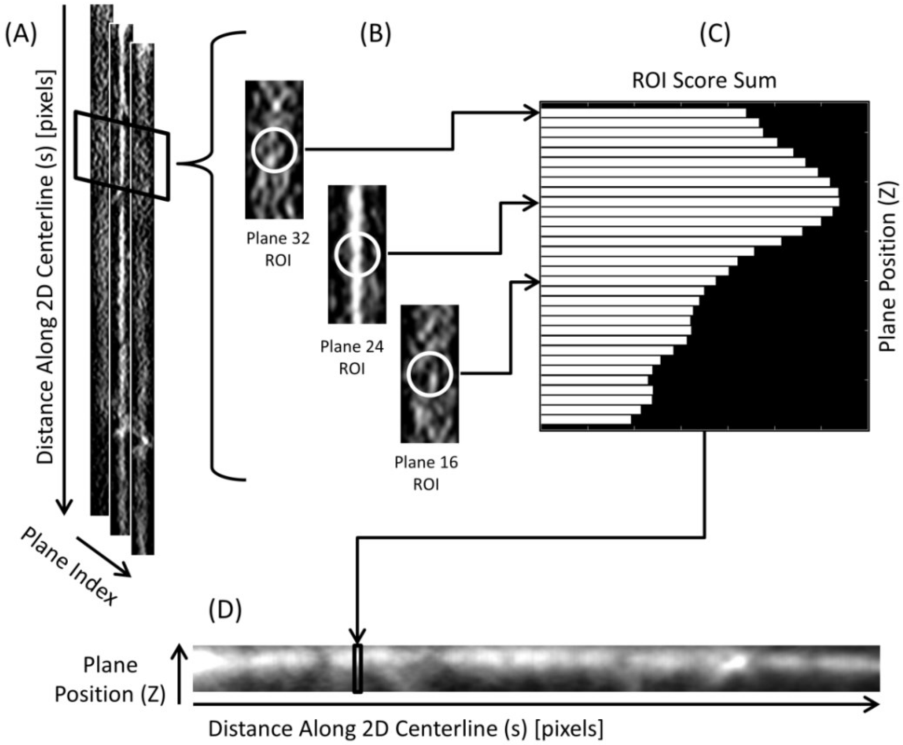

Figure 3.5 – Vessel Edge Strength Versus Plane Position.
(A) Summed edge score images are calculated for each image plane position. (B) Values inside ROIs are extracted from each image plane along the length of the vessel. (C) The values in each ROI are summed at each plane to make a distribution of ROI edge strength versus plane position. (D) This process is repeated along the length of the vessel to create a map of edge strength as a function of image plane and position along the vessel length. Note in (A) and (B), edge score images are only shown for 3 planes for clarity. Typically 32 image planes (as shown in (C)) are used by the algorithm.

For each point along the vessel edge in the summed edge strength image stack, the score strength for that point along the edge is calculated across each plane position. For each row along the central axis, values are summed within a circular ROI. By including values within an ROI instead of only using values along the central image axis, some spatial smoothing is introduced and true edge pixels that are off of the central axis due to errors in vessel edge segmentation are included. The pixels within the ROI are summed together at each image plane to create a distribution of edge strength versus plane position. This process is repeated for each row in the summed edge score stack to make a sequence of distributions of edge strength sum versus image plane position, as shown in Figure 3.5.

The final step in depth localization of the edges is to assign a depth for each position along the edge of the vessel. The previous implementation independently calculated the depth for each ROI along the vessel edge. In the revised sizing algorithm, the continuity between neighboring positions along the edge is exploited by fitting an active contour model through the edge strength sum distributions along the length of the vessel [55, 56]. An active contour model is a curve that is iteratively deformed to minimize the sum of internal and external energies acting on the curve. Assume an image matrix where the column represents distance along the vessel, the row corresponds to plane position, and value is the edge strength sum within the ROI as shown in Figure 3.6. Each column of the image contains one control point for the active contour. External energy is defined by the inverse of the intensity of the image. Internal energy is defined by the integral of the second derivative of the curve (so called "rigidity") along the horizontal direction[2]. Essentially, the curve should follow the peaks of each image column while minimizing the changes in curvature. To initialize the control points of the contour, a minimum cost path was calculated. The active contour model is deformed for multiple iterations (typically 1000) until it converges. The final position of each control point is used to interpolate between image plane positions to determine the depth of the vessel at each point along its length. Figure 3.7 provides an intuitive visualization of the final active contour model. A more detailed explanation of the active contour model used in this algorithm can be found in Appendix B.

---

[2] Active contours often have a second internal energy term, elastic energy, which is the overall length of the contour. In this case, there is no *a priori* knowledge that the length of the vessel segment should be minimized, so elastic energy term is omitted.

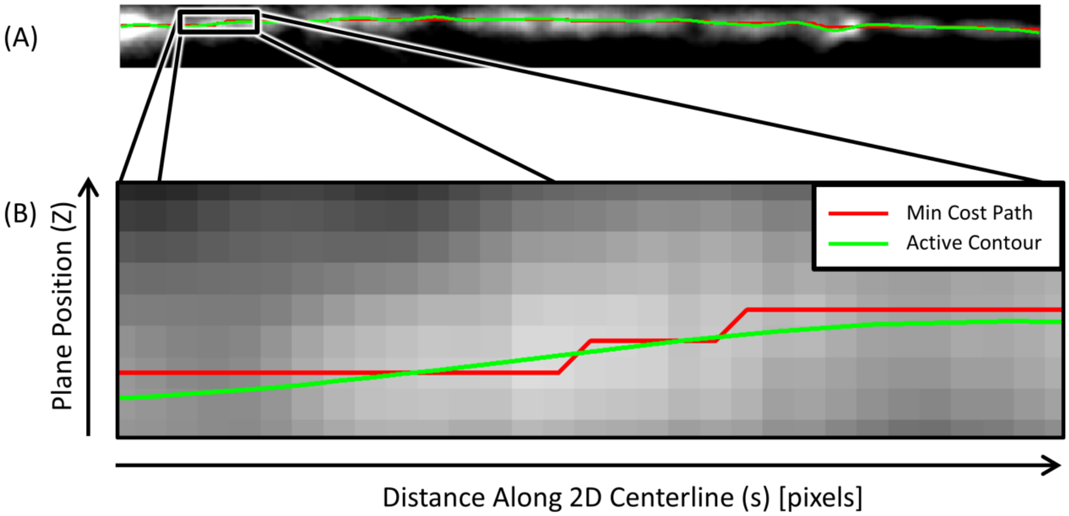

Figure 3.6 – Minimum Cost Path Versus Active Contour for Localizing Depth. (A) To determine the initial depth of the vessel edge at each point along its length, a minimum cost path (red) is fit through the score sum distributions across the entire vessel. The result is a piecewise linear function. (B) The minimum cost path is used to initialize the active contour model (green) for the vessel edge depth function. After multiple iterations, the active contour model (green) provides a smooth function of vessel edge depth along its length.

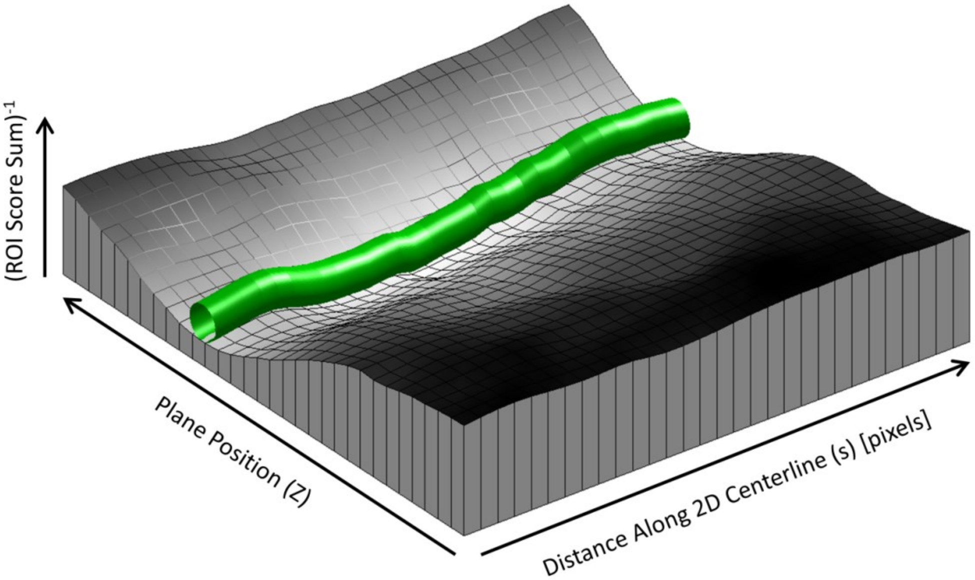

Figure 3.7 – Mesh Rendering of Edge Strength Distributions and Active Contour. An intuitive way to interpret the active contour process is to treat the contour as a flexible tube resting in a trench. The hose will gravitate toward the low regions of the trench, which correspond to high edge strength. The rigidity of the hose will keep it smooth and continuous.

3.3.4 Vessel Segment Length Measurement

From the active contour, the depth of the vessel for each point along the 2D vessel centerline is known. A simple transform is used to convert the 2D image coordinates plus the depth into 3D physical coordinates. This series of 3D points is used to create smooth piecewise 3D cubic spline (in physical units) that is parameterized by distance along the 2D centerline (in pixels). The final segment length, in physical units, is calculated by sampling the 3D spline at regular intervals and calculating the 3D arclength.

3.3.5 Model-based Diameter Measurement

The final diameter measurement is calculated using the same parameterized model fitting method as the previous implementation (see Section 2.2); however, the preprocessing steps have been changed to improve the robustness of the results across various imaging conditions. First, coordinates are defined for perpendicular profiles spaced regularly along and centered about the 2D centerline in the multiplane composite image. For each perpendicular profile, the point on the 3D centerline corresponding to the profile's center is calculated. The tomosynthesis image plane nearest to the point on the 3D centerline is determined, and intensities are extracted from the tomosynthetic image at that plane (not from the multiplane composite) along the profile. The pixel pitch of the tomosynthesis images changes with plane position, so spacing between samples along the perpendicular profile is normalized to ensure that the sample spacing, in physical units, is the same for each profile. This process is repeated for each perpendicular profile position, and the intensity profiles are stored in an image similar to the straightened vessel image used for 2D edge localization. Whereas before the perpendicular profiles were extracted from the 2D multiplane composite, these profiles are extracted from the original tomosynthetic images, which ensures that any artifacts in the multiplane composite due to plane selection errors are not propagated to the diameter measurements. Figure 3.8 outlines the process of creating the "nearest-plane" straightened vessel image for diameter measurements.

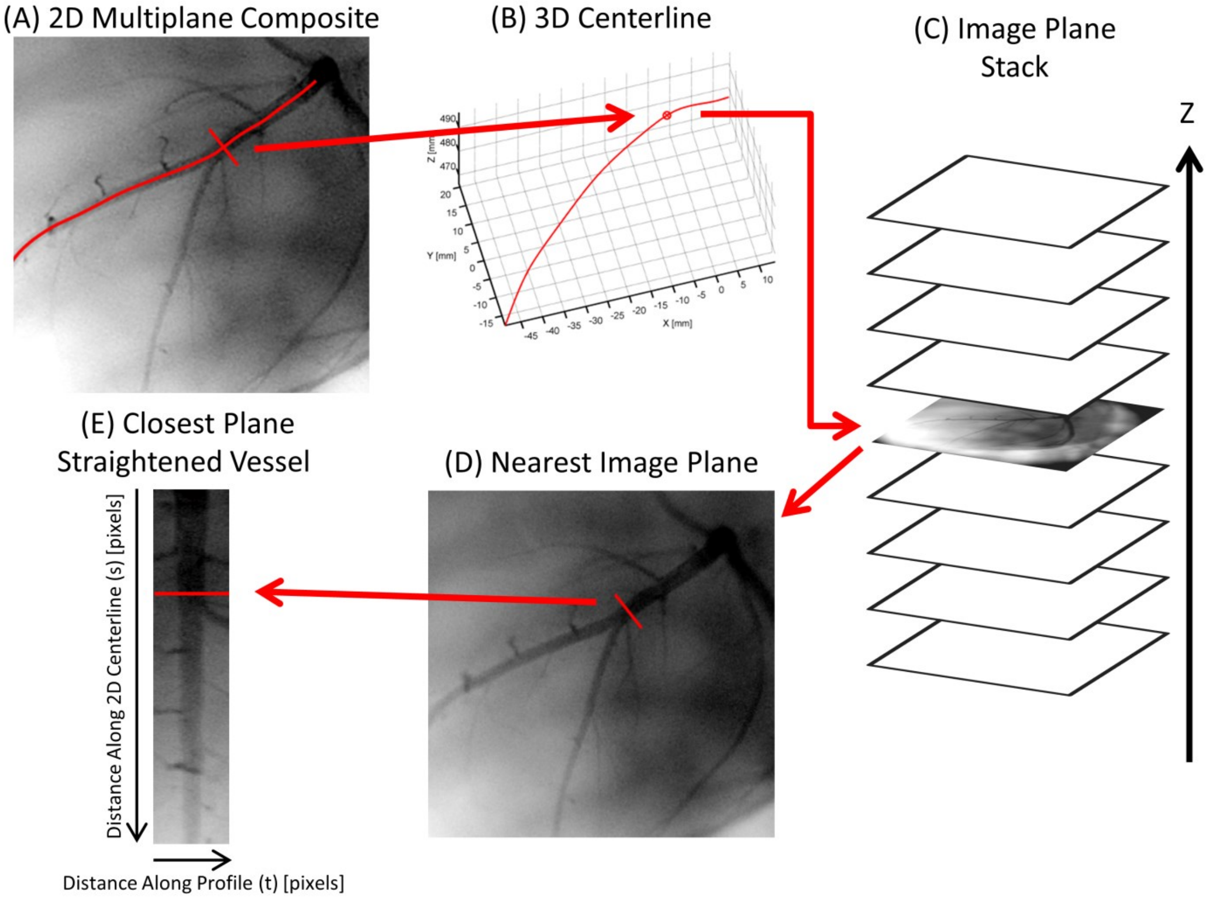

Figure 3.8 – Nearest-Plane Straightened Vessel Image for Diameter Measurements

(A) For a given position along the 2D vessel centerline on the multiplane composite, perpendicular profile coordinates are defined. (B) The point corresponding to the center of the profile is mapped to the 3D centerline. (C) The Z coordinate of the 3D centerline point is used to determine the nearest image plane in original plane stack. (D) The profile coordinates are normalized by the pixel spacing of the image plane and used to extract perpendicular profile. (E) Each extracted profile is used to build a straightened vessel image where the values were extracted directly from the tomosynthetic images instead of the multiplane composite image.

The nearest-plane straightened vessel image is preprocessed prior to measuring vessel diameters. First, the image is log-transformed, which helps to improve diameter accuracy for larger vessel diameters and when vessels are severely foreshortened. The log transform corrects an approximation in the previous implementation and makes the vessel profile values proportional to the path length through the vessel, matching the original assumption of the model based diameter measurement [31]. To improve the SNR of the vessel profiles prior to calculating vessel diameter, a moving average filter was applied across adjacent intensity profiles. Typically, profiles were extracted 1 pixel apart along the vessel 2D centerline and a 31 point 1D boxcar filter was used, which roughly corresponds to a 5 mm moving average filter along the vessel length (assuming the vessel is near isocenter and is not foreshortened).

Prior to the optimization of the parameterized vessel profile model to the measured profile, the model parameters are initialized. The main vessel profile, $v(t)$, has three parameters which control the shape and position along the length of the profile: the radius of the vessel (r), center of the vessel with respect to the profile (c), and the gain of the profile (α). Each parameter is a scalar value. The background intensity, $b(t)$, is modeled as a first order polynomial[3] such that $b(t) = b_1 t + b_0$. The set of initial parameters for the vessel profile model, $\{\hat{r}, \hat{c}, \hat{\alpha}, b_0, b_1\}$, are calculated from the results of the 2D minimum cost edge detection algorithm applied to the smoothed nearest-plane straightened vessel image. The positions along the profile where the left and right edges are detected, t_{left} and t_{right}, are used along with the measured profile, $\hat{p}(t)$, to initialize the parameters as shown in Figure 3.9. Parameter values of $\hat{r}$, $\hat{c}$, and t are scaled to

---

[3] In Chapter 2, $b(t)$ was modeled as a 5th order polynomial.

physical units from pixel dimensions by multiplying by the pixel size of the plane from which the intensity profile was extracted.

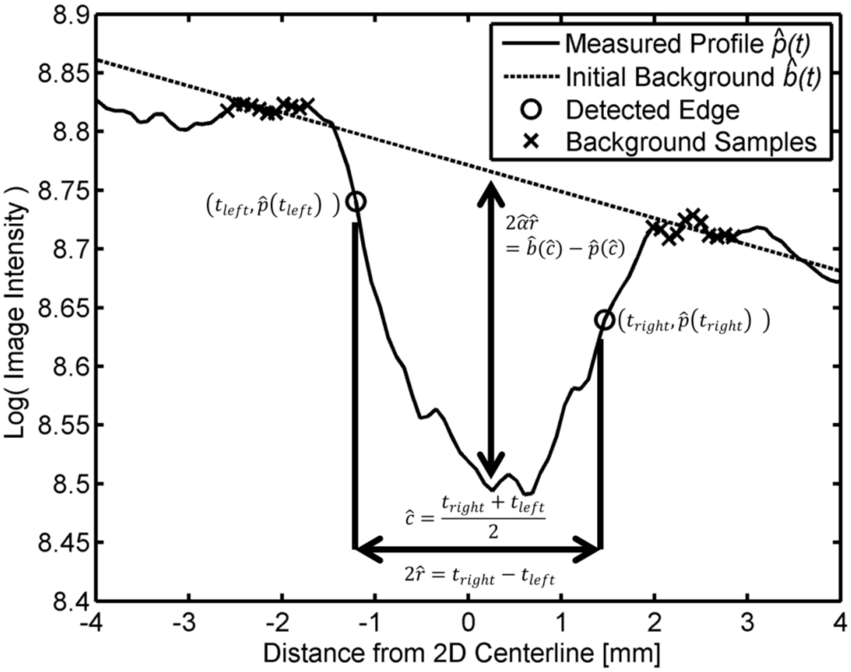

Figure 3.9 – Vessel Profile Model Parameter Initialization.
Minimum cost path edge detection results are used to initialize the parameters used in the model fitting algorithm. The initial radius, $\hat{r}$, is based on the distance between the two detected edges at t_{left} and t_{right}. The initial center of the profile, $\hat{c}$, is the midpoint between the two detected edges. The background $\hat{b}(t)$, is estimated as the least squares fit through a subset of points from the measured profile, which are offset a fixed distance outside of the detected edges. The gain factor, $\hat{\alpha}$, is estimated from the distance between the center of the measured profile, $\hat{p}(t)$ and the background estimate, $\hat{b}(t)$.

The line spread function $lsf(t)$ factors into the vessel diameter measurement. It is a function of SBDX geometry, image plane position, image reconstruction parameters, and the Z-coordinate of the 3D vessel centerline at the point where the intensity profile is being measured. Changes made from the LSF model in the original vessel sizing method were related to the rectangular geometry of the new detector and a better approximation of the focal spot shape and size. Specific details regarding the calculation of the LSF model can be found in Appendix A.

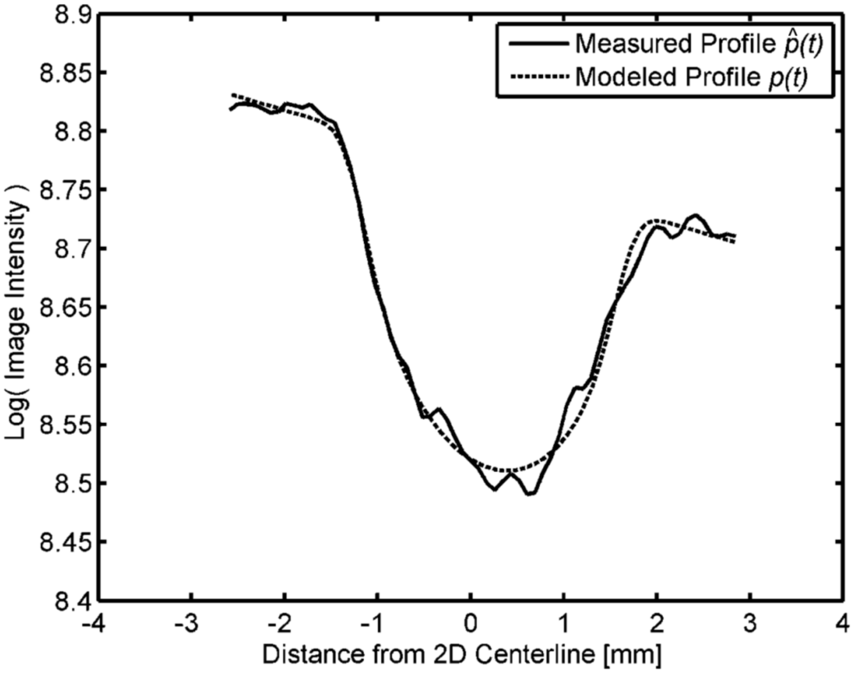

Figure 3.10 – Vessel Profile Model Fit.

Using the initial parameters described in Figure 3.9, the optimization method finds the set of parameters that minimizes the sum of squared error between the measured profile and the model. Note that the portion of the profile used has been truncated to extent of the background samples shown in Figure 3.9. This helps to mitigate the effects of nearby structures on the model fitting result.

With the initial parameters and LSF estimate, the parameter optimization routine is applied to minimize the error between the observed and modeled vessel profile, in a least squares sense as described in Chapter 2. Figure 3.10 shows an example the final vessel profile model based on the initial parameters described by Figure 3.9. The parameter space was searched using the Nelder-Mead simplex method. This process is repeated for each row in the smoothed nearest plane straightened vessel image to compute the vessel diameter along the entire vessel segment, where the vessel diameter is simply two times the optimal radius parameter, r. The position of the profile along the 2D centerline can be used to map the diameter results to a position along the physical 3D centerline of the vessel to produce a plot of vessel segment diameter versus length in physical units.

3.4 Conclusions

The newly proposed vessel sizing method is designed to compute vessel segment length and diameter measurements across a variety of imaging conditions, including the low SNR phantom images presented in Chapter 4 as well as the *in vivo* images in swine presented in Chapter 5. To increase robustness, previously described algorithms that are designed to work on vessel-like structures were employed to exploit the continuity of the vessel edges along the length of a segment. Similarly, the depth localization step was made more task-specific by using *a priori* knowledge to calculate edge strength based only on gradients perpendicular to the vessel edge, using edge strength from both edges simultaneously for depth localization, and using an active contour to find the depth of the vessel such that it fits the vessel as a whole. The active contour acts locally on the edge strength distribution across plane position, avoiding the need to use the threshold based method from the previous implementation. Lastly, the diameter measurement method was improved by exploiting prior edge location information to improve parameter initialization reliability, allowing for multiple profiles to be averaged prior to model fitting, and using the log-transformed vessel profile to improve the accuracy for thick and highly foreshortened vessels.

This page was intentionally left blank.

Chapter 4 – Vessel Sizing Performance Versus Vessel Signal Difference to Noise Ratio

4.1 Introduction

In Chapter 2, the feasibility of the tomosynthesis based, calibration-free vessel sizing algorithm was presented. The results showed that under near ideal imaging conditions, the out-of-plane blur of vessel edges could be used to build a 3D vessel centerline, from which absolute vessel length could be calculated. The magnification of the vessel could also be determined from the 3D centerline, which was used to accurately scale diameter measurements to physical units. The noise-free images used in the study were synthesized by averaging multiple image frames of an already high quality acquisition. To obtain similar high-quality, low-noise images in actual use would both exceed the limits of the SBDX system and require an excessive dose of x-rays to the patient. For such an algorithm to be used clinically, it needs to work under sub-optimal conditions. This motivated the work presented in Chapter 3, which was intended to make the algorithm robust when performed on images whose quality is closer to what is expected in practical use.

Imaging tasks such as detection, segmentation, and quantitative measurements are fundamentally influenced by the quality of the images being analyzed. The need to address various imaging conditions has been acknowledged in the work by other groups; however the breadth of such examinations is limited. Nearly all experimental validations examine vessel phantoms with various diameters [27, 28, 31, 57-67]. Additional variations include contrast media concentration [27, 57-60, 62], total phantom thickness[27, 58], and x-ray tube potential[27, 58, 65]. The aim of these studies was usually to examine systematic errors through the use of varied, but relatively low-noise images with different scenes. As such, these images were usually of high-quality, which is seldom achieved clinically with the exception of thin patients and non-oblique view angles. Very few, if any studies, have explored how their algorithm performs under poor imaging conditions.

For tasks analyzing an object or feature in the image, a simple and convenient way to measure image quality is the object's signal difference to noise ratio (SDNR). The signal difference, or contrast, is the change in signal level (x-ray intensity, photon counts, etc.) relative to the background signal. The noise is the fluctuation of the background signal, usually quantified by the standard deviation over a nearby region of constant average intensity. The ratio of these two measurements is the SDNR (sometimes called the contrast-to-noise, or CNR, in the literature). Simple detection tasks have been shown to be dependent on the SDNR of an object (e.g. Rose criterion). Segmentation and quantification tasks are similarly dependent on SDNR.

The SDNR of an object in x-ray imaging depends on the object being imaged and the imaging system parameters. Imaging parameters such as the tube potential (kV), tube current (mA), pulse width (ms), as well as any beam shaping filters or background attenuation material will affect the background noise (as well as object signal via beam hardening, detected scatter, etc.). The object material determines how it attenuates x-rays to create a signal. Frequently in QCA literature, the imaging setup is not fully described. For example, they may provide the tube potential, but omit the tube current. This makes it difficult to interpret reports of the accuracy and precision of vessel measurements because the imaging setup cannot be reproduced. Using the SDNR metric, details of the imaging parameters can largely ignored because the pertinent image quality information can be obtained directly from the images.

The following chapter examines how the improved vessel sizing algorithm presented in Chapter 3 performs with respect to vessel SDNR. Whereas past studies have focused almost exclusively on diameter measurements, the unique capability of the algorithm to localize the vessel in 3D makes it suitable to calculate vessel segment lengths, even when the vessels appear foreshortened. The other major claim of the algorithm is its ability to measure vessels without magnification calibration. As such, the studies presented here will show how vessel magnification, foreshortening, and SDNR interact to influence vessel length and diameter measurement accuracy and precision.

4.2 Methods

Three separate but complementary experiments were performed in this study. First, vessel phantoms and various thicknesses of PMMA background attenuator were imaged with the same x-ray operating point to produce a range of clinically relevant vessel SDNRs. The results of this experiment served as a baseline for the relationship between vessel measurement performance and SDNR. In the two subsequent experiments, the magnification and foreshortening of the vessels was varied in addition to vessel SDNR. Comparing the results with and without the added variable of magnification or foreshortening directed further investigation.

4.2.1 Vessel Phantom with Varied Total Thickness

A simple vessel phantom setup was created by positioning a series of vessel mimicking wires between stacks of PMMA sheets. The vessels wires were made of out of a magnesium-cadmium (MgCd) alloy whose contrast simulates 350 mg/mL iodinated contrast at diagnostic x-ray energies [46]. The vessel phantoms each had a nominal length of 40 mm, with diameters of 2.80 mm, 2.06 mm, 1.38 mm, 1.04 mm, 0.73 mm, and 0.53 mm. With the vessel phantoms positioned at mechanical isocenter, equal amounts of PMMA were positioned above and below the plane of the vessels. Total phantom thicknesses imaged were 18.6, 21.0, 23.3, 25.6, 28.0, 30.3, 32.6, and 35.0 cm.

4.2.2 Vessel Magnification Phantom

The magnification of an object imaged with SBDX was determined by its position along the source-detector axis. Due to its inverse geometry and reconstruction scheme, object magnification increased as the object moved closer to the detector and decreased as the object moved closer to the x-ray source plane, which was opposite of a conventional geometry. Different magnifications were achieved by positioning the plane of the vessel phantoms from 12 cm below mechanical isocenter to 12 cm above in 4 cm increments. This produced a change in vessel magnification from 90% to 113% relative to the magnification at isocenter. Two different total thickness of PMMA were used for background attenuation and filtration, 25.6 cm and 35.0 cm, with equal amounts placed above and below the vessel phantoms as shown in Figure 4.1. SDNR was varied in this experiment by post-acquisition integration of image frames.

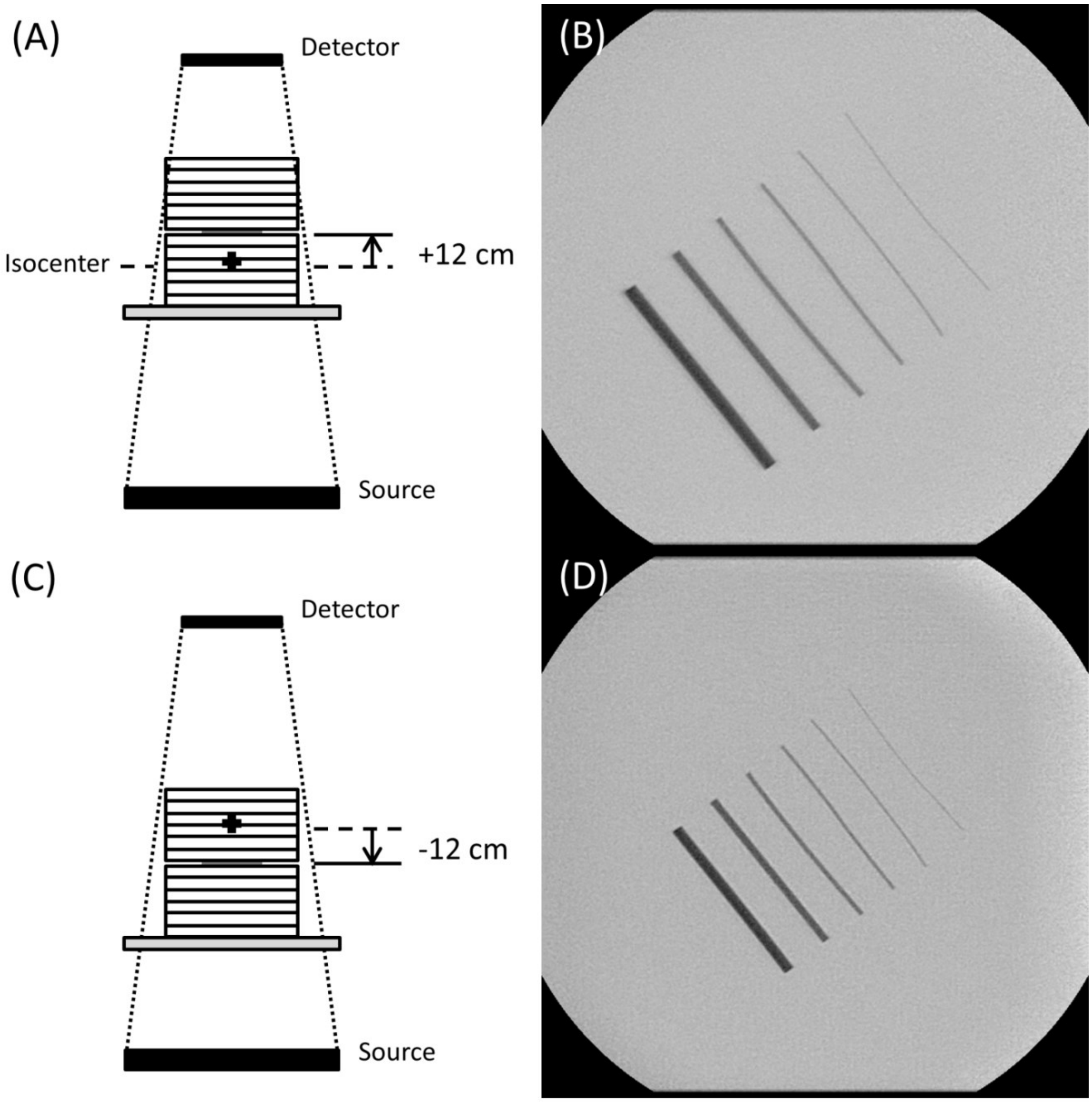

Figure 4.1 – Vessel Phantom Magnification

The MgCd vessel phantoms were positioned between two equally thick stacks of PMMA. The position of the vessel phantoms along the source detector axis determined their apparent size in the image. Relative to their appearance at isocenter (cross) moving the vessels above isocenter (A) increased their magnification as shown in (B). Moving the vessels below isocenter (C) decreased their magnification as shown in (D). Note that the system geometry is exaggerated for clarity.

4.2.3 Vessel Foreshortening Phantom

The apparent length of a vessel was determined by the angle of the vessel axis relative to the detector/image plane. When this angle, ϕ, was zero, the vessel length was accurately represented (i.e. non-foreshortened). When ϕ was greater than zero, the vessel length appeared shorter than in the non-foreshortened case. To create images where the vessel phantoms appeared foreshortened, the phantoms were rotated about an axis perpendicular to the source-detector direction. The rotating stage was constructed from a thin sheet of PMMA mounted between two upright sheets of PMMA such that it could create any value of ϕ between 0° and 90°. This "seesaw" apparatus shown in Figure 4.2 was the same device that was used in the feasibility study described in Chapter 2.

The set of MgCd wires used in the previous experiments served as the vessel phantoms for this setup. The wires were positioned symmetrically about and perpendicular to the axis of rotation so that the centers of the wires remained near isocenter. For additional attenuation, one 2.3 cm sheet was secured on the rotation stage above the vessel wires. Additional sheets of PMMA were placed below the stage and between the collimator exit and patient table for added attenuation.

Similar to the vessel magnification phantom, total the phantom thickness was either 25.6 cm or 35.0 cm, and the SDNR was varied by post-acquisition frame integration. As ϕ increased, the effective thickness of the PMMA stage and attached sheet increased by a factor of $1/\cos\phi$. To compensate, the number of sheets below the stage was reduced to keep the total radiographic thickness constant. Values of ϕ ranged from 0° to 75° in 15° increments. Table 4.1 lists the different thicknesses of PMMA for each section of the phantom at each value of ϕ.

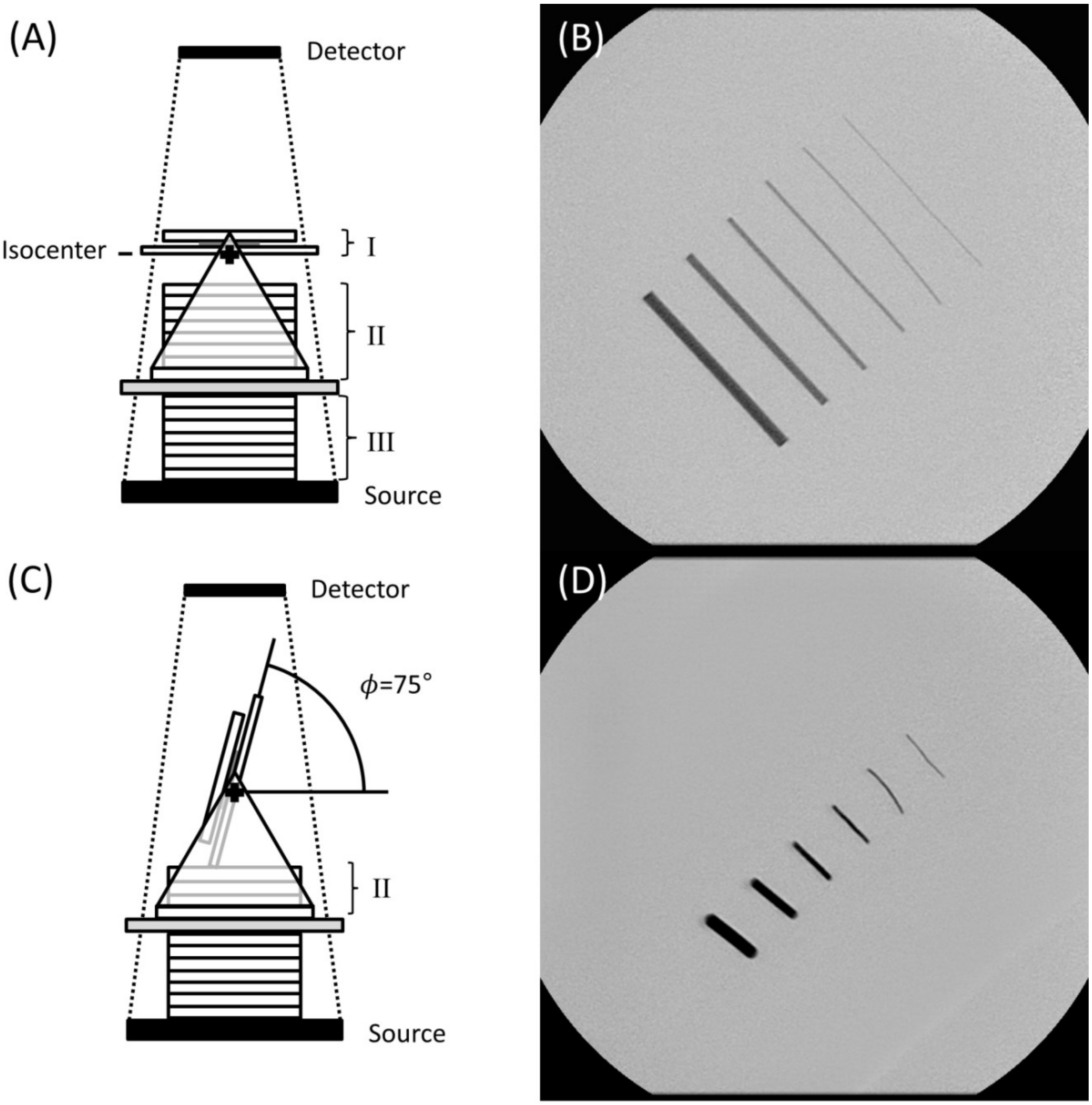

Figure 4.2 – Foreshortened Vessel Phantoms

(A) The foreshortened vessel phantom setup was constructed from PMMA and featured a stage that rotated orthogonal to the source and detector planes. (I) The MgCd vessel phantoms were sandwiched between two layers of PMMA on the rotating stage. (II) Additional background attenuation was created by a stack of PMMA between the rotating stage and the base of the setup. (III) A third stack of PMMA was placed on the collimator exit below the patient table. (B) When the platform was at 0° rotation, the vessels were not foreshortened. (C) As the stage was rotated, the thickness of the stack below the stage (II) was decreased to compensate for the increased path length through the stage (I). (D) Rotating the stage created foreshortened vessels.

Target Thickness [cm]	Angle (ϕ) [°]	I [cm]	I*$(\cos\phi)^{-1}$ [cm]	II [cm]	III [cm]	Actual Thickness [cm]	Mean Counts [photons/pixel]
35.0	0	2.9	2.9	17.5	14.6	35.0	23.2
35.0	15	2.9	3.0	17.5	14.6	35.1	22.7
35.0	30	2.9	3.4	17.2	14.6	35.1	22.5
35.0	45	2.9	4.1	16.3	14.6	35.0	22.8
35.0	60	2.9	5.8	14.6	14.6	35.0	23.5
35.0	75	2.9	11.3	9.0	14.6	34.8	26.4
25.6	0	2.9	2.9	17.5	5.2	25.6	160.9
25.6	15	2.9	3.0	17.5	5.2	25.7	157.6
25.6	30	2.9	3.4	17.2	5.2	25.8	156.1
25.6	45	2.9	4.1	16.3	5.2	25.7	158.1
25.6	60	2.9	5.8	14.6	5.2	25.6	162.1
25.6	75	2.9	11.3	9.0	5.2	25.5	179.4

Table 4.1 – Foreshortened Vessel Phantom Thicknesses

As the foreshortening angle ϕ increased, the effective thickness of the platform (I) increased. The thickness below the platform (II) was reduced to compensate and keep the total thickness of the phantom approximately constant. The thickness of PMMA between the collimator exit and patient table (III) was constant for a given target thickness. See Figure 4.2 for a schematic of the phantom setup.

4.2.4 Image Acquisition, Reconstruction, and Analysis

Image acquisition was performed using the latest available generation of SBDX hardware. The detector featured 320 x 160 elements, which were binned 2 x 2 to form a matrix of 160 x 80 elements with an effective element pitch of 0.66 mm. The long axis of the detector was oriented parallel to the fast scan direction (parallel to collimator rows). The collimator was the “slotted strut” revision. The real-time recording system was used to store raw detector images to the disk array for offline reconstruction. All images were acquired using the 120 kVp, 24 kWp operating point using 71 x 71 source hole positions (“7 inch” mode), running at 15 scan frames per second.

Images were reconstructed using a Matlab-based software reconstruction that simulates the real-time hardware engine. Standard parameters were used to reconstruct the initial set of images. For each phantom setup, a stack of 32 image planes with 5 mm between planes was reconstructed. The center of the plane stack was defined at the same level as the MgCd vessel phantoms. For the case of varying vessel magnification, the center of the plane stack moved according to the position of the phantom. For the foreshortened vessel phantom, the center of the plane stack was always defined at isocenter. Additional reconstruction parameters include shift parameter $m = 10$ and fractional binning with spread parameter $s = 1$. Alpha pattern correction was performed using the “ratio image” approach, as described in Ref. [3]. Briefly, for each phantom configuration (target thickness and vessel position/angle), an identical acquisition was acquired without the vessel wires (i.e. background attenuator only). For each vessel phantom image reconstructed, a highly averaged image of the background was reconstructed at the same plane position, and the vessel image was normalized by the background image on a pixel-by-pixel basis to remove the fixed pattern. Using this method avoids introducing any blurring or other artifacts caused by the local pattern correction method used for real-time reconstruction [2].

In order to assess how the algorithm results change with vessel SDNR, the SDNR of each phantom needed to be varied over the range of values expected in clinical use. For the first phantom setup, each of the eight phantom thicknesses produced a different SDNR for each vessel phantom wire. For the vessel magnification and foreshortening experiments, only two phantom thicknesses were imaged, which would create only two SDNRs for each MgCd wire phantom. To create additional SDNR levels, multiple frames from each acquisition were integrated. Groups of 4 and 8 frames of the 35 cm phantoms were integrated to produce two additional SDNR levels that were greater than single 35 cm thickness frames but less than images of the 25.6 cm phantom. Groups of 4 and 8 frames of the 25.6 cm phantom were integrated to produce images with greater SDNR than single 25.6 cm frames. These combinations produced six different noise levels at which the accuracy and precision of the vessel sizing algorithm could be examined in these two experiments. Figure 4.3 shows how different SDNRs were created by integrating frames from the two phantom thicknesses.

Vessel phantom SDNR was calculated from peak vessel signal and the variation of background intensity as follows. To measure the signal for each phantom thickness and vessel position/orientation, highly-averaged, low-noise images were created. For each diameter of MgCd wire, profiles were extracted perpendicular to the vessel centerline and averaged. The peak contrast C_{peak} for each wire was calculated as $C_{peak} = 1 - \left(\frac{s_{min}}{s_{background}}\right)$, where s_{min} was the minimum signal due to the vessel and $s_{background}$ was the background signal. The intrinsic signal to noise ratio, SNR_{image}, was also calculated for each phantom thickness/position/orientation as $SNR_{image} = \frac{\mu_{background}}{\sigma_{background}}$, where $\mu_{background}$ and $\sigma_{background}^2$ were the mean and variance of the signal as measured in an ROI next to the vessel phantoms. SNR_{image} was calculated from the average value of $\mu_{background}$ and $\sigma_{background}^2$ from 40 image frames. To calculate $\mu_{background}$, the mean of the signal of the ROI was calculated. To calculate $\sigma_{background}^2$, a difference image of two frames was created, and $\sigma_{background}^2$ was calculated as half of the variance within the ROI of the difference image. The SDNR for each vessel phantom was calculated as $SDNR = C_{peak} \cdot SNR_{image}$.

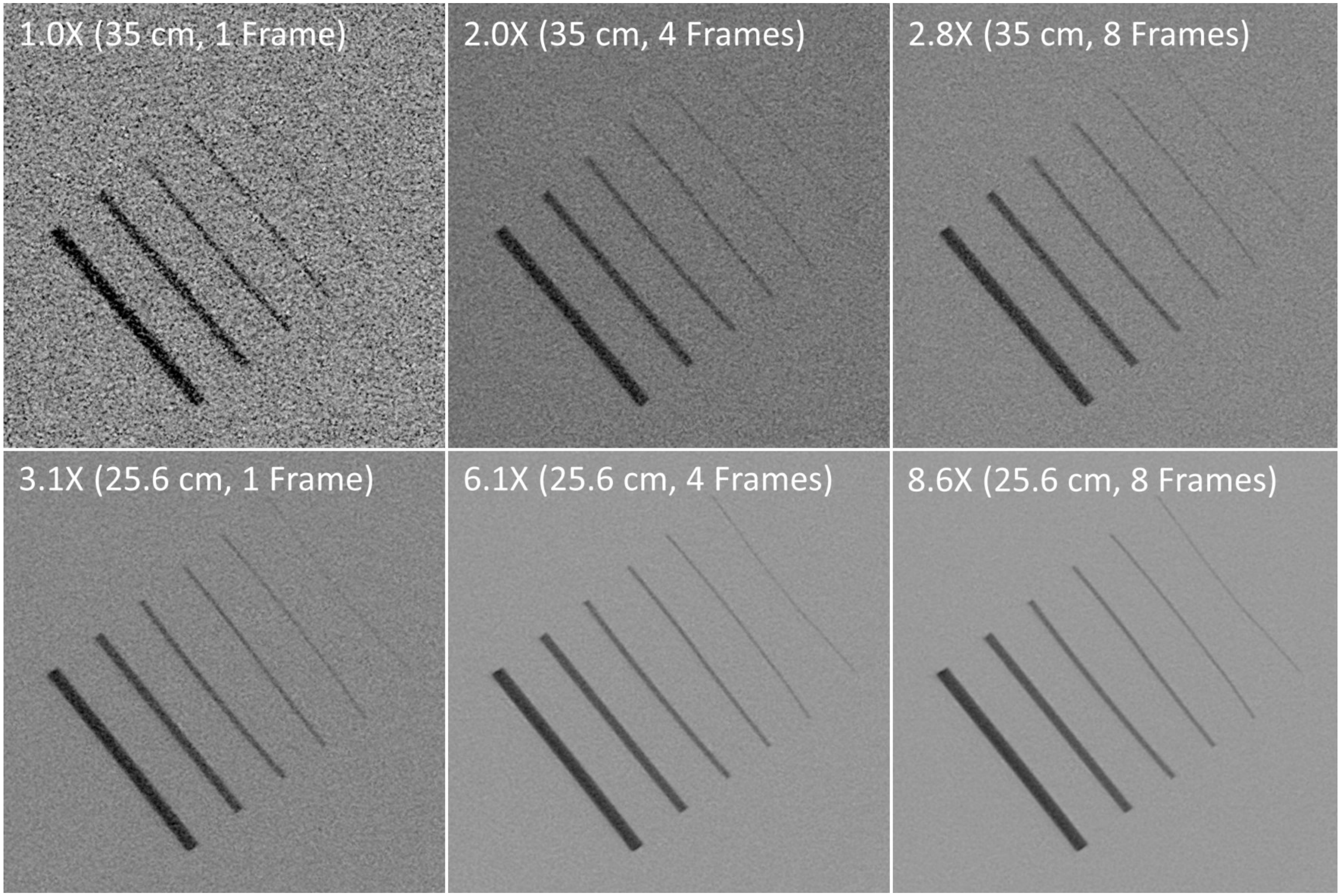

Figure 4.3 – Vessel Phantom Appearance at Different SDNRs.

A range of SDNRs for each vessel phantom was created by varying the thickness of PMMA and the number of image frames integrated. The top row has a total phantom thickness of 35 cm and single, 4, and 8 frames integrated (left to right). The bottom row has a total phantom thickness of 25.6 cm and single, 4 and 8 frames integrated (left to right). The relative SDNR overlaid on each image is the ratio of the SDNR of the 1.04 mm diameter vessel in the image to that of the upper left image. The 1.04 mm vessel is fourth vessel phantom from the left in each image.

The vessel sizing algorithm described in Chapter 3 was applied as follows. For each phantom setup (phantom thickness/position/angle) segment endpoints were defined for each of the six vessel phantom wires, and the same set of endpoints was used for all 40 frames analyzed for that particular setup. The segment endpoints for a given vessel phantom were based on the 2D vessel segmentation of a 40 frame average (i.e. low-noise) image for that setup. The 2D vessel centerline in the frame-averaged images was extrapolated to the ends of the vessel phantom, defined as the point where the log of the signal intensity along the extrapolated centerline was equal to $\frac{(s_{min}+s_{background})}{2}$. With the endpoints of each vessel phantom precisely defined, the endpoints of the inner 75% of the vessel phantom were calculated. These two endpoints served as the input to the vessel sizing algorithm when analyzing individual frames. By using inputs that correspond to the exact segment endpoints, variability due to the user selecting the endpoints in each image frame is avoided. The decision to use the inner 75% was determined by the vessel foreshortening experiment. When the 2.8 mm vessel phantom was tilted at 75° relative to the image plane, the blunt ends of the wire caused the cross sectional profile near the ends to vary. By using the only inner 75% of the vessel length, the algorithm only analyzed regions of the vessel with that had uniform cross sections along the source detector axis. This convention was used for each of the vessel phantoms for consistency. With the vessel segment endpoints defined for each vessel phantom, the rest of the vessel sizing algorithm proceeded as described in Chapter 3.

For each phantom thickness, position, angle, and number of frames integrated, the lengths and diameters of each vessel wire were measured and compared to the ground truth. The length was calculated from the arclength of the 3D centerline. Length error was defined as the calculated length minus 75% of the full wire segment length (nominally 30 mm) as measured with high precision calipers (± 0.02 mm). The diameter was measured at multiple points along the length of each vessel phantom by dividing the vessel into sub-segments approximately 5 mm in length. The default algorithm behavior as described in Chapter 3 was to extract profiles perpendicular to the centerline in 1 pixel increments along the length of the centerline. After the profiles were extracted, a 31 point moving average filter was applied to smooth the samples across adjacent profiles. Pixel spacing was nominally 0.161 mm, which meant that profiles were averaged over approximately 5 mm of vessel length prior to calculating the diameter, assuming no foreshortening. Therefore, the measured diameter at the center of each 5 mm sub-segment corresponded to the diameter measured from the average of all of the profiles within that 5 mm sub-segment. The diameter of each sub-segment as measured by the algorithm was compared to the ground truth, which was the average of diameter measurements using precision calipers at the two ends and the center of the vessel wire. The mean and frame-by-frame standard deviation of length and diameter measurements for each phantom condition were calculated to determine the accuracy and precision of the algorithm, respectively. Graphical plots of diameter and length error as a function of phantom position/angle and vessel SDNR were created to examine trends and to determine under what conditions, if any, the algorithm should or should not be used.

4.3 Results

Forty frames of each phantom condition (phantom thickness, number of frames integrated, phantom position/angle), were analyzed. The mean length and mean diameter, as well as mean error and standard deviation of the error across the 40 frames, were calculated for each diameter of MgCd wire. Measurement errors were examined against different experimental conditions (vessel phantom diameter, mean x-ray counts per pixel, phantom position, etc.), but in general it was observed that the peak SDNR of the vessel phantom was a consistent predictor of measurement accuracy and precision of both length and diameter across a range of conditions. The following sections highlight the most interesting trends for the three experiments performed and describe the accuracy and precision of the algorithm when it is used under normal imaging conditions.

4.3.1 Length and Diameter Versus Phantom Thickness

The initial experiment of varying the total phantom thickness while keeping the x-ray output of the source constant showed, as expected, that the SDNR of the vessel phantoms decreased with increased phantom thickness (Figure 4.4 and Table 4.2). This drop in SDNR was due to a reduction of primary x-rays reaching the detector, which by Poisson statistics resulted in lower image SNR, and a small increase in the amount of detected scatter, which decreased the contrast of the vessels. Increasing the phantom thickness also hardened the x-ray spectrum; at higher x-ray energies the vessel phantoms were less attenuating, reducing the contrast.

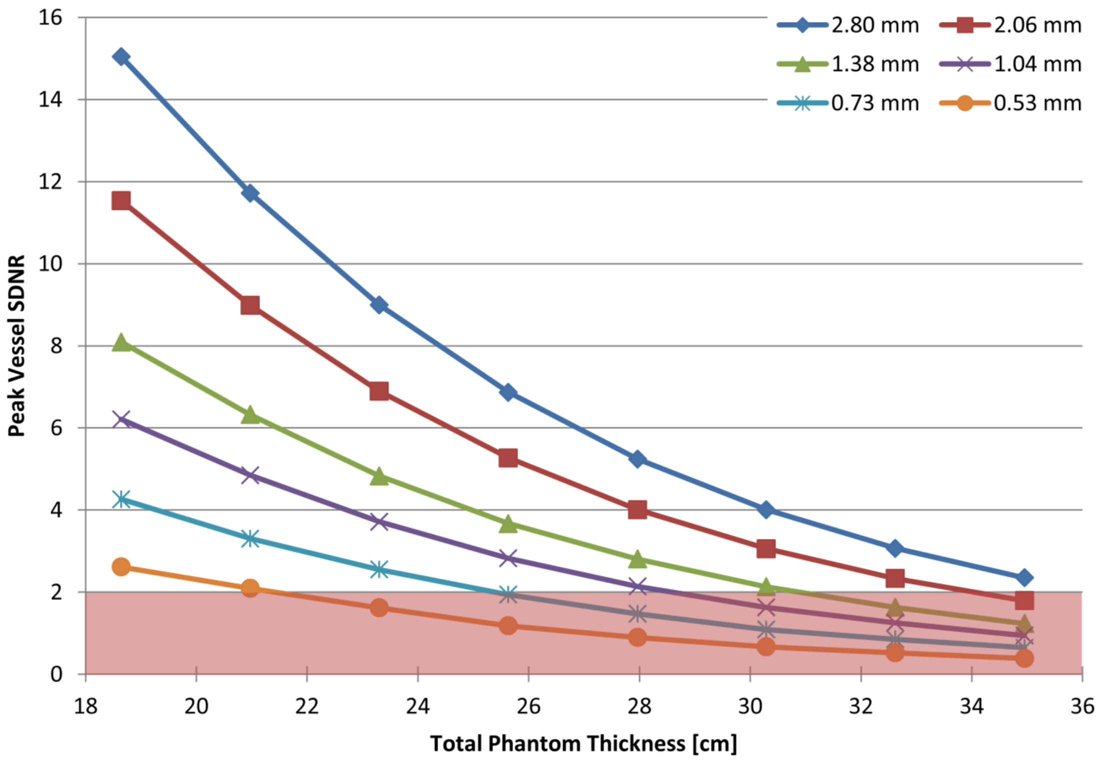

Figure 4.4 – Peak Vessel Phantom SDNR Versus Total Phantom Thickness at 120kV 24kW 7in 15Hz
The shaded region shows where the SDNR is less than 2.

On a broad scale, the peak SDNR of the vessel phantoms was shown to be a good predictor of length and diameter measurement performance. The length accuracy and precision as a function of vessel SDNR are shown in Figure 4.5, where both the mean error and standard deviation rapidly increase as the SDNR decreases from a value of about 1.5. A similar result is shown for the diameter error and standard deviation in Figure 4.6, where both increase sharply as the SDNR approaches 1 from larger SDNRs. Based on these observations, it was concluded that an SDNR of approximately 2 must be achieved for reliable vessel measurements. Figure 4.4 shows the region where the SDNR was less than 2 for each phantom thickness at the 120kV 24kW 7 inch 15Hz operating point, which produced the greatest SDNR on SBDX. For those conditions that yielded an SDNR greater than 2, the worst case error was estimated by quantifying the errors near SDNR 2. By binning the errors between the SDNRs of 1.8 and 2.2 (i.e. SDNR = 2 ± 10%), the mean length error (± 1 SD) was 0.37 ± 0.58 mm and the mean diameter error was 0.02 ± 0.12 mm. When grouped over a larger range of SDNRs (2 to 10), the length and diameter errors were 0.19 ± 0.57 mm and 0.03 ± 0.08 mm, respectively. Additional results can be found in Table 4.3.

		Vessel Phantom SDNR by Phantom Diameter [mm]					
Phantom Thickness [cm]	**Reference SDNR**	**2.80**	**2.06**	**1.38**	**1.04**	**0.73**	**0.53**
35.0	1.0	2.4	1.8	1.2	0.9	0.6	0.4
32.6	1.3	3.1	2.3	1.6	1.2	0.9	0.5
30.3	1.7	4.0	3.1	2.1	1.6	1.1	0.7
28.0	2.3	5.2	4.0	2.8	2.1	1.5	0.9
25.6	3.0	6.9	5.3	3.7	2.8	1.9	1.2
23.3	3.9	9.0	6.9	4.8	3.7	2.6	1.6
21.0	5.1	11.7	9.0	6.3	4.9	3.3	2.1
18.6	6.6	15.0	11.5	8.1	6.2	4.3	2.6

Table 4.2 – Vessel Phantom Peak SDNR by Total Phantom Thickness

Reference SDNR is the ratio of the SDNR of the 1.04 mm diameter vessel at the given phantom thickness to the SDNR of the same vessel phantom at 35 cm phantom thickness.

Phantom Thickness [cm]	Vessel SDNR Range	Length Error (mean ± 1 SD) [mm]	Diameter Error (mean ± 1 SD) [mm]
18.6 – 35.0	2 < SDNR < 10	0.19 ± 0.57	0.03 ± 0.08
18.6	2 < SDNR < 10	-0.03 ± 0.12	0.02 ± 0.08
21.0	2 < SDNR < 10	0.04 ± 0.18	0.02 ± 0.08
23.3	2 < SDNR < 10	0.02 ± 0.17	0.02 ± 0.07
25.6	2 < SDNR < 10	0.07 ± 0.29	0.02 ± 0.06
28.0	2 < SDNR < 10	0.24 ± 0.48	0.03 ± 0.08
30.3	2 < SDNR < 10	0.52 ± 0.71	0.04 ± 0.08
32.6	2 < SDNR < 10	0.66 ± 0.84	0.03 ± 0.09
35.0	2 < SDNR < 10	1.04 ± 1.61	0.03 ± 0.10
18.6 – 35.0	1.8 < SDNR < 2.2	0.37 ± 0.58	0.02 ± 0.12

Table 4.3 – Mean and Standard Deviation of Length and Diameter Error Across Different Phantom Thicknesses

Expected accuracy and precision of measurements for different phantom thicknesses.

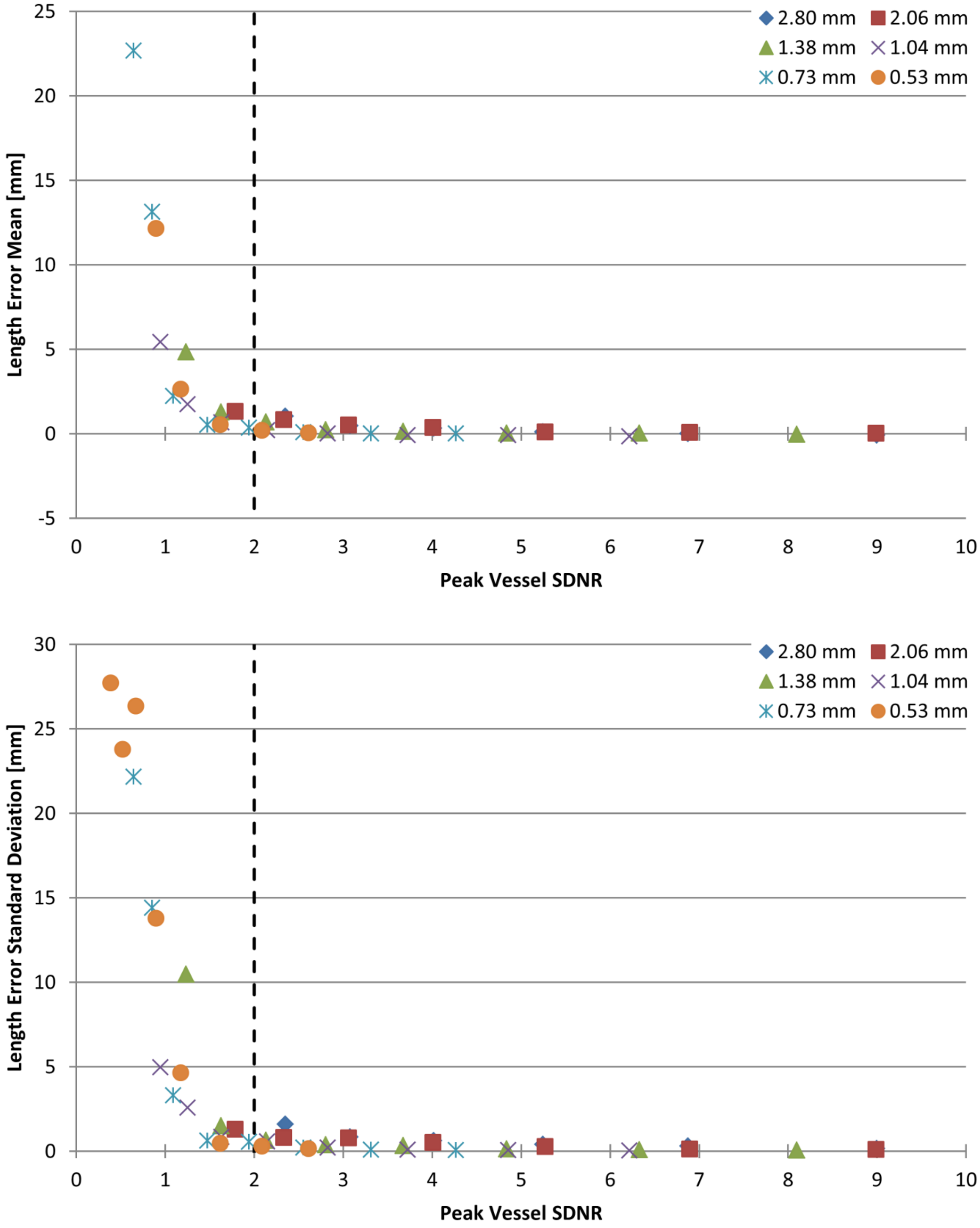

Figure 4.5 – Mean and Standard Deviation of Length Error Across Different Phantom Thicknesses
The mean length error (top) and standard deviation of length error (bottom) were calculated for each vessel phantom diameter at each phantom thickness from measurements across 40 image frames. Dashed line shows the cutoff point of a vessel peak SDNR of 2.

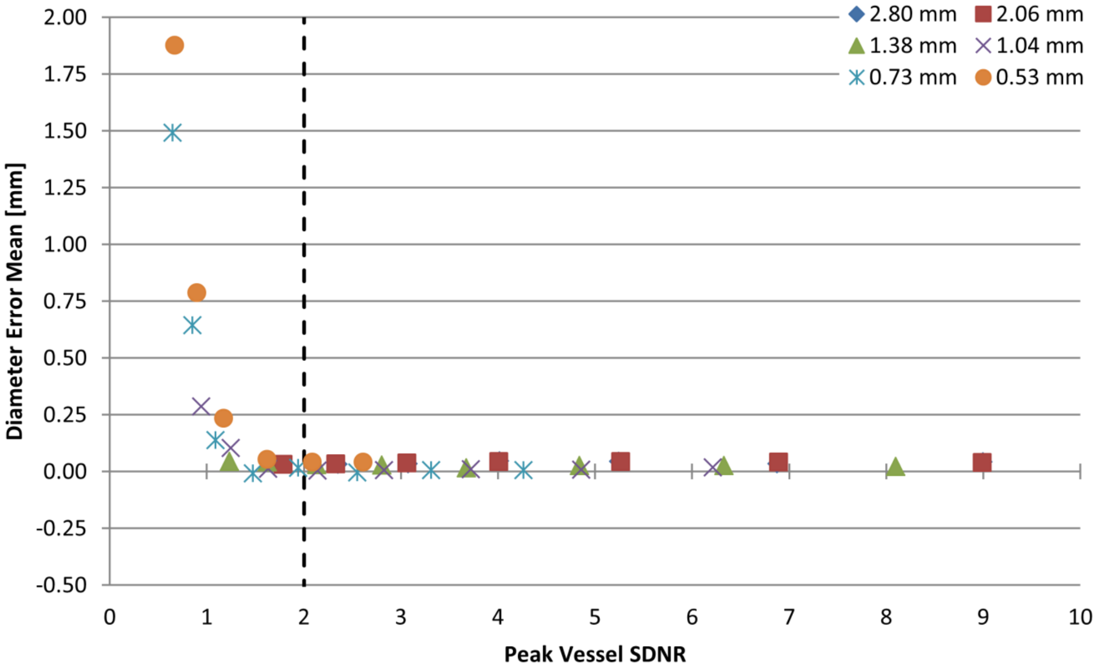

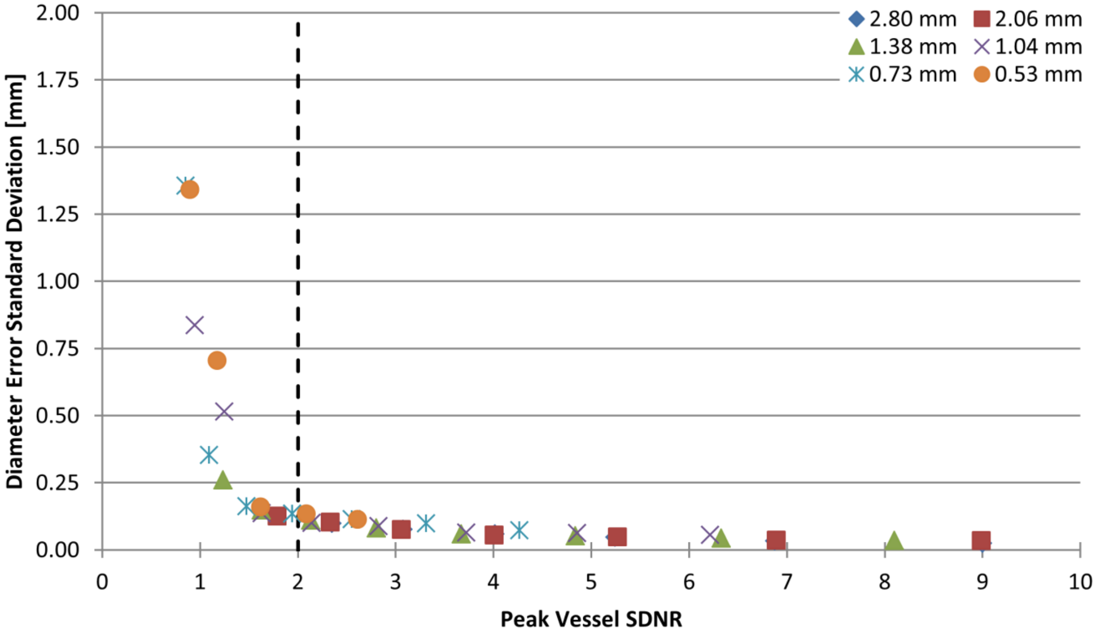

Figure 4.6 – Mean and Standard Deviation of Diameter Error Across Different Phantom Thicknesses
The mean diameter error (top) and standard deviation of diameter error (bottom) were calculated for each vessel phantom diameter at each phantom thickness from measurements across 40 image frames. Dashed line shows the cutoff point of a vessel peak SDNR of 2.

Upon closer examination of the length results from vessels with SDNRs between 2 and 10, it was observed that the vessel diameter was related to small differences in length accuracy and precision for the same SDNR. Figure 4.7 shows that larger diameter vessels have a greater mean error and standard deviation compared to smaller diameter vessels at the same peak SDNR. As the SDNR increases, both the mean error and standard deviation converge toward zero. The same figure shows the length measurements binned by SDNR across all vessel diameters (with a bin width of 0.5). The linear regression plot of the binned data helps the reader to appreciate the decreasing trend as SDNR improves when all vessel diameters were grouped together.

The diameter measurements across different phantom thicknesses showed a similar trend. When examined more closely over the SDNR range between 2 and 10 in Figure 4.8, the diameter mean error was relatively flat over this range, between 0 and 0.05 mm depending on the true diameter of the vessel. Over the same range, the standard deviation of the diameter measurements steadily decreased with increased SDNR. All of the vessel diameters seemed to fall on the same curve with the exception of the smallest diameter vessel phantoms (0.53 mm and 0.73 mm), which had a slightly higher standard deviation at the same SDNR.

Summary: For vessels located at isocenter, both length and diameter accuracy and precision decrease as the peak vessel SDNR falls below 2. For vessels with a SDNR between 2 and 10, the worst case length and diameter error was estimated to be 0.37 ± 0.58 mm and 0.02 ± 0.12 mm, respectively. The average accuracy and variability over the same range was calculated to be 0.19 ± 0.57 mm for length and 0.03 ± 0.08 mm for diameter.

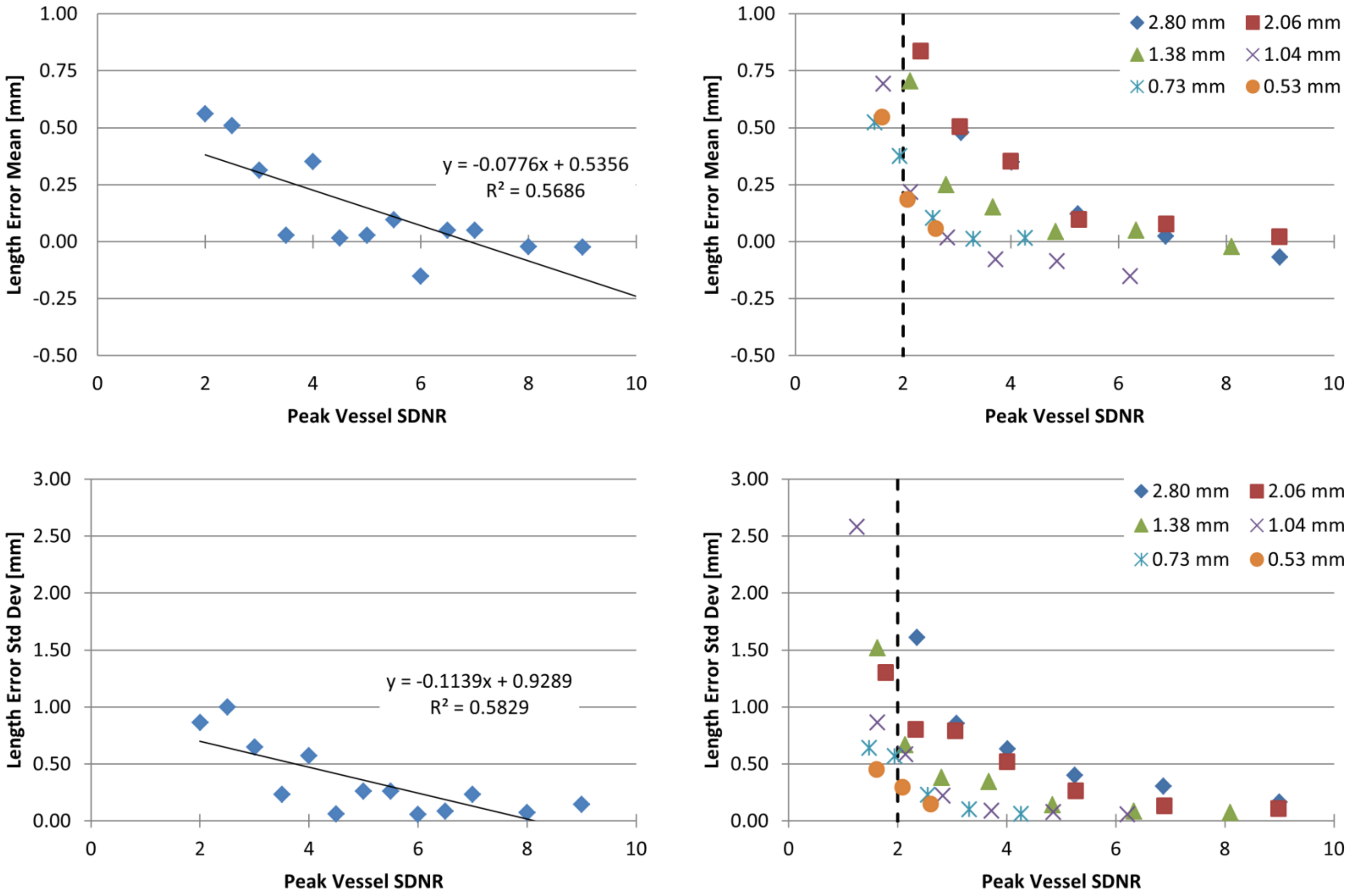

Figure 4.7 – Length Error for Vessels At Different Thicknesses Binned by Peak Vessel SDNR

(Left) Length errors were calculated across all vessel phantom diameters and total phantom thicknesses by grouping the measurements by SDNR using a bin width of 0.5. Only measurements from vessel phantoms with an SDNR between 2 and 10 are shown. (Right) The length errors over the same SDNR interval are shown grouped by vessel diameter and phantom setup (similar to Figure 4.5). Mean length error vs. SDNR is shown on the top; the standard deviation of the length error is on the bottom.

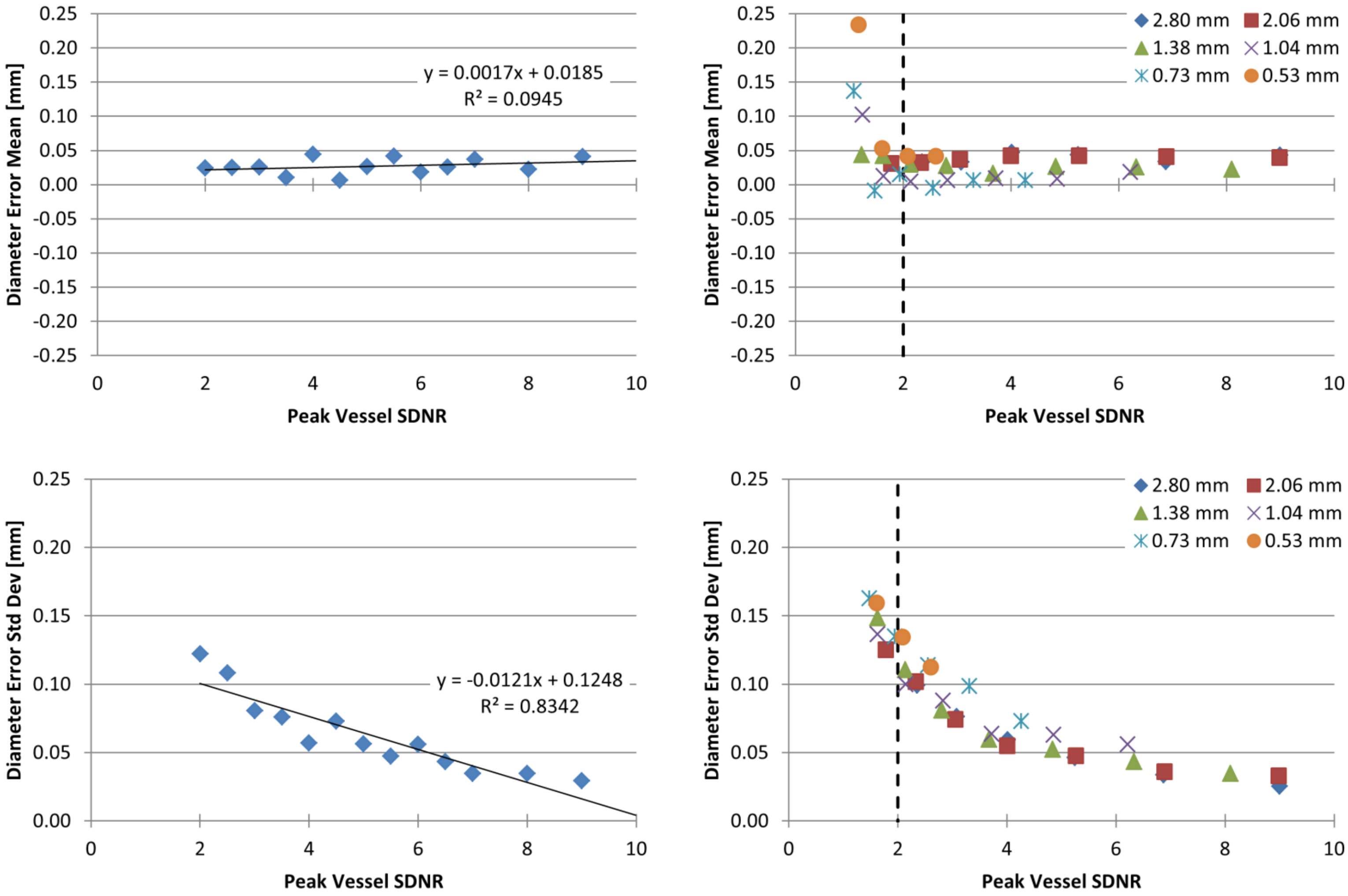

Figure 4.8 – Diameter Error for Vessels At Different Magnifications Binned by Peak Vessel SDNR

(Left) Diameter errors were calculated across all vessel phantom diameters and total phantom thicknesses by grouping the measurements by SDNR using a bin width of 0.5. Only measurements from vessel phantoms with an SDNR between 2 and 10 are shown. (Right) The diameter errors over the same SDNR interval are shown grouped by vessel diameter and phantom setup (similar to Figure 4.6). Mean diameter error vs. SDNR is shown on the top; the standard deviation of the diameter error is on the bottom.

4.3.2 Length and Diameter Versus Vessel Magnification

The vessel phantoms were imaged from 12 cm below mechanical isocenter to 12 cm above in 4 cm increments, which varied the magnification of the vessels between 90% and 113% relative to the magnification at isocenter. The vessel contrast and background pixel noise was found to be insensitive to phantom position. Consequently, the peak vessel SDNR for each diameter was the same for each vessel position, as shown in Table 4.4.

Figure 4.9 shows the mean and standard deviation of length measurements across 40 frames of the same imaging condition (phantom position, thickness, frames integrated) versus the peak vessel SDNR. Since the SDNR for a given vessel phantom diameter did not change for each phantom position, the data for each vessel diameter were clustered at discrete SDNRs along the graph. Again, there was a sharp increase in both length error and variability as the peak vessel SDNR decreased from 2 to 1. Length error near an SDNR of 2 (±10%) was 0.29 ± 0.61 mm.

Figure 4.10 shows the mean length error and standard deviation over SDNRs between 2 and 10. Looking at the clusters of data points from similar vessel phantoms, it was again observed that the vessel phantoms with greater diameters have greater errors and variability in the length measurements, although the difference was small and the clusters overlap in many cases. The average length error for all measurements falling within the SDNR range of 2 and 10 was 0.13 ± 0.54. Also in Figure 4.10, the plots binned by SDNR show a general decreasing trend as the SDNR increases.

Distance From Isocenter [cm]	Phantom Thickness [cm]	Frames Integrated	Reference SDNR	SDNR by Phantom Diameter [mm]					
				2.80	2.06	1.38	1.04	0.73	0.53
-12	35	1	1.0	2.3	1.7	1.2	0.9	0.6	0.4
-8	35	1	1.0	2.3	1.7	1.2	0.9	0.6	0.4
-4	35	1	1.0	2.3	1.7	1.2	0.9	0.6	0.4
0	35	1	1.0	2.3	1.7	1.2	0.9	0.6	0.4
4	35	1	1.0	2.3	1.7	1.2	0.9	0.6	0.4
8	35	1	1.0	2.3	1.7	1.2	0.9	0.6	0.4
12	35	1	1.0	2.3	1.7	1.2	0.9	0.6	0.4
-12	35	4	2.0	4.5	3.4	2.4	1.8	1.2	0.7
-8	35	4	2.0	4.5	3.4	2.4	1.8	1.2	0.7
-4	35	4	2.0	4.6	3.5	2.4	1.8	1.3	0.8
0	35	4	2.0	4.5	3.4	2.4	1.8	1.2	0.7
4	35	4	2.0	4.5	3.4	2.4	1.8	1.3	0.8
8	35	4	2.0	4.5	3.4	2.4	1.8	1.2	0.8
12	35	4	2.0	4.5	3.5	2.4	1.8	1.2	0.8
-12	35	8	2.8	6.5	4.9	3.4	2.6	1.8	1.1
-8	35	8	2.8	6.5	4.9	3.4	2.6	1.7	1.0
-4	35	8	2.8	6.4	4.8	3.4	2.6	1.8	1.1
0	35	8	2.8	6.4	4.9	3.4	2.6	1.8	1.0
4	35	8	2.8	6.4	4.9	3.4	2.5	1.8	1.1
8	35	8	2.8	6.4	4.9	3.4	2.6	1.8	1.1
12	35	8	2.8	6.4	4.9	3.4	2.6	1.8	1.1
-12	25.6	1	3.1	6.8	5.2	3.6	2.8	1.9	1.1
-8	25.6	1	3.1	6.8	5.2	3.7	2.8	1.9	1.2
-4	25.6	1	3.1	6.8	5.2	3.7	2.8	1.9	1.2
0	25.6	1	3.1	6.9	5.3	3.7	2.8	1.9	1.2
4	25.6	1	3.1	6.8	5.2	3.7	2.8	1.9	1.2
8	25.6	1	3.1	6.8	5.2	3.7	2.8	1.9	1.2
12	25.6	1	3.1	6.8	5.2	3.7	2.8	1.9	1.2
-12	25.6	4	6.1	13.5	10.3	7.2	5.5	3.8	2.2
-8	25.6	4	6.1	13.6	10.4	7.3	5.5	3.8	2.3
-4	25.6	4	6.1	13.8	10.5	7.4	5.6	3.8	2.4
0	25.6	4	6.1	13.7	10.5	7.4	5.6	3.8	2.4
4	25.6	4	6.1	13.8	10.6	7.4	5.6	3.9	2.4
8	25.6	4	6.1	13.5	10.4	7.3	5.5	3.8	2.4
12	25.6	4	6.1	13.7	10.5	7.4	5.6	3.9	2.5
-12	25.6	8	8.6	19.2	14.7	10.3	7.8	5.3	3.2
-8	25.6	8	8.6	19.2	14.7	10.3	7.8	5.4	3.3
-4	25.6	8	8.6	19.5	14.9	10.5	8.0	5.4	3.4
0	25.6	8	8.6	19.3	14.8	10.4	7.9	5.4	3.4
4	25.6	8	8.6	19.4	14.9	10.5	7.9	5.4	3.4
8	25.6	8	8.6	19.3	14.9	10.5	7.9	5.5	3.5
12	25.6	8	8.6	19.3	14.8	10.4	7.9	5.5	3.5

Table 4.4 – Vessel Phantom Peak SDNR by Phantom Position and Image SNR

Reference SDNR is the ratio of the SDNR of the 1.04 mm diameter vessel at isocenter for the given phantom thickness and number of frames integrated to the SDNR of the same vessel phantom at isocenter, 35 cm phantom thickness, and one frame.

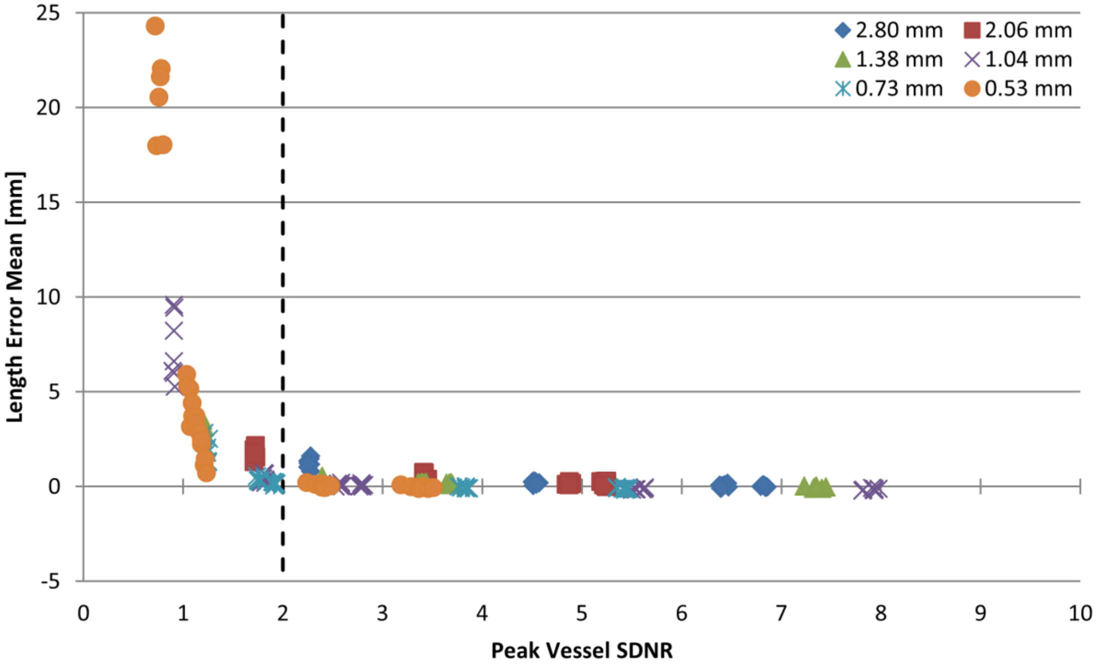

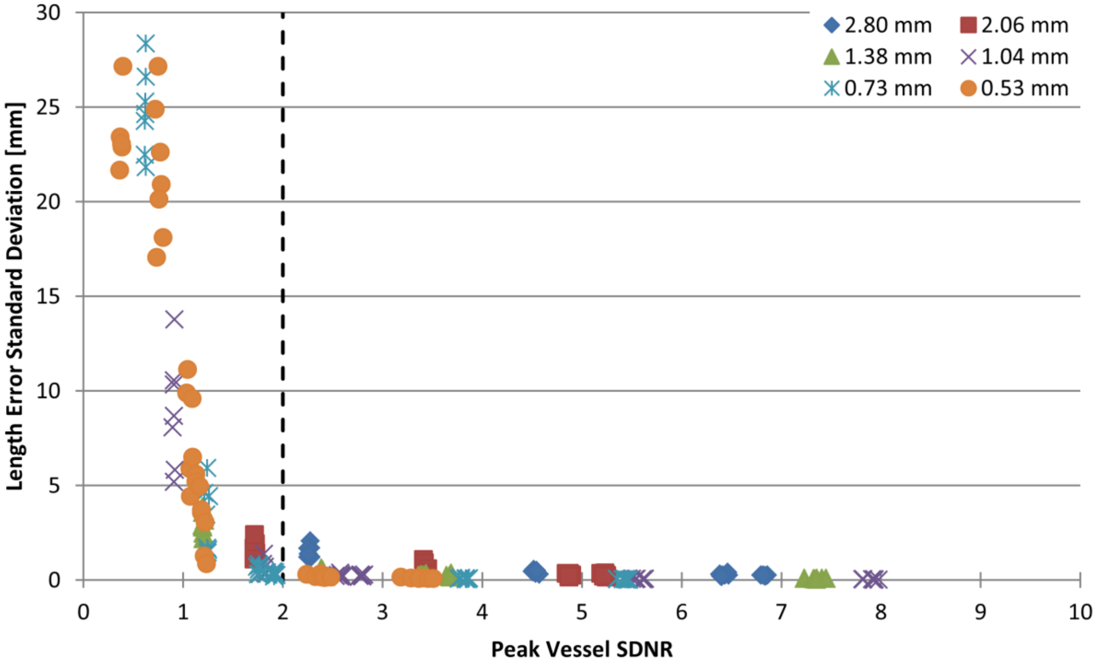

Figure 4.9 – Mean and Standard Deviation of Length Error Across Different Vessel Magnifications

Each point represents the mean (upper) or standard deviation (lower) of length errors calculated across 40 image frames for each phantom position, thickness, and number of frames integrated. Different magnifications were produced by positioning the vessel phantoms at different positions along the source-detector axis. Dashed line shows the cutoff point of a vessel peak SDNR of 2.

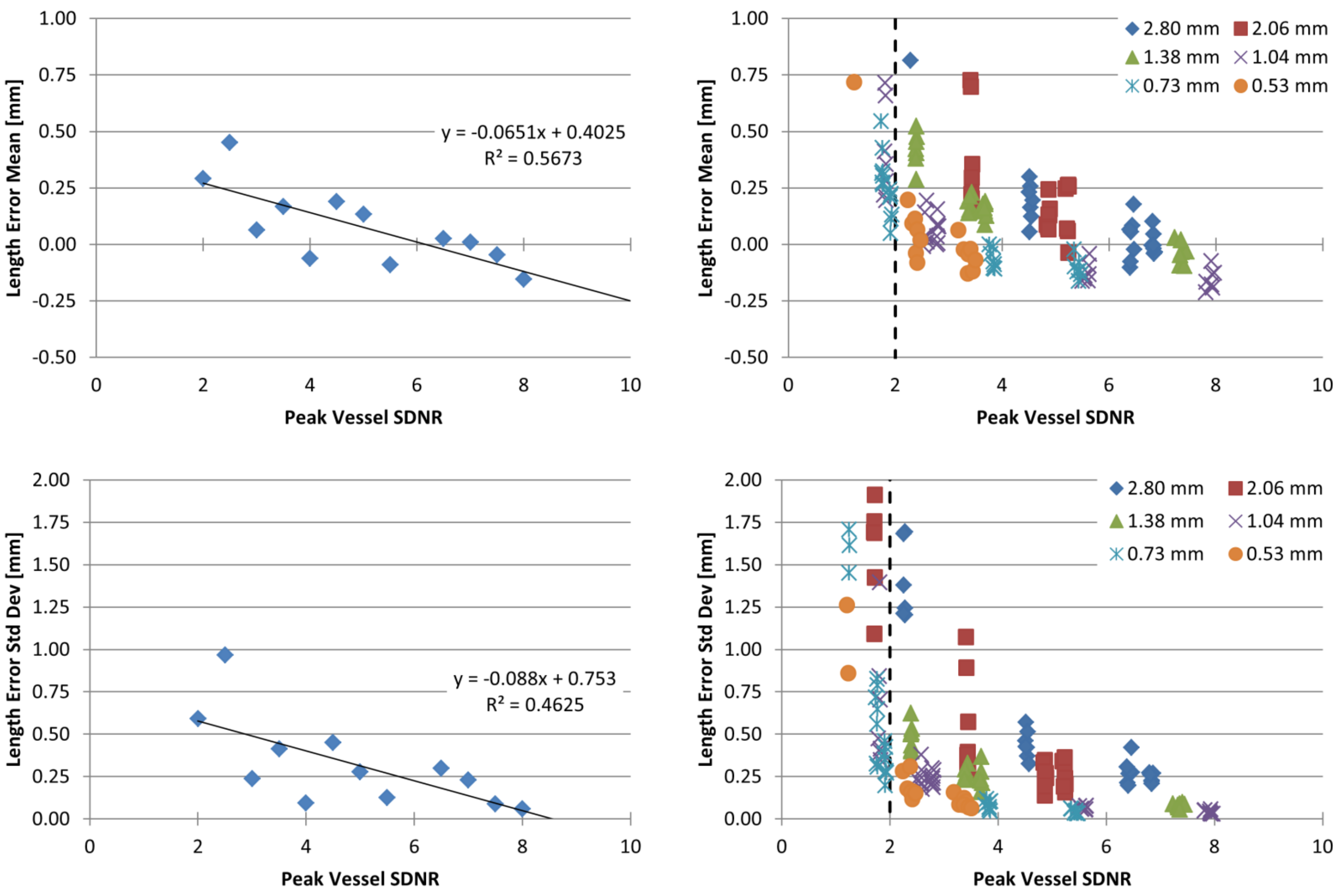

Figure 4.10 – Length Error for Vessels At Different Magnifications Binned by Peak Vessel SDNR

(Left) Length errors were calculated across all vessel phantom diameters, phantom positions (magnifications), and phantom thickness/frame integration combinations by grouping the measurements by SDNR using a bin width of 0.5. Only measurements from vessel phantoms with an SDNR between 2 and 10 are shown. (Right) The length errors over the same SDNR interval are shown grouped by phantom setup (similar to Figure 4.9). Mean length error vs. SDNR is shown on the top; the standard deviation of the length error is on the bottom.

In Figure 4.11, the algorithm's ability to accurately calculate the length of each vessel despite changing magnification is shown. This figure shows the length measurements relative to the true length using vessels whose peak SDNR was between 2 and 10. Using the 2D length (in pixels) of the vessel at isocenter as the reference, the magnification of the vessel increased as the vessel moved above isocenter and decreased as it moved below. If one were to perform conventional 2D-based QCA measurements of the vessel lengths at each position with the magnification calibrated from a known object at isocenter (equivalent to assuming all vessels are at isocenter), then the length measurements would have been as shown in Figure 4.11, "2D Length Measurement". Using the vessel sizing algorithm ("3D Length Measurement"), the magnification of the vessel was automatically determined, and the vessel length was accurately calculated regardless of its position relative to isocenter. The error of the 2D-based measurement closely followed the expected error due to the change in magnification, and the standard deviation of the 2D measurements was about 0.3%, or 0.1 mm. The error of the 3D based length measurement was near zero, with a standard deviation of 2% (around 0.6 mm) or less for each magnification. The absolute values at each magnification for vessel phantoms with SDNRs between 2 and 10 are listed in Table 4.5. While the variability of the 3D method was more than the 2D method, the 3D vessel sizing method still had sub-millimeter precision and accuracy, and it remained accurate without requiring a reference object to determine the vessel magnification.

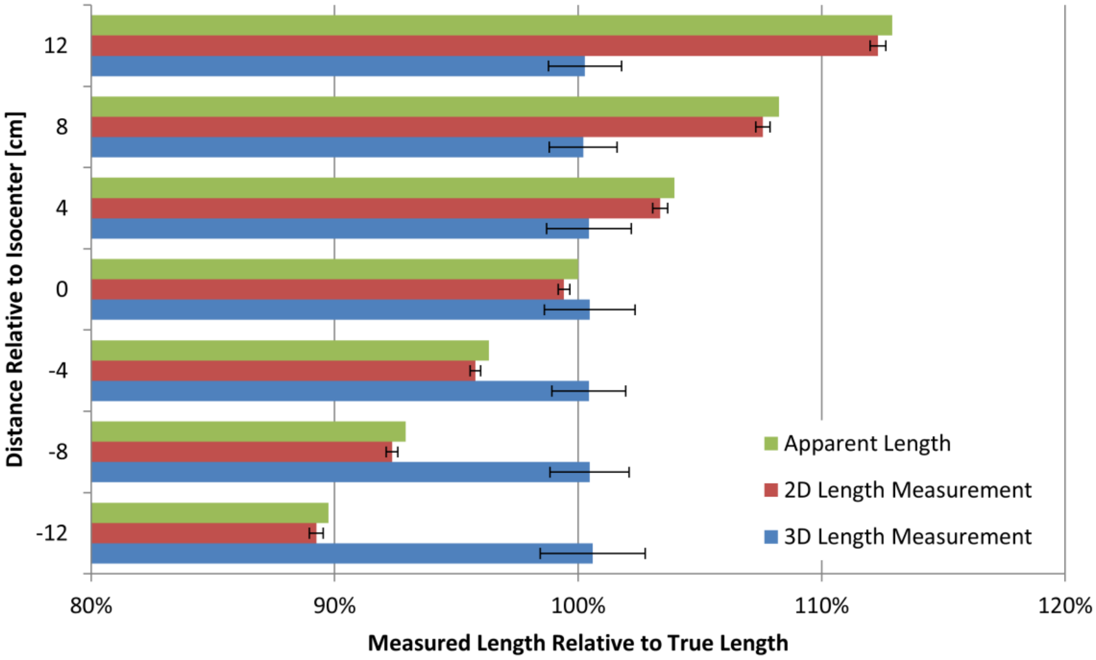

Figure 4.11 – Measured Length Relative to True Length Across Different Magnifications
The apparent length of the vessels relative to their length at isocenter (green) changes with vessel position above and below isocenter. Length measurements made from the 2D vessel centerline and scaled by the magnification at isocenter (red) track with the apparent length. When the sizing algorithm was used, the measured length (blue) accurately reflected the true length of the vessel segment. Error bars show ±1 standard deviation about the mean. This variation was consistent across vessel phantom magnification. Values were calculated across all measurements where peak SDNR was between 2 and 10.

Position Relative to Isocenter [cm]	Magnification Relative to Isocenter	Vessel SDNR Range	Length Error (mean ± 1 SD) [mm]	Diameter Error (mean ± 1 SD) [mm]
-12 to +12	90% - 113%	2 < SDNR < 10	0.13 ± 0.54	0.02 ± 0.08
-12	90%	2 < SDNR < 10	0.19 ± 0.68	0.02 ± 0.09
-8	93%	2 < SDNR < 10	0.15 ± 0.51	0.02 ± 0.08
-4	96%	2 < SDNR < 10	0.14 ± 0.48	0.02 ± 0.08
0	100%	2 < SDNR < 10	0.15 ± 0.59	0.03 ± 0.08
+4	104%	2 < SDNR < 10	0.14 ± 0.55	0.02 ± 0.08
+8	108%	2 < SDNR < 10	0.07 ± 0.44	0.02 ± 0.08
+12	113%	2 < SDNR < 10	0.09 ± 0.48	0.02 ± 0.07
-12 to +12	90% - 113%	1.8 < SDNR < 2.2	0.29 ± 0.61	0.00 ± 0.13

Table 4.5 – Mean and Standard Deviation of Length and Diameter Error Across Different Magnifications
Expected accuracy and precision of vessel measurements for different distances about isocenter

The diameter accuracy and precision versus SDNR shown in Figure 4.12 mirrored the results shown for different phantom thicknesses in Figure 4.6. The mean diameter error for values near SDNR equal to 2 ± 10% was 0.00 ± 0.13 mm. The zoomed-in view of diameter errors shown in Figure 4.13 showed the same pattern of a near constant diameter error for SDNRs greater than 2, decreasing variability of diameter measurements as SDNR increases, and a slight increase in the variability of narrow vessel phantoms (0.73 mm and 0.53 mm diameter) as compared to thicker vessels at the same SDNR. Over the range of SDNRs shown in Figure 4.13 (2 to 10), the mean diameter error was 0.02 ± 0.08 mm.

Summary: For vessels located in the region near isocenter ± 12 cm, length and diameter accuracy and precision were effectively constant despite changes in the magnification of the vessel. The average length and diameter errors for vessel phantoms with SDNRs of 2 ± 10% were 0.29 ± 0.61 mm and 0.00 ± 0.13 mm, respectively. The mean length measurement error of vessel phantoms with SDNRs between 2 and 10 were 0.13 ± 0.54 mm. Over the same SDNR range, the mean diameter error was 0.02 ± 0.08 mm. These errors are similar to those calculated by simply varying the phantom thickness as described in Section 4.3.1.

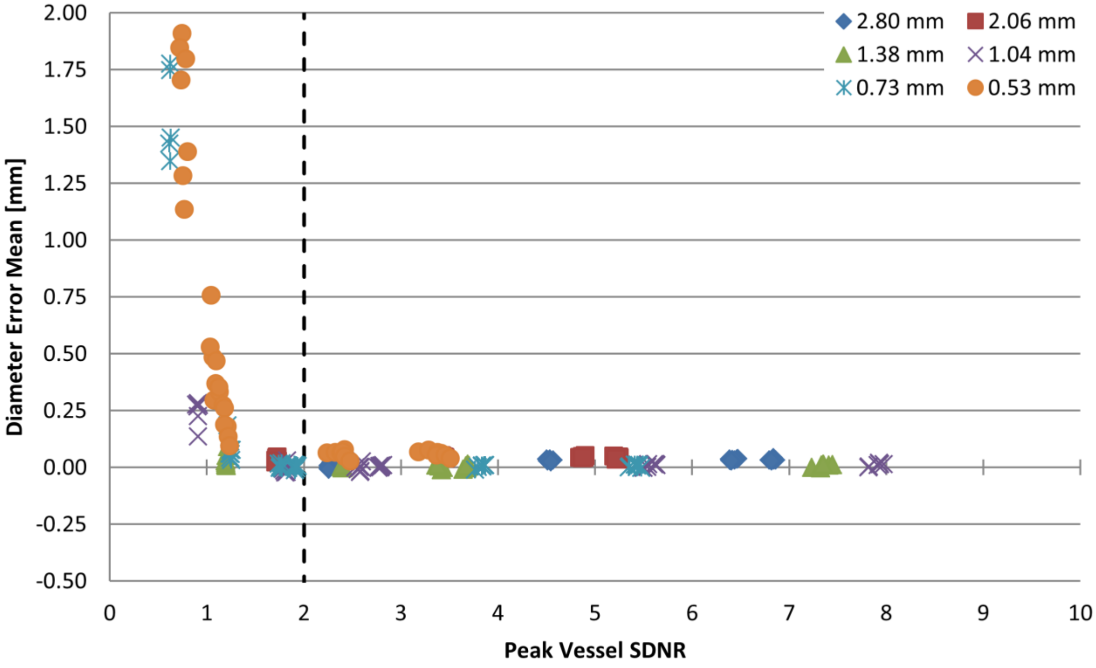

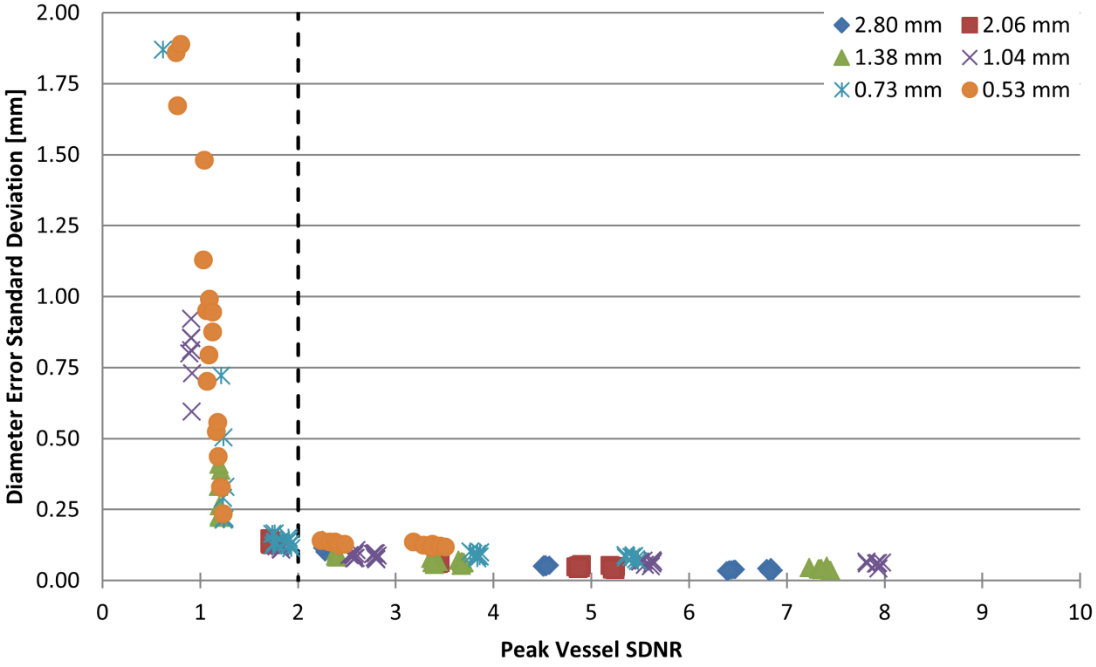

Figure 4.12 – Mean and Standard Deviation of Diameter Error Across Different Vessel Magnifications

Each point represents the mean (upper) or standard deviation (lower) of diameter errors calculated across 40 image frames for each phantom position, thickness, and number of frames integrated. Different magnifications were produced by positioning the vessel phantoms at different positions along the source-detector axis. Dashed line shows the cutoff point of a vessel peak SDNR of 2.

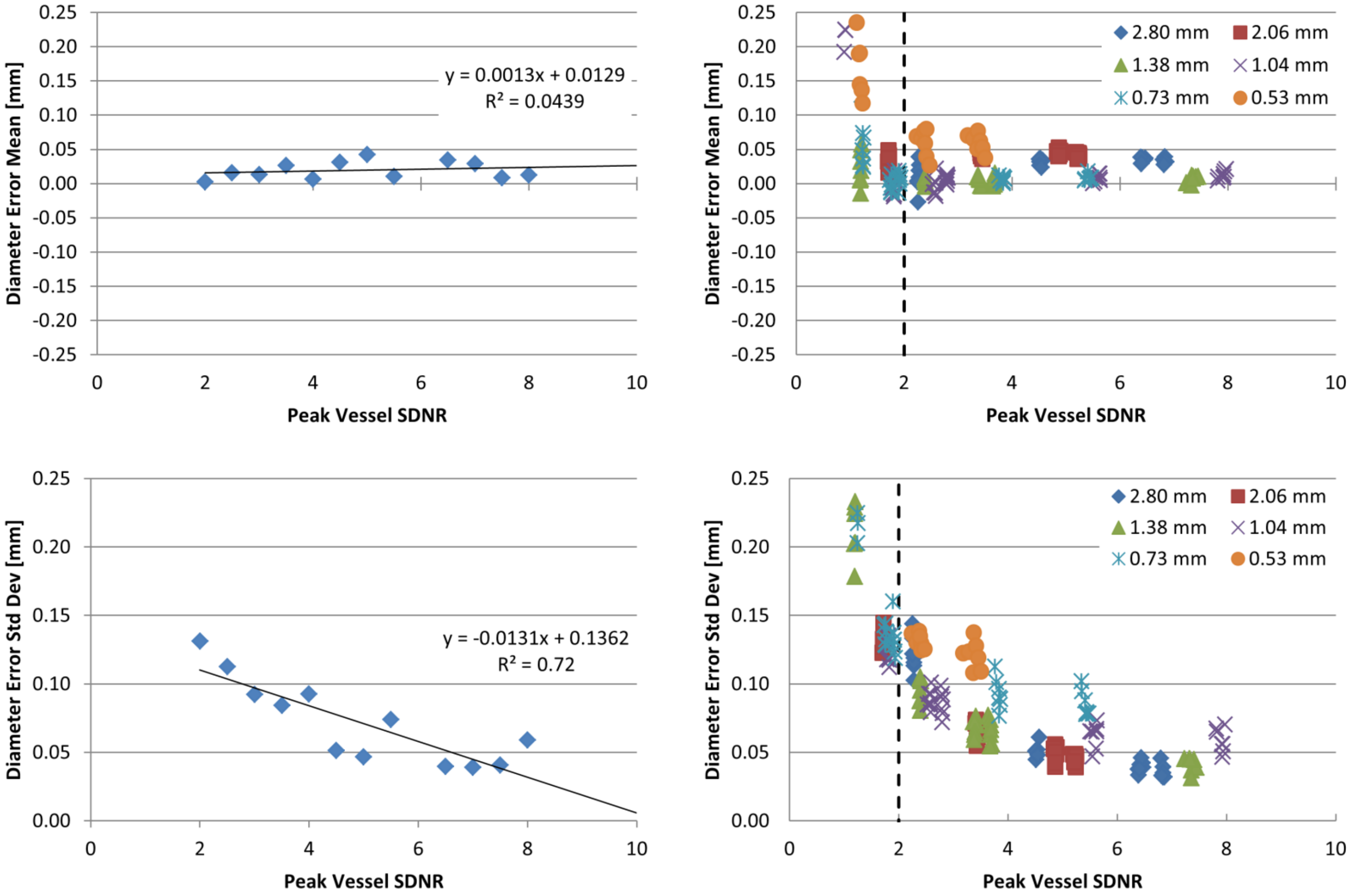

Figure 4.13 – Diameter Error for Vessels At Different Magnifications Binned by Peak Vessel SDNR

(Left) Diameter errors were calculated across all vessel phantom diameters, phantom positions (magnifications), and phantom thickness/frame integration combinations by grouping the measurements by SDNR using a bin width of 0.5. Only measurements from vessel phantoms with an SDNR between 2 and 10 are shown. (Right) The diameter errors over the same SDNR interval are shown grouped by phantom setup (similar to Figure 4.12). Mean diameter error vs. SDNR is shown on the top; the standard deviation of the diameter error is on the bottom

4.3.3 Length and Diameter Versus Vessel Foreshortening

In the first two experiments of this study, the peak vessel SDNR was a function of the phantom thickness and number of frames integrated. In the experiment in which the vessels were incrementally angled relative to the image plane, creating foreshortened vessels, the path length through the vessel increased with ϕ, which increased the contrast (and SDNR) of the vessel phantoms. Table 4.6 lists the SDNRs for each vessel phantom across different values of ϕ, phantom thickness, and number of frames integrated. As a result, the plots of length and diameter measurement errors were more distributed across a range of SDNRs as compared to the vessel magnification experiment, where the data were clustered together.

In examining the mean length error and standard deviation across vessels with various degrees of foreshortening, it was apparent that the angle of the vessel, ϕ, in addition to the SDNR, affected the length measurement. Figure 4.14 shows the same relationship between SDNR and length accuracy and precision as was demonstrated in the other two experiments (see Figure 4.5 and Figure 4.9) with the addition of some outliers. In particular, there were data that deviated below the main trend for mean length error and above the main trend for length error standard deviation. The outliers are seen in all vessel phantom diameters. By reexamining the data as a function of the foreshortening angle ϕ, as shown in Figure 4.15, it was revealed that the outliers could be attributed to measurements performed on vessels that were severely foreshortened (i.e. $\phi = 60°, 75°$). In Figure 4.16, the length data are separated into two groups based on ϕ, showing data from 0° to 45° and 60° to 75°. When the vessel angle was less than or equal to 45°, the data followed the trend previously observed in Sections 4.3.1 and 4.3.2 without any obvious deviations.

Angle (ϕ)	Phantom Thickness [cm]	Frames Integrated	Reference SDNR	Vessel Phantom SDNR by Phantom Diameter [mm]					
				2.80	2.06	1.38	1.04	0.73	0.53
0°	35	1	1.0	2.3	1.7	1.2	0.9	0.6	0.4
15°	35	1	1.0	2.3	1.8	1.2	0.9	0.6	0.4
30°	35	1	1.0	2.5	1.9	1.3	1.0	0.7	0.4
45°	35	1	1.0	2.9	2.2	1.6	1.2	0.8	0.5
60°	35	1	1.0	3.6	2.9	2.1	1.7	1.1	0.7
75°	35	1	1.0	4.5	3.9	3.1	2.5	1.7	1.1
0°	35	4	2.0	4.6	3.5	2.4	1.8	1.2	0.7
15°	35	4	2.0	4.7	3.5	2.4	1.8	1.2	0.8
30°	35	4	2.0	5.0	3.8	2.6	2.0	1.3	0.8
45°	35	4	2.0	5.7	4.5	3.2	2.4	1.6	1.0
60°	35	4	2.0	7.1	5.7	4.2	3.3	2.2	1.4
75°	35	4	2.0	9.1	7.9	6.2	5.1	3.5	2.2
0°	35	8	2.9	6.5	4.9	3.4	2.5	1.7	1.0
15°	35	8	2.9	6.6	5.0	3.4	2.6	1.7	1.1
30°	35	8	2.9	7.0	5.4	3.7	2.8	1.8	1.1
45°	35	8	2.9	8.1	6.3	4.6	3.5	2.3	1.4
60°	35	8	2.9	10.0	8.0	5.9	4.7	3.1	2.0
75°	35	8	2.9	12.9	11.1	8.7	7.2	4.9	3.1
0°	25.6	1	3.2	7.0	5.3	3.7	2.8	1.9	1.2
15°	25.6	1	3.2	7.0	5.3	3.7	2.8	1.9	1.1
30°	25.6	1	3.2	7.5	5.7	4.0	3.1	2.0	1.3
45°	25.6	1	3.2	8.5	6.7	4.9	3.7	2.4	1.6
60°	25.6	1	3.2	10.4	8.5	6.3	5.1	3.4	2.2
75°	25.6	1	3.2	13.1	11.4	9.3	7.7	5.2	3.4
0°	25.6	4	6.3	13.9	10.6	7.3	5.6	3.7	2.3
15°	25.6	4	6.3	14.0	10.6	7.3	5.6	3.7	2.3
30°	25.6	4	6.3	14.9	11.4	8.0	6.2	4.0	2.6
45°	25.6	4	6.3	17.0	13.3	9.7	7.4	4.8	3.2
60°	25.6	4	6.3	20.7	16.9	12.5	10.2	6.7	4.3
75°	25.6	4	6.3	26.3	22.8	18.7	15.5	10.5	6.9
0°	25.6	8	8.8	19.5	14.8	10.2	7.9	5.2	3.2
15°	25.6	8	8.8	19.6	14.9	10.3	7.9	5.2	3.2
30°	25.6	8	8.8	20.9	16.0	11.1	8.7	5.7	3.6
45°	25.6	8	8.8	24.2	19.0	13.8	10.5	6.9	4.5
60°	25.6	8	8.8	29.4	24.0	17.8	14.5	9.5	6.1
75°	25.6	8	8.8	37.6	32.7	26.8	22.1	15.0	9.9

Table 4.6 – Vessel Phantom Peak SDNR by Foreshortening Angle.

Reference SDNR is the ratio of the SDNR of 1.04 mm diameter vessel at 0° for the given phantom thickness and number of frames integrated to the SDNR at 35 cm phantom thickness and one frame.

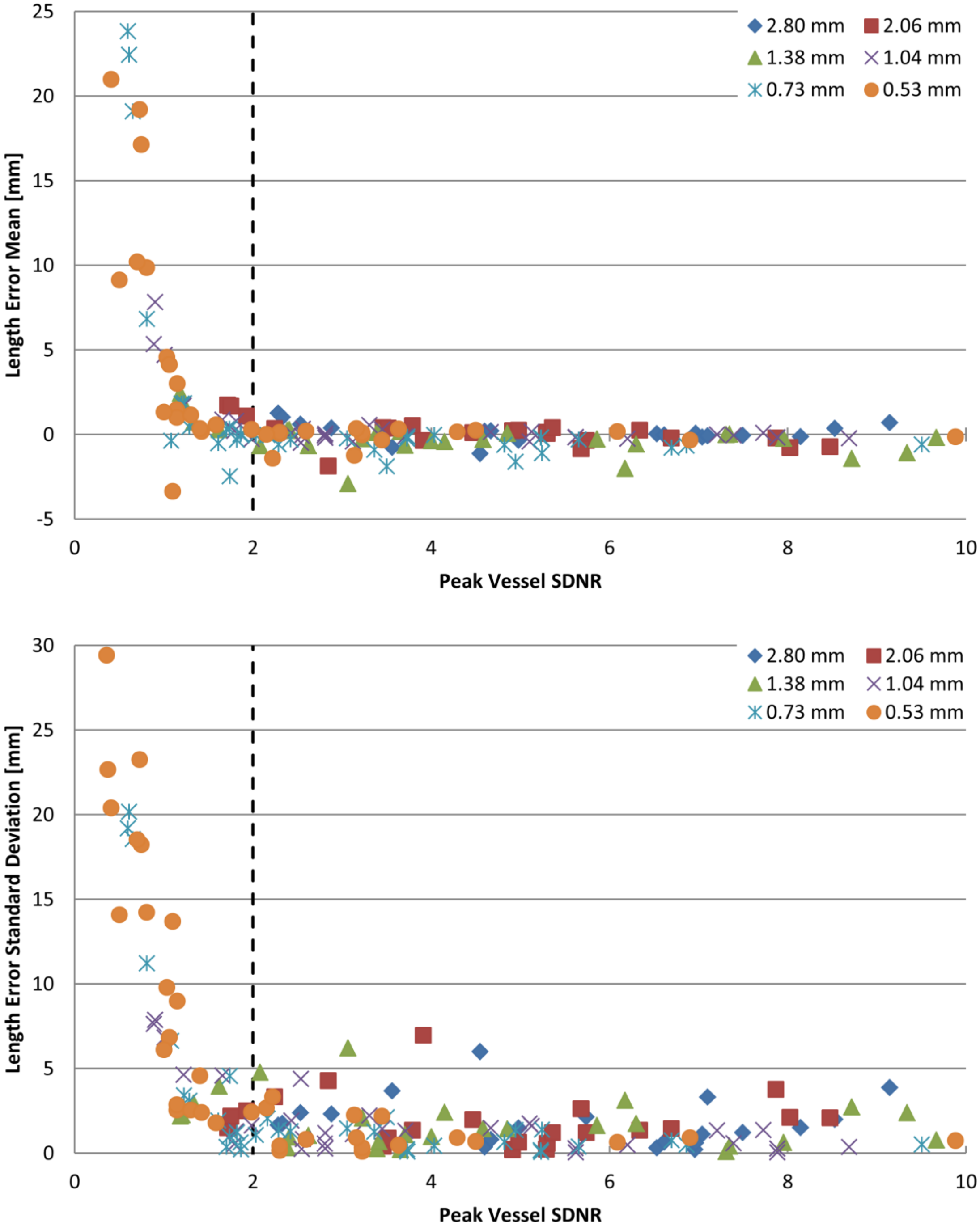

Figure 4.14 – Mean and Standard Deviation of Length Error Across Different Degrees of Foreshortening
Each point represents the mean (upper) or standard deviation (lower) of length errors calculated across 40 image frames for each total phantom thickness, number of frames integrated, and the angle of the vessel phantoms relative to the image plane. Dashed line shows the cutoff point of a vessel Peak SDNR of 2.

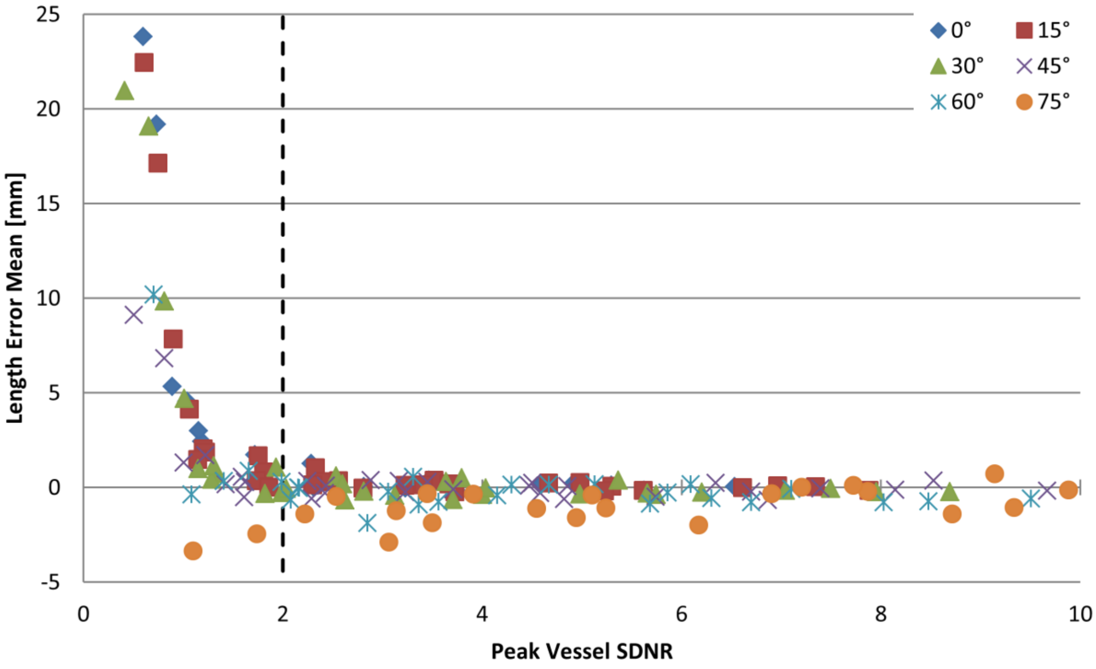

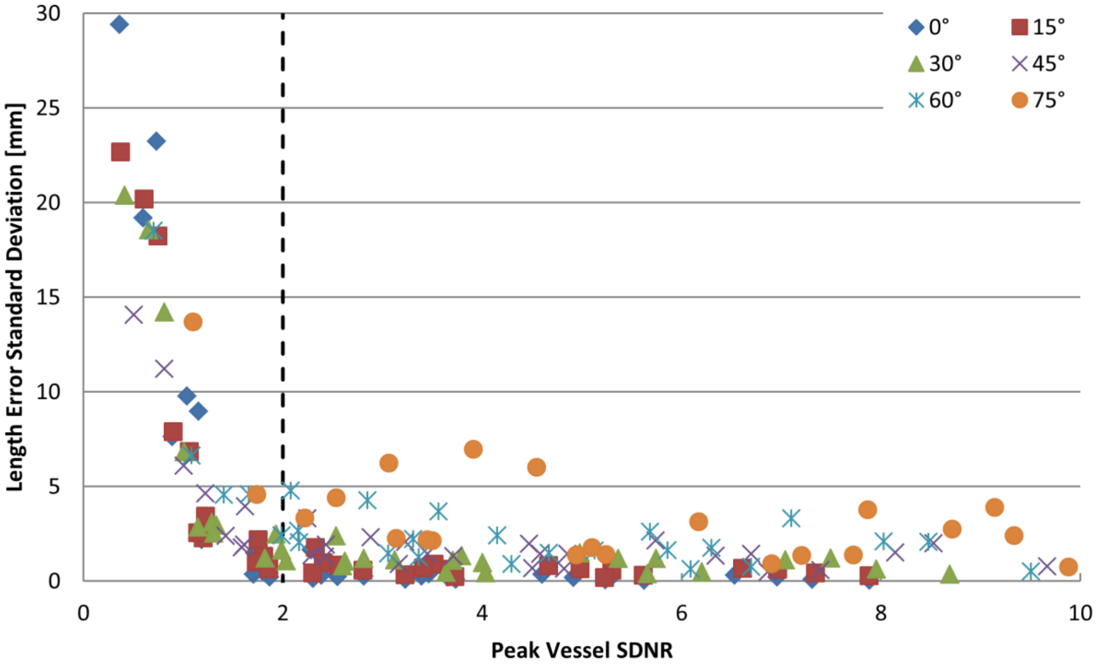

Figure 4.15 – Mean and Standard Deviation of Length Error Across Different Degrees of Foreshortening Presented by Foreshortening Angle

These data are the same as those presented in Figure 4.14, except the symbols are grouped by angle relative to the image plane instead of the true vessel phantom diameter.

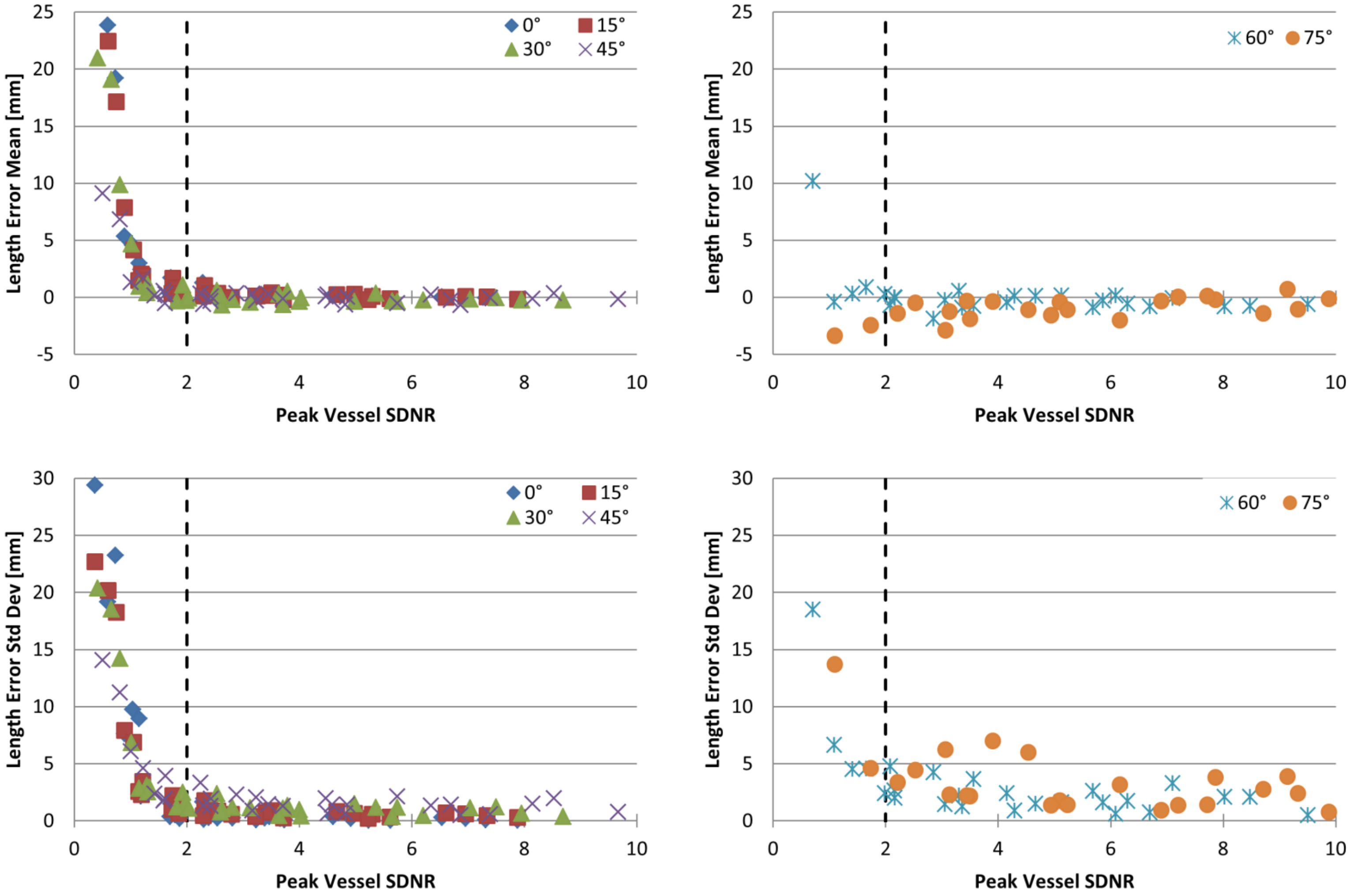

Figure 4.16 – Mean and Standard Deviation of Length Error Across Different Degrees of Foreshortening 0° - 45° vs. 60° - 75°
These data are the same as those presented in Figure 4.15, except the data from 0° to 45° have been separated from data at 60° to 75°. When vessels are only moderately foreshortened, (0-45°), the trend follows the non-foreshortened vessels length data shown in Figure 4.5 and Figure 4.9.

Focusing on the results for SDNRs between 2 and 10 and angles between 0° and 45°, as shown in Figure 4.17, the data were slightly less cohesive than in the other experiments, presumably due to the effect that small angle foreshortening had on length measurements. Binning the data showed a general trend of decreasing mean error and standard deviation of length measurements as SDNR increased over this interval. On mean length error over this interval was 0.01 ± 1.12 mm. Within the SDNR range of 2 ± 10%, the mean length error was slightly larger at 0.18 ± 1.47 mm.

When the length errors were examined as a function of the intrinsic image SNR, it was apparent that both SDNR and vessel angle affected the length measurement. Figure 4.18 shows how the length error mean and standard deviation change as a function of ϕ across different image SNRs. When the image SNR was low (due to low x-ray fluence, thick phantom) the lengths were overestimated at small angles and underestimated at large angles. For example, at the lowest image SNR (35 cm PMMA, 1 frame), the length was overestimated by 1.28 mm at 0° and underestimated by 1.22 mm at 75°. As the image SNR increased, the mean length errors at all angles converged toward zero. The highest SNR images (25.6 cm PMMA, 8 frames integrated) had an approximately 9 fold increase in SNR, and the average length errors in these images were reduced to -0.11 mm at 0° and -0.44 mm at 75°. The standard deviation of the length errors increased with foreshortening angle for each image SNR, however the magnitude of the increase diminished with increased image SNR. The length standard deviation at the lowest image SNR was 1.67 mm at 0° and 5.99 mm at 75°. At the highest image SNR, the length error standard deviation was 0.10 mm and 1.08 mm at 0 and 75°, respectively. In general, increasing the image SNR reduced the mean and standard deviation of the length error.

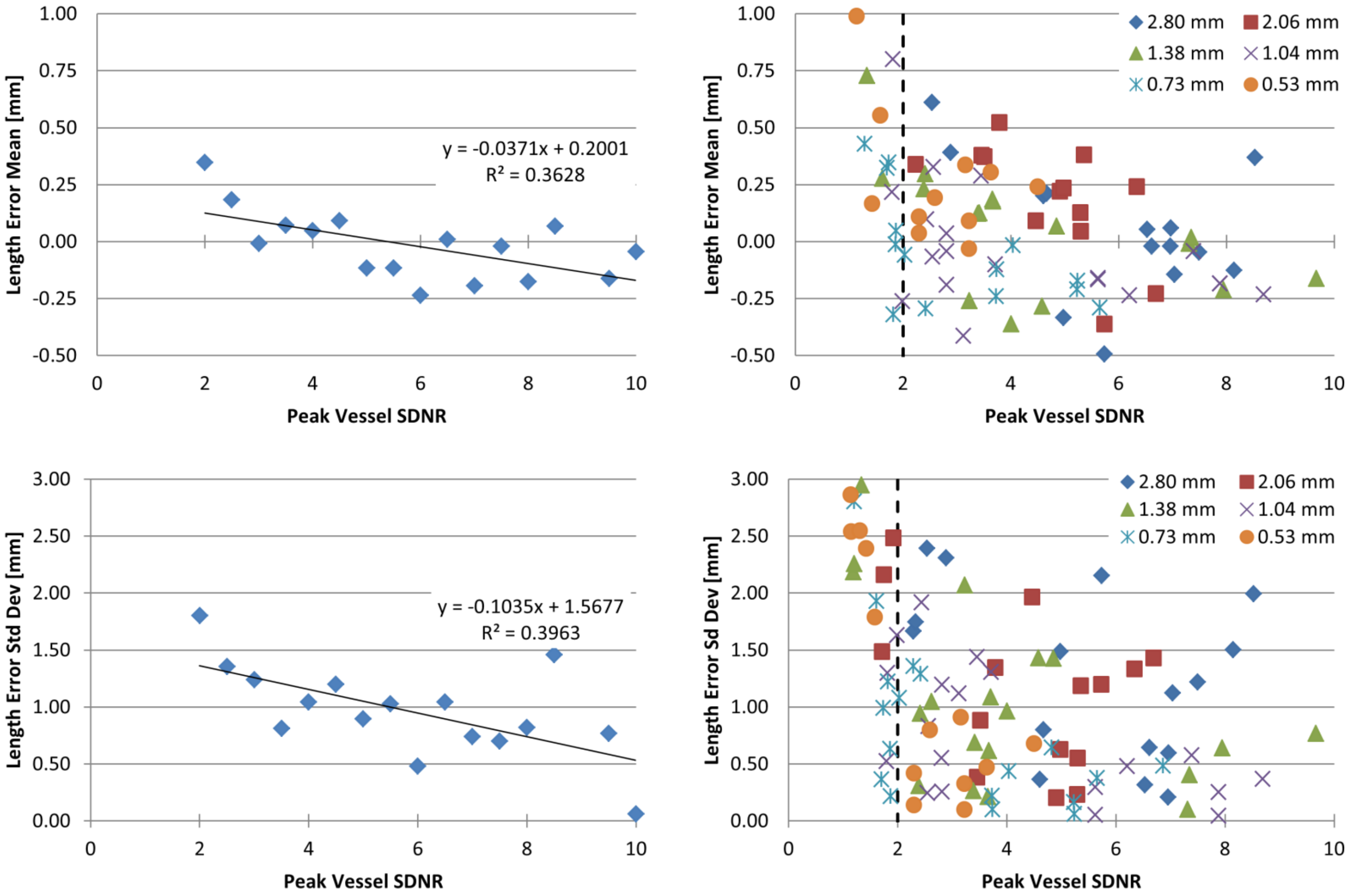

Figure 4.17 – Length Error of Foreshortened Vessels at Different Angles (0° – 45°) Binned by Peak Vessel SDNR

(Left) Length errors were calculated across all vessel phantom diameters, phantom thickness/frame integration combinations, and vessel angles between 0° and 45° by grouping the measurements by SDNR using a bin width of 0.5. Only measurements from vessel phantoms with an SDNR between 2 and 10 are shown. (Right) The length errors over the same SDNR interval are shown grouped by phantom setup (similar to Figure 4.14). Mean length error vs. SDNR is shown on the top; the standard deviation of the length error is on the bottom.

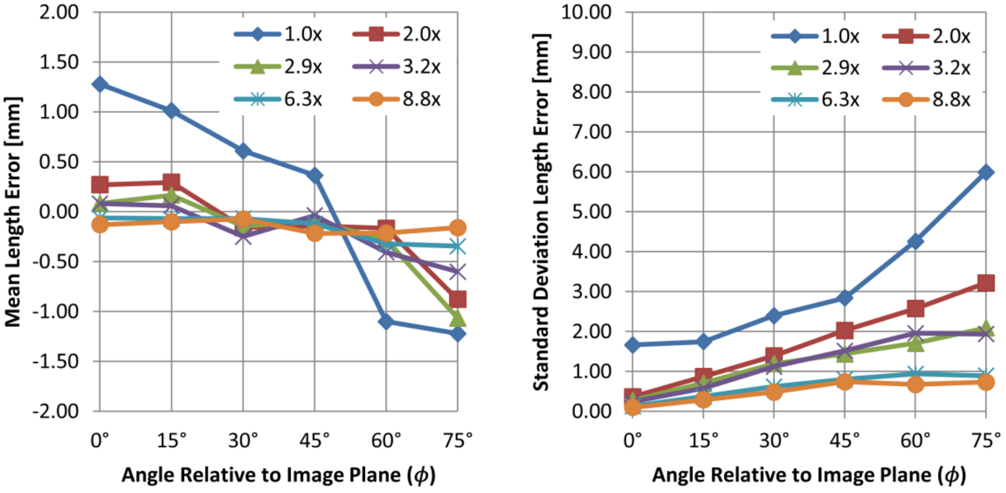

Figure 4.18 – Mean and Standard Deviation of Length Errors Versus Angle Relative to Image Plane for Each Image SNR.

Mean and standard deviation were calculated across all vessel diameters with a SDNR between 2 and 10 for the given image SNR and angle. Legend indicates the SDNR of the 1.04 mm diameter vessel relative to the SDNR for 1.04 mm diameter vessel in one frame of the 35 cm PMMA phantom at 0°.

This relationship between length error magnitude and variability is presented in relative terms in Figure 4.19. Using conventional 2D methods to measure the vessel segment length, the measured length tracked with $1/\cos\phi$. When the vessel sizing algorithm was used, the mean length error remained less than 3% across all angles and was less than 1% for angles between 0° and 45°. The variability of this method increased as the angle increased, starting at 1.7% at 0° and increasing to 11% at 75°. Note that even with the increased variability in the length measurement using the vessel sizing algorithm, the error would be much less than using the 2D method, especially at steep angles (~75°). For example, mean length error at 75° was -73.7 ± 1.5% using a 2D measurement method and 2.7 ± 10.9% using the vessel sizing algorithm.

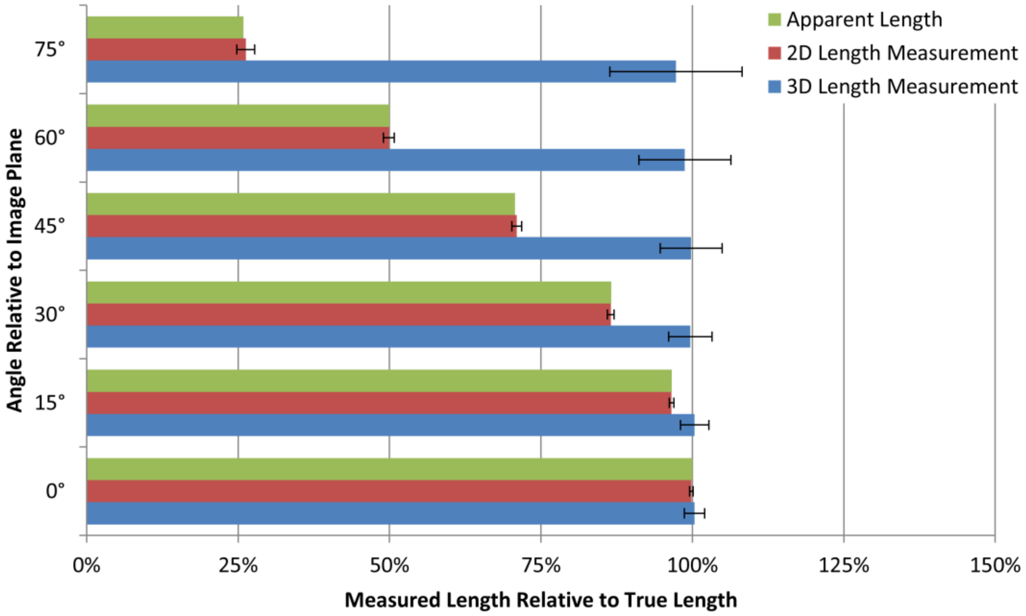

Figure 4.19 – Measured Length Relative to True Length Across Different Angles
The apparent length (green) of the vessels decreases relative to their true length by a factor of $1/\cos\phi$. The 2D length (red) was calculated from the 2D centerline, scaled by the magnification at isocenter. The 3D length (blue) was calculated from the algorithm's 3D centerline. Error bars show ±1 standard deviation about the mean. Values were calculated across all measurements where peak SDNR was between 2 and 10.

Unlike the length measurements, diameter errors and variability were independent of the angle relative to the image plane (ϕ) and followed the previous trends of Sections 4.3.1 and 4.3.2. The mean diameter error and standard deviation across foreshortening angles are shown in Figure 4.20. A magnified view of mean diameter error and the standard deviation between SDNRs of 2 and 10 is shown in Figure 4.21, where diameter errors were constant between 0.0 and 0.05 mm. The mean diameter over this SDNR range was 0.03 ± 0.08 mm. For measurements with a SDNR within 2 ± 10% and foreshortening angle ϕ less than 45°, the mean diameter error was 0.01 ± 1.12 mm. The standard deviation decreased with increased SDNR, with most data following the same curve and slightly more variability in measurements of small diameter vessel phantoms (0.53 mm and 0.73 mm diameters). The lack of appreciable outliers suggested that foreshortening angle has no effect on diameter measurements.

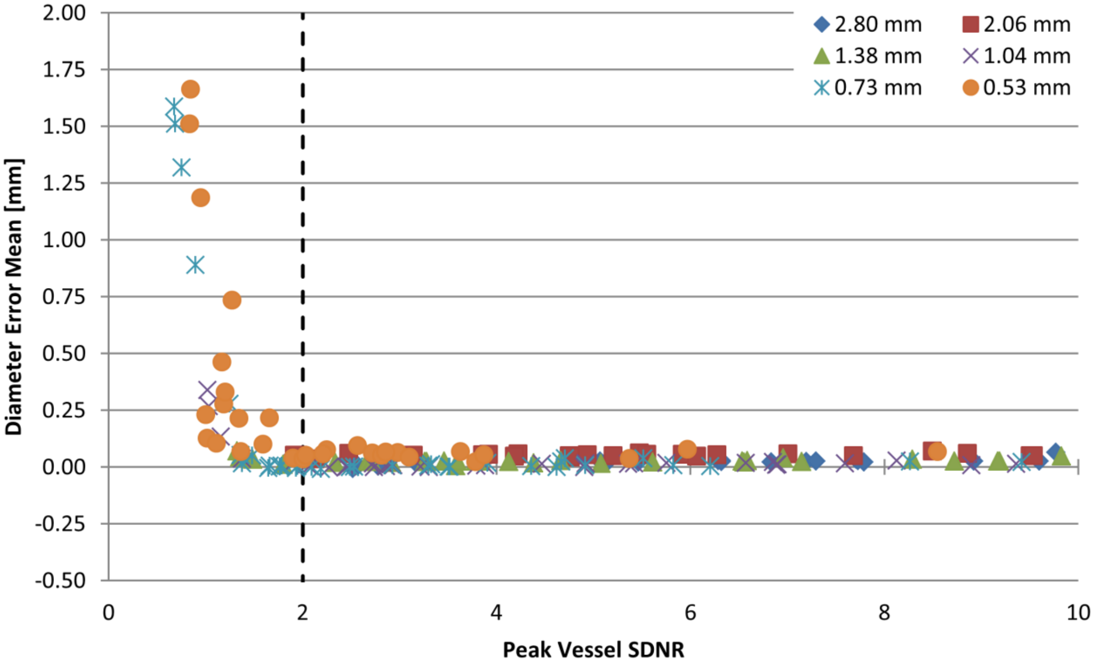

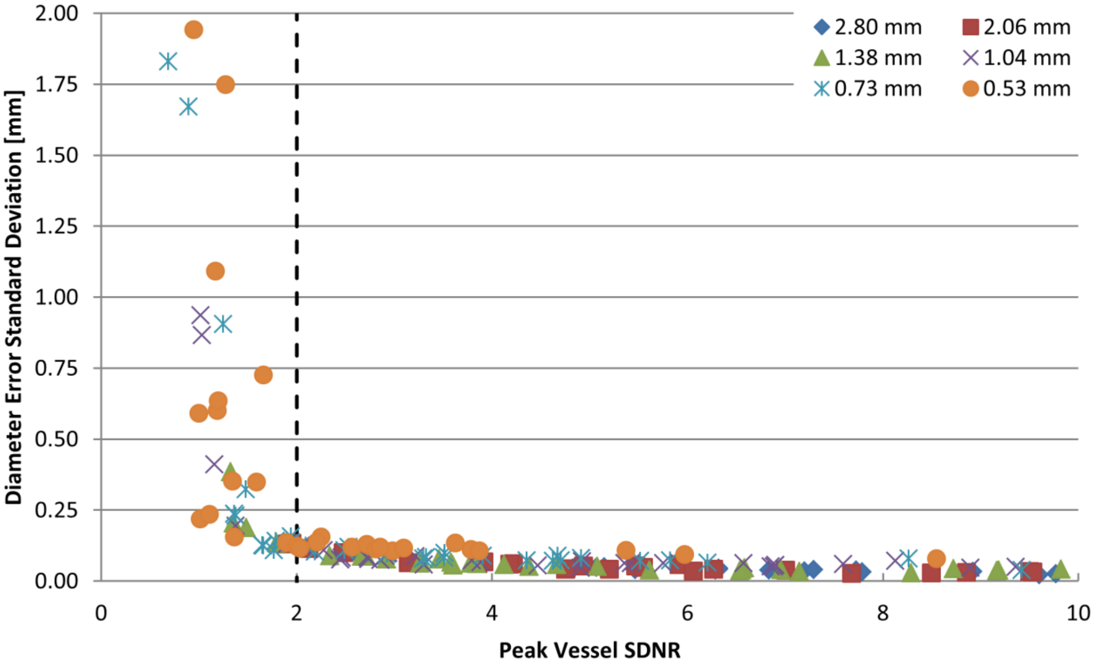

Figure 4.20 – Mean and Standard Deviation of Diameter Error Across Different Degrees of Foreshortening Each point represents the mean (upper) or standard deviation (lower) of diameter errors calculated across 40 image frames for each total phantom thickness, number of frames integrated, and the angle of the vessel phantoms relative to the image plane. Dashed line shows the cutoff point of a vessel Peak SDNR of 2.

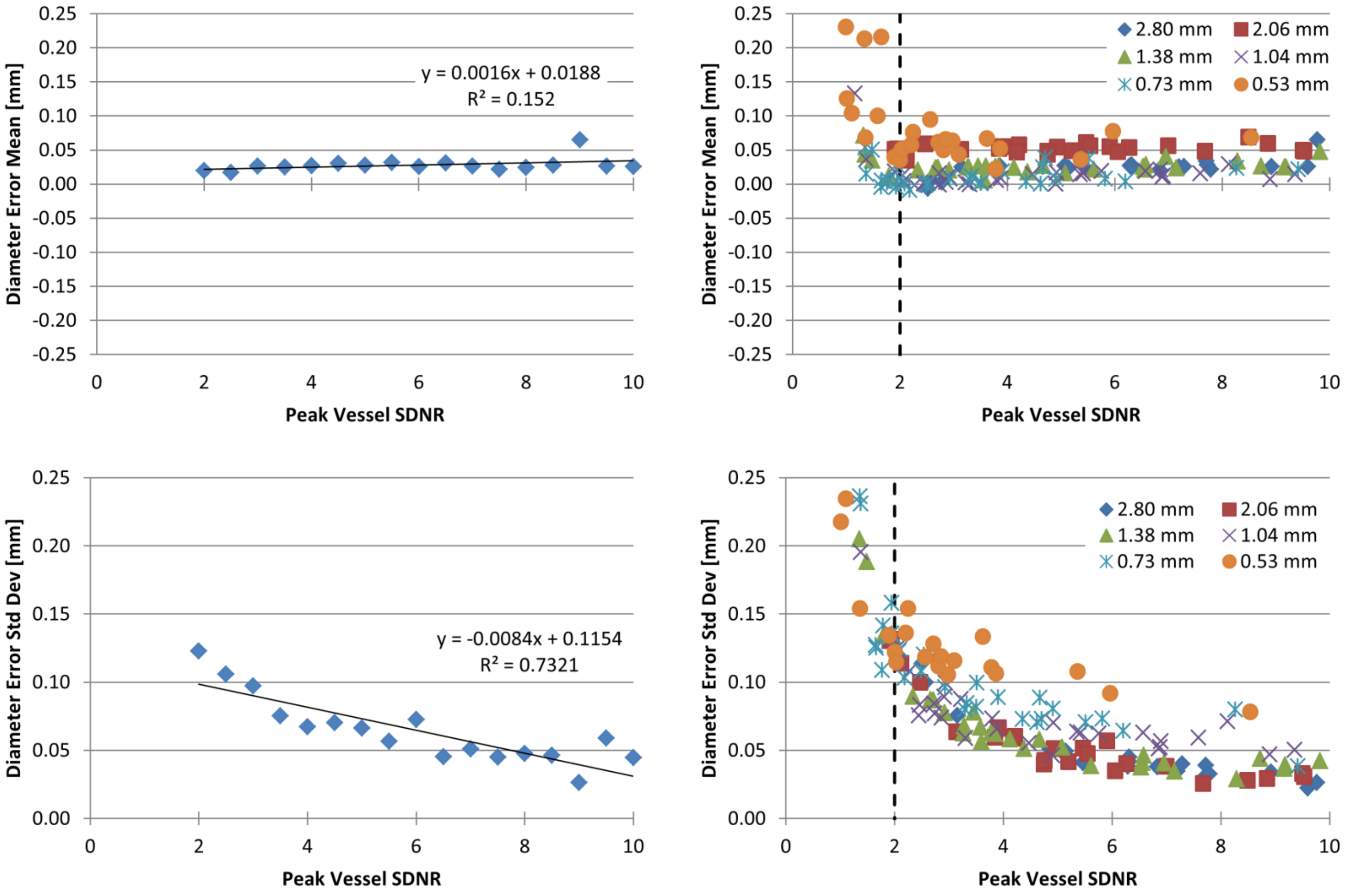

Figure 4.21 – Diameter Error for Vessels At Different Angles (0° – 75°) Binned by Peak Vessel SDNR

(Left) Diameter errors were calculated across all vessel phantom diameters, phantom thickness/frame integration combinations, and vessel angles by grouping the measurements by SDNR using a bin width of 0.5. Only measurements from vessel phantoms with an SDNR between 2 and 10 are shown. (Right) The diameter errors over the same SDNR interval are shown grouped by phantom setup (similar to Figure 4.20). Mean diameter error vs. SDNR is shown on the top; the standard deviation of the diameter error is on the bottom.

Summary: The accuracy and precision of the vessel sizing algorithm across foreshortening angles is summarized in terms of physical units in Table 4.7. For all vessel phantoms with a peak SDNR between 2 and 10 at all angles, the length error was -0.21 ± 1.98 mm, which was reduced to 0.01 ± 1.12 mm when restricted to angles between 0° and 45°. On an angle by angle basis, the length error was 0.11 ± 0.54 mm at 0°. As the angle increased and the vessels became more foreshortened, the mean error became negative (the vessel length was slightly underestimated) and the standard deviation of the error increased to become -0.87 ± 3.47 mm at 75°. The diameter error was relatively static across all angles with a mean around 0.03 ± 0.08 mm. At the SDNR threshold of 2 ± 10% and the angle relative to the image plane between 0 and 45°, the mean length error was 0.18 ± 1.47 mm and the diameter error was 0.01 ± 0.12 mm. By allowing the vessels to be angled relative to the image plane, the precision of the length measurements decreased relative to the other two experiments in this study, which only measured non-foreshortened vessels. The diameter accuracy and precision was unchanged by foreshortening.

Angle Relative to Image Plane	Foreshortening Relative to 0°	Vessel SDNR Range	Length Error (mean ± 1 SD) [mm]	Diameter Error (mean ± 1 SD) [mm]
0° - 75°	0% - 74%	2 < SDNR < 10	-0.21 ± 1.98	0.03 ± 0.08
0° - 45°	0% - 29%	2 < SDNR < 10	0.01 ± 1.12	0.02 ± 0.08
0°	0%	2 < SDNR < 10	0.11 ± 0.54	0.02 ± 0.08
15°	3%	2 < SDNR < 10	0.12 ± 0.75	0.03 ± 0.08
30°	13%	2 < SDNR < 10	-0.11 ± 1.14	0.02 ± 0.08
45°	29%	2 < SDNR < 10	-0.06 ± 1.63	0.02 ± 0.08
60°	50%	2 < SDNR < 10	-0.40 ± 2.41	0.03 ± 0.08
75°	74%	2 < SDNR < 10	-0.87 ± 3.47	0.05 ± 0.08
0° - 45°	0% - 29%	1.8 < SDNR < 2.2	0.18 ± 1.47	0.01 ± 0.12

Table 4.7 – Mean and Standard Deviation of Length and Diameter Error Across Different Angles

Expected accuracy and precision of measurements for vessels for each angle relative to the image plane. Foreshortening was calculated as $1 - \frac{apparent\ length}{true\ length}$.

4.4 Discussion

We have demonstrated that the vessel sizing algorithm calculates accurate vessel dimensions over a range of magnifications, degrees of foreshortening, and vessel SDNRs. This study has shown that the peak SDNR of a vessel segment was a reliable predictor of accuracy and precision of both length and diameter measurements when SDNR was ~2 or greater. Assuming an SDNR greater than 2 as a basic requirement, length and diameter errors were no greater than 0.37 ± 0.58 mm and 0.02 ± 0.12 mm, respectively, when the vessels were at isocenter and were not foreshortened. When non-foreshortened vessels positioned above or below isocenter (isocenter ± 12 cm) were considered, errors over the same SDNR interval were 0.29 ± 0.61 mm for length measurements and 0.00 ± 0.13 mm for diameter measurements. Foreshortening the vessel phantoms had an effect on the length measurements, but when vessel segments angled between 0° and 45° were considered, the length and diameter errors were 0.18 ± 1.47 mm and 0.01 ± 0.12 mm, respectively, over the same SDNR interval. Overall, sub-millimeter accuracy was achieved for both length and diameter measurements on average. The variability of length measurements (quantified by the error standard deviation) was typically less than 1 mm and less than 2 mm for all but the most extreme cases of vessel foreshortening. The variability of diameter measurements was typically less than or equal to 0.12 mm.

In general, the errors in segment length were overestimations of the true length with the exception of highly foreshortened vessels, where the algorithm underestimated the length of the vessel segment. When the algorithm creates the 3D centerline of the vessel, it uses the 2D centerline as the starting point and calculates a depth for each point along the 2D centerline. For a non-foreshortened vessel, the ideal result would have the algorithm assign a constant depth for each point along the vessel, which would result in no error. When noise is present in the image, variation is introduced in the depth localization of the vessel, causing what would ideally be a straight line to appear "wavy". The net effect is that the waviness increases the arclength of the line, causing the 3D length to be overestimated. Smoothing of the 3D centerline can reduce these types of errors, but it may not eliminate them completely. Figure 4.22 shows an example of how image noise can cause overestimation of non-foreshortened vessels.

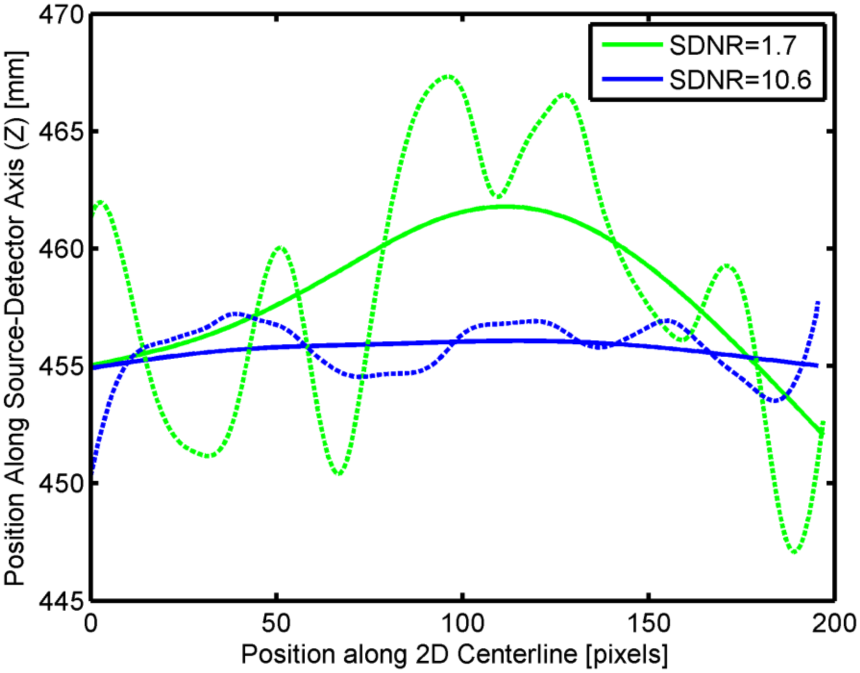

Figure 4.22 – Length Overestimation of Non-Foreshortened Vessels

The 2.06 mm diameter vessel phantom was imaged parallel to the image plane (non-foreshortened). The z component of the 3D centerline generated under low and high SDNR conditions is shown. The high SDNR centerline (dashed blue) has some variation which is reduced by smoothing the centerline (solid blue). The low SDNR centerline (dashed green) has considerably more variation. Even after smoothing, the Z coordinate of the centerline still varies (solid green), leading to overestimation of the vessel length.

In the case of a vessel that is not parallel to the image plane, the length measurements can be greater than or less than the true length, depending on the circumstances. Overestimation can again occur due to image noise creating a “wavy” centerline, whose arclength is greater than a straight centerline along the same trajectory. Image noise can also cause the overall angle of the vessel segment relative to the image plane to differ from the truth. If the angle is lesser than or greater than the true angle, the vessel length will be underestimated or overestimated, respectively, as shown in Figure 4.23. In the case of non-foreshortened vessels, the angle of the vessel relative to the image plane cannot be underestimated because the true angle is zero. Hence, when the vessel is parallel to the image plane, only overestimation can occur, but when the vessel is not parallel to the image plane, the length can be overestimated or underestimated.

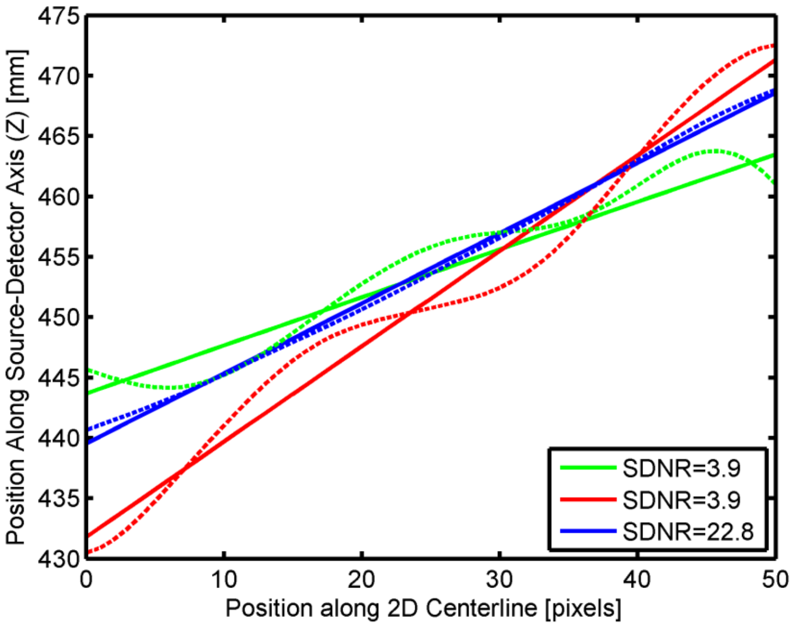

Figure 4.23 – Length Overestimation and Underestimation of Foreshortened Vessels

The 2.06 mm diameter vessel phantom was imaged at 75° relative to the image plane. Under high SDNR conditions (blue) both the original centerline (dashed) and smoothed (solid) centerline followed the true trajectory. Two low SDNR results generated from two frames of the same acquisition. The length was underestimated in one instance (green) and overestimated (red) in the other. Smoothing the noisy centerlines reduced the fluctuations, but the trajectory of the result was incorrect.

Figure 4.18 showed an increase in length error variation (standard deviation) for foreshortened vessels. One factor that may have contributed to increased variability of foreshortened vessel length measurements was the reduction in apparent length created by foreshortening. The minimum cost path and active contour model methods used in this and other vessel measurement algorithms rely on using information along the entire length of the vessel to determine an optimal result. As the length of vessel available for analysis was reduced, the robustness of the minimum cost path was also diminished. Consider the case of analyzing a vessel segment one sample long; it gets no benefit from a minimum cost path approach. Translating this principle to the foreshortening experiment, as the vessels become foreshortened, there are fewer sample points to influence the 3D localization step, which reduces the robustness of the technique. Consider Figure 4.24, where the same, non-foreshortened vessel was analyzed at different SDNR levels using increasing fractions of the full phantom length. The experiments in this chapter measured 30 mm of the full 40 mm length. As the measured length was reduced to 20, 10, 8, and 5 mm, the mean and standard deviation of the length error increased for a given SDNR. When vessels were foreshortened, there was less vessel length to analyze to form the 3D centerline, which reduced the accuracy and precision of length measurements.

Another contributing factor to increased length variability of foreshortened vessels was the increased path length through the vessel. As the effective thickness of the vessel increased, it spanned a greater range along the depth direction. This decreased the peak sharpness of the edge across the plane stack. For an infinitely thin object, the object will appear sharpest at the image plane closest to the object. A thick object cross section, however, may span several image planes. While one part of the object is in-plane and in-focus, another part is out-of-plane and out-of-focus. The in-plane edge and the out-of-plane edge are superimposed, and this combination is not as sharp as an in-plane edge alone. This reduced sharpness of the edge strength versus plane position reduced the precision of the depth localization step. This caused a vessel with the same SDNR to have more variability in the length measurements for a foreshortened vessel versus a non-foreshortened vessel. Figure 4.25 illustrates the effect that foreshortening has on effective thickness and vessel edge strength across plane position.

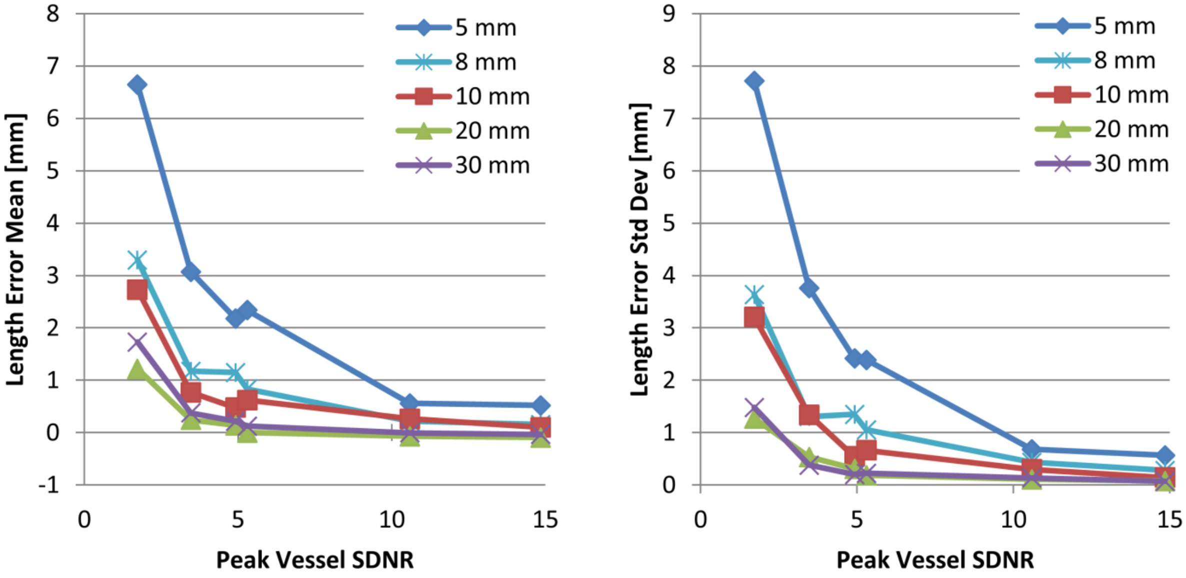

Figure 4.24 – Effect of Apparent Segment Length on Length Error Accuracy and Precision
Various (non-foreshortened) lengths of the 2.06 mm diameter vessel phantom were measured at different peak vessel SDNRs, and the mean and standard deviation of the length error was calculated across 40 measurements for each length. Under low SDNR conditions, the shorter vessel segments showed greater length errors and variability than longer segments. As the SDNR increases, the length error mean and standard deviation appear to converge.

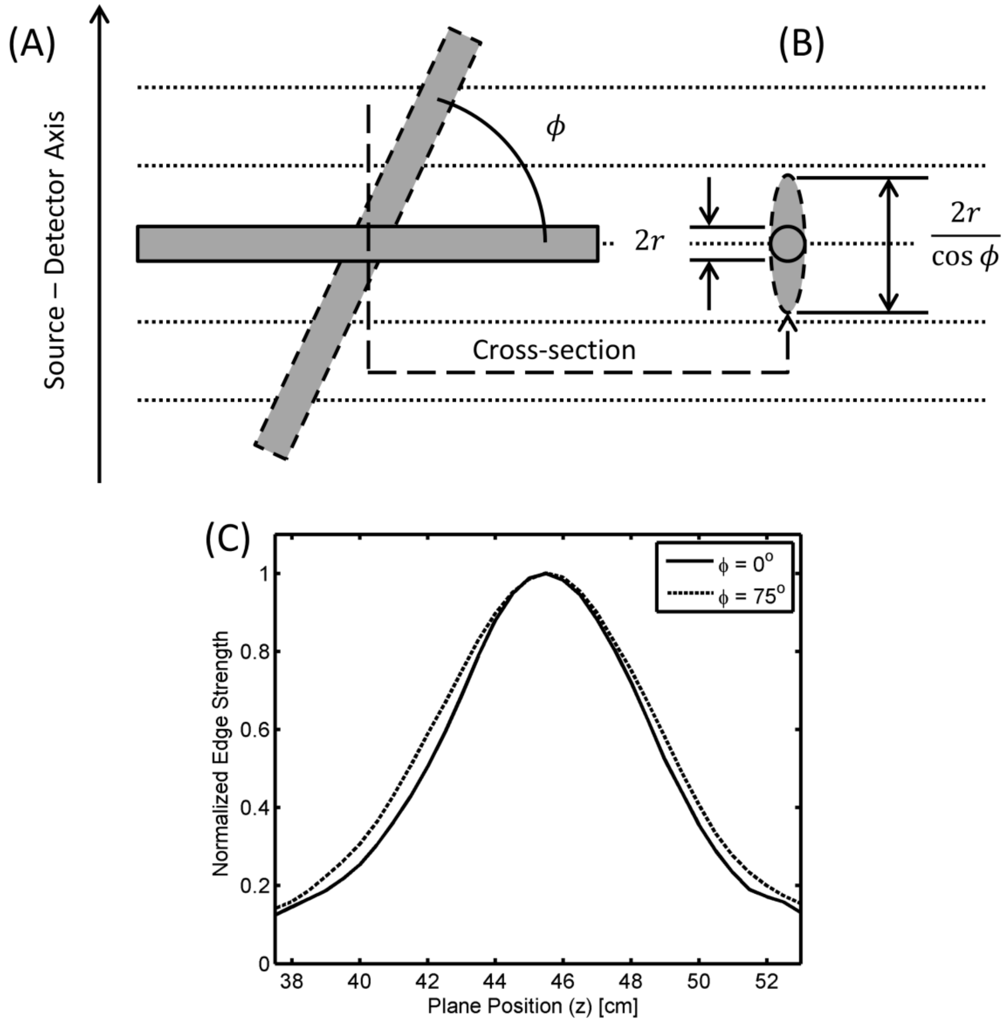

Figure 4.25 – Increased Length Variability of Foreshortened Vessels

(A) Vessels appear foreshortened when the vessel axis is angled relative to the image planes (dotted lines). Here, a vessel with a diameter of $2r$ is shown parallel to the image planes (solid outline) and at angle ϕ relative to the image planes (dashed outline). (B) Angling the vessel increases the path length through the vessel along the source detector axis by a factor of $1/\cos\phi$. (C) The increased pathlength has the effect of widening the edge strength profile across image plane position, which may lead to increased variability in the length measurement.

To isolate the effect of vessel foreshortening on length measurement accuracy and precision, length results were compared between non-foreshortened and foreshortened segments with the same apparent length, diameter, and SDNR. When the vessel phantoms were angled at 75°, the apparent length of the central 30 mm analyzed was about 55 pixels long (or 8 mm after scaling to magnification at isocenter). The non-foreshortened vessel phantoms from the same experiment were re-analyzed with the algorithm limited to the central 55 pixels of the vessel, and the results were compared to those at 75° with similar SDNR. Table 4.8 shows that when the factors of vessel diameter, apparent length, and SDNR are fixed, vessel foreshortening leads to length underestimation and increased variability.

Mean diameter error tended to be constant for SDNR greater than 2, below which the measured diameter tended to overestimate, rather than underestimate the true diameter. Most of the data at low SDNRs was from small diameter vessel phantoms. With the diameter measurement constrained to values greater than zero, erroneous measurements due to noise were more likely to be greater than the true value, leading to overestimation on average. When the model based diameter measurement fails, it is usually due to noise in the intensity profile that obscures the vessel signal. The optimal parameter fit creates a profile that follows the noise envelope rather than the vessel signal, as shown in Figure 4.26. The optimal diameter that fits the noise envelope was almost always greater than the true diameter of the vessel being measured, leading to overestimation.

Nominal Vessel Diameter [mm]	SDNR at 0°	SDNR at 75°	Length Error at 0° (mean ± 1 SD) [mm]	Length Error at 75° (mean ± 1 SD) [mm]
2.80	4.60	4.55	1.25 ± 1.40	-1.12 ± 5.99
2.80	13.91	13.11	0.18 ± 0.33	1.14 ± 2.68
2.06	3.46	3.91	1.17 ± 1.31	-0.37 ± 6.95
2.06	10.59	11.12	0.22 ± 0.43	0.58 ± 3.02
1.38	3.39	3.07	0.90 ± 1.34	-2.90 ± 6.22
1.38	7.31	8.72	0.36 ± 0.57	-1.41 ± 2.74
1.38	10.25	9.34	0.14 ± 0.24	-1.07 ± 2.38
1.04	2.55	2.54	0.91 ± 1.43	-0.50 ± 4.40
1.04	5.62	5.10	0.15 ± 0.43	-0.42 ± 1.76
1.04	7.88	7.72	0.01 ± 0.34	0.10 ± 1.37
0.73	3.73	3.50	0.24 ± 0.25	-1.89 ± 2.12
0.73	5.24	5.24	0.11 ± 0.17	-1.09 ± 1.40
0.53	2.30	2.22	0.35 ± 0.41	-1.42 ± 3.32
0.53	3.23	3.14	0.26 ± 0.35	-1.25 ± 2.25

Table 4.8 – Length Measurement Error and Variability of Non-Foreshortened and Foreshortened Vessels at Similar SDNR and Equal Apparent Length

For each vessel segment, length measurement accuracy and precision are compared between non-foreshortened vessels ($\phi = 0°$) and highly foreshortened vessels ($\phi = 75°$). For each comparison, the SDNR varied by no more than 1.5. The apparent length of the segment analyzed was the same for both non-foreshortened and foreshortened cases (about 55 pixels or 8 mm at isocenter).

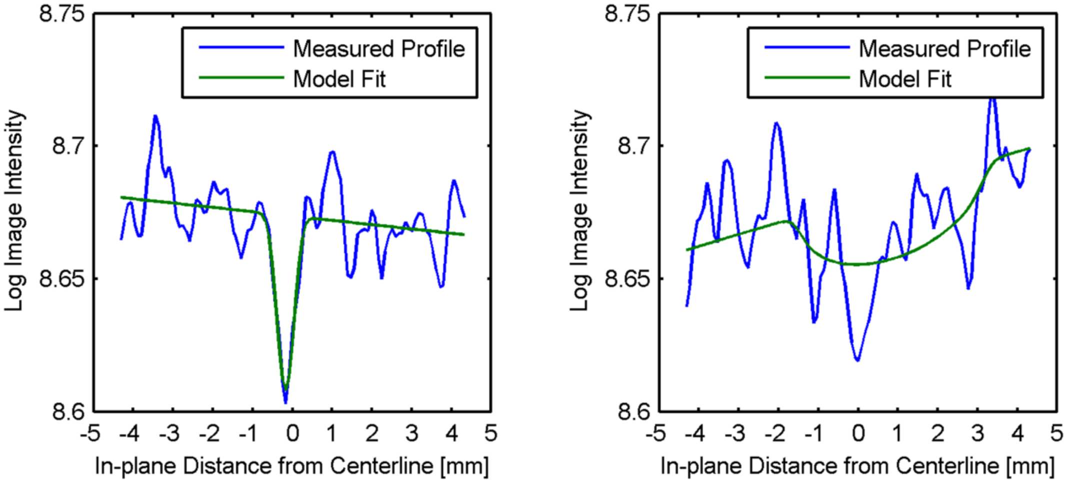

Figure 4.26 – Diameter Measurement Errors

Two instances of model based diameter measurements are shown for the same 0.53 mm diameter vessel phantom. On the left, the model successfully matches the signal created from the vessel phantom. On the right, the model follows the general envelope of the noise rather than finding the vessel signal, overestimating the true vessel diameter.

4.4.1 Comparison to Previous Studies

To the best of our knowledge, very few studies of the effects of SDNR on quantitative vessel measurements exist. Studies examining vessel *length* measurements from fluoroscopic images have not been performed presumably because measuring the diameter is a greater challenge, making length measurements trivial. However, conventional QCA methods have no way to compensate for foreshortening; phantom studies on foreshortened vessels would predictably fail. Figure 4.11 and Figure 4.19 show that length measurements based on 2D centerlines from minimum cost paths are consistent but dependent on view angle and magnification due to the nature of projection imaging. Some methods which perform a 3D reconstruction of the coronary tree from two or more views have examined the accuracy of vessel segment length measurements in phantoms [68-70]. The goal of these studies was to demonstrate the feasibility of their methods under ideal rather than suboptimal conditions.

The relationships between vessel *diameter* measurements and imaging conditions have been studied in more detail. In Ref [61], the diameter measurement accuracy and precision were examined for a number of algorithms at SDNRs of 5 and 50 (calculated in the same way as our study). The results showed that model based diameter measurements are accurate at low SDNRs and that increasing the SDNR decreased variability in the measurements. In Ref. [60], the accuracy of diameter measurements was compared to true vessel diameter and iodine concentration (both of which directly impact SDNR). As the diameter and concentration decreased (i.e. SDNR decreased), the accuracy steadily decreased until a point was reached in which it exponentially degraded. Diameter measurement variability was also studied as a function of true diameter, which showed the diameter variability dramatically increase as the true diameter (and SDNR) decreased toward 0.5 mm. The paper by Pappas and Lim (Ref. [31]), which was the basis for the model-based diameter measurement used in the SBDX vessel sizing algorithm, showed that diameter variability increases as the true diameter (and SDNR) decreases. These trends are consistent with the findings of this chapter.

4.4.2 Limitations

The results presented in this chapter apply to a particular set of parameters for the vessel sizing algorithm. The steps of 2D vessel segmentation, 3D depth localization, and the model-based diameter measurement each have an associated set of parameters. Some of these parameters enforce smoothness constraints of 2D and 3D edges and centerlines, which improve the performance of the algorithm in the presence of noise at the expense of limiting the complexity of the 2D and 3D vessel representation. Other steps such as averaging multiple vessel profiles together before measuring the diameter may not be applicable in all cases. In this experiment, profiles were averaged over approximately 5 mm of vessel length (31 pixels of centerline length). While this works for vessels whose diameter is static over a region, it may introduce errors if the diameter is changing quickly, as one would expect near an acute stenosis. While reducing the number of profiles averaged would improve the algorithm's ability to resolve a particular diameter to a particular region of the vessel, it would come at the expense of increased variability in the measurement. Each parameter in the algorithm will in some way affect the accuracy or precision of the algorithm, and an exhaustive study examining all possible parameter combinations was not feasible. The set of parameters used in this study was the result of working with a limited set of both phantom and *in vivo* animal model image data, and it was found to work well across most settings. As the algorithm is applied to new imaging conditions, such as clinical human cases, additional parameter optimization may be required.

The apparent length of the segment analyzed was shown in Figure 4.24 to have an effect on length measurement results. In this study, the results were examined across a 30 mm segment regardless of apparent length. An additional study may be required to determine a minimum apparent vessel segment length to be analyzed to ensure an accurate and precise measurement.

The segment endpoints used at inputs to the algorithm were precisely defined from low-noise images to be the ideal starting points. In practical use, these points would be defined by a human user on realistic, noisy images. In our experience, the algorithm produces similar results as long as the endpoints are within the vessel boundaries, but the location of the initial endpoints can affect the results. To better characterize how this method works in the real world, an observer variability study would be needed, in which users choose the endpoints of the vessel segments. The measurement accuracy and variability could be compared to the results in this chapter to determine the effect that human interaction has on the final result.

Although SDNR is easy to calculate and gives a tangible measure of image quality for assessing algorithm performance, comparisons to other experiments is still challenging. Even if the imaging setup were fully described, identical experimental conditions are only possible using the same imaging system and phantom. Comparing across systems requires the reader to consider system specific characteristics such as the modulation transfer function (MTF), noise power spectrum (NPS), and temporal resolution. These may affect how an algorithm performs even if the SDNR of the target object is matched.

4.5 Conclusion

This study demonstrates that the vessel sizing algorithm presented in Chapter 3 can accurately measure vessel segment length and diameter over a variety of phantom thicknesses, magnifications, and degrees of foreshortening. These measurements were successfully performed without any magnification calibration from individual SBDX scan frames, which is more efficient than methods that require a calibration object or multiple views to reconstruct 3D vessel geometries. Provided that minimal image quality standard can be maintained, this method can enhance the user's ability to quickly match a device size to a coronary vessel.

Chapter 5 – *In Vivo* Validation of Vessel Sizing in Healthy Swine Model

5.1 Introduction

Although phantom-based validations provide insight into the performance of an algorithm under tightly controlled conditions, the ultimate test of a method must be done on the target anatomy under clinically relevant conditions. This is especially true for image-based tasks involving the heart, where beating motion, respiratory motion, and heterogeneous background structures are virtually impossible to simulate in the laboratory. Using an animal model, the challenging imaging conditions of *in vivo* measurements can be recreated and used estimate the accuracy and precision of the vessel sizing algorithm in real-world use. The greatest challenge of this approach is defining the ground truth to which to compare the new method.

Many studies have compared methods for measuring vessel dimensions *in vivo*. At the time that conventional quantitative coronary angiography (QCA) was first developed in the 1970s, there were no other modalities to which the QCA results could be compared. Typically, a vessel phantom whose dimensions were precisely known was imaged under conditions to simulate an *in vivo* setting. To simulate heterogeneous background anatomy, the vessel phantom was placed on or inside of an anthropomorphic chest phantom [71, 72], inside the pericardial space of a human cadaver [59], or on the chest of a live human patient [60, 73]. To image a phantom with a complex background *and* cardiac and respiratory motion, the vessel phantoms were implanted inside the coronary artery of an animal model [74-77], or sewn to the epicardial surface [78]. Validating QCA measurements of actual artery *in vivo* required explanting the artery post mortem and measuring the dimension using microscopy [29, 79]. Keeping the vessel in a physiologic-like state (pressurized, under tension) after removing it from the body remained a challenge. While these ground truth measurements were precise, they were never based on an actual coronary artery *in vivo*, which limited their predictive value of real world performance.

The development of advanced cardiovascular imaging has enabled *in vivo* validations which compare measurements between two or more modalities. Coronary computed tomography angiography (CCTA) is non-invasive, fast, and provides a 3D representation of the coronary arteries. Diameter measurements made from CCTA have been compared to QCA measurements [80, 81], although the resolution of CCTA limits the applicability for absolute diameter measurements of small vessels. A more accurate modality for vessel lumen diameter measurements is intravascular ultrasound (IVUS), which is the gold standard for vessel imaging and vessel sizing during interventions [24]. Multiple studies have compared conventional QCA to IVUS for measuring diameter [82-87] and length [88]. When imaging a section of vessel with IVUS, the user must guide the probe through the vessel of interest and record serial cross sectional images as the IVUS probe is withdrawn. Due to the invasive and time-consuming nature of IVUS imaging, it is not appropriate for measuring an entire coronary tree. Consequently, a combination of CCTA for length and IVUS for diameter is used to validate measurements made using the SBDX vessel sizing method.

In this chapter, a multimodal image-based *in vivo* validation of the SBDX vessel sizing algorithm using a healthy porcine model is presented. Coronary arteries were imaged using CCTA and IVUS for ground truth vessel length and diameter, respectively. Angiography was performed using SBDX, and the vessel sizing algorithm described in Chapter 3 was applied. Co-localization of the vessels was performed by dividing the arteries into segments based on side branch points [88, 89]. Results are presented which show that the vessel sizing algorithm can accurately measure vessel dimensions *in vivo*, which when used clinically would help to guide accurate interventional device selection.

5.2 Methods

5.2.1 Animal Prep

Three healthy juvenile swine (~40 kg) were imaged under a protocol approved by the institutional animal care and use committee at the University of Wisconsin – Madison. The animals were first anaesthetized using telazol and xylazine, followed by intubation and mechanical ventilation under 2% isofluorane. Vascular access to the femoral artery was obtained for conventional angiography and IVUS imaging. Venous access through the ear was used for administration of drugs as well as iodinated contrast injection during the CCTA. Amioderone, metoprolol, and lidocane were administered intravenously as needed throughout the experiment to prevent arrhythmias. Heparin was administered as needed to prevent thrombus formation.

5.2.2 Image Acquisition

5.2.2.1 Conventional X-ray Angiography and Intravascular Ultrasound

Conventional x-ray angiography (XA) of the left coronary arteries was performed using a Philips H5000 fluoroscopy system in the animal catheterization lab. A diagnostic catheter (AR

1.0 6fr, Medtronic, Minneapolis, MN) was guided into the left main coronary artery. Prior to contrast injection, 500 μg intracoronary nitroglycerine was injected to dilate the artery and prevent spontaneous spasm. A cine angiogram was recorded using 350 mgI/mL iohexol (Omnipaque, GE Healthcare, Waukesha, WI) using an x-ray view to minimize foreshortening of the main and branch vessels in the LAD and LCx, typically 30 LAO and 20 RAO, respectively.

A roadmap of the left coronary arteries was created from an end-diastolic frame of the angiogram. A plastic transparency was taped to the fluoroscopic display, and the luminal edges of the coronary arteries were traced onto the transparency, noting the location of major branches. This served as a guide to plan positioning of the IVUS imaging catheter probe.

Intravascular ultrasound imaging of the coronary arteries was performed by first steering a guide wire (0.035", Choice PT, Boston Scientific, Natick, MA) into the distal LAD. A 40 MHz rotating IVUS probe (Revolution, Volcano Corporation, San Diego, CA) was inserted over the guide wire into the distal LAD, and the position of the probe relative to the vessels in the angiogram was recorded. A 500 μg dose of intracoronary nitroglycerine was administered immediately prior to the start of IVUS imaging. Serial cross-sectional IVUS images were recorded along the length of the LAD up to the left main artery using continuous imaging during a fixed-rate mechanical pullback (30 frames per second, 0.5 mm/s or 1.0 mm/s pullback speed). During the IVUS pullback, the IVUS frame indices showing major branch points were annotated using the IVUS software. This procedure was repeated for the LCx. The IVUS recordings were exported in DICOM format for offline analysis after the experiment.

5.2.2.2 Coronary Computed Tomography Angiography

Coronary CT angiography was performed using a GE Discovery CT750 64 slice CT scanner. After performing scout images but before the CCTA, zatebradine HCl (Torcis Bioscience, Bristol, UK) was administered to lower the heart rate to below 80 BPM (typically 6 mg/dose). The CCTA was performed under breath hold conditions by suspending mechanical ventilation at end-expiration during scanning. If needed, 10 mg vecuronium was administered prior to scanning to prevent residual respiratory motion. The CCTA was performed with an iodinated contrast injection using a power injector through the ear vein (iohexanol, 320 mgI/mL, Visipaque, GE Healthcare, Waukesha, WI), with a 66 mL contrast injection volume at 6 mL/sec, followed by a 60 mL saline chaser at 6 mL/sec. Scan parameters were as follows: retrospective cardiac gating, 120kV, 600 mA, helical pitch 0.24. Images were reconstructed at 75% R-R (end-diastole), with 0.39 x 0.39 x 0.625 mm voxel size.

5.2.2.3 Scanning Beam Digital X-ray

Angiography for SBDX vessel sizing was performed in the SBDX lab using the prototype system. All three experiments were performed using the most recent detector design (320 x 160 detector elements binned to 160 x 80 for 0.66 mm effective detector element pitch). At the time of these experiments, real-time reconstruction and display capability was still under development. To facilitate catheter placement in the animal for angiographic imaging, a portable fluoroscopy unit (PFU) (OEC 9800, GE Healthcare, Waukesha, WI) was positioned in line with the SBDX gantry. Using the patient table position readout and the known translation between the isocenters of SBDX and the PFU, catheter positioning and angiographic view selection was performed using the PFU, and the animal was translated on the table to an identical view with

SBDX while keeping the diagnostic catheter in place. Figure 5.1 shows the equipment layout for the SBDX imaging portion of the experiment.

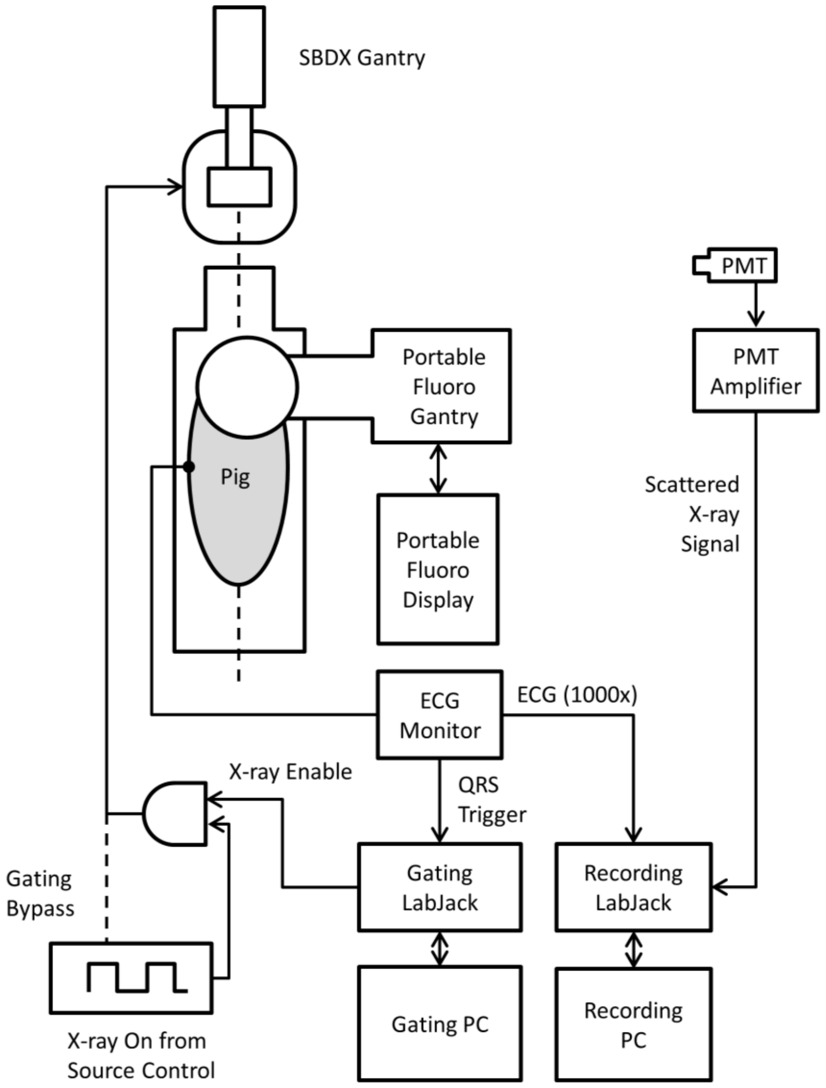

Figure 5.1 – Schematic of the SBDX Image Acquisition.
The portable fluoroscopy unit (PFU) was positioned in line with the SBDX gantry. The PFU was used for catheter positioning and finding a suitable angiographic view, after which the animal was translated to the SBDX gantry. The animal was connected to an ECG monitor, which output the ECG waveform and QRS Trigger pulse. The photomultiplier tube (PMT) positioned at the edge of the room detected scattered x-rays when the SBDX source was active. The output of the PMT and ECG waveform were digitized and recorded to determine the % R-R interval for each frame. The QRS trigger was digitized by the gating computer, where timing delays were inserted and used to control the X-ray on signal from the SBDX source computer. For the third experiment, real-time recording was available, and ECG gating circuitry was bypassed.

The first two experiments were performed before the continuous fluoroscopic (15 fps) recording capability was available. Images were acquired using the "radiographic mode", in which single frame (1/15th second) acquisitions were triggered using an ECG gating circuit tuned for end-diastole (approximately 75% R-R interval). The hardware based QRS trigger from the physiological monitor (Vital-Guard 450C, Ivy Biomedical Systems, Inc., Branford, CT) was monitored in real-time using a data acquisition board (LabJack U12, LabJack Corporation, Lakewood, CO) controlled using LabView (LabView 2011, National Instruments, Austin, TX). An auxiliary circuit was constructed to block the "x-ray on" signal from SBDX until a predefined delay from the QRS trigger. Due to limitations of this recording technique, only a single frame from every other heartbeat was recorded. At the time of the third experiment, continuous real-time recording of SBDX scan data (15 fps) was available, which made the ECG triggering circuitry unnecessary. Instead, end-diastolic frames were obtained retrospectively using the recorded ECG and scattered x-ray waveforms.

In all three experiments, a photomultiplier tube (PMT) with amplifier was positioned in the lab to detect the start of each SBDX scan frame from scattered x-rays. The raw (1000x) ECG signal from the physiological monitor and the output from the PMT amplifier were recorded simultaneously using a separate LabJack based data acquisition system. This was used to calculate the true percent R-R interval for each image frame retrospectively. Figure 5.2 shows an example of recorded ECG and PMT signals.

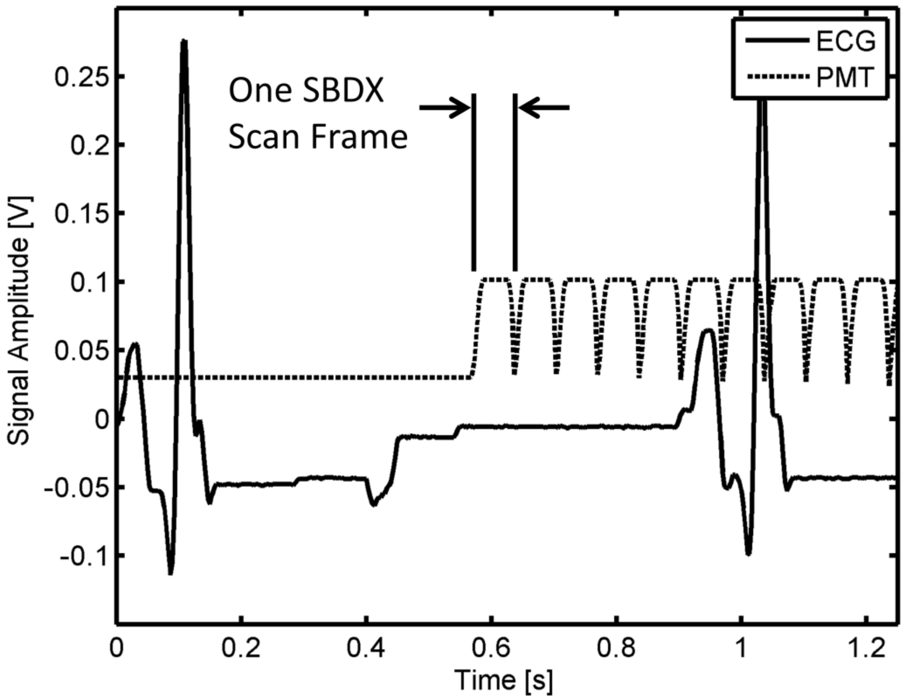

Figure 5.2 – ECG and PMT Recording for SBDX Cardiac Gating.
The animal's ECG from the physiological monitor and the output of the PMT were recorded using a data acquisition card and a PC. The PMT detected scattered x-rays when the SBDX x-ray source was turned on, which was used to determine the relative position of each frame between R waves of adjacent heart beats.

The angiographic protocol followed that which was used for conventional angiography, using femoral access to position a diagnostic catheter into the left main artery. Immediately prior to imaging with SBDX, intracoronary nitroglycerine (500 μg) was injected to dilate the vessel. Cineangiography of the left coronary vessels (LAD and LCx) was performed at multiple views and operating points (kV, scan frame rate) to create different imaging scenes and SNR levels. Contrast injections during angiography were performed by hand using iohexol (Omnipaque 350), and each angiographic run lasted approximately 10 seconds. For the third experiment only, additional "filter packs" were placed on top of the collimator exit to get the half value layer to match that of the clinical Philips FD10 cardiac fluoroscopy system.

Raw SBDX scan data were downloaded from the storage array and reconstructed using a Matlab simulation of the hardware-based reconstruction algorithm. Frames from each image sequence were reconstructed as a 32 plane image stack with 5 mm plane spacing, and with the stack positioned symmetrically about the heart. Other reconstruction parameters include shift parameter $m = 10$, fractional binning with spread parameter $s = 1$, and dynamic alpha pattern correction. Multiplane composites were created from a subset of 16 out of the 32 image planes which were closest to the vessel of interest as determined by visually estimating the tomographic blur of the target vessel. Multiplane composite algorithm used was provided by Triple Ring Technologies and was invoked using default parameters.

5.2.3 Vessel Segment Sizing Analysis

5.2.3.1 Diameter Measurement from IVUS

The IVUS images were preprocessed prior to segmentation for diameter measurements. First, the reticles superimposed on the images were removed by segmenting the reticle pixels using a simple threshold, followed by replacing the pixel values with linearly interpolated intensity values from neighboring non-reticle pixels. Residual image artifacts were negligible.

A semi-automated segmentation method was applied to the IVUS imaging sequences to obtain luminal contours on the transverse (cross-sectional) images. To ensure that the measurements from the IVUS images were performed at end-diastole, an image-based cardiac gating algorithm was applied to identify the end-diastolic image frame from each heartbeat [90]. This algorithm measures relative cardiac motion from the normalized cross-correlation coefficient (NCC) between two IVUS image frames. The NCC is used to determine the frame within each heart beat where cardiac motion is minimized, which is assumed to be at end-diastole. The NCC is also used to determine the correspondence between end-diastolic frames across adjacent heartbeats. The reader is referred to Ref. [90] for a more comprehensive explanation and implementation details. The end result of the algorithm is a sequence of indices corresponding to the end-diastolic IVUS image frames from each heartbeat. Figure 5.3 demonstrates the need for and results from the cardiac gating algorithm.

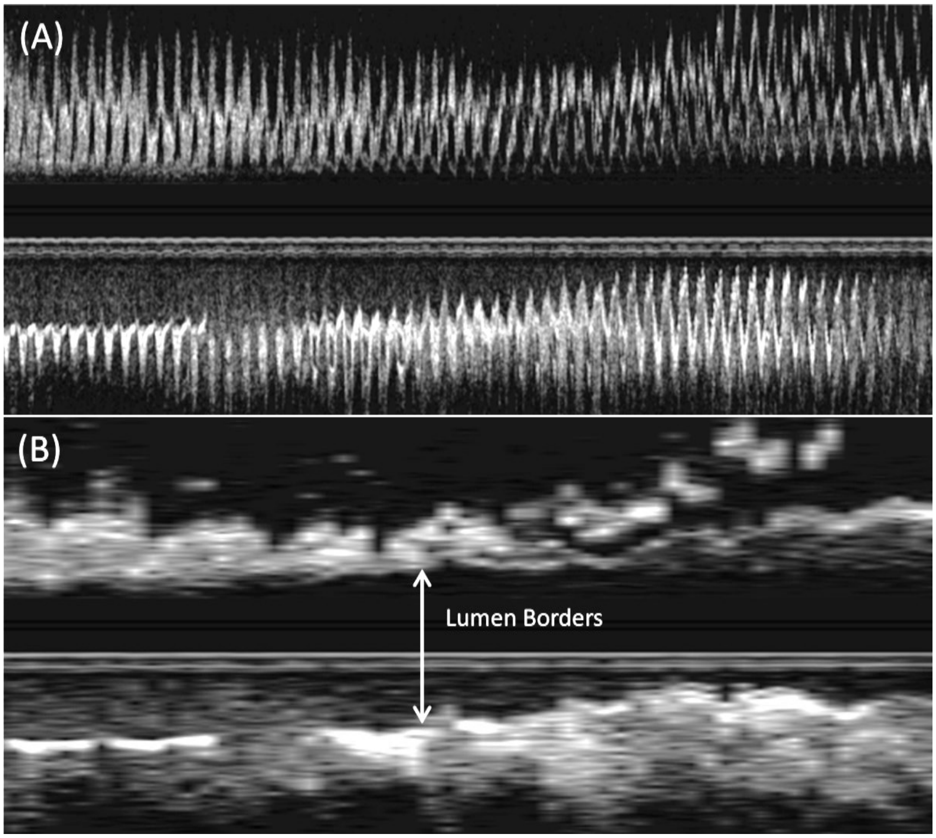

Figure 5.3 – Cardiac Gating of Intravascular Ultrasound Image Sequence

(A) Longitudinally reformatted images of an IVUS pullback sequence show the effect of cardiac motion on the position of lumen borders. (B) After applying the cardiac gating algorithm, interpolation between end-diastolic frames produces smooth longitudinal images for segmentation.

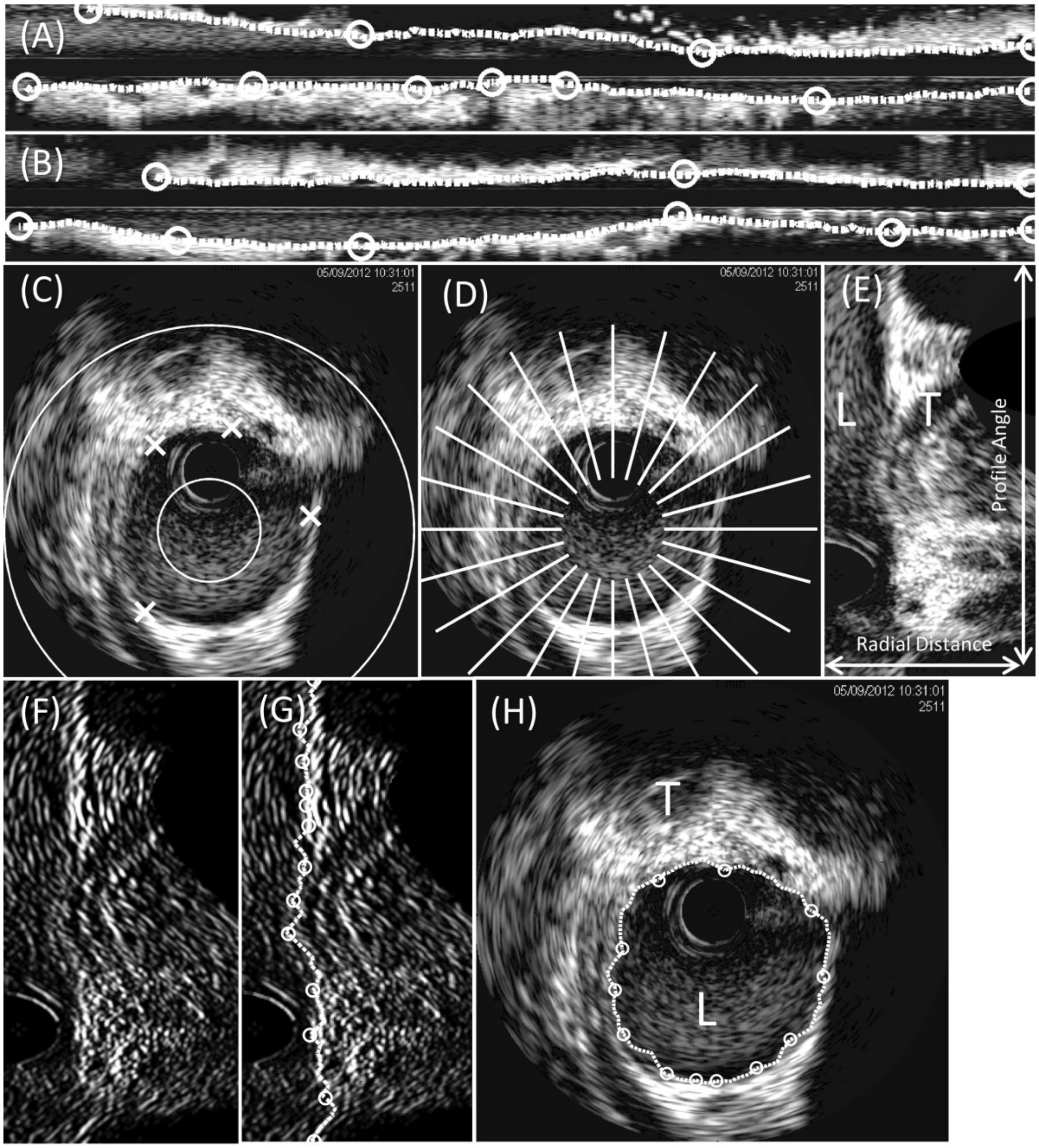

Figure 5.4 – IVUS Segmentation of Vessel Lumen Border

(A) and (B) The vessel lumen was initially segmented from two orthogonal cardiac-gated longitudinal images. A minimum cost path algorithm was used to define the lumen path between user specified points. (C) The longitudinal contours were transferred to transverse IVUS images (Xs). The four points from the contours were used to define an annular region of interest. (D) Radial profiles were defined within the annular ROI. Actual profiles were defined more densely than shown. (E) The radial profiles extracted to create a “straightened” lumen image, where the division between the lumen (L) and the surrounding tissue (T) can be defined by a vertical path. (F) The straightened lumen image was edge filtered to enhance the lumen border. (G) The minimum cost path algorithm was applied between user defined points to segment the luminal border. (H) The lumen border was transferred back to the original transverse image where it was used to calculate lumen area and minimum lumen diameter.

A semi-automated segmentation method was implemented to consistently and rapidly identify the lumen borders for the purpose of measuring lumen diameter. The analysis method closely follows previously described methods [91-93]. Figure 5.4 walks through the steps of the algorithm. For each cardiac gated IVUS sequence, longitudinally reformatted images were created by extracting radial intensity profiles from the cross sectional images across all images in the cardiac gated sequence. Linear interpolation was used to fill in the space between image frames in the cardiac gated sequence. Next, two orthogonal longitudinal images were selected based on the visibility of the lumen border and absence of image artifacts, specifically the shading artifact caused by the guide wire. In each image, the longitudinal lumen border was segmented by applying an edge detection filter to the image and using dynamic programming to find the optimal edge contour in each image. The longitudinal lumen contours were manually corrected as needed by forcing the contour to go through user selected points. The coordinates of the longitudinal lumen contours were mapped onto the original transverse images to initialize lumen edge segmentation.

For each transverse IVUS image in the cardiac gated sequence, the four longitudinal contours (2 per longitudinal image) were used to define four points approximately along the transverse lumen contour. An annular region of interest was defined centered on the average of the four points, with inner and outer diameters defined respectively as 50% and 200% of the diameter of a circle fit to the four longitudinal contour points. Radial contours were extracted over 360° in 1° increments from the inner to the outer diameter of the ROI to create a “straightened” lumen image where one axis corresponded to radial distance from the ROI inner diameter and the other axis corresponded to the angle of the profile. A one-dimensional gradient filter was applied to the image, and the optimal edge contour was defined again using a dynamic programming approach. The user could correct errors in the contour by forcing the path through specific points. The final edge contour on the straightened lumen image was mapped back to the original transverse IVUS image for diameter calculation.

Two methods were used to calculate the lumen diameter from the transverse lumen contours. The first method was based on the area of the transverse lumen contour. For a given lumen area A_{IVUS}, the radius $r_{IVUS}$was calculated by assuming a circular area model such that $r_{IVUS} \equiv \sqrt{A_{IVUS}/\pi}$. The lumen diameter d_{IVUS} is given by $2 \cdot r_{IVUS}$. This method should be robust against errors in the contour due to noise, which would even out over the entire contour. Even under noise-free conditions, this method for diameter calculation may overestimate the true lumen diameter of the vessel if the plane of the IVUS image is not perpendicular to the true vessel centerline (due to IVUS catheter deflection). If the normal vector of IVUS image plane deviates from the true vessel centerline by angle θ, the lumen will appear to have an elliptical cross section and the lumen area will overestimate the true area by a factor of $1/cos\theta$, which propagate to an overestimation of the diameter by a factor of $\surd(1/cos\theta)$. Alternatively, the lumen diameter from an IVUS lumen contour could be measured from the minimum diameter, which is defined as the shortest distance between two points on the lumen contour that goes through the lumen centroid. While this method is insensitive to probe orientation within the vessel, it may underestimate the true diameter due to artifacts and noise affecting the lumen contour. For the purposes of comparison to SBDX vessel sizing diameters, both methods of calculating IVUS lumen diameter were considered.

Vessel segment endpoints were identified based on the distal carina of branching vessels. For each vessel branch, the cardiac gated image frame on the distal side of the branch was identified in which the main vessel lumen and the lumen of the branch were continuous as shown in Figure 5.5. Vessel segment endpoints were confirmed with annotations made during the IVUS recording in which the vessel probe position could be seen relative to the conventional angiogram. Although vessel segment lengths from IVUS could be calculated from the frame index, imaging frame rate, and pullback rate, these were not used for the gold standard length because the IVUS probe follows the path of the guide wire, not the vessel centerline. These lengths did serve as a cross check for those obtained from the CCTA to confirm that the same branches were being used for segment endpoints.

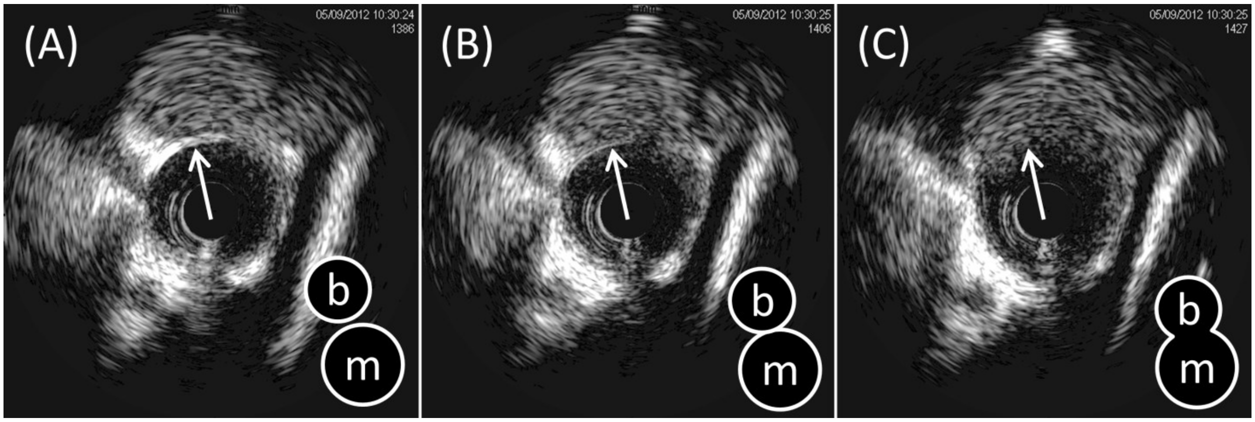

Figure 5.5 – Branch Carina Location in IVUS Images.
(A) Distal to the branch, tissue separating the main vessel and the branch vessel is apparent (arrow). (B) As the IVUS probe is withdrawn, the separation between the main and branch vessel thins. (C) The branch location is recorded as the most distal frame in the cardiac gated sequence where there is no visible separation between the lumen of the main and branch vessels. The diagrams in the lower right corner of each image illustrate the proximity of the branch (b) and main (m) lumen.

5.2.3.2 Length Measurements from CCTA

Analysis of the CCTA images was performed on a GE Advantage W Workstation (GE Healthcare, Waukesha, WI). Vessel lengths were measured at end-diastole by analyzing images reconstructed at 75% R-R interval. Using the vessel segmentation tools built into the Volume Viewer application, semi-automated 3D centerline tracing of the LAD and LCx was performed by identifying the distal end of the vessel and the branch point from the left main. Curved reformatted images of the LAD and LCx were generated based on the 3D centerlines, which presented the vessel as 2D cut plane through a “straightened” 3D vessel volume, as shown in Figure 5.6. From these images, the position of the distal edge of each branching vessel was manually identified and recorded as a function of length along the 3D centerline using the built-in measurement tools. The distances between each of these reference points served as the segment length ground truth values after cross checking the segment lengths against IVUS.

5.2.3.3 Segment Measurements using SBDX Vessel Sizing

SBDX images were first reviewed for suitability prior to executing the vessel sizing method on arterial segments. SBDX image frames were excluded unless the following criteria were met: 1) the coronary artery was filled with iodinated contrast, 2) two or more branches were clearly visible, 3) the image was free from artifacts, and 4) the heart was at end-diastole. For the first two experiments which used prospective ECG gating, each image that met these requirements was analyzed. For the third experiment, in which real-time recording was available, the image frame from each heartbeat that was closest to 75% R-R was analyzed.

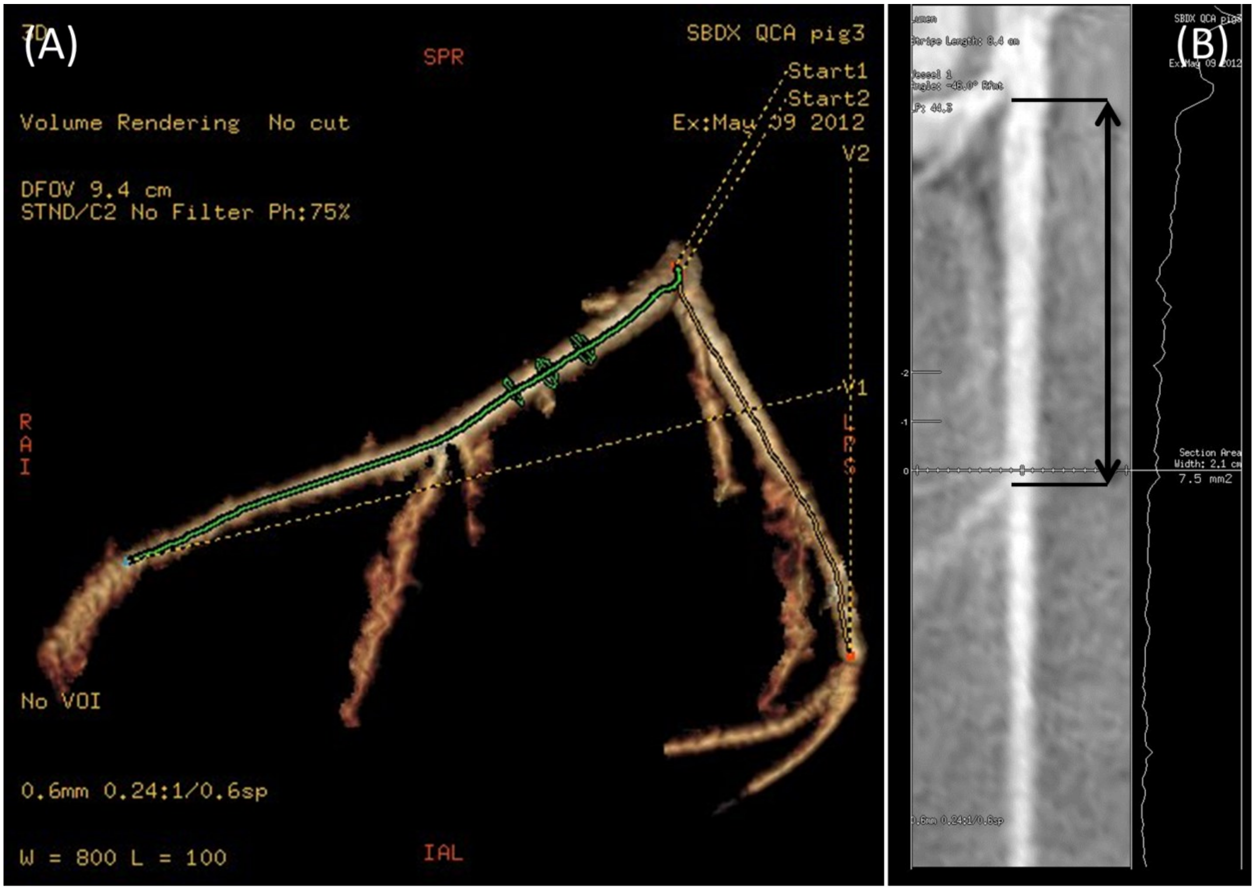

Figure 5.6 – Length Measurements from CCTA.
(A) Coronary vessels were segmented from the CT volume. Three-dimensional centerlines of the LAD and LCx were defined using semi-automatic methods. (B) Curved reformats of the coronary vessels were used to make length measurements between branch points.

For each valid image frame, a vessel dependent multiplane composite was created. For each of the left coronary arteries (LAD and LCx), the plane of best focus was manually identified out of the 32 plane image stack. Then, a multiplane composite was constructed using a subset of 16 planes centered symmetrically about the plane of best focus for that particular vessel. Analysis of the LAD and LCx may have been performed using different multiplane composites, depending on the view angle.

Using the multiplane composite, the location of each vessel branch was identified. The points along the approximate 2D centerline of the vessel corresponding to the distal carina of the branching vessel were manually identified and recorded for each image frame. In addition, the most proximal and distal points along the LAD and LCx were recorded. Using the full vessel endpoints, the SBDX vessel sizing algorithm was applied, resulting in 3D length and diameter measurements of the entire vessel as a function of position along the 2D vessel centerline. Measurements for individual segments were performed by finding the points on the full 2D vessel centerline closest to the user defined segment endpoints, calculating the 3D segment length from the corresponding range on the full 3D vessel centerline, and extracting diameter measurements over the range defined by the segment endpoints. Figure 5.7 shows the steps of SBDX vessel sizing measurements.

The parameters used in the SBDX vessel sizing algorithm were set to their default values as described in Chapter 3. Regarding the diameter measurements in particular, a moving average filter was applied to the perpendicular vessel profiles prior to the model-based diameter measurement. Given that the vessel profiles were extracted at 1 pixel increments along the 2D centerline, the moving average filter was 31 samples long, and the approximate pixel size was 0.161 mm, the diameter results can be considered an average diameter over approximately 5 mm of vessel length.

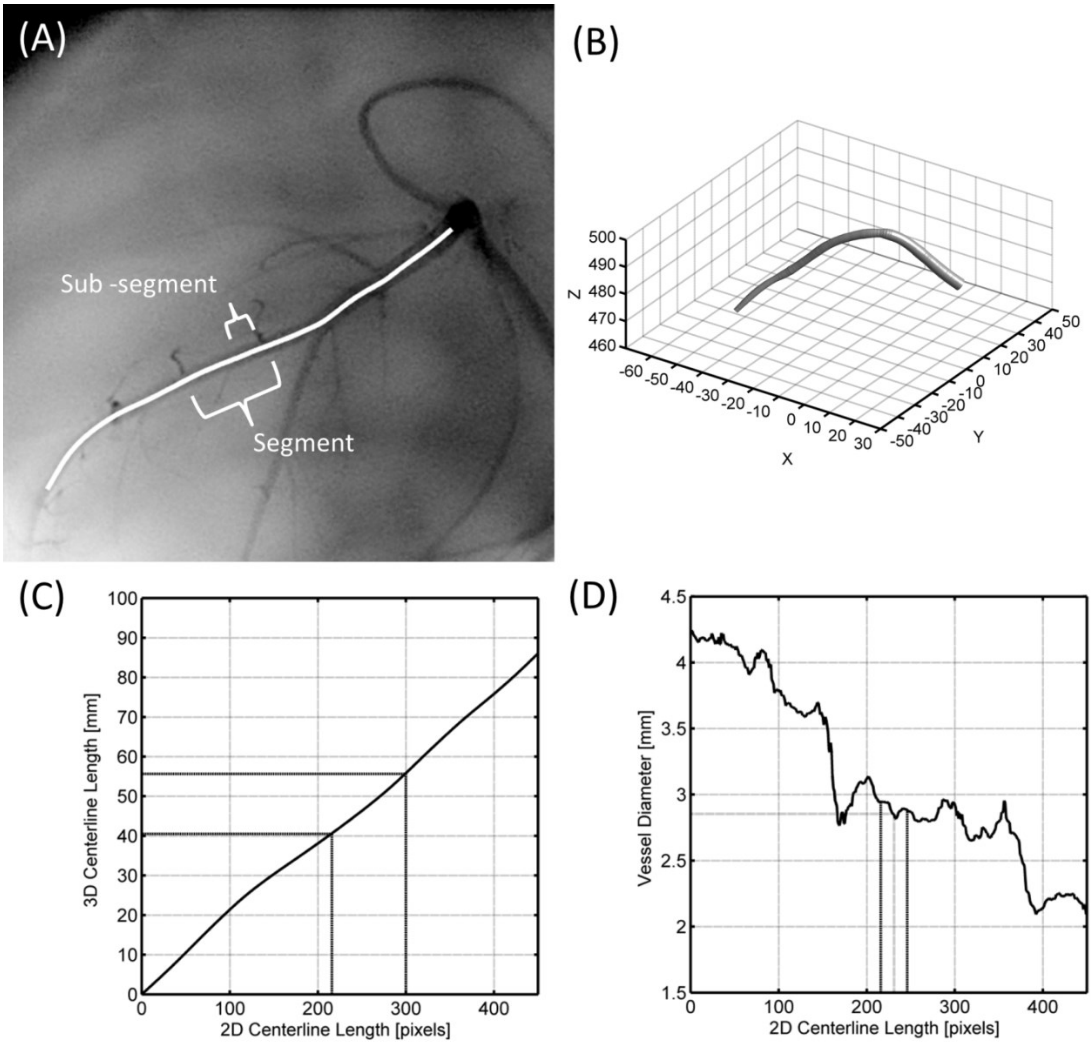

Figure 5.7 – Length and Diameter Measurements from SBDX

(A) Vessel segment endpoints were defined by side branches. Segment lengths were compared to CCTA measurements. Sub-segments were defined as approximately 5 mm lengths of full segments. Average vessel diameter within a sub-segment was compared to the average IVUS diameter over the same region. (B) A surface rendering of the vessel sizing algorithm result shows the trajectory of the 3D centerline. (C) The segment length in physical units was calculated as the arclength of the 3D centerline over the segment region. (D) SBDX intensity profiles were averaged over the length of the sub-segment prior to calculating the diameter, so the physical diameter of the sub-segment was equal to value at the center of the sub-segment region.

5.2.4 Vessel Segment Comparison and Statistical Analysis

Vessel segments of the LAD and LCx were defined in each image frame based on the vessel branches that were positively identified in the image. In order to test segments with a range of lengths, segments were defined by each possible pair-wise combination of branches as shown in Figure 5.8. Thus, the longer segments were made up of one or more smaller segments.

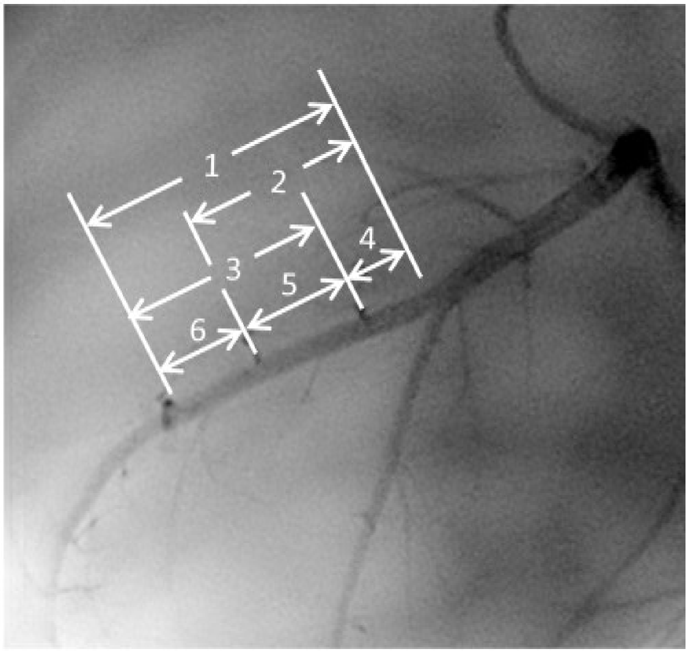

Figure 5.8 – Segment Combinations for Length Measurements.
To measure vessel segments over a range of lengths, adjacent segments were combined to create larger segments. Here, three adjacent segments can be combined to form segments with 6 different lengths.

For each of these segments the segment length from SBDX was compared to the segment length from the CCTA and the length error was calculated. The average length error and standard deviation were calculated for each segment within each experiment and across all experiments as a whole. The least squares linear regression between CCTA and SBDX lengths was calculated to determine the linear relationship between the two methods. Pearson's correlation coefficient was calculated to measure the correlation between the two techniques. SBDX-derived results were plotted against the CCTA results as a calibration curve to show the correlation between the two methods.

Vessel diameters calculated with SBDX were compared to the IVUS diameters calculated using the lumen area and minimum diameter method. For this purpose, each vessel was divided into 5 mm long, non-overlapping sub-segments. The SBDX diameter measurement from the point in the middle of the sub-segments corresponded to the average diameter over that segment due to the length of the moving average filter applied to the profiles prior to applying the model-based method (See Figure 5.7D). This sub-segment analysis was only performed on segments created from neighboring branches (i.e. segments that did not contain or overlap other segments). The SBDX diameter for the sub-segments was compared to the average IVUS diameter over the same 5 mm section of the vessel, as measured from the cardiac gated IVUS image sequence. Diameter error was calculated for each sub-segment as the difference between the SBDX diameter and IVUS diameter, where a negative error means that SBDX underestimated the diameter relative to IVUS. Similar to the length measurements, mean diameter error and standard deviation were calculated across each experiment and for all experiments together. Least squares linear regression, Pearson's correlation coefficient, and calibration curve plots were also calculated for diameter measurements.

5.3 Results

The multimodal imaging protocol was successfully completed on all three animals. Table 5.1 summarizes the acquisition of images across the different modalities. Conventional angiography and IVUS imaging were performed on the LAD and LCx of each animal, although the IVUS imaging for the LCx of Pig 2 was corrupted and could not be used. CCTA was performed on each animal without issue. SBDX angiographic images for vessel sizing analysis were acquired to varying degrees on each animal; Pigs 1 and 2 had fewer frames to analyze due to the limited frame rate of the ECG gating system for SBDX (1 frame every 2 seconds) and variability in the response of the gating system led to variability in the % R-R of individual frames. Pig 3 was imaged with the real-time acquisition system, so more frames were acquired and retrospective gating allowed for measurements consistently near 75% R-R interval.

Table 5.2 summarizes the length measurements performed based on CCTA and the SBDX algorithm. The number of measurements in each experiment varied with the number of SBDX image frames and the number of segments that could be identified in each frame. Table 5.3 compares length measurements between SBDX and CCTA. Length error was calculated as SBDX length – CCTA length. Overall, length errors were similar across all three experiments, with average errors of -0.65 ± 1.99 mm, -0.78 ± 1.90 mm, and -0.22 ± 1.42 mm. Overall error was -0.49 ± 1.76 mm. The negative mean difference between the measurements indicates that the vessel sizing algorithm tended to underestimate the true segment length. Length measurements correlated strongly between the two methods with correlation coefficients of 0.99

in all cases. Least squares line fits between the SBDX and CCTA length data had near unity slope. Figure 5.9 shows this strong relationship graphically.

			SBDX Acquisitions						
Pig	**IVUS Imaging**	**CCTA Successful**	**kVp**	**kWp**	**Scan Rate [frames/sec]**	**Rotation [°]**	**Orientation [°]**	**Num Frames**	**Mean % R-R**
1	LAD, LCx	Yes	90	19	15	20 LAO	0	5	83
			90	19	15	30 RAO	0	4	67
			120	24	15	30 RAO	0	6	73
2	LAD Only	Yes	100	21	15	18 RAO	10 CAU	7	64
			120	24	15	18 RAO	10 CAU	2	88
			100	21	15	32 LAO	12 CAU	1	60
			120	24	15	32 LAO	12 CAU	4	81
			100	21	15	0	0	3	84
			120	24	15	0	0	2	77
3	LAD, LCx	Yes	120	24	15	30 LAO	10 CAU	1	76
			120	24	10	30 LAO	10 CAU	4	74
			100	21	15	30 LAO	10 CAU	5	76
			100	21	15	30 LAO	10 CRA	4	76
			120	24	15	30 LAO	10 CRA	4	75
			120	24	10	30 LAO	10 CRA	4	73
			120	24	15	30 RAO	25 CAU	5	75
			100	21	10	30 RAO	25 CAU	4	77
			100	21	15	30 RAO	25 CAU	6	75

Table 5.1 – Summary of Multimodal Image Acquisition.

Pig	Num Seg	Num Meas	SBDX Length [mm]	CCTA Length [mm]
1	24	145	24.79 [3.74, 62.52]	25.44 [6.10, 59.40]
2	16	99	31.58 [4.41, 73.80]	32.36 [6.60, 72.50]
3	10	185	21.23 [7.36, 46.57]	21.45 [8.50, 46.50]
All	50	429	24.82 [3.74, 73.80]	25.32 [6.10, 72.50]

Table 5.2 – Summary of Length Results.

Length measurements presented as mean [min, max].

Pig	Num Meas	Length Error [mm]	Linear Fit	Pearson Correlation (r)
1	145	-0.65 ± 1.99	y = 1.00x + 0.60	0.99
2	99	-0.78 ± 1.90	y = 1.00x + 0.76	0.99
3	185	-0.22 ± 1.42	y = 1.01x + 0.11	0.99
All	429	-0.49 ± 1.76	y = 1.01x + 0.34	0.99

Table 5.3 – Comparison of Length Measurements.

Error was calculated as SBDX length – CCTA length and presented as mean ± 1 standard deviation. Linear fit assumes y = CCTA length and x = SBDX length.

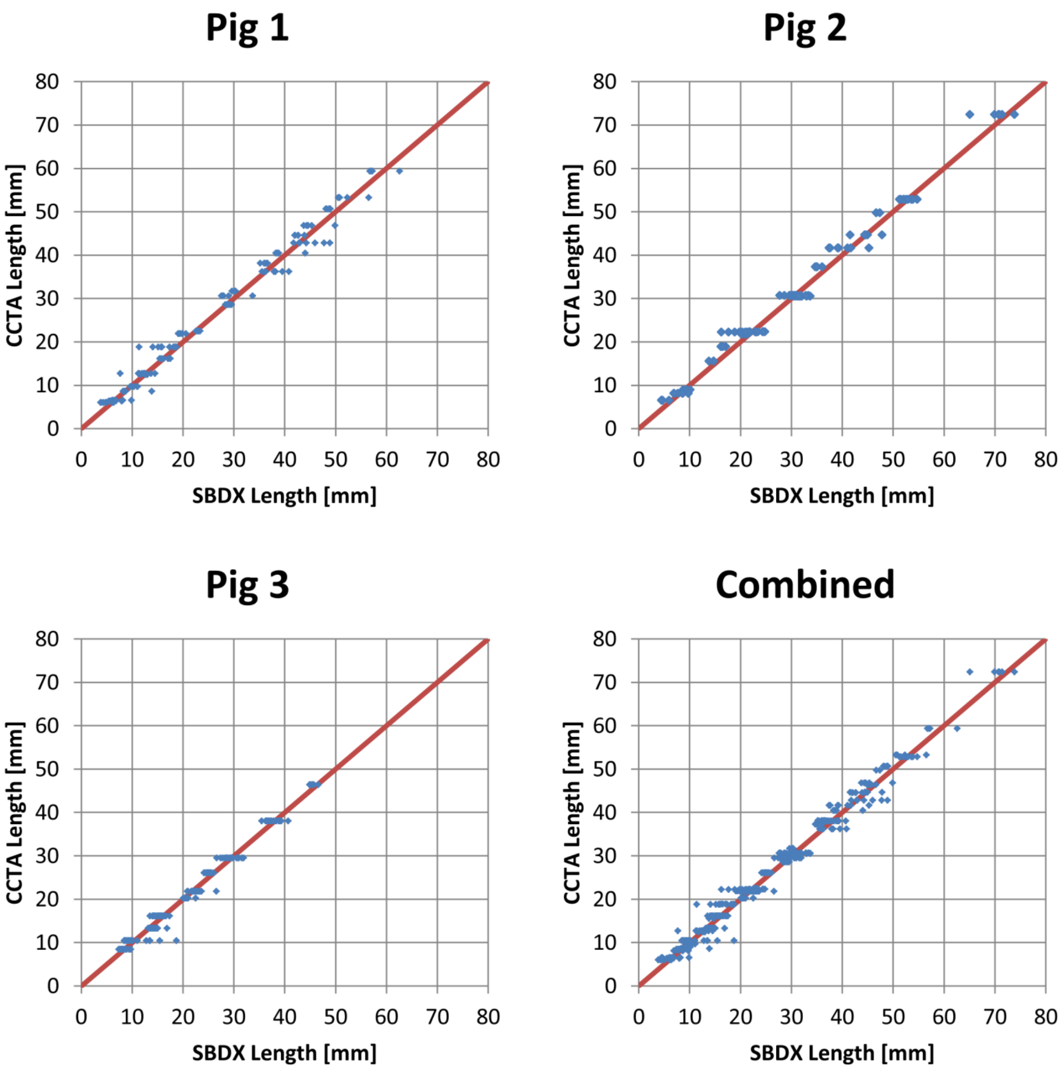

Figure 5.9 – SBDX Length Measurement Compared to CCTA.

SBDX lengths from the vessel sizing algorithm are plotted against ground truth (CCTA) measurements. Line represents unity slope.

The mean and standard deviation of the length errors were slightly lower for the third experiment. The third experiment used real-time recording with retrospective determination of R-R interval, which produced more consistent end-diastolic frames than the prospective gating used in the first two experiments. This, in turn may have led to results more consistent with the CCTA, which was reconstructed at 75% R-R interval.

To demonstrate the ability of the proposed algorithm to calculate segment length in the presence of foreshortening, segment lengths were calculated using a conventional, 2D approach and compared to lengths from CCTA. First, the length of the segment's 2D centerline was calculated in terms of pixels. In lieu of a calibration object to calculate the vessel magnification, the 3D centerline was used. The depth of the segment's 3D centerline was calculated by sampling the 3D centerline at regular intervals. The average depth was used to calculate the magnification of the segment and scale the 2D centerline length from pixels to physical units. Figure 5.10 shows a comparison of length results calculated using the 3D centerline only and using the 2D centerline plus the mean depth. The segment lengths computed using the 2D centerline correlated with the CCTA measurements but tended to underestimate the true length due to foreshortening. Table 5.4 summarizes length errors when using the 2D centerline. On average, the 2D method underestimated the vessel segment length by several millimeters. Comparing these results to the 3D method, which had average errors less than 1 mm, the vessel sizing method was more accurate than conventional 2D methods for measuring vessel length.

Pig	Num Meas	Length Error (3D) [mm]	Length Error (2D) [mm]	Mean Foreshortening
1	145	-0.65 ± 1.99	-1.78 ± 1.63	8%
2	99	-0.78 ± 1.90	-5.79 ± 6.69	17%
3	185	-0.22 ± 1.42	-1.97 ± 1.74	9%
All	429	-0.49 ± 1.76	-2.79 ± 3.89	11%

Table 5.4 – Comparison of 3D to 2D Length Measurement Error.

In addition to the 3D centerline-based method, vessel segment lengths were calculated using the length of the 2D segment centerline (in pixels) and the average magnification of the vessel segment, similar to conventional QCA methods. Overall, the 2D method was less accurate and less precise than the 3D method. Foreshortening was calculated as $1 - \frac{\text{2D Length}}{\text{CCTA Length}}$.

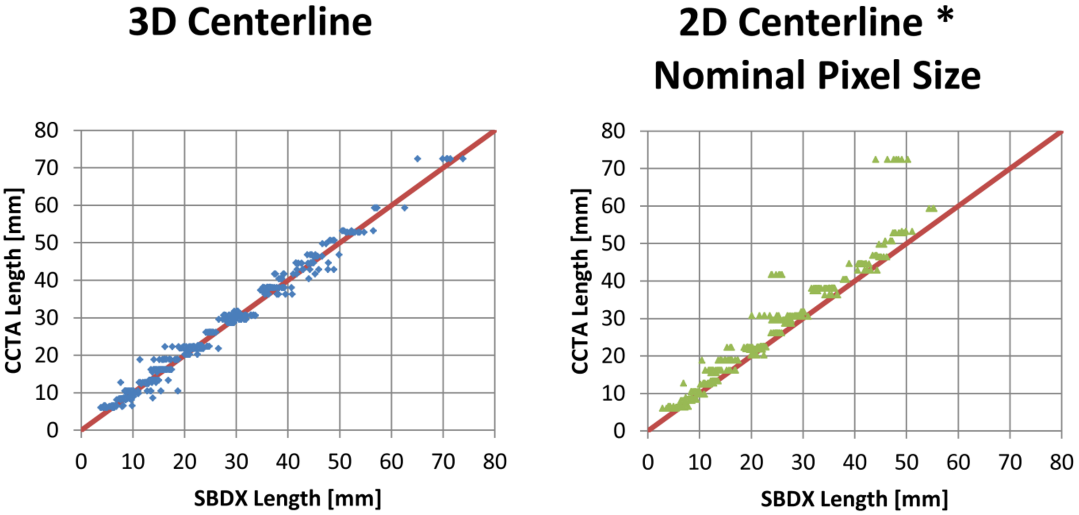

3D Centerline

2D Centerline * Nominal Pixel Size

Figure 5.10 – 3D Length to 2D Length Measurement Comparison.

On the left are length results derived from the 3D centerline of the vessel sizing algorithm. On the right is the product of the length of the 2D centerline from each segment multiplied by the pixel size of an image plane located at the average depth of the segment (as determined by the 3D centerline). Large deviations from the unity slope line are likely due to vessel foreshortening.

Diameter measurements using SBDX and comparisons to measurements with IVUS are summarized in Table 5.5. The results were similar across all three experiments. The measurement differences between SBDX and IVUS are shown in Table 5.6. When using the "area" method for IVUS diameter, mean differences with SBDX were -0.18 ± 0.29 mm, -0.09 ±

0.28 mm, and -0.15 ± 0.24 mm, respectively, with the overall difference of -0.14 ± 0.26 mm. The mean difference for each experiment was negative, indicating SBDX underestimated the IVUS diameter when the IVUS lumen area was used to calculate the diameter. Using the minimum diameter from the IVUS lumen segmentation, the mean differences compared to SBDX were -0.02 ± 0.28 mm, 0.11 ± 0.27 mm, and 0.09 ± 0.26 mm, with an overall difference of 0.07 ± 0.27 mm. In contrast to the "area" method for IVUS diameter calculation, SBDX slightly overestimated the diameter relative to IVUS when the minimum lumen diameter was used. The relationship between the sign of the mean difference and the IVUS diameter measurement methods was as expected. Based on mean error, the SBDX diameter measurements agreed better with the IVUS measurements calculated using the minimum diameter method.

Pig	Num Sub-Segments	Num Meas	SBDX Diameter [mm]	IVUS Diameter (Area) [mm]	IVUS Diameter (Min) [mm]
1	10	71	2.51 [2.08, 3.13]	2.69 [2.23, 3.04]	2.53 [2.06, 2.89]
2	12	104	2.69 [1.93, 3.62]	2.77 [2.42, 3.90]	2.58 [2.24, 3.60]
3	11	172	2.92 [2.27, 3.86]	3.07 [2.71, 3.64]	2.83 [2.32, 3.42]
All	33	347	2.76 [1.93, 3.86]	2.90 [2.23, 3.90]	2.69 [2.06, 3.60]

Table 5.5 – Summary of Diameter Measurements
Diameter measurements presented as mean [min, max].

	IVUS (Area)			IVUS (Min)		
Pig	Diameter Error [mm]	Linear Fit	Pearson Correlation (r)	Diameter Error [mm]	Linear Fit	Pearson Correlation (r)
1	-0.18 ± 0.29	y = 1.06x	0.24	-0.02 ± 0.28	y = 1.00x	0.26
2	-0.09 ± 0.28	y = 1.03x	0.82	0.11 ± 0.27	y = 0.95x	0.83
3	-0.15 ± 0.24	y = 1.05x	0.51	0.09 ± 0.26	y = 0.97x	0.47
All	-0.14 ± 0.26	y = 1.04x	0.72	0.07 ± 0.27	y = 0.97x	0.70

Table 5.6 – Comparison of Diameter Measurements
Error was calculated as SBDX diameter – IVUS diameter and presented as mean ± 1 standard deviation. Linear fit assumes y = IVUS diameter and x = SBDX diameter. Due to the narrow range of diameters measured, the linear fit was constrained to go through the origin.

Figure 5.11 and Figure 5.12 show the diameter results graphically. Data points were clustered around the unity slope line. The plots in Figure 5.12 appear similar to those in Figure 5.11, with the distributions results in Figure 5.12 shifted slightly down relative to the in Figure 5.11. Due to the limited range of vessel diameters measured, the linear fit line was forced through the origin, resulting in line slopes near unity. Without forcing the linear fit through the origin, the slopes of the lines were much less than one. For each sub-segment, one IVUS measurement was compared to multiple SBDX measurements because multiple SBDX images of the same sub-segment were measured. When plotted as shown in Figure 5.11, this one-to-many comparison appeared as horizontal clusters, which would skew the linear fit model to have a more horizontal slope (i.e. a slope less than one). Ideally, one IVUS measurement would be compared to one SBDX measurement, but time required for multiple IVUS acquisitions and the increased risk of complications (mainly thrombosis formation) made multiple IVUS measurements not feasible.

The correlation between IVUS and SBDX diameter measurements was relatively weak as indicated by the Pearson's correlation coefficient, ranging from 0.24 to 0.83. This may also be due to the experiment and not the method being tested. Within each experiment, most of the vessel sub-segments measured had similar diameters, ranging between 1.93 and 3.86 mm. Given that the variability (standard deviation) in the diameter error is about 0.25 mm, the data form a cloud around the unity slope line. Compare this to the length data shown in Figure 5.9, where the variability is on the order of 2 mm, but the measurements span a range of about 70 mm. To better characterize the correlation between the two measurements, a wider range of vessel diameters would need to be imaged with the two modalities.

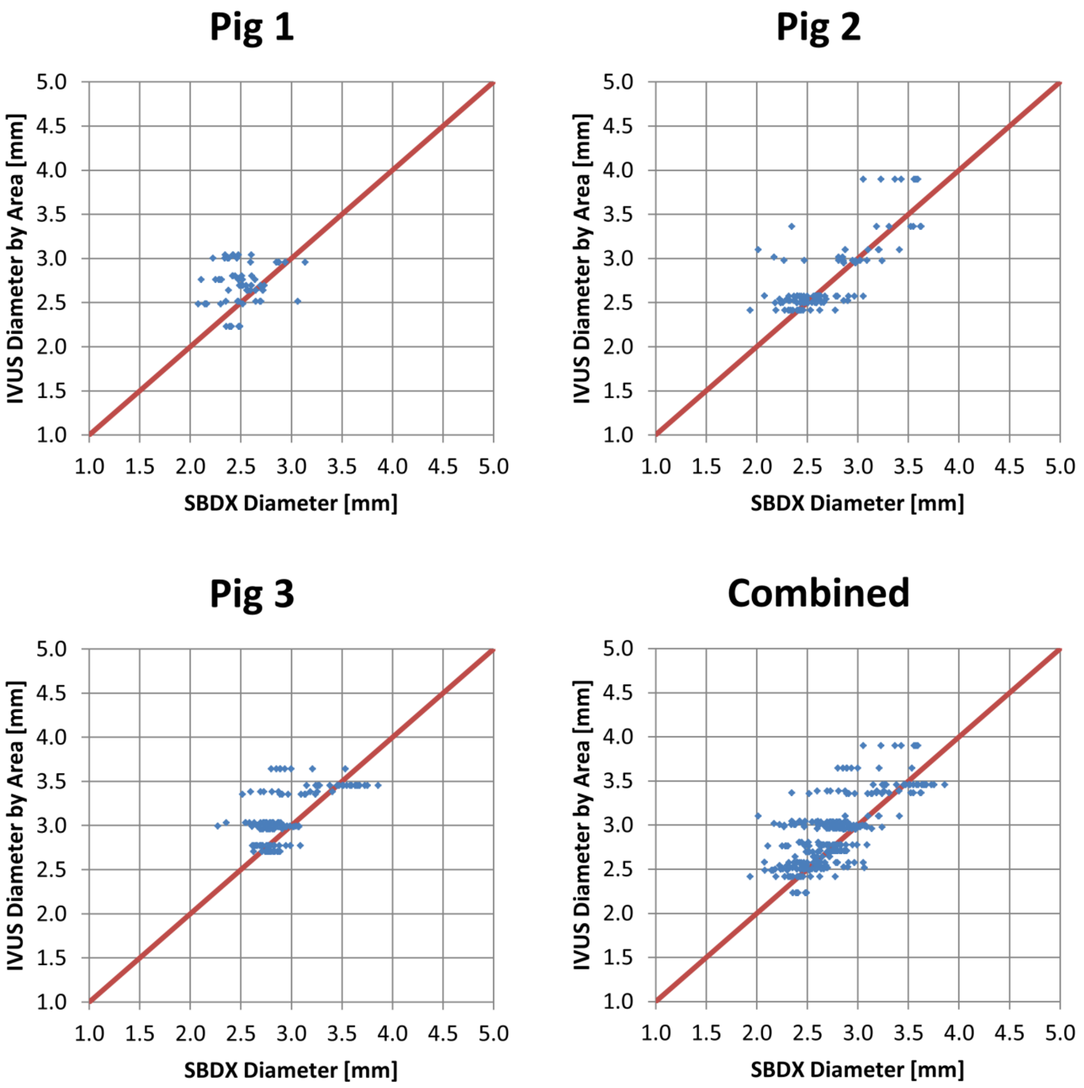

Figure 5.11 – Diameter Measurements from SBDX Compared to IVUS Calculated from Cross Sectional Area.

Vessel diameters calculated using the vessel sizing algorithm are plotted against the average IVUS diameter, which is derived from cross sectional area of the segmented lumen. The line represents unity slope.

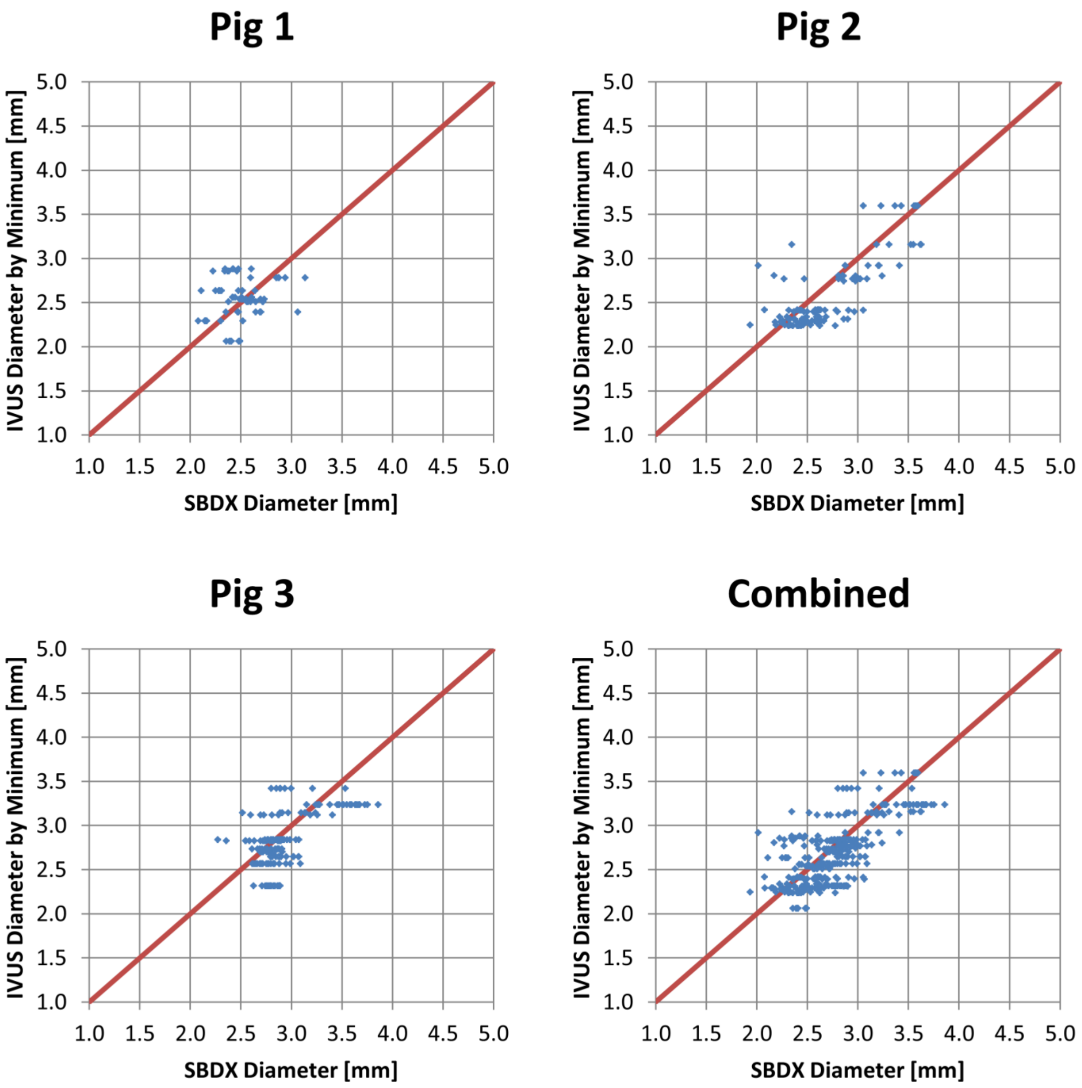

Figure 5.12 – Diameter Measurements from SBDX Compared to IVUS Calculated from Minimum Diameter. Vessel diameters calculated using the vessel sizing algorithm are plotted against the average IVUS diameter, which is derived from the minimum diameter across the segmented lumen. The line represents unity slope.

The number of segments analyzed in each image varied due to a number of factors. Not all SBDX angiographic views enabled clear identification of the bifurcation carina, which served as the reference points between the different modalities. Motion blur and incomplete filling of the vessel with iodinated contrast also limited our ability to identify reference branch points. IVUS imaging was limited by the extent to which the probe could be guided into the distal regions of the vessel without occluding the vessel. Consequently, only the proximal portions of the LAD and LCx were imaged with IVUS. In contrast, the CCTA provided length measurements over the entire coronary artery tree. Many length measurements were performed on vessel segments to which there was no corresponding IVUS imaging.

5.4 Discussion

The SBDX vessel sizing algorithm accurately measured both vessel length and diameter in a healthy swine model with sub-millimeter accuracy. On average, length measurements with SBDX were within 0.49 mm of the result obtained with CCTA. Diameter measurements with SBDX were on average within 0.14 mm or 0.07 mm of measurements performed with IVUS, depending on how the IVUS diameter was calculated. Given that interventional devices come in length increments of 4-5 mm and diameter increments of 0.25 mm, SBDX vessel sizing should be accurate enough to guide an interventionalist to select a device that matches vessel dimensions. The variability of the measurements (quantified by the standard deviation of the error) was 1.97 mm for the length and 0.26-0.27 mm for the diameter. These values represent the uncertainty of a measurement from a single image frame. With the algorithm fully automated (after the user identifies the segment of interest), the results of multiple image frames could be averaged together to improve the precision.

The measured variability of vessel measurements with SBDX depended on a number of factors, some of which are not related to the algorithm itself. In these experiments, each vessel was measured only once using the gold standard method (CCTA for length, IVUS for diameter). To put the variability of SBDX measurements into perspective, the multiple gold standard measurements of the same vessel would need to be performed to calculate the statistical variability of those modalities and compare to the SBDX method.

Some of the diameter errors may be attributed to the fact that IVUS and SBDX imaging were not performed at the same point in time. Physiological changes over the course of the experiment may have caused vessel dimensions to vary between modalities. This potential problem would be easily addressed once real-time reconstruction and display is available for the current generation of SBDX hardware. This would allow IVUS imaging to be performed under SBDX guidance, followed immediately by SBDX angiography for vessel sizing, minimizing the time discrepancy between the two measurements.

While some physiologic changes in the animal model are out of the investigators control, special care should be taken by the investigators to ensure consistent conditions for imaging with each modality. Regularly administering vasodilators such as intracoronary nitroglycerine before each measurement will keep the vessel maximally dilated for each acquisition. Attention must also be paid to the contrast injections to ensure that filling of the vessels is consistent between angiographic runs. Previous studies have shown that the accuracy and precision of conventional

QCA measurements is reduced when the concentration of contrast media is less than 100% [27, 57-60]. Vigilance to these details may help reduce errors in vessel measurements.

The accuracy and precision of length measurements made with the SBDX vessel sizing algorithm were dependent on the user's ability to accurately identify the distal carina of each branch in each angiographic view. This presents two limitations on our ability to validate the proposed algorithm. First, this introduces a source of error that is not due to the algorithm itself but due to the user of the algorithm. This would affect any QCA-like algorithm being tested. Second, these points are most conspicuous when the plane of the bifurcation is parallel to the image plane (i.e. the vessel is not foreshortened). One of the strengths of the SBDX vessel sizing algorithm is its ability to accurately measure the lengths of foreshortened vessels, but this is difficult to demonstrate *in vivo* because it is difficult to identify branch points on foreshortened vessels. A potential solution to both issues is to measure the length of an objected embedded in the coronary arteries, which has discrete end points and a fixed, well defined length. This has been done *in vivo* by measuring catheters with discrete markers [37] and deployed stents with known dimensions [68, 94, 95]. By measuring well defined, discrete objects within the coronary arteries the algorithm's ability to measure the length of foreshortened vessels *in vivo* can be tested while reducing the influence of operator errors.

5.4.1 Sizing Results as a Function of Vessel SDNR

In Chapter 4, the relationship between the vessel signal difference to noise ratio (SDNR) and algorithm accuracy and precision was demonstrated using phantoms. To determine if those relationships hold true *in vivo*, the SDNR of each segment was calculated, and length and diameter errors were examined as a function of vessel SDNR. For each segment, the mean signal difference was calculated from perpendicular intensity profiles of the vessel and averaged across image frames. The noise component for a given segment was calculated from subtraction images between phase-matched frames. The pixel variance within an ROI defined within a flat region near the segment was measured on each subtraction image. The noise was calculated as the square root of one half of the variance and averaged across all difference images. The errors of length and diameter measurements were grouped into bins according to SDNR using a bin width of 0.5. For all of the measurement errors in each bin, the mean and standard deviation were calculated and plotted against SDNR. In Figure 5.13, the length error mean and standard deviation were plotted using all of the segments, which showed that the mean length error was relatively flat over SDNRs between 2 and 8. The length error standard deviation was steadily decreasing as SDNR increased over the same interval. To better match the conditions of Chapter 4, where only 30 mm segments were measured, the analysis was narrowed to segments with a CCTA length between 20 and 40 mm. The resulting plots, also shown in Figure 5.13, show a similar trend.

A similar analysis of the *in vivo* diameter error was performed as shown in Figure 5.14. The relationship between mean diameter error and SDNR was similar for both methods of calculating the vessel diameter from IVUS (lumen area and minimum diameter), with the only notable difference being the IVUS minimum diameter results being offset by about 0.1 mm relative to the IVUS lumen area results. Both curves show that the SBDX algorithm underestimated the vessel diameter at low SDNR, differing from the phantom results that showed overestimation at low SDNR. Both curves show that the mean error flattens with increased SDNR. The curves showing the standard deviation versus SDNR were nearly identical despite the different IVUS measurement method. Both cases showed that diameter error variability decreased as SDNR increased.

In general, the average error and variability showed similar trends *in vivo* and in phantoms (both decreased in magnitude as SDNR increased), but the magnitudes were greater *in vivo* than in phantoms for the same SDNR. Differences in the mean error between phantom and *in vivo* studies may be due in part to errors in the *in vivo* ground truth measurements, which were more variable than the caliper measurements of the MgCd vessel phantom wires. Increased variability of *in vivo* errors may be due to cardiac motion, overlapping anatomy, and different SBDX operating points (kV, frame rate). In addition, fewer samples were used to calculate the mean and standard deviation for each SDNR bin than were used in the phantom study presented in Chapter 4 (tens of samples versus hundreds). This created more variability in the mean and standard deviation curves. Some of the variability could be reduced in the experimental design by performing “gold standard” imaging of the same animal multiple times (repeated CCTA and IVUS measurements). However, increasing the amount of imaging would come at the expense of increased time under anesthesia and iodinated contrast load, and significantly increased time between gold standard and SBDX imaging.

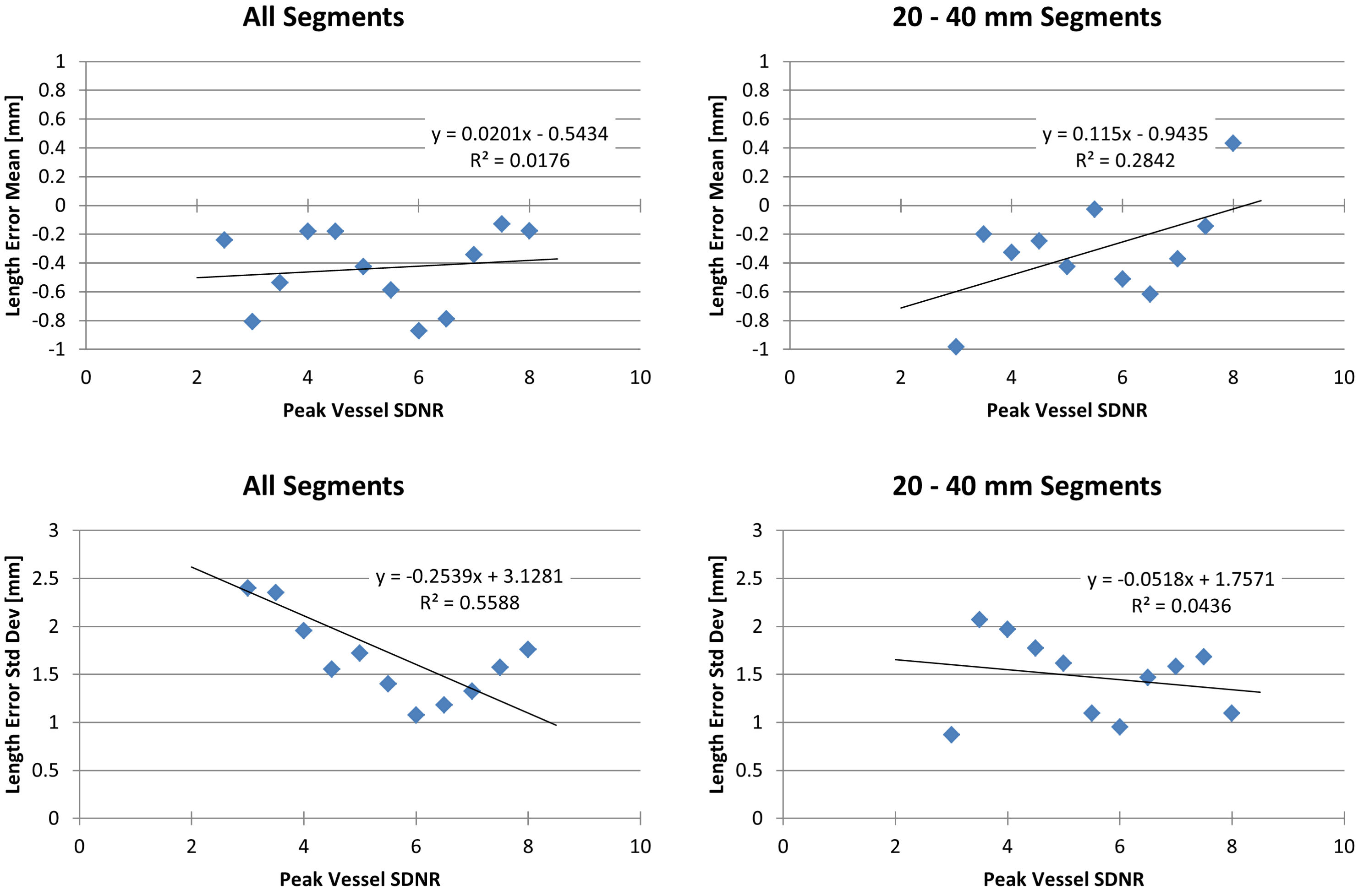

Figure 5.13 – Length Error Mean and Standard Deviation Versus Binned Vessel Peak SDNR

Length measurements were binned according to vessel SDNR (bin size of 0.5). For each bin, the mean (top) and standard deviation (bottom) of the length error was calculated. The plots on the left were created using segments of all lengths. The plots on the right used only segments whose CCTA length was between 20 and 40 mm for comparision to similar plots in Chapter 4, where the segment length was 30 mm.

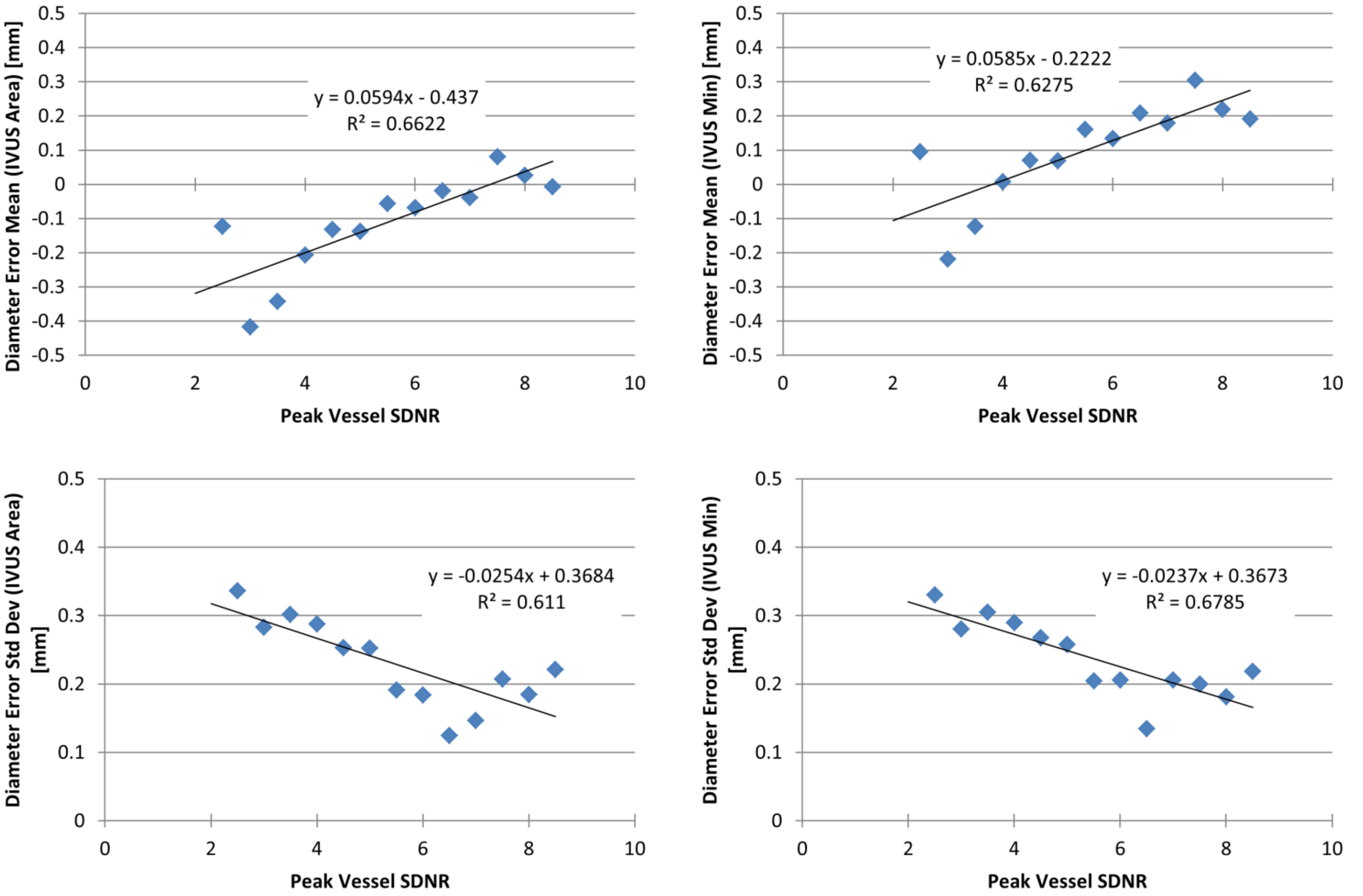

Figure 5.14 – Diameter Error Mean and Standard Deviation Versus Binned Peak Vessel SDNR

Diameter measurements were binned according to vessel SDNR (bin size of 0.5). For each bin, the mean (top) and standard deviation (bottom) of the diameter error was calculated. Results are shown using the IVUS diameter measurements based on the lumen area (left) and minimum diameter (right).

5.4.2 Comparisons to Other Studies

Other groups have compared diameter measurements *in vivo* between conventional QCA and IVUS. Davies et al. [83] showed a that conventional QCA underestimated vessel diameter by 0.12 ± 0.37 mm and 0.02 ± 0.34 mm (mean ± 1 standard deviation), when one or two angiographic views are used, respectively. Sinha et al. [86] measured differences between QCA and IVUS of 0.02 ± 0.12 mm, 0.04 ± 0.15 mm¸ 0.17 ± 0.23 mm, and 0.19 ± 0.17 mm, depending on the distance from the ostium of the artery. In both studies, the minimum IVUS diameter was compared to the QCA result. For the same type of measurement, the SBDX vessel sizing algorithm had a mean difference of 0.07 ± 0.28 mm, which put its accuracy and precision on par with existing methods.

5.4.3 Limitations and Future Work

Characterizing the relationship between diameter measurements with IVUS and SBDX was limited by the similar vessel sizes found all three of the animals imaged. Only juvenile swine were used in this study; using animals of different ages and sizes would provide a greater variety in coronary vessel sizes. Within the same animal, measuring both peripheral and coronary vessels would provide a wider range of vessel sizes; however the peripheral vessels are stationary and would not present the real-world challenge of imaging the heart.

In clinical practice this method would be used to measure the length of a stenosis, not a healthy vessel segment. Testing the algorithm on actual stenoses presents challenges when animal models are used. The typical animal models used to examine coronary arteries are too young to have any natural coronary artery disease. It is possible to create an artificial stenosis *in vivo* by inserting an object into the coronary artery (in which case the dimensions are known) [75-77] or surgically implanting a device outside of the artery to narrow the vessel lumen [79, 96, 97]. These methods require more surgical prep and may increase the risk of complications during the study. A more ideal situation would be to evaluate SBDX vessel sizing in true clinical interventions. This would allow for retrospective studies over a wide patient population with various levels of coronary artery disease, as has been done by other groups [83, 84, 88, 89, 98]. The *in vivo* study presented in this paper provides a necessary intermediate step towards this type of clinical validation.

5.5 Conclusion

The SBDX vessel sizing algorithm provides accurate measurements of vessel segment length and diameter *in vivo*. These measurements were performed from single angiographic frames, and without requiring magnification calibration, which makes this method more convenient than the current gold standard of IVUS. Clinically, this method could be used to guide or verify interventional device size selection to increase procedure efficiency, lower costs, and potentially improve outcomes.

Chapter 6 – Conclusions and Future Work

The work presented in this dissertation demonstrates the clinical potential for calibration-free vessel sizing using the tomosynthetic imaging capabilities of Scanning Beam Digital X-ray (SBDX) technology. The initial proof-of-concept study demonstrated the technique using a bare-bones algorithm, vessel phantoms, and near-ideal imaging conditions. This study demonstrated that the depth localization principle could indeed be used to overcome the limitations of conventional projection-based quantitative coronary angiography (QCA) by eliminating the need for a calibration object and non-foreshortened views. This feasibility study was followed by a redesign of the algorithm to improve its robustness against image noise and complex image scenes and to minimize required user interaction. The performance of the revised algorithm was then tested in detail using vessel phantoms to characterize the conditions under which valid vessel measurements can be expected and to quantify the accuracy and precision of the measurements assuming those conditions are met. It was concluded that the peak vessel signal difference to noise ratio (SDNR) should be at least 2 and vessel foreshortening angles should be limited to 45° in order to ensure sub-millimeter accuracy of both diameter and length. Finally, we demonstrated the accuracy of the algorithm *in vivo*, where cardiac motion, respiratory motion, and a heterogeneous background created clinically realistic imaging conditions. In these *in vivo* studies, the results of the vessel sizing algorithm agreed with "gold standard" measurement methods (IVUS, CCTA) with sub-millimeter accuracy on average. This progression of studies has shown that this technique has the potential to be a fast and accurate tool for measuring coronary vessels.

Several areas of future research were suggested by the results of this work. The studies presented in Chapter 4 (Vessel sizing vs. SDNR) offered a great deal of insight into the behavior of the vessel sizing algorithm under different imaging conditions and geometries. These results, as well as those presented in Chapter 5, were obtained using a single set of algorithm parameters. The parameters control various aspects of algorithm behavior such as the degree of the smoothness enforced on 2D and 3D contours, the stopping conditions for iterative optimization steps, and the sizes of filtering kernels and regions of interest. The parameter set that was used was selected because it performed well over a range of imaging scenes. However an exhaustive search over parameter space under all imaging scenarios could conceivably yield a better set of parameter values. Additionally, it was noted that the accuracy of length measurements was dependent on the apparent length of the vessel. This suggested that there should be a minimum requirement for the apparent length of a vessel segment and that the minimum requirement is dependent on the vessel SDNR.

The SBDX images used in this work did not have any post-processing applied to reduce image noise or enhance vessel signal. Commercial systems regularly employ post-processing methods, for example temporal filtration fluoroscopic mode [99], or feature-preserving spatial filtration in angiographic mode [100, 101]. How image processing might affect the vessel sizing algorithm performance remains an open question. To the extent that noise can be reduced without significantly altering vessel signal integrity, it may be possible to obtain the current performance at lower pre-processing SDNR levels.

Although validation with animal models is an important translational step, testing the algorithm on clinical images of human hearts with actual coronary artery disease is the ultimate validation. A study of this type would likely follow the same format of the animal validation, comparing results of the vessel sizing algorithm to those obtained from “gold standard” imaging. Once a clinical SBDX system is available, this type of study could be performed retrospectively using patients that have already undergone a diagnostic CCTA, coronary angiography (with SBDX) and IVUS imaging performed as part of a routine intervention. After the algorithm has been validated in humans, it could be incorporated into the clinical workflow to help guide interventional tasks, such as device selection.

Prior to a clinical implementation, some work is required to develop a user interface that is appropriate for use by clinicians and cath-lab technologists. For this, existing QCA packages provide a good template. The interface needs to allow the user to select a frame from a coronary angiogram, identify a vessel segment to be measured, and receive the results in a convenient format. To further expedite decision making, the clinical application could automatically detect the lesion and suggest an interventional device based on available sizes. The interface should be responsive and easy to use so that improves procedural flow instead of hindering it.

Although the focus of the vessel sizing algorithm was on measuring discrete segments to guide device sizing, it may have the potential to generate a full 3D model of the coronary tree. If the algorithm were designed to automatically segment the coronary tree, the 3D model could then be used to visualize the vasculature of the entire heart and gain a more complete perspective of the anatomy. The 3D model could be used to make measurements of various segments without requiring the user to select each segment individually. In addition, the geometry of the coronary tree model and imaging system could be used to suggest unobstructed views of a given coronary segment. The greatest challenge to segmenting the entire coronary tree is in differentiating between overlapping vessels and branching vessels to ensure that the individual segments are connected correctly. If such a coronary tree model could be accurately constructed from a single SBDX frame, it would have several advantages over other methods because it requires only a single image frame. Radiation dose and iodine dose would be lowered in comparison to C-arm rotational acquisition, and all of the data used to construct the coronary tree would be acquired at a single point in time, obviating the need for retrospective ECG gating and multiple cardiac cycles.

Appendix A – Line Spread Function Model for SBDX

A key component to the model-based diameter measurement used in the vessel sizing method was an accurate estimate of the line spread function (LSF)[31]. The LSF captures the blurring inherent to the imaging system along one direction. By incorporating the LSF into the diameter measurement, a better fit is obtained between the modeled and observed vessel profile, which in turn produces more accurate vessel parameters. While this improves the diameter measurements across all vessel diameters, it is particularly important for measuring small diameter vessels (< 1 mm). For these vessels, the observed profile is dominated by the size of the LSF rather than the vessel diameter, and not accounting for the LSF results in systematic overestimation of small diameter vessels. The LSF of an x-ray imaging system (including SBDX) is dependent on a number of factors including detector element size, focal spot size and shape, source-detector distance and source-object distance. With tomosynthesis imaging, the LSF is also determined by the image plane position and the distance from the image plane to the object. Direct measurements of the LSF would require countless measurements to cover every image plane position and object position combination. A more practical solution is to model the LSF using linear systems theory and *a priori* knowledge of the imaging scene. The depth localization capability of SBDX combined with the system geometry and image formation process provides all of the necessary information to construct an accurate LSF estimate.

The LSF presented here is based on the modeled optical transfer function (OTF) of the SBDX system described in Ref. [2]. The OTF is primarily modeled as the product of several geometric and reconstruction parameters, as given by the following:

$$OTF(\xi,\eta) = F(\xi,\eta) \cdot \mathrm{sinc}(\Delta_d\xi, \Delta_d\eta) \cdot \mathrm{sinc}(r_{rest}\xi, r_{rest}\eta) \\ \cdot \mathrm{sinc}\left(\Delta_p\xi, \Delta_p\eta\right) \cdot \mathrm{sinc}\left(b_{tx}\xi, b_{ty}\eta\right) \tag{A.1}$$

where $\mathrm{sinc}(a\xi, a\eta) = \mathrm{sinc}(a\xi) * \mathrm{sinc}(a\eta)$, ξ is the horizontal spatial frequency, and η is the vertical spatial frequency. The back-projected detector element size, Δ_d, is determined by the image plane position as $\Delta_d = \Delta_D \cdot (z/Z_D)$, where Δ_D is the detector element pitch, z is the distance from the source plane to the image plane, and Z_D is the source to detector distance. The pixel size Δ_p, is given by $\Delta_p = \frac{Z_d - z}{Z_d} \cdot \frac{\Delta_S}{m}$, where Δ_S is the source position pitch, and m is a reconstruction parameter, typically set to 10. The restoration kernel r_{rest}, is typically on the order of Δ_p, (see Sections A.1 and A.2). The size of the rectangular out-of-plane blurring kernel was defined by b_{tx} and b_{ty}, where

$$b_{tx} = \frac{|\Delta z| W_D}{Z_D - z - \Delta z} \tag{A.2}$$

$$b_{ty} = \frac{|\Delta z| H_D}{Z_D - z - \Delta z} \tag{A.3}$$

Δz is the distance from the vessel centerline to the image plane along the Z direction, and W_D and H_D are the physical width and height of the detector, respectively.

The OTF component corresponding to the focal spot size and shape, $F(\xi,\eta)$, corresponds to an elliptical pillbox convolved with a 2D Gaussian in the image domain. In the frequency domain, $F(\xi,\eta)$ is given by

$$F(\xi,\eta) = 2\cdot \mathrm{jinc}\left(\sqrt{(ar_x\xi)^2 + \left(ar_y\eta\right)^2}\right)\cdot e^{-2\pi^2\left(a\sigma_x^2\xi^2 + a\sigma_y^2\eta^2\right)} \tag{A.4}$$

$$\mathrm{jinc}(X) = \frac{J_1(2\pi X)}{2\pi X} \tag{A.5}$$

$$a = \frac{z}{Z_D}\cdot\frac{Z_D - z_{CL}}{z_{CL}} \tag{A.6}$$

where J_1 is a first order Bessel function of the first kind. The parameters r_x and r_y are the horizontal and vertical semi-axes of the elliptical pillbox, respectively, and σ_x and σ_y are the horizontal and vertical width parameters for the 2D Gaussian component, respectively. The scaling factor a accounts for the magnification of the focal spot given the depth of the 3D vessel centerline, z_{CL}, the position of the image plane from which the vessel profile was extracted, z, and the source to detector distance, Z_D.

To obtain the LSF from the OTF, the projection slice theorem is applied. The OTF is not necessarily radially symmetric due to out of plane blurring and the focal spot shape. Therefore, the angle of the slice through the OTF needs to match the angle of the vessel profile being measured. For a vessel profile extracted at angle θ with respect to the X-axis, the LSF for that profile is given by

$$lsf_\theta(t) = \int_{-\infty}^{\infty} OTF(\rho\cos\theta, \rho\sin\theta)e^{2\pi i\rho t}d\rho. \tag{A.7}$$

The resulting $lsf_\theta(t)$ is used as one of the inputs into the parameterized model fitting algorithm to determine the vessel diameter from the extracted profile (see Chapter 2).

A.1 Line Spread Function Model Parameters for Chapter 2 (Feasibility)

The feasibility study presented in Chapter 2 was performed on the previous generation of the SBDX system. The most notable difference between the previous and current generations was the detector geometry. The previous generation featured a square detector, with 48 x 48 detector elements and a detector element pitch, Δ_D, of 1.14 mm. This affected the size of the blurring kernel due the back-projected detector element size Δ_d. In addition, the square detector meant that W_D and H_D were equal, as were the components of the out-of-plane blurring kernels, b_{tx} and b_{ty}. In other words, objects were blurred equally along the X and Y directions as the object moved away from the image plane.

The focal spot size was calculated by deconvolving the measured system MTF with the remaining sources of system blur (pixel size, backprojected detector element size, etc). To simplify the calculation, the focal spot used in the LSF calculations was assumed to be a circular pillbox. No Gaussian component of the focal spot was modeled. Under this assumption, the diameter of the focal spot was measured to be 0.9 mm at the source plane.

The restoration kernel r_{rest} was set equal to $1.732 * \Delta_p$, where Δ_p is the pixel size at the image plane. The scaling factor of 1.732 (i.e. $\sqrt{3}$) meant that the back-projected detector element samples were spread over square region with an area 3 times that of the area of a pixel. This value was used by convention for this generation of the SBDX system.

A.2 Line Spread Function Model for Chapters 4 and 5 (SDNR and *In vivo*)

The phantom studies in Chapter 4 as well as the animal model study in Chapter 5 were performed using a slightly different set of parameters to model the system LSF. The studies in these two chapters were performed using the current generation of the SBDX detector. This detector had 160 x 80 detector elements (width x height) and a detector element pitch of 0.66 mm. This reduced the size of the back-projected detector element size Δ_d and changed the out-of-plane blurring kernel sizes b_{tx} and b_{ty}. The rectangular detector caused the blurring to be greater along the X direction relative to the Y direction for same distance from the image plane.

Rather than inferring the size of the detector focal spot from the MTF, the focal spot component $F(\xi, \eta)$ was derived from an actual focal spot measurement made using the operating point with which the images in Chapter 4 and Chapter 5 were acquired (120 kV, 24 kW, 7 inch, 15 Hz). The focal spot was imaged using a pinhole aperture placed on the collimator exit, and the dimensions of the focal spot image at the detector were scaled to account for focal spot magnification. It was assumed that the focal spot can be modeled as an elliptical pillbox convolved with a 2D Gaussian as described in Equation A.4. The model had four parameters (r_x, r_y, σ_x, and σ_y), which were calculated by optimizing the parameters to fit the model to the focal spot image in a least squares sense. The parameter values used for the studies in Chapter 4 and Chapter 5 were 0.367 mm, 0.332 mm, 0.092 mm, and 0.088 mm for r_x, r_y, σ_x, and σ_y, respectively. Figure A.1 shows the focal spot image and the focal spot model.

The conventional value for the restoration kernel, r_{rest}, was changed from $1.732 * \Delta_p$, to simply Δ_p with the upgrade to the new detector. Thus, the back-projected detector element values were spread over a square area equal to the pixel size for a given image plane.

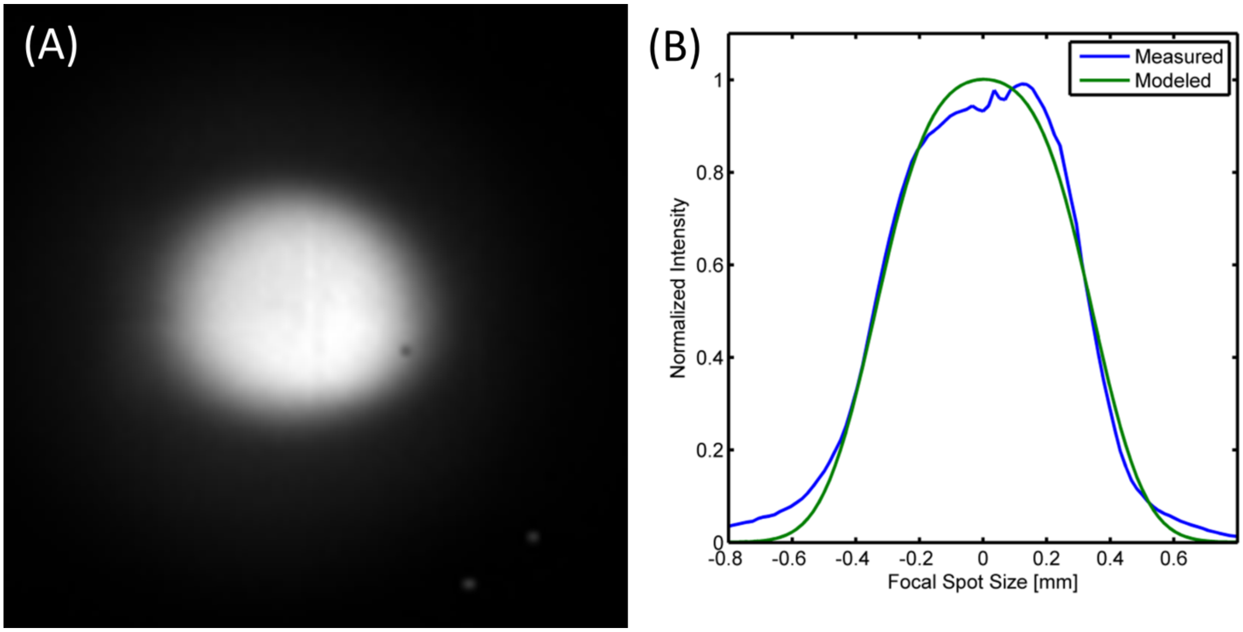

Figure A.1 – Focal Spot Measurement

(A) An image of the focal spot was created using a pinhole aperture on the exit side of the collimator and integrating multiple frames to create a low-noise image. (B) The focal spot was modeled as an elliptical pillbox convolved with a 2D Gaussian. The parameters of the model were optimized in a least squares sense to match the measured focal spot.

Appendix B – Active Contour Model for Depth Localization

The active contour model (sometimes called "snakes") is a powerful tool for image segmentation [55, 56]. It provides a continuous curve that locally minimizes several task-specific energy criteria to segment a feature if interest. The typical presentation of an active contour assumes a two dimensional closed contour. However, our implementation of the active contour for the defining a 3D vessel centerline assumes an open contour model. In addition, the positions of the points along the active contour are fixed in one dimension. Referencing Figure 3.6, the contour must span all of the columns in the image so that the depth is defined along the entire length of the vessel. The goal of deforming the active contour is to determine the vertical position (corresponding to vessel depth) for each point on the contour subject to a rigidity constraint which keeps the contour smooth. Therefore, the deformation of the contour is essentially one dimensional.

The following is a description of the depth localization step of the vessel sizing algorithm using the active contour framework. For simplicity, it is presented in the continuous domain, although in practice it is applied to discrete pixel values and an active contour with a finite number of discrete control points. Some additional implementation details are provided to further explain how the active contour was implemented, and why.

Starting from the results of the 2D vessel edge segmentation from the multiplane composite image, suppose there are two contours corresponding to the right and left edges of the vessel, $\boldsymbol{R}(s)$ and $\boldsymbol{L}(s)$, where $\boldsymbol{R}(s) = \left(X_R(s), Y_R(s)\right)$ and $\boldsymbol{L}(s) = \left(X_L(s), Y_L(s)\right)$ and s corresponds to length along the 2D vessel centerline over the interval $[0, l]$, where l is the total vessel segment length, in pixels. The straightened edge image $E_R(s,t,z)$ is defined as the pixel value of the image extracted t pixels from $\boldsymbol{R}(s)$, perpendicular to $\boldsymbol{R}(s)$, where positive t corresponds to right of the tangent of $\boldsymbol{R}(s)$, from a tomosynthetic image plane positioned a depth of z . Similarly, $E_L(s,t,z)$ is defined by $\boldsymbol{L}(s)$. Parameter t is defined over the interval $[-t_p, t_p]$.

The edge score image $S_L(s,t,z)$ is derived from an edge image $E_L(s,t,z)$ as described below through a series of transformations which is similar to the score image stack creation from the original vessel sizing algorithm.

$$E_L{}'(s,t,z) = \nabla_t \log\big(E_L(s,t,z)\big) \tag{B.1}$$

$$E_L{}''(s,t,z) = (1 - e^{E_L{}'(s,t,z)})*100 \tag{B.2}$$

$$S_L(s,t,z) = \begin{cases} E_L{}''(s,t,z) & E_L{}''(s,t,z) > 0 \\ 0 & otherwise \end{cases} \tag{B.3}$$

The same applies for $S_R(s,t,z)$. The two edge score images are summed together to increase the signal from the vessel edge while mitigating the effects of noise and side branches.

$$S(s,t,z) = S_L(s,t,z) + S_R(s,t,z) \tag{B.4}$$

An ROI mask $M(s,t)$ is applied to $S(s,t,z)$ and the values within it are summed to make the score sum image $SS(s,z)$, where

$$SS(s,z) = \int\int S(s,t,z) \cdot M(s,t,s) dsdt \tag{B.5}$$

$$M(s,t,s_0) = \begin{cases} 1 & \sqrt{(s-s_0)^2+t^2} \\ 0 & otherwise \end{cases} \tag{B.6}$$

The active contour $Z(s)$ is a curve fit through $SS(s,z)$ which calculates the depth z for a given value of s. It minimizes the energy term $\epsilon = \epsilon_{int} + \epsilon_{ext}$, the sum of the internal and external energies of the curve. The internal energy, ϵ_{int}, is calculated by the integral of the second derivative,

$$\epsilon_{int} = \int \beta(s) \left| \frac{d^2 Z(s)}{\mathrm{ds}^2} \right|^2 \tag{B.7}$$

where $\beta(s)$ is a weighting parameter. The external energy ϵ_{ext} is a function of where the active contour $Z(s)$ falls on the score sum image $SS(s,z)$. A potential energy function $P(s,z)$ is defined.

$$P(s,z) = w(\max\left(SS(s,z)\right) - SS(s,z)) \tag{B.8}$$

$$\epsilon_{ext} = \int_0^l P(s,z)ds \tag{B.9}$$

where w is another user defined weighting parameter.

In deforming $Z(s)$ to minimize ϵ, the curve is only adjusted along the z direction. After multiple iterations, $Z(s)$ provides a smooth continuous function of vessel depth as a function of position along the 2D vessel centerline. In practice, the 2D vessel centerline and edges are discretely sampled, and the image planes are only defined for specific depths. The score sum image is only defined at discrete values, which are determined by the spacing of the samples such that

$$SS[i,j] = SS(i\Delta s, j\Delta z) \tag{B.10}$$

where Δs, is typically 1 pixel and Δz is typically 5 mm. At isocenter, 1 pixel is equal to 0.161 mm. This relatively large difference in the physical spacing of the samples of $SS[i,j]$ is the reason why a minimum cost path approach is not feasible for defining $Z(s)$. The minimum cost path approach connects nodes defined only at discrete values of i and j. A transition from j to $j+1$ for example would create an unrealistic jump vessel depth of 5 mm. To make the spacing of the values of $SS[i,j]$ more isotropic, either more image planes would need to be reconstructed at sub millimeter depth intervals or the score sum image could be interpolated and resampled to have isotropic sampling. Assuming a typical plane stack of 32 planes with 5 mm plane spacing, and a 2D vessel segment centerline approximately 200 samples long, resampling to make Δz equal to 0.161 millimeters would result in finding the optimal path from 650 starting points. Finding the minimum cost path for such a large matrix would be time prohibitive. In addition, the minimum cost path approach does not allow the user to explicitly constrain the curvature of the solution.

While the active contour model is a continuous function, it is defined by a finite series of control points between which it is interpolated. In this implementation, the active contour $Z(s)$ has control points at $Z(i\Delta s)$ for $i = 0,1, \dots \frac{l}{\Delta s}$. In order to calculate the deformation due to internal energies at sample i, the values for $i-2, i-1, i, i+1, i+2$ are required [56]. For the typical case described in the literature of a closed 2D contour, the values for i can wrap around from N-1 to 0, assuming N total samples. In the case of an open contour, it does not make sense to wrap the values. The following is modification of the numerical implementation proposed by [56] to handle the case of an open contour. At the start of each iteration, ignore the values of $Z[i]$ for $i = 0,1$ ($i = N-2, N-1$). Instead, use the values of $Z[2]$, $Z[3]$, and $Z[4]$ ($Z[N-5]$, $Z[N-4]$, and $Z[N-3]$), to define a 2nd order polynomial, and extrapolate to find the values of $Z[0]$ and $Z[1]$ ($Z[N-2]$ and $Z[N-1]$). Next, set the rigidity weighting parameter $\beta[i]$, to zero for $i = 0,1$ ($i = N-2, N-1$). The net effect of these changes will be that the samples at $i = 0,1$ ($i = N-2, N-1$) will be deformed by external forces but not affected by internal forces. The effect of minimizing the internal forces on $i = 2$ ($i = N-3$) is indirectly applied to the samples at the end by the extrapolation step, which ensures that they stay consistent with the curve and are not entirely dictated by external energies.

References

[1] D. Lloyd-Jones, *et al.*, "Heart disease and stroke statistics--2010 update: a report from the American Heart Association," *Circulation,* vol. 121, pp. e46-e215, 2010.

[2] M. A. Speidel, B. P. Wilfley, J. M. Star-Lack, J. A. Heanue, and M. S. Van Lysel, "Scanning-beam digital x-ray (SBDX) technology for interventional and diagnostic cardiac angiography," *Med Phys,* vol. 33, pp. 2714-2727, 2006.

[3] M. A. Speidel, *et al.*, "Comparison of entrance exposure and signal-to-noise ratio between an SBDX prototype and a wide-beam cardiac angiographic system," *Med Phys,* vol. 33, pp. 2728-2743, 2006.

[4] M. A. Speidel, A. P. Lowell, J. A. Heanue, and M. S. Van Lysel, "Frame-by-frame 3D catheter tracking methods for an inverse geometry cardiac interventional system," *Proc SPIE,* vol. 6913, 2008.

[5] M. A. Speidel, M. T. Tomkowiak, A. N. Raval, and M. S. Van Lysel, "Three-dimensional tracking of cardiac catheters using an inverse geometry x-ray fluoroscopy system," *Med Phys,* vol. 37, pp. 6377-6389, 2010.

[6] B. J. Gersh, *Mayo Clinic heart book : the ultimate guide to heart health*, 2nd ed. New York: W. Morrow, 2000.

[7] E. Cheneau, *et al.*, "Predictors of subacute stent thrombosis: results of a systematic intravascular ultrasound study," *Circulation,* vol. 108, pp. 43-7, 2003.

[8] K. Fujii, *et al.*, "Stent underexpansion and residual reference segment stenosis are related to stent thrombosis after sirolimus-eluting stent implantation: an intravascular ultrasound study," *J Am Coll Cardiol,* vol. 45, pp. 995-8, 2005.

[9] R. Kuntz, *et al.*, "The importance of acute luminal diameter in determining restenosis after coronary atherectomy or stenting," *Circulation,* vol. 86, pp. 1827-1835, 1992.

[10] A. B. Nichols, R. Smith, A. D. Berke, R. A. Shlofmitz, and E. R. Powers, "Importance of balloon size in coronary angioplasty," *J Am Coll Cardiol,* vol. 13, pp. 1094-100, 1989.

[11] A. Colombo, *et al.*, "Intracoronary stenting without anticoagulation accomplished with intravascular ultrasound guidance," *Circulation,* vol. 91, pp. 1676-88, 1995.

[12] G. Roubin, *et al.*, "Influence of balloon size on initial success, acute complications, and restenosis after percutaneous transluminal coronary angioplasty. A prospective randomized study," *Circulation,* vol. 78, pp. 557-565, 1988.

[13] S. P. Schwarzacher, J. A. Metz, P. G. Yock, and P. J. Fitzgerald, "Vessel tearing at the edge of intracoronary stents detected with intravascular ultrasound imaging," *Cathet Cardiovasc Diagn,* vol. 40, pp. 152-155, 1997.

[14] Y. Honda, P. G. Yock, and P. J. Fitzgerald, "Impact of residual plaque burden on clinical outcomes of coronary interventions," *Catheter Cardiovasc Interv,* vol. 46, pp. 265-276, 1999.

[15] L. Räber*, et al.*, "Impact of Stent Overlap on Angiographic and Long-Term Clinical Outcome in Patients Undergoing Drug-Eluting Stent Implantation," *J Am Coll Cardiol,* vol. 55, pp. 1178-1188, 2010.

[16] S. Ellis*, et al.*, "Restenosis after placement of Palmaz-Schatz stents in native coronary arteries. Initial results of a multicenter experience," *Circulation,* vol. 86, pp. 1836-1844, 1992.

[17] A. Chieffo*, et al.*, "Intraprocedural Stent Thrombosis During Implantation of Sirolimus-Eluting Stents," *Circulation,* vol. 109, pp. 2732-2736, 2004.

[18] S. Shirai*, et al.*, "Impact of Multiple and Long Sirolimus-Eluting Stent Implantation on 3-Year Clinical Outcomes in the j-Cypher Registry," *JACC Cardiovasc Interv,* vol. 3, pp. 180-188, 2010.

[19] S. Kasaoka*, et al.*, "Angiographic and intravascular ultrasound predictors of in-stent restenosis," *J Am Coll Cardiol,* vol. 32, pp. 1630-1635, 1998.

[20] Y. Kobayashi*, et al.*, "Stented segment length as an independent predictor of restenosis," *J Am Coll Cardiol,* vol. 34, pp. 651-659, 1999.

[21] L. National Heart, and Blood Institute; National Institutes of Health; U.S. Department of Health and Human Services. (2012, 8/21/2013). *How is coronary angioplasty done?* Available: http://www.nhlbi.nih.gov/health/health-topics/topics/angioplasty/howdone.html

[22] F. Sera*, et al.*, "Optimal stent-sizing with intravascular ultrasound contributes to complete neointimal coverage after sirolimus-eluting stent implantation assessed by angioscopy," *JACC Cardiovasc Interv,* vol. 2, pp. 989-94, 2009.

[23] A. L. Gaster*, et al.*, "Continued improvement of clinical outcome and cost effectiveness following intravascular ultrasound guided PCI: insights from a prospective, randomised study," *Heart,* vol. 89, pp. 1043-1049, 2003.

[24] M. C. McDaniel, P. Eshtehardi, F. J. Sawaya, J. S. Douglas, Jr., and H. Samady, "Contemporary clinical applications of coronary intravascular ultrasound," *JACC Cardiovasc Interv,* vol. 4, pp. 1155-67, 2011.

[25] J. L. Orford, A. Lerman, and D. R. Holmes, "Routine intravascular ultrasound guidance of percutaneous coronary intervention: a critical reappraisal," *J Am Coll Cardiol,* vol. 43, pp. 1335-42, 2004.

[26] D. Hausmann*, et al.*, "The safety of intracoronary ultrasound. A multicenter survey of 2207 examinations," *Circulation,* vol. 91, pp. 623-30, 1995.

[27] J. H. C. Reiber*, et al.*, "Coronary Artery Dimensions from Cineangiograms¿ Methodology and Validation of a Computer-Assisted Analysis Procedure," *IEEE Trans Med Imag,* vol. 3, pp. 131-141, 1984.

[28] S. R. Fleagle*, et al.*, "Automated analysis of coronary arterial morphology in cineangiograms: geometric and physiologic validation in humans," *IEEE Trans Med Imag,* vol. 8, pp. 387-400, 1989.

[29] A. B. Nichols, C. F. Gabrieli, J. J. Fenoglio, Jr., and P. D. Esser, "Quantification of relative coronary arterial stenosis by cinevideodensitometric analysis of coronary arteriograms," *Circulation,* vol. 69, pp. 512-22, 1984.

[30] O. Nalcioglu*, et al.*, "Background subtraction algorithms for videodensitometric quantification of coronary stenosis," *Machine Vision and Applications,* vol. 1, pp. 155-162, 1988.

[31] T. N. Pappas and J. S. Lim, "A new method for estimation of coronary artery dimensions in angiograms," *IEEE Trans Acoust Speech Signal Process,* vol. 36, pp. 1501-1513, 1988.

[32] M. T. Tomkowiak, M. A. Speidel, A. N. Raval, and M. S. Van Lysel, "Calibration-free device sizing using an inverse geometry x-ray system," *Med Phys,* vol. 38, pp. 283-293, 2011.

[33] J. H. C. Reiber*, et al.*, "Quantitative Coronary Arteriography," in *Coronary Radiology*, M. Oudkerk and M. F. Reiser, Eds., ed Berlin: Springer-Verlag, 2009, pp. 41-65.

[34] W. Wunderlich*, et al.*, "Three-D localization of the coronary segment and calibration catheter to correct for differential magnification in quantitative coronary angiography," in *Computers in Cardiology 1999*, 1999, pp. 371-374.

[35] M. Treitl*, et al.*, "Assessment of the Vessel Lumen Diameter and Degree of Stenosis in the Superficial Femoral Artery before Intervention: Comparison of Different Algorithms," *J Vasc Interv Radiol,* vol. 20, pp. 192-202, 2009.

[36] F. Moselewski*, et al.*, "Comparison of measurement of cross-sectional coronary atherosclerotic plaque and vessel areas by 16-slice multidetector computed tomography versus intravascular ultrasound," *Am J Cardiol,* vol. 94, pp. 1294-7, 2004.

[37] S. J. Chen and J. D. Carroll, "3-D reconstruction of coronary arterial tree to optimize angiographic visualization," *IEEE Trans Med Imag,* vol. 19, pp. 318-36, 2000.

[38] B. Movassaghi, V. Rasche, M. Grass, M. A. Viergever, and W. J. Niessen, "A quantitative analysis of 3-D coronary modeling from two or more projection images," *IEEE Trans Med Imag,* vol. 23, pp. 1517-31, 2004.

[39] U. Jandt, D. Schafer, M. Grass, and V. Rasche, "Automatic generation of 3D coronary artery centerlines using rotational X-ray angiography," *Med Image Anal,* vol. 13, pp. 846-58, 2009.

[40] U. Jandt, D. Schafer, M. Grass, and V. Rasche, "Automatic generation of time resolved motion vector fields of coronary arteries and 4D surface extraction using rotational x-ray angiography," *Phys Med Biol,* vol. 54, pp. 45-64, 2009.

[41] E. Hansis, J. D. Carroll, D. Schafer, O. Dossel, and M. Grass, "High-quality 3-D coronary artery imaging on an interventional C-arm x-ray system," *Med Phys,* vol. 37, pp. 1601-9, 2010.

[42] A. M. Neubauer*, et al.*, "Clinical feasibility of a fully automated 3D reconstruction of rotational coronary X-ray angiograms," *Circ Cardiovasc Interv,* vol. 3, pp. 71-9, 2010.

[43] J. T. Dobbins, III and D. J. Godfrey, "Digital x-ray tomosynthesis: current state of the art and clinical potential," *Phys Med Biol,* vol. 48, pp. R65-R106, 2003.

[44] R. C. Chan, W. C. Karl, and R. S. Lees, "A new model-based technique for enhanced small-vessel measurements in X-ray cine-angiograms," *IEEE Trans Med Imag,* vol. 19, pp. 243-255, 2000.

[45] R. C. Gonzalez and R. E. Woods, *Digital Image Processing*, 3rd ed. Upper Saddle River, NJ: Pearson/Prentice Hall, 2008.

[46] T. Betts, "Metallic Alloys for use in Radiographic Phantoms," PhD Thesis, Medical Physics, University of Wisconsin, Madison, 2010.

[47] J. A. Garcia*, et al.*, "Determination of optimal viewing regions for X-ray coronary angiography based on a quantitative analysis of 3D reconstructed models," *Int J Cardiovasc Imaging,* vol. 25, pp. 455-462, 2008.

[48] J. P. Janssen, G. Koning, P. J. de Koning, J. C. Tuinenburg, and J. H. Reiber, "A novel approach for the detection of pathlines in X-ray angiograms: the wavefront propagation algorithm," *Int J Cardiovasc Imaging,* vol. 18, pp. 317-24, 2002.

[49] P. M. van der Zwet, I. M. Pinto, P. W. Serruys, and J. H. Reiber, "A new approach for the automated definition of path lines in digitized coronary angiograms," *Int J Card Imaging,* vol. 5, pp. 75-83, 1990.

[50] C. Kirbas and F. Quek, "A review of vessel extraction techniques and algorithms," *ACM Comput. Surv.,* vol. 36, pp. 81-121, 2004.

[51] F. K. H. Quek and C. Kirbas, "Vessel extraction in medical images by wave-propagation and traceback," *IEEE Trans Med Imag,* vol. 20, pp. 117-131, 2001.

[52] E. W. Djikstra, "A note on two problems in connexion with graphs," *Numerische Mathematik,* vol. 1, pp. 269-271, 1959.

[53] N. J. Nilsson, *Problem-Solving Methods in Artificial Intelligence*. New York: McGraw-Hill, 1971.

[54] J. M. Tenenbaum, "Accomodation in Computer Vision," Ph. D., Computer Science, Stanford University, 1971.

[55] M. Kass, A. Witkin, and D. Terzopoulos, "Snakes: Active contour models," *International Journal of Computer Vision,* vol. 1, pp. 321-331, 1988.

[56] C. Xu and J. L. Prince, "Medical Image Segmentation Using Deformable Models," in *Handbook of Medical Imaging, Volume 2: Medical Image Processing and Analysis*, J. M. Fitzpatrick and M. Sonka, Eds., ed Bellingham: SPIE Press, 2000, pp. 129-174.

[57] J. R. Spears*, et al.*, "Computerized image analysis for quantitative measurement of vessel diameter from cineangiograms," *Circulation,* vol. 68, pp. 453-461, 1983.

[58] W. H. Leung, W. Sanders, and E. L. Alderman, "Coronary artery quantitation and data management system for paired cineangiograms," *Cathet Cardiovasc Diagn,* vol. 24, pp. 121-34, 1991.

[59] D. M. Herrington, M. Siebes, and G. D. Walford, "Sources of error in quantitative coronary angiography," *Cathet Cardiovasc Diagn,* vol. 29, pp. 314-21, 1993.

[60] G. Finet and J. Liénard, "Parameters that influence accuracy and precision of quantitative coronary arteriography," *Int J Card Imaging,* vol. 12, pp. 271-287, 1996.

[61] K. R. Hoffmann*, et al.*, "Vessel size measurements in angiograms: A comparison of techniques," *Med Phys,* vol. 29, pp. 1622-1633, 2002.

[62] H. Fujita, K. Doi, L. E. Fencil, and K. G. Chua, "Image feature analysis and computer-aided diagnosis in digital radiography. 2. Computerized determination of vessel sizes in digital subtraction angiography," *Med Phys,* vol. 14, pp. 549-56, 1987.

[63] J. Haase*, et al.*, "Experimental validation of geometric and densitometric coronary measurements on the new generation Cardiovascular Angiography Analysis System (CAAS II)," *Cathet Cardiovasc Diagn,* vol. 30, pp. 104-14, 1993.

[64] D. M. Weber, "Absolute diameter measurements of coronary arteries based on the first zero crossing of the Fourier spectrum," *Med Phys,* vol. 16, pp. 188-196, 1989.

[65] M. Sonka, G. K. Reddy, M. D. Winniford, and S. M. Collins, "Adaptive approach to accurate analysis of small-diameter vessels in cineangiograms," *IEEE Trans Med Imag,* vol. 16, pp. 87-95, 1997.

[66] U. Dietz*, et al.*, "Comparison of QCA systems," *Int J Card Imaging,* vol. 13, pp. 271-80, 1997.

[67] T. Sandor, A. D'Adamo, W. B. Hanlon, and J. Spears, "High precision quantitative angiography," *IEEE Trans Med Imag,* vol. 6, pp. 258-65, 1987.

[68] S. Tu, N. R. Holm, G. Koning, Z. Huang, and J. H. Reiber, "Fusion of 3D QCA and IVUS/OCT," *Int J Cardiovasc Imaging,* vol. 27, pp. 197-207, 2011.

[69] S. Tu, G. Koning, W. Jukema, and J. H. Reiber, "Assessment of obstruction length and optimal viewing angle from biplane X-ray angiograms," *Int J Cardiovasc Imaging,* vol. 26, pp. 5-17, 2010.

[70] D. Meerkin, H. Marom, O. Cohen-Biton, and S. Einav, "Three-dimensional vessel analyses provide more accurate length estimations than the gold standard QCA," *J Interv Cardiol,* vol. 23, pp. 152-9, 2010.

[71] J. C. Gurley*, et al.*, "Comparison of simultaneously performed digital and film-based angiography in assessment of coronary artery disease," *Circulation,* vol. 78, pp. 1411-20, 1988.

[72] S. Y. Molloi, A. Ersahin, W. W. Roeck, and O. Nalcioglu, "Absolute cross-sectional area measurements in quantitative coronary arteriography by dual-energy DSA," *Invest Radiol,* vol. 26, pp. 119-27, 1991.

[73] J. H. C. Reiber, G. Koning, C. D. Von Land, and P. M. J. Van Der Zwet, "Why and how should QCA systems be Validated?," in *Progress in Quantitative Coronary Arteriography*, J. H. C. Reiber and P. W. Serruys, Eds., ed Dordrecht: Kluwer Academic Publishers, 1994, pp. 34-48.

[74] J. Wiesel, A. M. Grunwald, C. Tobiasz, B. Robin, and M. M. Bodenheimer, "Quantitation of absolute area of a coronary arterial stenosis: experimental validation with a preparation in vivo," *Circulation,* vol. 74, pp. 1099-106, 1986.

[75] G. Mancini*, et al.*, "Automated quantitative coronary arteriography: morphologic and physiologic validation in vivo of a rapid digital angiographic method [published erratum appears in Circulation 1987 Jun;75(6):1199]," *Circulation,* vol. 75, pp. 452-460, 1987.

[76] J. Haase*, et al.*, "In-vivo validation of on-line and off-line geometric coronary measurements using insertion of stenosis phantoms in porcine coronary arteries," *Cathet Cardiovasc Diagn,* vol. 27, pp. 16-27, 1992.

[77] H. Gewirtz and A. S. Most, "Production of a critical coronary arterial stenosis in closed chest laboratory animals. Description of a new nonsurgical method based on standard cardiac catheterization techniques," *Am J Cardiol,* vol. 47, pp. 589-96, 1981.

[78] D. M. Weber, S. Y. Molloi, J. D. Folts, W. W. Peppler, and C. A. Mistretta, "Geometric quantitative coronary arteriography. A comparison of unsubtracted and dual energy-subtracted images," *Invest Radiol,* vol. 26, pp. 649-54, 1991.

[79] M. A. Simons*, et al.*, "Quantitative Digital Subtraction Coronary Angiography Using Videodensitometry: An In Vivo Analysis," *Invest Radiol,* vol. 23, pp. 98-106, 1988.

[80] A. Aldrovandi*, et al.*, "Evaluation of coronary atherosclerosis by multislice computed tomography in patients with acute myocardial infarction and without significant coronary artery stenosis: a comparative study with quantitative coronary angiography," *Circ Cardiovasc Imaging,* vol. 1, pp. 205-11, 2008.

[81] N. Funabashi, Y. Kobayashi, M. Perlroth, and G. D. Rubin, "Coronary artery: quantitative evaluation of normal diameter determined with electron-beam CT compared with cine coronary angiography initial experience," *Radiology,* vol. 226, pp. 263-71, 2003.

[82] R. Blasini, F. J. Neumann, C. Schmitt, J. Bokenkamp, and A. Schomig, "Comparison of angiography and intravascular ultrasound for the assessment of lumen size after coronary stent placement: impact of dilation pressures," *Cathet Cardiovasc Diagn,* vol. 42, pp. 113-9, 1997.

[83] A. G. Davies, D. Conway, S. Reid, A. R. Cowen, and M. Sivananthan, "Assessment of coronary stent deployment using computer enhanced x-ray images-validation against intravascular ultrasound and best practice recommendations," *Catheter Cardiovasc Interv,* vol. 81, pp. 419-27, 2013.

[84] I. De Scheerder*, et al.*, "Intravascular ultrasound versus angiography for measurement of luminal diameters in normal and diseased coronary arteries," *Am Heart J,* vol. 127, pp. 243-51, 1994.

[85] S. E. Nissen*, et al.*, "Application of a new phased-array ultrasound imaging catheter in the assessment of vascular dimensions. In vivo comparison to cineangiography," *Circulation,* vol. 81, pp. 660-6, 1990.

[86] A. M. Sinha*, et al.*, "Multidetector-row computed tomography vs. angiography and intravascular ultrasound for the evaluation of the diameter of proximal coronary arteries," *Int J Cardiol,* vol. 110, pp. 40-5, 2006.

[87] F. G. St Goar*, et al.*, "Intravascular ultrasound imaging of angiographically normal coronary arteries: An in vivo comparison with quantitative angiography," *J Am Coll Cardiol,* vol. 18, pp. 952-958, 1991.

[88] J. Lee*, et al.*, "Assessment of three dimensional quantitative coronary analysis by using rotational angiography for measurement of vessel length and diameter," *Int J Cardiovasc Imaging,* vol. 28, pp. 1627-1634, 2012.

[89] S. Tu*, et al.*, "In vivo comparison of arterial lumen dimensions assessed by co-registered three-dimensional (3D) quantitative coronary angiography, intravascular ultrasound and optical coherence tomography," *Int J Cardiovasc Imaging,* vol. 28, pp. 1315-1327, 2012.

[90] S. M. O'Malley, J. F. Granada, S. Carlier, M. Naghavi, and I. A. Kakadiaris, "Image-based gating of intravascular ultrasound pullback sequences," *IEEE Trans Inf Technol Biomed,* vol. 12, pp. 299-306, 2008.

[91] W. Li*, et al.*, "Semi-automatic contour detection for volumetric quantification of intracoronary ultrasound," in *Computers in Cardiology 1994*, 1994, pp. 277-280.

[92] G. Koning*, et al.*, "Advanced contour detection for three-dimensional intracoronary ultrasound: a validation--in vitro and in vivo," *Int J Cardiovasc Imaging,* vol. 18, pp. 235-48, 2002.

[93] C. von Birgelen*, et al.*, "Morphometric analysis in three-dimensional intracoronary ultrasound: an in vitro and in vivo study performed with a novel system for the contour detection of lumen and plaque," *Am Heart J,* vol. 132, pp. 516-27, 1996.

[94] R. T. Fuessl*, et al.*, "In vivo validation of intravascular ultrasound length measurements using a motorized transducer pullback system," *Am J Cardiol,* vol. 77, pp. 1115-8, 1996.

[95] M. Ciszewski*, et al.*, "Comparison of stent length reported by the stent's manufacturer to that determined by quantitative coronary angiography at the time of implantation versus that determined by coronary computed tomographic angiography at a later time," *Am J Cardiol,* vol. 111, pp. 1111-6, 2013.

[96] K. P. Gallagher, J. D. Folts, and G. G. Rowe, "Comparison of coronary arteriograms with direct measurements of stenosed coronary arteries in dogs," *Am Heart J,* vol. 95, pp. 338-47, 1978.

[97] R. L. Kirkeeide, K. L. Gould, and L. Parsel, "Assessment of coronary stenoses by myocardial perfusion imaging during pharmacologic coronary vasodilation. VII. Validation of coronary flow reserve as a single integrated functional measure of stenosis severity reflecting all its geometric dimensions," *J Am Coll Cardiol,* vol. 7, pp. 103-13, 1986.

[98] R. J. Peters, *et al.*, "Videodensitometric quantitative angiography after coronary balloon angioplasty, compared to edge-detection quantitative angiography and intracoronary ultrasound imaging," *Eur Heart J,* vol. 21, pp. 654-61, 2000.

[99] R. Aufrichtig and D. L. Wilson, "X-ray fluoroscopy spatio-temporal filtering with object detection," *IEEE Trans Med Imag,* vol. 14, pp. 733-746, 1995.

[100] M. Stahl, T. Aach, and S. Dippel, "Digital radiography enhancement by nonlinear multiscale processing," *Med Phys,* vol. 27, pp. 56-65, 2000.

[101] M. Söderman, *et al.*, "Image Noise Reduction Algorithm for Digital Subtraction Angiography: Clinical Results," *Radiology,* 2013.